Synthesis and characterization of 2D complex oxide films in the SrTiO /Pt(111)/Al O (0001) system

Catalina Ruano Merchán

UNIVERSITÉ DE LORRAINE

INSTITUT JEAN LAMOUR

C2MP

THÈSE

Pour l'obtention du titre de

Docteure de l'Université de Lorraine

(mention Science des matériaux)

Présentée et soutenue publiquement le 31 mars 2022
par

CATALINA RUANO MERCHÁN

Synthesis and characterization of 2D complex oxide films in the $SrTiO_3/Pt(111)/Al_2O_3(0001)$ system

Composition du jury :

Président :	M. Yannick FAGOT-REVURAT	Professeur, Université de Lorraine
Rapporteurs :	Mme. Anouk GALTAYRIES	Maître de Conférences, Chimie ParisTech - PSL
	M. Rémi LAZZARI	Directeur de recherche, Sorbonne Université
Examinateurs :	M. Wolf WIDDRA	Professeur, Martin Luther Universität, Halle
	Mme. Laurence MASSON	Professeure, Aix Marseille Université
Directeur :	M. Vincent FOURNÉE	Directeur de Recherche, Université de Lorraine
Co-Directrice :	Mme. Muriel SICOT	Chargée de recherche, Université de Lorraine
Invité :	M. Olivier COPIE	Chargé de recherche, Université de Lorraine

Institut Jean Lamour - UMR 7198 - Département CP2S - Équipe 203
École Doctorale C2MP

Remerciements

Foremost, I would like to express my sincere gratitude to the members of the jury. Special thanks to the referees Dr. Anouk Galtayries and Dr. Rémi Lazzari, for the time you devoted to the reading of my manuscript. Thanks to Dr. Wolf Widdra, Dr. Laurance Masson and Dr. Yannick Fagot and Dr. Olivier Copie as well, for agreeing to be part of this committee and for all your kind comments and interesting discussions.

I would like to thank Thierry Belmonte for his welcome at the IJL and all the administration staff of the IJL and the École Doctoral C2PM for their support and help over the past three years. Specially tanks to Christine Sartori and Juliette Barbat. I also would like to thank The École doctorale C2MP for granting a doctoral contract with the Université de Lorraine for funding my thesis.

The completion of this thesis could not be possible without the expertise, the guidance and the advices of my supervisors. Muriel Sicot, thank you for having accepted me to explore with you the fascinating field of the oxide quasicrystals. Thanks for the enriching discussions and for conducing me during my formation as a scientist. I learnt a lot from you. Vincent Fournée, I would like to thank you as well for considering me for this project. Thank you for guiding me during experiments, for all the explanations about the techniques and the inspiration yo gave me to pursue an academic career. I would like to thank you as well for helping me during my arrival to Nancy as well for inviting me to play with the snow! I will never forget it.

My deepest gratitude to Olivier Copie who guide me in every step during the development of this work. As the PLD expert at the IJL, I thank you for the time spent in the sample fabrication and all the explanations regarding the technique and the physics involved. I also appreciate very much the time that you devoted to the reading of my manuscript. Thank you for all the discussions and the valuable feedback. Thank you as well for the encouragement you gave me along these years.

A debt of gratitude is also owed to Ludovic Pasquier from the C.C. Daum for all his support during the sample's fabrication at the TUBE. It was a pleasure to work with you! I greatly appreciate your commitment to your work as well as all the technical explanations and the guidance I received during the MBE depositions.

I would also like to give special thanks to Julian Ledieu for all his help specially during the last part of this thesis. The new approximant phases reported here were discovered in the ASURE platform at your charge! Thank you for managing the time

and organization so I could do the experiments that I needed. I greatly appreciate the time you devoted to teaching me how to do use the equipments and how to do transfers. Thank you for all your advices, ideas and all the scientific discussions as well.

The theoretical studies presented in this thesis were supervised by Émilie Gaudry. All my gratitude to you. Thank you for sharing with me your expertise in the DFT, and for all the fruitful scientific discussions.

Special thanks to Marie-Cécile for your warm welcome to the team, for your kindness and committed work to the team. It was a pleasure to share with you these years of thesis.

My sincere thanks to Stéphane Andrieu and Karine Dumesnil from Team 101 for their collaboration throughout the development of this project, specially during the MBE depositions.

To my "comité de suivi" Thomas Hauet and Christophe Chatelain, my deepest appreciation for your time dedicated to follow the development of my thesis work. Thank you for your appropriate advices and remarks.

I would like to specially thanks as well, Sašo Šturm and Sorour Semsari Parapari from the Jožef Stefan Institute in Slovenia, for their collaboration in the TEM measurements.

I appreciate as well the fruitful discussions with Stefan Förster and Sebastian Schenk during the international conferences were we had the opportunity to meet. Thank you for your availability, your kindness and for being open to share ideas and perspectives with us.

My time at the IJL wouldn't be the same without the company, the support and the good moments shared with exceptional PhD students and postdocs who became friends and even family. I am grateful as well for the opportunity given to me of expanding my borders getting to know amazing people from different countries and cultures. I thank sincerely to Alberto, Alexis, Zil, Alejandro, Claudia, Mauricio, Lorena, Luigi, Kaushalya and Sayva.

I am specially grateful with Dominique, Sébastien, Kathleen, Miguel, Corentin, Kanika, Mihai and Mimi (Yiming). "A sweet friendship refreshes the soul", says a Proverb. I can't thank you enough for your sweet friendship reflected in support, love, help and kindness to me.

I'm beyond grateful to Thiago Dorini. The theoretical investigations performed by Thiago under the supervision of Émilie Gaudry contributed to a better under-

standing of the oxide quasicrystals. Thank you for sharing with me your expertise in the *ab initio* calculations and explaining to me with all patience the procedure and results. Surpassing the scientific discussions, your continuous support and understanding during these years were invaluable to me. All my gratitude to you as well, for fulling my days with hope and happiness. Your optimism encouraged me to don't stop believing.

To my Brazilian friends Rafa, Myrla, Chaves, Leandro and Giselle: todo meu amor e gratidão pelos momentos vividos com vocês. Levar-vos-ei sempre no meu coração, na minha memória.

I would like to thank my friends who are family to me: David, Jean-Maurice, Timéa, Doréa and Gerson. All my affection to you.

Last but not least, I have to give credit were it is due. To my family. Gracias por todo el apoyo enviado con tanto cariño desde la distancia. Sus oraciones, su amor casi tangible entre cada llamada, entre cada zoom, me ha sostenido durante estos años. Este trabajo de tesis les pertenece completamente.

To all women in science.

Résumé

La formation d'oxydes bidimensionels de structures quasicristallines ou approximants a été rapportée récemment. Ces phases complexes sont obtenues par réduction de films de pérovskites $BaTiO_3$ ou $SrTiO_3$ déposés sur des monocristaux de Pt(111). Elles représentent une nouvelle famille d'oxydes ultra-minces supportés par des métaux, ainsi qu'une nouvelle classe de materiaux quasipériodiques, avec potentiellement de nouvelles proprietés physico-chimiques qui restent à explorer. Ici, nous utilisons une approche d'empilement de couches minces dans laquelle le monocristal est remplacé par une couche tampon de Pt(111), déposée par épitaxie par jet moléculaire (MBE) sur un substrat d'Al_2O_3(0001). Un film ultra-mince de $SrTiO_3$ a ensuite été déposé par dépôt laser pulsé (PLD). L'empilement de films est entièrement caractérisé par des techniques de diffraction (LEED, RHEED, XRD), de microscopie (STM, Nano-SAM, TEM) et de spectroscopie (XPS, AES). Nous rapportons la découverte de trois nouveaux approximants obtenus par réduction de ce système par recuit à haute température dans des conditions de vide poussé (UHV). Ces phases peuvent être décrites par trois pavages différents construits avec des éléments du pavage de Niizeki-Gähler (NGT). Un modèle atomique déterminé par des calculs *ab initio* (DFT), en accord avec les observations expérimentales, est proposé. Cette approche en couche mince peut être utile pour explorer la formation de phases d'oxyde 2D complexes dans d'autres combinaisons métal-oxyde.

Abstract

The formation of two-dimensional oxides with quasicrystalline or approximant structures has recently been reported. These complex phases are obtained by reduction of $BaTiO_3$ or $SrTiO_3$ perovskite films deposited on single crystals of Pt(111). They represent a new family of ultra-thin oxides supported on metals, as well as a new class of quasiperiodic materials, with potentially new physicochemical properties that remain to be explored. Here we use a thin film stacking approach in which the single crystal is replaced by a Pt(111) buffer layer, deposited by molecular beam epitaxy (MBE) on an Al_2O_3(0001) substrate. An ultra-thin film of $SrTiO_3$ was then deposited by pulsed laser deposition (PLD). The film stack is fully characterized by diffraction (LEED, RHEED, XRD), microscopy (STM, TEM, Nano-SAM) and spectroscopy (XPS, AES) techniques. We report the discovery of three novel approximants obtained by reducing this system by annealing at high temperature under high vacuum (UHV) conditions. These phases can be described by three different tilings constructed with the Niizeki-Gähler tiling elements (NGT). An atomic model studied by *ab initio* calculations (DFT), in agreement with the experimental observations, is proposed. This thin-film approach can be useful for exploring the formation of complex 2D oxide phases in other metal-oxide combinations.

Synthèse

Cette synthèse constitue un résumé étendu des travaux de thèse réalisés à l'institut Jean Lamour. Après une brève introduction, les objectifs généraux de la thèse sont exposés ainsi que les principales méthodes expérimentales et théoriques utilisées. Dans une deuxième partie, nous présentons les principaux résulats obtenus tout au long de la thèse. Les conclusions et perspectives feront l'objet de la dernière partie.

Introduction

Au cours des deux dernières décennies, de grands progrès ont été réalisés dans le domaine de la fabrication, la caractérisation et la modélisation théorique de films d'oxyde ultrafins (UTOx) supportés par des métaux. Dans la limite bidimensionnelle (2D), les UTOx peuvent présenter des structures atomiques et électroniques qui diffèrent de celles des oxydes massifs. La structure et les propriétés physiques des UTOx sont fortement influencées par les interactions à l'interface oxyde/métal. Ils peuvent présenter des propriétés remarquables comme par exemple la présence d'un gaz d'électron 2D confiné à l'interface oxyde/métal [1]. De nombreuses phases d'oxydes 2D ont été élaborés sur différentes surfaces métalliques et présentent des structures atomiques qui n'ont pas d'équivalents en volume [1, 2]. Il s'agit d'une nouvelle classe de matériaux 2D. La compréhension des règles fondamentales guidant la formation des UTOx et les relations entre leurs structures atomiques locales et leurs propriétés physico-chimiques font toujours l'objet de recherches actives.

Ces matériaux 2D peuvent être décrits le plus souvent à partir de motifs structuraux constitués de tuiles élémentaires telles que des carrés ou des triangles, auxquelles sont associées une décoration chimique, par exemple MO4 et MO3 (M : un métal, O : oxygène). Ces tuiles peuvent être assemblées pour paver le plan de différentes manières formant des structures de complexité variable [1]. Pour une combinaison métal/oxyde donnée, différents motifs structuraux peurent être formés avec une stœchiométrie, des paramètres de réseau, un état de charge et des relations épitaxiales particulières avec le substrat [1].

Parmi ces oxydes 2D dont la structure n'a pas d'équivalent en volume, la dé-

couverte d'oxydes quasicristallins (OQC) bidimensionnels en 2013 par Förster et al. représente certainement une forme de complexité ultime [3]. Ces nouvelles phases quasicristalline se forment à partir de films minces d'oxydes ternaires épitaxiées sur un substrat métallique d'orientation (111). Leurs structures peuvent être décrites par un assemblage de tuiles élémentaires comprenant des carrés, des triangles et des losanges d'angle au sommet égal à 30°. En 2013, Förster *et. al.* ont observé la formation d'un OQC 2D à partir d'un film mince de $BaTiO_3$ déposés par épitaxie sur un substrat monocristallin de Pt(111) [3]. Quatre ans plus tard, Schenk *et. al.* ont reporté la formation d'un OQC à l'interface d'un film mince de $SrTiO_3$ épitaxié également sur un substrat de Pt orienté (111) [4], démontrant que la formation d'OQC pouvait être étendue à différentes combinaisons oxydes/métaux. Ces découvertes ont fait émerger un nouveau champ de recherche, à l'interface entre le domaine des matériaux apériodiques et celui des oxydes ultraminces. Les OQC de symétrie dodécagonale observés coexistent fréquemment avec des phases périodiques dites "approximantes", c'est-à-dire des phases à grande maille présentant un ordre local similaire à celui présent dans les phases quasicristallines [5]. L'existence de phases approximantes est intéressante, car la périodicité retrouvée permet d'utiliser les outils de la physique des solides. En particulier, il est possible d'effectuer des calculs *ab initio* à partir de modèles de structure atomique, ce qui est une étape importante vers la compréhension de toutes les structures observées [6, 7]. Jusqu'à présent, ces structures ont été trouvées à partir de deux pérovskites elaborées sur un substrat de Pt. De plus, au début de cette thèse, seules deux combinaisons oxyde/métal avaient été explorées : $BaTiO_3$/Pt(111) et $SrTiO_3$/Pt(111). Au cours des trois dernières années, des approximants OQC ont été trouvés dans d'autres systèmes, tels que $BaTiO_3$/Ru(0001) et $BaTiO_3$/Pd(111) [8, 9]. Il existe un grand nombre de combinaisons d'oxydes ternaires supportés sur des métaux et force est de constaté que seul un très petit nombre de ces combinaisons a été étudié jusqu'à présent.

Ces idées ont motivé les études de cette thèse dans le cadre du projet OXYQUASI, où ces nouveaux concepts fascinants d'oxydes apériodiques à la limite 2D sont étudiés. OXYQUASI poursuit trois grands objectifs généraux. Tout d'abord, la compréhension des phénomènes impliqués lors de la croissance de couches minces d'oxydes sur les métaux (i.e. étude de la liaison chimique et des contraintes aux interfaces) qui favorisent l'apparition de la quasicristallinité. Deuxièmement, la synthèse d'un ensemble de nouveaux OQC avec des propriétés adaptables en utilisant une approche d'empilement de couches minces (où le métal n'est pas un substrat monocristallin mais une couche tampon épitaxiée) élargissant la famille des OQC. Troisièmement, la caractérisation des propriétés des OQC 2D (par exemple, les propriétés électroniques, magnétiques, catalytiques et de mouillage, ou la possibilité de les utiliser comme patron pour le "nanopatterning"). L'objectif principal de cette thèse est de progresser dans la synthèse d'un OQC par empilement de films, com-

binant des techniques de croissance épitaxiale et de caractérisation de surface. La procédure générale est la suivante : d'abord, un film mince de Pt(111) est épitaxié sur un substrat de saphire α-Al_2O_3(0001) par épitaxie par jet moléculaire (MBE). Par la suite, un film mince de $SrTiO_3$ est déposé par dépôt laser pulsé (PLD). Les différentes étapes du processus de croissance sont suivies par diffraction des électrons de haute énergie en incidence rasante (RHEED). La spectroscopie de photoémission induite par rayon X (XPS) et la microscopie électronique à balayage Auger (Auger Nano-SEM) sont utilisées pour caractériser la composition chimique de la surface. Des mesures de diffraction des rayons X ont également été prises pour déterminer les relations épitaxiales de l'empilement de couches De plus, des études de microscopie électronique à transmission en haute résolution (HRTEM) ont été réalisées en collaboration avec l'institut Jožef Stefan de Ljubljana en Slovénie pour étudier l'empilement des couches.

Ces empilements seront ensuite étudiés au cours de cycles de traitement d'oxydoréduction (comme indiqué dans la réf. [10]) où differentes phases UTOx pourront être formés. La complexité de ce projet réside dans les conditions expérimentales difficiles nécessaires à la formation de structures 2D apériodiques dans ces systèmes, par exemple les hautes températures (>800°C) et les basses pressions ($<10^{-8}$ mbar). Après la procédure de recuit, la surface résultante est étudiée par diffraction d'électrons à basse énergie (LEED), microscopie à effet tunnel (STM) et XPS.

Croissance de $SrTiO_3$/(Ti)/Pt(111)//α-Al_2O_3(0001)

La première étude présentée dans ce manuscrit s'intéresse à la croissance de films minces de $SrTiO_3$ sur une surface de Pt(111)//α-Al_2O_3(0001) par un empilement de couches minces. En particulier, nous souhaitons étudier les contraintes d'interface qui pouvent conduire le film d'oxyde à former des structures apériodiques à l'approche de la limite 2D [11]. Nous avons choisi une approche d'empilement de couches minces (au lieu d'utiliser des substrats métalliques monocristallins [12, 13, 3, 4]) car elle permet l'exploration de différentes combinaisons oxyde/métal, si des matériaux avec de petits écarts de paramètres de maille sont trouvés. Ainsi, des matériaux aux propriétés adaptables pourraient être synthétisés. Pour tester cette méthode nous avons décidé de partir d'une combinaison déjà étudiée : $SrTiO_3$/Pt(111) [4]. Ici, des couches minces (de 0,4 à 30 nm) de $SrTiO_3$ ont été déposées par PLD sur une couche de 10 nm de Pt(111). Dans certains cas, nous avons rajouté 1 nm de Ti dans le but de créer une solution solide avec le Pt, avec un paramètre de maille légèrement différent, et donc moduler les contraintes interfaciales. Les métaux ont été déposés par MBE sur un substrat α-Al_2O_3(0001).

Les clichés RHEED enregistrés à température ambiante (RT) après le dépôt de 10 nm de Pt sur un substrat α-Al_2O_3(0001) à une temperature de surface de 400°C (Th :

température mesurée avec un thermocouple), présentent des tiges de troncature allongées et fines indiquant une surface lisse. De plus, le même cliché est répété tous les 60° confirmant une symétrie de surface d'ordre six du film mince.

Les mesures de diffraction des rayons X à haute résolution (HRXRD) $\omega - 2\vartheta$ du film de 10 nm de Pt elaboré sur un substrat de α-Al_2O_3(0001) révèlent les réflexions du substrat ainsi que les réflexions *hhh* de Pt. Aucune réflexion provenant d'autres plans n'est présente, ce qui indique que le Pt est bien orienté (111). Les oscillations de Laue autour des pics du Pt indiquent une bonne cristallinité et une haute qualité d'interface et de surface. Le φ-scan du film de Pt et du substrat montrent six pics séparés de 60° pour le substrat et le film, ce qui met en évidence la symétrie six et de la croissance épitaxiale du Pt(111) sur le substrat. Après la croissance de la couche tampon, les échantillons seront exposés à des températures élevées : > 800°C lors de la préparation du film $SrTiO_3$ et ∼ 1000°C lors du traitement thermique nécessaire à l'obtention d'un UTOx. Les caractérisations par nano-microscopie Auger à balayage (Nano-SAM) et spectroscopie d'électrons Auger (AES) ont montré que le recuit du film de 10 nm Pt(111) déposé sur α-Al_2O_3(0001) à des températures supérieures à 600°C (T_{Pyro} : Température mesurée avec un pyromètre bichromatique) pourrait conduire à un démouillage localisé du film, mais la majeure partie de la surface reste couverte par la couche tampon de Pt, cela semble acceptable pour le dépôt ultérieur de films minces $SrTiO_3$ et l'obtention de phases UTOx/métal par recuit à haute température.

A la naissance du projet, nous avions supposé qu'il était important de favoriser l'épitaxie (111) du $SrTiO_3$ sur Pt(111) pour l'obtention de phases UTOx. Pour cette raison, et d'après les résultats de la littérature sur le sujet qui indiquent que le dépôt de 1 à 3 nm de Ti supplémentaire avant ou après la croissance de Pt sur α-Al_2O_3(0001) favorise la croissance de films de $SrTiO_3$ orientés (111) [14, 15], nous avons deposé par MBE sur certains échantillons une couche d'un nm de Ti sur le film de Pt. L'évolution chimique de la couche tampon Ti/Pt lors du recuit a été étudiée par XPS. Des spectres à différentes températures, de RT jusqu'à 500°C (Th) ont été obtenus pour certain niveaux de cœur. La relation entre l'aire du pic de Ti $2p_{3/2}$ et Pt $4d_{3/2}$ par rapport à la température montre qu'à des températures supérieures à 250°C un processus d'interdiffusion de Ti dans Pt a lieu.

L'évolution structurale de la couche tampon lors du recuit a été étudiée également par RHEED et XRD. La figure montre les clichés RHEED pris à différentes températures pendant le recuit de RT jusqu'à 1050°C (mesure Th équivalente à 875°C T_{Pyro}). Juste après le dépôt de Ti, les clichés RHEED mettent en évidence une faible qualité de surface. Pendant le recuit, les clichés présentent des tiges de troncatures plus fines répétées tous les 60°, confirmant une symétrie de surface d'ordre six épitaxié sur le film de Pt. Des tiges de diffraction supplémentaires sont présentes à des températures comprises entre 530°C et 820°C (Th). Après un recuit à plus haute

température, une amélioration de la cristallinité de surface de la couche Ti/Pt est observée, conduisant à des clichés de diffraction très nets. De plus, les réflexions supplémentaires ne sont pas présentes après 900°C conduisant uniquement à des tiges situées approximativement aux mêmes positions que celles du cliché de diffraction du film de Pt. Ceux-ci pourraient s'expliquer par la formation possible d'un alliage Pt-Ti lors du recuit qui modifie la structure de surface. Puis, lorsque la température augmente, le Ti diffuse plus profondément dans la couche de Pt pour former une solution solide, faisant à nouveau apparaître un cliché de diffraction très proche du cliché initial.

Les mesures HR-XRD montrent que le paramètre de maille de la couche tampon diminue légèrement après l'ajout de Ti et recuit ultérieur sous vide. Après recuit, le film mince résultant présente un paramètre de maille réduit par rapport à celui du Pt(111) pur. Cela pourrait favoriser le dépôt épitaxial de orientation (111) en raison d'un plus faible désaccord paramétrique avec la surface. En conséquence, ce dernier est réduit de 0,4% entre $SrTiO_3$ et Pt à 0,1% pour $SrTiO_3$ sur le film Ti/Pt recuit.

Pour obtenir plus d'informations sur l'empilement des films, des études de microscopie électronique en transmission à haute résolution (HRTEM) ont été realisées.
Un empilement de couches minces composé de $SrTiO_3$(10 nm)/Ti(1 nm)/Pt(111)(10 nm)//Al_2O_3(0001) a été étudié par microscopie électronique en transmission à champ sombre annulaire à grand angle (HAADF-STEM).
Les résultats nous amènent à conclure que le recuit de la couche tampon Ti/Pt(111) jusqu'à 800°C (Th), ne conduit pas à la formation d'un composé de Pt- Ti mais à une solution solide. Cet étude en complément des analyses XPS et XRD suggère que des changements chimiques et structuraux se produisent lorsque la couche tampon Ti/Pt est recuite. A environ 900°C (Th), le Ti diffuse dans la couche de Pt sous forme de solution solide sans former des composés de Pt-Ti.

Des couches minces de $SrTiO_3$ de différentes épaisseurs (de 0,4 à 30 nm) ont été déposées sous différentes conditions de pression et de température sur la surface Pt(111) ou Ti/Pt(111) par PLD. Des paramètres tels que l'épaisseur du film, la température et la pression durant le dépôt, le recuit après dépôt et le nettoyage de la surface de la couche tampon, ont été modifiés au cours du processus PLD afin d'améliorer la qualité de la surface du film $SrTiO_3$. La croissance a été contrôlée par RHEED.

Un dépôt d'un film lisse ultra-mince d'environ 0,4 nm de $SrTiO_3$ sur la surface des couches de Pt et de Ti/Pt a été réalisé à RT, sous vide à 8×10^{-9} mbar. La surface a ensuite été recuite à 800°C (Th, équivalente à 660°C T_{Pyro}) dans une atmosphère d'oxygène (1×10^{-6}mbar) pendant quelques minutes pour recristalliser ces films d'oxyde. Après refroidissement à RT, des pics plus nets sont obtenus à partir des tiges allongées et nettes répétées tous les 60°, qui confirment une symétrie

de surface lisse d'ordre six épitaxiée sur la structure Pt(111). Pour le film déposé sur la couche tampon de Ti/Pt, le cliché RHEED obtenu était pointé, indiquant une surface plus rugueuse de $SrTiO_3$. Par conséquent la surface résultante pourrait être couverte par des îlots $SrTiO_3$ principalement orientés (111).

Un film de 0,8 nm de $SrTiO_3$ a été déposé à 800°C (Th, équivalent à 665°C T_{Pyro}) dans une atmosphère d'oxygène (1×10^{-5}mbar). Les clichés RHEED pointés provenant du film $SrTiO_3$ à RT après refroidissement, indiquent que le film ultra mince présente des îlots de surface et des orientations possiblement différentes du (111).

Afin de réaliser des études de structure, telles que XRD ou TEM, des films d'oxyde plus épais ont été déposés. Pour préserver l'orientation (111) du film d'oxyde, des films de $SrTiO_3$ de 10 nm, 5 nm et 2 nm ont été déposés sur des couches de Ti/Pt(111). Avant le dépôt d'oxyde, les surfaces métalliques ont été recuites. Les clichés RHEED correspondant à des films de 20 Å et 50 Å (déposés à RT sous ultra vide (10^{-9}mbar) puis recuits en 10^{-5} mbar d'oxygène à 750°C (Th)) ont tendance à être pointés et flous, ce qui signifie que ces surfaces présentent une plus grande rugosité et sont moins bien orientées que les films de 0,4 nm de $SrTiO_3$

Phases 2D obtenues à partir de $SrTiO_3$ déposées sur $Pt(111)//Al_2O_3(0001)$

Depuis la découverte des OQC, quatre structures approximantes ont été rapportées dans la littérature. Ces phases sont : l'approximant de phase σ, obtenu à partir des systèmes épitaxiés $BaTiO_3$ sur Pt(111) [6] et Ru(0001) [8] ; un approximant monoclinique, dérivé du système $SrTiO_3$/Pt(111) [4] ; un approximant hexagonal, dérivé du système $BaTiO_3$/Pt(111) [16], et une variante de la phase σ, trouvée dans le système $BaTiO_3$/Pd(111) [9].

La deuxième étude de ce travail de thèse concerne la formation de nouvelles phases 2D complexes après réduction du film de $SrTiO_3$/(Ti/)Pt(111)//Al_2O_3(0001) synthétisé en utilisant l'approche d'empilement de couches minces présentée dans la section précedente. Cette méthode a été employée avec succès en tant que moyen possible d'explorer différentes combinaisons d'UTOx élaborés sur des métaux (111) et de rechercher de nouveaux types d'OQC. Au total, nous avons identifié, grâce au LEED et au STM, trois approximants OQC et d'autres structures hexagonales complexes. Les différentes phases se forment en fonction des conditions de préparation.

Nous avons appliqué des cycles d'oxydo-réduction au film mince de $SrTiO_3$ déposé sur Pt(111) (ou Ti/Pt(111)) deposé sur α-Al_2O_3(0001). Un premier recuit sous 1×10^{-6} mbar de O_2 à 630°C (T_{Pyro}) a été réalisé pour éliminer la contamination de la surface (vérifié par XPS et LEED). (Toutes les températures rapportées dans cette partie sont des mesures T_{Pyro}).

Approximant carré géant : Cette phase a été trouvée pour les échantillons suivants : (***(A)*** (0.8 nm) $SrTiO_3$/(10 nm) Pt(111)//Al_2O_3(0001) et ***(B)*** (2 nm) $SrTiO_3$/(1 nm)Ti/(10 nm) Pt(111)//Al_2O_3(0001).

Une fois la surface de l'échantillon dégazée, un recuit ultérieur à 850°C sous vide (10^{-8} mbar) a été effectué. Après recuit, une nouvelle structure avec une symétrie dodécagonale apparente a été formée observée et caractérisée par LEED et STM. Les clichés LEED à 20 eV présentent 12 taches de diffraction. À des énergies de faisceau plus élevées, des taches de diffraction d'ordre supérieur sont observées, conduisant à un cliché LEED très similaire à celui rapporté précédemment pour l'OQC [4].

La structure de l'espace réel et les arrangements atomiques locaux ont été déterminés à partir d'images STM résolues atomiquement prises à température ambiante. Bien que le LEED montre un cliché dodécagonal apparent typique d'un OQC, la transformée de Fourier (FFT) de l'image de l'espace réel révèle un réseau périodique presque carré, indiquant qu'un approximant s'est formé au lieu d'un OQC [17, 18] . La FFT a été utilisée pour déterminer les paramètres du réseau dans le plan : 42,2± 0,6 Å× 43,2 ± 0,6 Å, et un angle entre les bords de 89,7 ± 0,4°. Les protubérances brillantes observées sur les images STM se trouvent aux nœuds des mêmes éléments de pavage Niizeki-Gähler (NGT) utilisés pour décrire les structures dodécagonales [19]. Ces éléments de pavage sont disposés de telle sorte que la maille élémentaire contienne 72 tuiles, à savoir 48 triangles, 18 carrés et 6 losanges avec un rapport d'éléments de pavage de 2,66 :1 :0,33. C'est le double du nombre de tuiles nécessaires pour décrire l'approximant monoclinique précédemment rapporté dérivé du $SrTiO_3$/Pt(111) [4], mais le rapport reste le même. En outre, elle est juste légèrement différente de la structure NGT idéale de la phase dodécagonale QC donnée par 2,73 :1 :0,37. La maille élémentaire contient 47 atomes aux sommets, correspondant à une densité de surface de 2,20 nm^{-2}, inférieure aux valeurs rapportées pour la phase OQC (2,46 nm^{-2}). A partir de l'image STM, une distance moyenne de 6,4 ± 0,3 Å entre les points brillants est déduite. La longueur des éléments de pavage déduite de la maille élémentaire élémentaire idéale est de 6,53 Å, pour l'axe vertical, et de 6,68 Å, pour l'axe horizontal. Un axe de la maille unitaire approximative est parallèle à la direction $[12\bar{3}]$ de la couche tampon hexagonale de Pt.

Approximant hexagonal : Cette phase a été trouvé pour les échantillons ***(A)*** et ***(B)*** décrits au début du paragraphe précedent.

Avec l'augmentation du nombre de cycles d'oxydo-réduction dans les mêmes conditions expérimentales que celles décrites précédemment, une nouvelle phase UTOx a été observée avec une grande maille élémentaire hexagonale. Cette structure a été mis en évidence dans les images STM à haute résolution, ainsi que la décoration en pavage dodécagonal. Les dimensions de la maille élémentaire sont

27.8 ± 0.6 Å× 28.1 ± 0.6 Å. Cette maille élémentaire hexagonale peut être décorée avec les mêmes éléments NGT. Il contient 29 tuiles, soit 20 triangles, 6 carrés et 3 losanges. Une longueur d'arête commune de 6,7 ± 0,2 Å est déduite de la distance moyenne entre les points brillants. Des motifs dodécagonaux constitués de 6 carrés et de 12 triangles décorent les sommet de la maille élémentaire. Il manque généralement une protubérance à chaque nœud de la maille élémentaire hexagonale. Dans d'autres zones de la surface, ce site est occupé et apparaît comme un point brillant, suggérant la présence d'atomes légèrement surélevés par rapport au plan moyen. La maille élémentaire contient 19 ou 18 protrusions visibles dans les images STM, correspondant à une densité de surface comprise entre 2,65 et 2,80 nm^{-2}, significativement plus grande que celle de l'OQC idéal ou l'approximant carré. Les ratios d'éléments de pavage de la phase hexagonale sont de 3,33 :1 :0,5, ce qui diffère considérablement de l'OQC idéal ou de l'approximant carré. L'évolution structurelle du film UTOx, de l'approximant carré à l'approximant hexagonal, pourrait être liée à un changement de la stœchiométrie avec le nombre de cycles de recuit. Le cliché LEED de la phase hexagonale montre l'existence de quatre domaines rotationnels non équivalents, qui sont tournés par rapport à la direction $[1\bar{1}0]_{Pt}$ de 15°, 27°, 34° et 45° respectivement.

Approximant σ : Cette phase a été trouvé pour un échantillon ***C*** : (5 nm) $SrTiO_3$/(1 nm) Ti/(10 nm) Pt(111)//Al_2O_3(0001).

La phase approximant σ (également connu sous le nom de 3^2.4.3.4 pavage d'Archimède ou pavage carré) [6] a été obtenue après deux cycles lors d'un recuit sous vide (10^{-8}mbar) à 900°C pendant 15 min. Nous rapportons ici pour la première fois l'observation de cette phase dans le système $SrTiO_3$/Pt(111). Les clichés LEED montrent 12 taches intenses de diffraction caractéristiques des clichés LEED des structures OQC rapportées.

Des images STM à la résolution atomique mettent en évidence un arrangement périodique. Les FFT correspondantes confirment un réseau presque carré avec un paramètre de réseau réciproque plus grand par rapport à l'approximant de type carré géant décrit précédemment. A partir de l'image STM, la distance entre les atomes de surface a été déterminée à 6,4±0,3 Å.
Cette valeur est légèrement inférieure à la distance moyenne de 6,7 Å entre les protubérances rapportée pour l'approximant σ observé dans $BaTiO_3$/Pt(111) [6]. La FFT a été utilisée pour déterminer les paramètres de réseau dans le plan : 12,5 ± 0,2 Å × 12,5 ± 0,1 Å également plus petit que les paramètres de réseau signalés 12,9 × 13.1 Å de l'approximant σ derivé du $BaTiO_3$/Pt(111) [6].

Etude théorique des approximants 2D OQC : La théorie de la fonctionnelle de la densité (DFT) a été utilisée pour étudier des films UTOx déposés sur Pt(111). Les

charges moyennes sur chaque atome ont été calculées en utilisant l'approche de Bader [20]. Les propriétés structurales et électroniques des approximants 2D carré géant et hexagonal derivés du $SrTiO_3$/Pt(111) ont été étudiées à l'aide de deux structures modèles construites sur la base des pavages complexes identifiés expérimentalement.

Ces modèles sont constitués de motifs structuraux (triangles équilatéraux, carrés et losanges d'angle au sommet égal à 30°) partageant une même longueur de côté. La structure atomique de chaque type de tuiles a été implémentée en utilisant les modèles proposés par Cockayne *et al.* [7]. Ainsi, la composition chimique des triangles, carrés et losanges sont $SrTiO_3$, $SrTi_4O_4$ et $SrTi_2O_2$, respectivement. Les atomes de Sr sont situés aux sommets du pavage. Chaque atome de Ti est lié à trois atomes d'oxygène (symétrie locale d'ordre 3), et chaque atome d'oxygène est situé entre deux atomes de Ti.

Le transfert de charge se produit à l'interface Pt-UTOx, provenant des éléments électropositifs (Sr, Ti) vers les éléments électronégatifs (Pt et O). Ainsi, les interactions électrostatiques contribuent probablement à la localisation des cations de Ti à proximité du substrat de Pt chargé négativement, tout en repoussant les atomes négatifs d'O [7]. Ceci est encore confirmé par la déformation de densité de charge, qui indique des différences de charges non négligeables à l'interface Pt-UTOx. Plus généralement, les effets électroniques sont connus pour impacter le "rumpling" et les énergies d'adhésion.

Pour les approximantes carré géant et hexagonal, des images STM ont été simulées pour les polarités positives et négatives. Le contraste claire est attribué aux atomes de Sr protubérant, tandis que les atomes de Ti et O ne sont pas visibles, en accord avec avec la position moyenne de chaque type d'atome par rapport au plan de surface et leur densité d'états (DOS) calculée. Dans l'ensemble, le bon accord entre les images STM simulées et expérimentales suggère que les modèles structuraux considérés dans ce travail sont réalistes pour décrire les nouveaux complexe UTOx synthétisé ici.

Phases hexagonales complexes : D'autres phases complexes d'UTOx ont également été observées après augmentation du nombre de cycles de recuit. Une structure de type nid d'abeille (HC pour honeycomb en anglais) et des structures en forme de labyrinthe ont été identifiées par LEED et STM. Elles coexistent habituellement dans différentes zones de la surface, avec les phases approximantes, probablement dues à des gradients de température à la surface de l'échantillon. Les différentes morphologies observées pour ces phases complexes sont interprétées comme résultant de la présence d'adatomes de Sr décorant un réseau HC de Ti_2O_3, avec des taux d'occupation différents.

Conclusions et perspectives

Dans cette thèse, nous avons présenté une approche "tout film mince" pour étudier les systèmes ABO_3/M(111) d'une manière plus polyvalente et moins coûteuse qu'en utilisant des substrats métalliques monocristallins. L'empilement multicouche consistait en un film mince de $SrTiO_3$ déposé par PLD sur une couche tampon Pt(111) épitaxié sur substrat de α-Al_2O_3(0001) par MBE. Les relations épitaxiales aux interfaces Pt//Al_2O_3 et $SrTiO_3$/Pt ont été caractérisées par une combinaison de RHEED, XRD et HRTEM. Il a été montré qu'un nm supplémentaire de Ti déposé au-dessus de la couche de Pt puis recuit pour former une solution solide réduisait la distance interplanaire et le paramètre de réseau de la couche tampon, diminuant la différence avec le paramètre de maille de surface du $SrTiO_3$ de 0,4% à 0,1% . Des études HRTEM ont révélé que Ti diffuse dans la couche de Pt formant une solution solide de Pt-Ti. Un démouillage local et partiel de la couche de Pt a été observé par Nano-SAM, lors d'un recuit à des températures supérieures à 600°C (T_{Pyro}). Néanmoins, des films ultra-minces lisses et homogènes d'environ 0,4 nm, de $SrTiO_3$ ont été déposés sur la couche tampon de Pt. Des films d'oxyde plus épaises, de 0,8, 2 et 5 nm, ont montré des clichés RHEED caractéristiques d'une surface plus rugueuse, suggérant que des îlots de $SrTiO_3$ sont formés à la surface. En fait, les phases UTOx rapportées ont été obtenues à partir de ces surfaces d'oxyde 3D supportées sur une couche tampon de Pt(-Ti)(111) déposée sur α-Al_2O_3(0001).

Les phases UTOx ont été obtenues par de recuits à haute température de l'empilement de couches minces. Deux nouveaux approximants OQC ont été découverts : un approximant de type carré avec une maille élémentaire géante et un grand approximant hexagonal. La phase σ approximant (déjà observée dans le système $BaTiO_3$/Pt(111)) a été observé pour la première fois dans de $SrTiO_3$ supporté sur Pt(111). Leurs structures ont été étudiées par STM, LEED et DFT. Les images STM à haute résolution des trois phases montrent des points brillants situés aux au nœuds de trois pavages différents construits avec les mêmes tuiles de base carrée, triangle et losange à 30° possédant une longueur commune d'environ 6,7 Å. Le rapport de tuile est différent pour les deux phases. Le nombre de tuiles nécessaires pour décrire l'approximant carré est deux fois plus grand que pour l'approximant monoclinique précédemment rapporté dans le système $SrTiO_3$/Pt(111). En utilisant les pavages déduits expérimentalement pour ces trois nouvelles phases, des modèles de structure ont été élaborés en adoptant la décoration de tuiles proposée par Cockayne *et al.* [7], dans laquelle les atomes de Sr sont situés au nœud du pavage et dans lequel chaque atome de Ti est lié à trois atomes d'oxygène et chaque atome d'oxygène est situé entre deux atomes de Ti. Ainsi, les compositions chimiques des triangles, carrés et losanges sont respectivement $SrTiO_3$, $SrTi_4O_4$ et $SrTi_2O_2$, et les compositions globales des phases carré et hexagonal respectivement sont $Sr_{0.36}TiO_{1.54}$ et

$Sr_{0.38}TiO_{1.56}$. Les approximants carrés et hexagonal ont des enthalpies de formation et des énergies d'adhésion similaires. Les deux phases subissent une relaxation structurale importante lorsqu'elles sont supportées par de Pt (111), ce qui entraîne un corrugation de la couche d'oxyde. Le transfert de charge a lieu depuis les éléments électropositifs (Sr, Ti) vers les éléments électronégatifs (Pt et O). Selon l'optimisation structurelle, les cations Ti se trouvent plus près du substrat de Pt chargé négativement que les atomes O et Sr. Les images STM simulées sont en excellent accord avec les images expérimentales, soutenant ainsi les modèles structuraux proposés pour les deux nouvelles phases d'oxyde 2D. En conséquence, les atomes de Sr sont principalement imagés par STM car ils dépassent du plan de surface moyen des films minces UTOx, bien que la principale contribution à la DOS provienne des atomes de Ti. Enfin, les calculs DOS suggèrent que les deux nouveaux approximants OQC ont des propriétés physiques et chimiques différentes. Des phases hexagonales complexes supplémentaires ont également été observées lors de l'augmentation du nombre de procédures de recuit. Un réseau HC et une structure en forme de labyrinthe ont été observées par STM coexistant parfois avec les approximants carré et hexagonal conduisant à des clichés LEED complexes. Nous avons mis en évidence que le taux de couverture de Sr en surface tel que les atomes de Sr soit adsorbés sur le réseau TiOx définit l'apparition de différentes structures.

Perspectives

L'approche du "tout film mince" proposée ici pourra être étendue à l'avenir à différentes familles de ABO_3/M(111) afin d'explorer le vaste paysage offert par les nombreuses pérovskites et supports métalliques potentiels pour la découverte de nouveaux matériaux UTOx 2D. Par exemple, la couche tampon de Pt pourrait être remplacée par des métaux de transition qui croissent par épitaxie sur le substrat α-Al_2O_3(0001), comme Pd(111) [21] Ir(111) [22] ou Ru(0001) [23]. Une étude concernant la croissance de ces métaux par MBE sur Al_2O_3(0001) et le dépôt ultérieur de films ultra-minces de $SrTiO_3$ par PLD serait nécessaire.

Dorini *et al.* ont exploré par des méthodes de calculs *ab initio* plus de 60 systèmes ABO_3/M(111) en permutant le métal alcalin A (= Ba, Sr, ans Ca), le métal de transition *B* (= Ti, V, Cr, Mn, Fe, Co, Ni) et le support métallique M (= Pt, Pd, Au) pour la phase σ [24]. Les auteurs ont trouvé que $BaFeO_3$, $BaCoO_3$ et $BaNiO_3$ sont de bons candidats comme UTOx structurellement stable lorsqu'ils sont supportés sur Pt ou Au. De plus, ces matériaux pourraient avoir des propriétés magnétiques intéressantes. Sur la base de ce travail, la croissance d'un film ultra-mince de $BaFeO_3$ pourrait être envisagée par PLD sur une couche tampon de Pt(111) développée sur α-Al_2O_3(0001).

Le contrôle expérimental de la température et de la pression doit être amélioré pendant les cycles de recuit. L'utilisation de plaquettes porte-échantillon non per-

cées contribue à obtenir un recuit de surface homogène. Un meilleur système de pompage pourrait aider à recuire l'échantillon à des températures supérieures à 850°C tout en maintenant une pression inférieure à 10^{-9}mbar, favorisant l'obtention d'OQCs et d'approximantes OQC.

Les phases UTOx étant sous stoechiométriques en Sr, une source de Sr pourrait être installée afin de compenser le déficit en Sr et recommencer les cycles de recuit à partir d'un film stoechiométrique de $SrTiO_3$.

La structure électronique pourrait être étudiée par des techniques de photoémission, en particulier par spectroscopie photoélectronique résolue en angle (ARPES). La formation possible d'un gaz d'électrons 2D (2DEG) à la surface d'un approximant $SrTiO_3$ pourrait également être étudiée. La littérature a rapporté que $SrTiO_3$ est un système modèle pour étudier les gaz d'électrons 2D [25]. Des états conducteurs 2D ont été observés initialement à l'interface entre $SrTiO_3$ et $LaAlO_3$ [26]. Ensuite, il a été découvert à la surface d'un monocristal de $SrTiO_3$ [27]. Par conséquent, l'étude de la structure de la bande 2DEG à la surface des approximants découverts dans cette thèse pourrait être intéressante.

Jusqu'à présent, les approximants obtenus dans cette thèse ont été déterminés comme étant constitué d'une seule couche d'épaisseur atteignant la limite 2D. Nous pourrions envisager de ne reprise d'épitaxie en redéposant une couche mince d'oxyde sur les phases d'oxydes 2D obtenues par réduction d'un premier dépôt. L'étude des propriétés électroniques locales de nos échantillons à l'aide de la microscopie/spectroscopie à effet tunnel à balayage à basse température (LT-STM/STS) pourrait être également envisagée pour accéder à la densité d'états locale avec une grande résolution spatiale. De telles mesures pourraient fournir la structure électronique des approximants avec une résolution atomique. A titre d'exemple, une comparaison directe entre les propriétés électroniques des différentes phases pourrait ainsi être obtenue.

Certaines de ces phases d'oxydes 2D pourraient être utilisées comme patron pour former des nanostructures. Par exemple, les défauts de surface ordonnés observés dans l'approximant OQC hexagonal (attribués à une lacune d'atomes de Sr) peuvent agir comme des centres de nucléation pour les métaux déposés sur la surface de l'approximant, ce qui pourrait conduire à la formation d'un réseau ordonné de nano-îlots métalliques [28].

D'autres propriétés de ces phases complexes, telles que les propriétés catalytiques, pourraient être explorées expérimentalement et théoriquement. Les sites d'adsorption les plus favorables des phases approximantes pourraient être déterminés au moyen de calculs *ab initio*, par exemple. Les oxydes ternaires ABO_3 sont des matériaux qui contiennent des métaux de transition ayant des propriétés catalytiques. K. Kovnir *et al.* ont introduit le concept d'isolation du site actif en catalyse. Les films d'oxyde 2D pourraint remplir ces conditions, en présentant des sites ato-

miques de métaux actifs bien isolés géométriquement les uns des autres et stabilisés par le réseau d'oxyde. [29].

Bibliographie

[1] G. Barcaro and A. Fortunelli. 2D oxides on metal materials : Concepts, status, and perspectives. *Physical Chemestry Chemical Physics*, 21 :11510, 2019.

[2] C. Wu, M. R. Castell, J. Goniakowski, and C. Noguera. Stoichiometry engineering of ternary oxide ultrathin films : Ba_x Ti_2O_3 on Au(111). *Physical Review B*, 91(15) :155424, 2015.

[3] S. Förster, K. Meinel, R. Hammer, M. Trautmann, and W. Widdra. Quasicrystalline structure formation in a classical crystalline thin-film system. *Nature*, 502(7470) :215–218, 2013.

[4] S. Schenk, S. Förster, K. Meinel, R. Hammer, B. Leibundgut, M. Paleschke, J. Pantzer, C. Dresler, F. O. Schumann, and W. Widdra. Observation of a dodecagonal oxide quasicrystal and its complex approximant in the $SrTiO_3$-Pt(111) system. *Journal of Physics : Condensed Matter*, 29(13) :134002, 2017.

[5] S. Förster, S. Schenk, E. M. Zollner, O. Krahn, C-T. Chiang, F. O. Schumann, A. Bayat, K-M Schindler, M. Trautmann, R. Hammer, K. Meinel, W. A. Adeagbo, W. Hergert, J. I. Flege, J. Falta, M. Ellguth, C. Tusche, M. DeBoissieu, M. Muntwiler, T. Greber, and W. Widdra. Quasicrystals and their Approximants in 2D Ternary Oxides. *Physica Status Solidi (B)*, 257(7) :1900624, 2020.

[6] S. Förster, M. Trautmann, S. Roy, W. A. Adeagbo, E. M. Zollner, R. Hammer, F. O. Schumann, K. Meinel, S. K. Nayak, K. Mohseni, W. Hergert, H. L. Meyerheim, and W. Widdra. Observation and Structure Determination of an Oxide Quasicrystal Approximant. *Physical Review Letters*, 117(9) :095501, 2016.

[7] E Cockayne, M. Mihalkovič, and C. L. Henley. Structure of periodic crystals and quasicrystals in ultrathin films of Ba-Ti-O. *Physical Review B*, 93(2) :020101, 2016.

[8] E. M. Zollner, F. Schuster, K. Meinel, P. Stötzner, S. Schenk, B. Allner, S. Förster, and W. Widdra. Two-Dimensional Wetting Layer Structures of Reduced Ternary Oxides on Ru(0001) and Pt(111). *Physica Status Solidi (B)*, 257(7) :1900655, 2020.

[9] F. E. Wührl, O. Krahn, S. Schenk, S. Förster, and W. Widdra. Antiphase Domain Boundary Formation in 2D Ba–Ti–O on Pd(111) : An Alternative to Phase Separation. *Physica Status Solidi (B)*, (2100389), 2021.

[10] S. Förster, J. Flege, E. M. Zollner, F. O. Schumann, R. Hammer, Al. Bayat, K-M Schindler, J. Falta, and W. Widdra. Growth and decay of a two-dimensional oxide quasicrystal : High-temperature in situ microscopy. *Annalen der Physik*, 529(1-2) :1600250, 2017.

[11] S. Förster and W. Widdra. Ultrathin Perovskites : From Bulk Structures to New Interface Concepts. In F. P. Netzer and A. Fortunelli, editors, *Oxide Materials at the Two-Dimensional Limit*, pages 361–380. Springer International Publishing, Cham, 2016.

[12] S. Förster, K. Meinel, K-M Schindler, and W. Widdra. Oxygen-deficient ordered phases of ultrathin $BaTiO_3$ films on Pt(111). *Surface and Interface Analysis*, 44(6) :628–634, 2012.

[13] S. Förster and W. Widdra. Growth, structure, and thermal stability of epitaxial $BaTiO_3$ films on Pt(111). *Surface Science*, 604(23-24) :242163–2169, 2010.

[14] S. Schmidt, D. O. Klenov, S. P. Keane, J. Lu, T. E. Mates, and S. Stemmer. Atomic structure of (111) $SrTiO_3$/Pt interfaces. *Applied Physics Letters*, 88(13) :131914, 2006.

[15] G. Panomsuwan, O. Takai, and N. Saito. Controlled crystalline orientation of $SrTiO_3$ thin films grown on Pt(111)/Ti/alpha-Al_2O_3(0001) substrates : Effect of growth temperature and Ti layer thickness. *Applied Surface Science*, 309 :95–105, 2014.

[16] M. Maniraj, L. V. Tran, O. Krahn, S. Schenk, W. Widdra, and S. Förster. Hexagonal approximant of the dodecagonal oxide quasicrystal on Pt(111). *Physical Review Materials*, 5(8) :084006, 2021.

[17] C. Ruano M., L. Pasquier, S. Andrieu, K. Dumesnil, J. Ledieu, O. Copie, V. Fournée, and M. Sicot. New quasicrystal approximants in the $SrTiO_3$/Pt(111)/Al_20_3(0001) system. *Proceeding of the ECMetAC Days, online conference*, 2020.

[18] S. Schenk, O. Krahn, S. Förster, and W. Widdra. Dodecagonal oxide quasicrystal approximant with 72 tiling elements. *Proceeding of the ECMetAC Days, online conference*, 2020.

[19] F. Gähler. Crystallography of dodecagonal quasicrystals. *Theoretische Physik, ETH-Honggerberg,*, page 13, 1988.

[20] This software is provided by the Henkelman group (University of Texas) and it can be found at http ://theory.cm.utexas.edu/bader.

[21] A. Aleman, C. Li, H. Zaid, H. Kindlund, J. Fankhauser, S. V. Prikhodko, M. S. Goorsky, and S. Kodambaka. Ultrahigh vacuum dc magnetron sputter-deposition of epitaxial Pd(111)/Al_2O_3(0001) thin films. *Journal of Vacuum Science & Technology. A*, 36(3) :030602, 2018.

[22] Shinji, K., Atsuhito, S, Yuta, S., and Hideyuki, K. Epitaxial growth and electrochemical transfer of graphene on Ir(111)/α-Al_2O_3 (0001) substrates. *Applied Physics Letters*, page 109, 2016.

[23] P. Sutter, P. Albrecht, and E. Sutter. Graphene growth on epitaxial Ru thin films on sapphire. *Applied Physics Letters*, 97 :213101–213101, 2010.

[24] T. Dorini Trevizam, F. Brix, C. Chatelier, A. Kokalj, and E. Gaudry. Two-dimensional oxide quasicrystal approximants with tunable electronic and magnetic properties. *Nanoscale*, 13(24) :10771–10779, 2021.

[25] S. Gonzalez, C. Mathieu, O. Copie, V. Feyer, C. M. Schneider, and N. Barrett. Room temperature 2D electron gas at the (001)-$SrTiO_3$ surface. *Applied Physics Letters*, 111(18) :181601, 2017.

[26] A. Ohtomo and H. Y. Hwang. A high-mobility electron gas at the $LaAlO_3/SrTiO_3$ heterointerface. *Nature*, 427(6973) :423–426, 2004.

[27] A. F. Santander-Syro, O. Copie, T. Kondo, F. Fortuna, S. Pailhès, R. Weht, X. G. Qiu, F. Bertran, A. Nicolaou, A. Taleb-Ibrahimi, P. Le Fèvre, G. Herranz, M. Bibes, N. Reyren, Y. Apertet, P. Lecoeur, A. Barthélémy, and M. J. Rozenberg. Two-dimensional electron gas with universal subbands at the surface of $SrTiO_3$. *Nature*, 469(7329) :189–193, 2011.

[28] V. Repain, G. Baudot, H. Ellmer, and S. Rousset. Two-dimensional long-range–ordered growth of uniform cobalt nanostructures on a Au(111) vicinal template. *Europhysics Letters (EPL)*, 58(5) :730–736, 2002.

[29] K. Kovnir, M. Armbrüster, D. Teschner, T.V. Venkov, F.C. Jentoft, A. Knop-Gericke, Yu. Grin, and R. Schlögl. A new approach to well-defined, stable and site-isolated catalysts. *Science and Technology of Advanced Materials*, 8(5) :420–427, 2007.

Contents

Résumé **ix**

Abstract **xi**

Synthèse **xiii**

Bibliographie xxv

Glossary **xxxiii**

Index **xxxvii**

Introduction **1**

Bibliography 3

Chapter 1
Introduction to 2D oxide materials: from perovskites to quasicrystals **5**

1.1 The oxide-metal hybrid system 6

1.1.1 Generalities on oxide structures 7

1.1.1.1 Binary oxide structures 7

1.1.1.2 Increasing complexity: ternary oxide structures 8

1.1.2 Ternary oxides supported on metals 9

1.1.3 Structural motifs 12

1.2 Aperiodic order in UTOx supported on metals 14

1.2.1 Quasiperiodic structures 15

1.2.2 Approximant structures 17

1.2.3 Quasicrystals and their Approximants in 2D Ternary Oxides . . 17
1.2.3.1 The discovery of 2D oxide QC 17
1.2.3.2 Preparation and stability 21
1.2.3.3 OQC approximants 21
Bibliography 26

Chapter 2
Experimental methods **33**

2.1 Thin film growth methods 34
2.1.1 Description of the film stacking 35
2.1.2 The TUBE 36
2.1.3 Molecular Beam Epitaxy 38
2.1.4 Pulsed Laser Deposition 40
2.2 Surface characterization methods 42
2.2.1 ASURE platform 43
2.2.2 Surface structure characterization 45
2.2.2.1 Reflection high-energy electron diffraction 45
2.2.2.2 Low energy electron diffraction 51
2.2.3 Chemical analysis 54
2.2.3.1 X-ray photoelectron spectroscopy 55
2.2.3.2 Auger electron spectroscopy 58
2.2.4 Microscopy techniques 60
2.2.4.1 SCAN platform 60
2.2.4.2 Nano-Scanning Auger Microscopy 61
2.2.4.3 Scanning tunnelling microscopy 63
Bibliography 66

Chapter 3
Growth of $SrTiO_3$ on Pt(111)/ α-Al_2O_3(0001) **69**

3.1 Measurements of the sample temperatures 70
3.2 Pt(111) grown on α-Al_2O_3(0001): state of the art 71
3.2.1 Substrate preparation 74

3.2.2 10 nm of Pt(111) grown on Al_2O_3(0001) by MBE 75
3.3 Growth of Ti/Pt(111) buffer layer on α-Al_2O_3(0001) 81
3.3.1 1 nm of Ti grown on Pt(111)/Al_2O_3(0001) by MBE 81
3.3.1.1 Chemical evolution of the buffer layer upon annealing 83
3.3.1.2 Structural evolution of the buffer layer upon annealing 85
3.4 $SrTiO_3$ thin films deposited on Pt(111) by PLD 90
3.4.1 Crystal structure and epitaxial relationships:state of the art . . 90
3.4.2 Thin films of $SrTiO_3$ on (Ti/)Pt(111) by PLD results 92
3.5 TEM investigations 96
Bibliography 100

Chapter 4
Complex 2D oxide phases in reduced $SrTiO_3$ grown on Pt(111)/Al_2O_3(0001)105

4.1 Cleaning and annealing procedure 106
4.2 Giant square-like approximant 109
4.3 Large hexagonal approximant 112
4.4 σ-phase approximant 115
4.5 Theoretical investigation of the 2D OQC approximants 117
4.6 Complex hexagonal phases 125
Bibliography 133

Conclusions and perspectives **137**

Bibliography 140

Glossary

2D:	2-dimensional
3D:	3-dimensional
AES:	Auger Electron Spectroscopy
AFM:	Atomic Force Microscopy
ARPES:	Angle-Resolved Photoemission Spectroscopy
ASURE:	(from French) Alliage SUrface et REactivité
DFT:	Density Functional Theory
DOS:	Density of States
EDXS:	Energy Dispersive X-ray Spectroscopy
FIB:	Focus Ion Beam
FT:	Fourier Transform
FFT:	Fast Fourier Transform
HC:	Honeycomb
HAADF:	High-Angle Annular Dark-Field
HAADF-STEM:	High-Angle Annular Dark-Field Scanning Transmission Electron Microscopy
HRTEM:	High-Resolution Transmission Electron Microscopy
HRXRD:	High Resolution X-Ray Diffraction
IJL:	Jean Lamour Institute
LEED:	Low Energy Electron Diffraction
LEEM:	Low-Energy Electron Microscopy
MBE:	Molecular Beam Epitaxy
M:	Metal
ML:	Monolayers
NGT:	Niizeki-Gähler tiling
OQC:	Oxide Quasicrystal
QC:	Quasicrystal
RHEED:	Reflection High-Energy Electron Diffraction
RT:	Room Temperature
PLD:	Pulsed Laser Deposition
SAM:	Scanning Auger Microscopy
SCAN:	Structural and Chemical Analysis of Surfaces at the Nanoscale
SEM:	Scanning Electron Microscopy

STM:	Scanning Tunneling Microscopy
SXRD:	Surface X-ray Diffraction
TUBE:	inTerconnection under Ultrahigh vacuum of chamBers for Elaboration and characterization for novel materials
UHV:	Ultra-High Vacuum
UTOx:	Ultra-thin films of oxides
XPS:	X-ray Photoemission
XRD:	X-Ray Diffraction

Index

a	Lattice parameter (Å)
d_{hkl}	interatomic distance (Å)
ΔH_f	Formation enthalpy (eV/atom)
E_{adh}	Energy of adhesion (eV/Å^2)
E_{coh}	Energy of adhesion (eV/atom)
$\mathbf{k}$	Wave vector
Q	Average charge (e)
R	Rumpling (Å)
T_{Pyro}	Temperature measured with a bichromatic pyrometer (K or °C)
T_{Th}	Temperature measured with a thermocouple (K or °C)
z^-	Anions
z^+	Cations
μ	Chemical potential (eV)
ρ	Electron density
ϑ	Diffraction angle (°)

Introduction

In the last two decades great advances have been reported in the fabrication, characterization, and computational modelling of ultra-thin oxide films (UTOx) supported on metals. In the 2D limit, UTOx present atomic and electronic structures that are quite different from bulk oxides. They can also exhibit electron confinement at the metal-oxide interface and are influenced strongly by the UTOx/support interaction [1]. For example, several morphologies at atomic level of oxides grown on (111)-metals have been observed whose structures have no equivalent in bulk form [1, 2]. The understanding of the fundamental rules guiding the formation of UTOx and the relationships between their local atomic structures and their physicochemical properties is still a subject of active research.

These 2D materials can be described most often from structural motifs consisting in elementary tiles such as squares and triangles defined by its stoichiometry MO_4 (M: a metal) and MO_3 respectively (MO_2, MO_5,... structural motifs can be defined as well). These tiles can be assembled together to pave the plane in different ways forming structures of varying complexities [1]. For a given metal/oxide combination different structural motifs could be formed with a particular stoichiometry, lattice parameters, charge state and epitaxial relationships with the substrate [1].

In particular, dodecagonal oxide quasicrystals (OQC) are 2D UTOx structures derived from ternary oxide thinfilms grown epitaxially on a well oriented (111)-metal which can be described in terms of the structural motifs such as squares, equilateral triangles and 30° rhombs. In 2013 Förster *et.al.* observed the formation of a 2D OQC from a $BaTiO_3$ thinfilm grown epitaxially on a 3-fold single crystal substrate of Pt(111)[3]. Four years later, Schenk, *et.al.* reported the formation of an OQC at the interface of a thinfilm of $SrTiO_3$ grown as well on a (111)-oriented Pt substrate [4], demonstrating that OQC formation could be extended to a different ternary oxides/metals combinations. These discoveries gave rise to a new class of quasicrystalline materials and moreover to an additional facet of atomic-level phenomena in complex ternary oxides.

Dodecagonal OQCs have been observed frequently coexisting with periodic approximant phases [5] allowing to perform *ab initio* calculations that try to find a structure model, which is an important step towards the comprehension of all ob-

served structures [6, 7]. So far, these structures have been found starting from only these two mentioned perovskites grown on a Pt substrate. Moreover, at the beginning of this thesis there were only two oxide/metal combinations that had been explored: $BaTiO_3$/Pt(111) and $SrTiO_3$/Pt(111). During the last three years, OQC approximants were found in other systems, such as $BaTiO_3$/Ru(0001) and $BaTiO_3$/Pd(111) [8, 9]. Still, there are only few combinations of ternary oxides supported on (111)-metals that have been investigated up to now.

These ideas motivated the creation of the OXYQUASI project, where these new fascinating concepts of aperiodic oxides at the 2D limit are investigated. OXYQUASI has three main general objectives. First, the understanding of the phenomena involved during the thinfilms growth of oxides on metals (i.e., study of the chemical bonding and frustration at the interfaces) that favour the appearance of quasicrystallinity. Second, the synthesis of a set of new OQCs with tunable properties using a thinfilm stacking approach (where the metal is not a single crystal substrate but an epitaxial buffer layer) expanding the OQC family. Third, the characterization of possible 2D OQCs properties (e.g. electronic, magnetic, catalytic and wetting properties, or the possibility to use them as templates for nanopatterning).

The present thesis has been developed in the frame of the OXYQUASI project. Here, the main objective is to progress in the synthesis of an OQC by film stacking, combining epitaxial growth and surface characterization techniques. The general procedure is as follows: First, a thin film of Pt(111) is epitaxially grown on α-Al_2O_3(0001) substrate by Molecular Beam Epitaxy (MBE) (in collaboration with Stéphane Andrieu, Karine Dumesnil from the *Spintronic and Nanomagnetism Team* and Ludovic Pasquier from the *Daum platform* at the IJL). Subsequently, a thin film of $SrTiO_3$ is deposited by Pulsed Laser Deposition (PLD) (in collaboration with Olivier Copie from the *Spintronic and Nanomagnetism Team* at the IJL). The different stages of the growth process are followed by RHEED. X-Ray photoemission (XPS) and Auger nano Scanning electron microscopy (Auger nano-SEM) are used to characterize the chemical composition of the surface. Epitaxially of the Pt layer and lattices parameters are verified by X-Ray Diffraction. Once the sample is ready, the next step is to obtain an UTOx through an annealing procedure as reported in ref. [10]. The complexity of this project lies in the challenging experimental conditions needed to the formation of aperiodic 2D structures in these systems, for instance high temperatures (>800°C) while keeping low pressures (<10^{-8}mbar). After annealing procedure, the resulted surface is investigated by low energy electron diffraction (LEED), scanning tunnelling microscopy (STM) and XPS. The thinfilm stacking was investigated as well by means of high resolution transmission electron microscopy (HRTEM) by Sašo Šturm and Sorour Semsari Parapari in collaboration with the Jožef Stefan Institute in Slovenia.

The present manuscript is divided into four main parts detailed as follows: Chap-

ter 1 starts with a description of important concepts and current status of UTOx supported on metals. Then, the reader will find a review of the fundamental concepts of aperiodic order with a special focus in the state of the art of OQCs and OQC approximants.

Chapter 2 gives a description of the experimental methods used during the different stages of this project. The first part of this chapter is dedicated to the thin-film growth techniques. The second one, focusses on surface characterization techniques.

Chapter 3 is dedicated to the sample fabrication by thinfilm stacking. Each stage of the $SrTiO_3$/Pt(111)//Al_2O_3(0001) stacking is described. The results of the structural and chemical characterizations are discussed.

Chapter 4 presents the main results of this work: the observation and characterization of different complex phases derived from ultra-thin films of $SrTiO_3$ supported on Pt(111)//Al_2O_3(0001). In this chapter the reader can find the description of two new OQC approximant phases, in addition to the first report of the observation of the σ-phase approximant derived from $SrTiO_3$/Pt system. *Ab initio* calculations were performed (by Thiago T. Dorini and Émilie Gaudry) leading to a structure model and STM simulations for these OQC approximant phases. Interfacial properties were calculated as well. Other complex 2D hexagonal phases were found in this system depending on the preparation conditions. They are discussed here as well.

At the end of this manuscript the reader can find general conclusions and future perspectives.

Bibliography

[1] G. Barcaro and A. Fortunelli. 2D oxides on metal materials: Concepts, status, and perspectives. *Physical Chemestry Chemical Physics*, 21:11510, 2019.

[2] C. Wu, M. R. Castell, J. Goniakowski, and C. Noguera. Stoichiometry engineering of ternary oxide ultrathin films: Ba_x Ti_2O_3 on Au(111). *Physical Review B*, 91(15):155424, 2015.

[3] S. Förster, K. Meinel, R. Hammer, M. Trautmann, and W. Widdra. Quasicrystalline structure formation in a classical crystalline thin-film system. *Nature*, 502(7470):215–218, 2013.

[4] S. Schenk, S. Förster, K. Meinel, R. Hammer, B. Leibundgut, M. Paleschke, J. Pantzer, C. Dresler, F. O. Schumann, and W. Widdra. Observation of a dodecagonal oxide quasicrystal and its complex approximant in the $SrTiO_3$-Pt(111) system. *Journal of Physics: Condensed Matter*, 29(13):134002, 2017.

[5] S. Förster, S. Schenk, E. M. Zollner, O. Krahn, C-T. Chiang, F. O. Schumann, A. Bayat, K-M Schindler, M. Trautmann, R. Hammer, K. Meinel, W. A. Adeagbo, W. Hergert, J. I. Flege, J. Falta, M. Ellguth, C. Tusche, M. DeBoissieu, M. Muntwiler, T. Greber, and W. Widdra. Quasicrystals and their Approximants in 2D Ternary Oxides. *Physica Status Solidi (B)*, 257(7):1900624, 2020.

[6] S. Förster, M. Trautmann, S. Roy, W. A. Adeagbo, E. M. Zollner, R. Hammer, F. O. Schumann, K. Meinel, S. K. Nayak, K. Mohseni, W. Hergert, H. L. Meyerheim, and W. Widdra. Observation and Structure Determination of an Oxide Quasicrystal Approximant. *Physical Review Letters*, 117(9):095501, 2016.

[7] E Cockayne, M. Mihalkovič, and C. L. Henley. Structure of periodic crystals and quasicrystals in ultrathin films of Ba-Ti-O. *Physical Review B*, 93(2):020101, 2016.

[8] E. M. Zollner, F. Schuster, K. Meinel, P. Stötzner, S. Schenk, B. Allner, S. Förster, and W. Widdra. Two-Dimensional Wetting Layer Structures of Reduced Ternary Oxides on Ru(0001) and Pt(111). *Physica Status Solidi (B)*, 257(7):1900655, 2020.

[9] F. E. Wührl, O. Krahn, S. Schenk, S. Förster, and W. Widdra. Antiphase Domain Boundary Formation in 2D Ba–Ti–O on Pd(111): An Alternative to Phase Separation. *Physica Status Solidi (B)*, (2100389), 2021.

[10] S. Förster, J. Flege, E. M. Zollner, F. O. Schumann, R. Hammer, Al. Bayat, K-M Schindler, J. Falta, and W. Widdra. Growth and decay of a two-dimensional oxide quasicrystal: High-temperature in situ microscopy. *Annalen der Physik*, 529(1-2):1600250, 2017.

Chapter 1

Introduction to 2D oxide materials: from perovskites to quasicrystals

Contents

1.1 The oxide-metal hybrid system 6
1.1.1 Generalities on oxide structures 7
1.1.2 Ternary oxides supported on metals 9
1.1.3 Structural motifs 12
1.2 Aperiodic order in UTOx supported on metals 14
1.2.1 Quasiperiodic structures 15
1.2.2 Approximant structures 17
1.2.3 Quasicrystals and their Approximants in 2D Ternary Oxides 17
Bibliography 26

When approaching the 2D limit, the structure and properties of ultra-thin oxide films (UTOx) can differ drastically from the related bulk material. In particular, completely new 2D structures with aperiodic order could be formed (depending on the preparation conditions) when UTOx are grown on metal surfaces, representing promising materials in view of fundamental science and technological applications. This is the subject of discussion of the present chapter. This chapter is divided as follows: a description of the 2D oxide-metal hybrid systems will be given in the first section. The structure of ternary oxides supported on metals will be discussed along with the observed structural motifs at the oxide surface in the 2D limit. In the second section a review of the investigations related to aperiodic order in UTOx will be given. Quasiperiodic and approximant structures will be discussed as first, in order to introduced to the reader quasicristallinity in 2D ternary oxides and their related approximant phases.

1.1 The oxide-metal hybrid system

UTOx are considered as a new class of materials with properties different from their bulk counterpart [1]. Although they present structural and electronic phenomena reminiscent of the bulk oxides, studies on this kind of systems realized that due to effects of 2D confinement and the interactions with the substrate, novel emergent phenomena appeared [2] (for instance, ferromagnetism at the interface of antiferromagnetic materials [3]; high mobility 2D electron gas at the interface between insulating $SrTiO_3$ and $LaAlO_3$ [4] that can also be superconducting and magnetic). The film thickness at which deviations from the bulk behaviour occurs may depend on the particular material and its diverse physical or chemical properties [1]. On the other hand, metal surfaces were the first material surfaces to be rigorously studied [2]. Thus, nowadays the surface science of metal single crystals is well established and its preparation is relatively easy [1]. Using metal surfaces as support for oxides growth may be advantageous. For instance, as metals are chemically different from oxides, the analysis of the composition or the identification of possible defects of the thin film could be easier to perform. In addition, the metallic conductivity allows the investigation of the UTOx by electron-based techniques [5].

For oxides at the 2D limit, the behaviour of the oxide-metal hybrid system is largely determined by the interactions at the interface. Several degrees of freedom (structural, electronic, chemical and magnetic) contribute to the interfacial interactions [1]. Although they are intimately coupled, here in this chapter, we will concentrate on the aspects mainly associated with the atomic structure and the chemistry at the interface. The interplay and the balance between parameters such as the lattice mismatch and symmetry, the mixing of the electronic energy levels as well as the chemical affinities and bonding at the interface, determine the atomic geome-

try of the 2D oxide layer. Besides, phenomena such as polarity compensation, strain release, charge transfer and the finite size effects could be completely different from the bulk oxide structure [1]. Therefore, the chemical bonding at the interface is a result of the local epitaxial relationship summed to the influence of the surface and adhesion energy of the overlayer in the total energy of the system [1]. These could lead to the formation of various geometries and phases as will be discussed in the following sections.

1.1.1 Generalities on oxide structures

Bulk oxide structures could be visualized from two different perspectives: as a stacking sequence of layers alternating, for instance, hexagonal planes of oxygen (anions) and metal atoms (cations); or as the combination of metal-oxygen polyhedral coordination blocks, connected and nested via shared corners, edges and planes of the polyhedra. If the metal surface is intended to provide mainly a rigid support for the 2D oxide layer, noble metal surfaces of group VIII or Ib are typically chosen [1].

1.1.1.1 Binary oxide structures

Some structure examples of binary oxides MO, MO_2, M_2O_3 where M=metal, are presented in Fig.1.1. The most common are (a) the rock salt, (b) the wurzite, (c) the fluorite, (d) the rutile and (e) the corundum (an example for each structure is presented as well). A wide range of structures and properties are intrinsic to these materials [6].

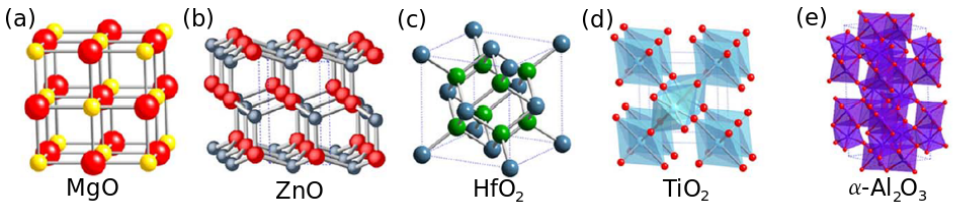

Figure 1.1 – Common binary oxide crystal structures: (a) rocksalt, (b) wurzite, (c) fluorite, (d) rutile, and (e) corundum (reproduced from [6]).

Nowadays, 2D systems from different binary oxides (i.e., oxides in Fig.1.1) are being studied for a variety of potential applications. Among them, the most popular are microelectronics (for instance, ultrathin SiO_2 films grown on Si have been the basis of metal-oxide field effect transistors [1]) and catalysis (MgO films grown on Mo or Au) [7].

1.1.1.2 Increasing complexity: ternary oxide structures

Ternary oxides present complex structures which lead to interesting properties highly desirable for technological applications. For example piezoelectricity (i.e., $FeTiO_3$ which has an ilmenite structure), large band gap insulators, superconductivity (i.e., $MgAl_2O_3$ with a spinel structure), among others [6]. Fig.1.2 shows common ternary oxide crystal structures including the (a) ilmentite, (b) the spinel, (c) the perovskite structure and derivatives such as (d) the Ruddlensden-Popper series and (e) layered perovskites. By far the most interesting aspect of complex oxides is the ability to engineer or tune their physical properties. This can be very well done in oxides with perovskite structure [6]. In the following, special focus will be given on ternary oxides with perovskite structure.

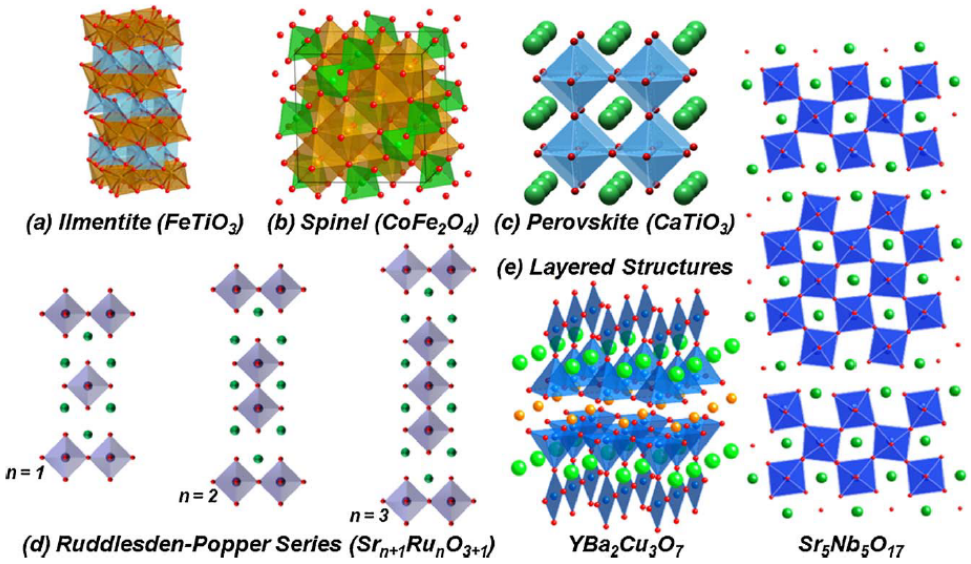

Figure 1.2 – Common ternary oxide crystal structures: (a) ilmentite, (b) the spinel, (c) the perovskite structure and perovskite derivatives: (d) the Ruddlensden-Popper series and (e) layered perovskites (reproduced from [6]).

Perovskite oxides are represented by the formula ABO_3, where A and B are two different types of cations. Cation A carries a charge of 2+ or 3+ while cation B carries a charge of 4+ or 3+. Together with three O^{2-} anions, they form a cubic (or pseudocubic) structure as presented in Fig.1.3 (top) [5]. This structure can accommodate almost 30 different elements on the A site and over half of the periodic table on the B site as shown in Fig.1.3 [8]. The characteristic features of these materials are, on the one hand, strong electron correlations that consist in the interaction of the charge, orbital and spin degrees of freedom, and on there other hand, ordered phases resulting from symmetry lowering transition accompanied by the

spontaneous development of order parameters like, e.g. elastic strain, electric polarization and/or magnetization. These are the key building blocks giving rise to a wealth of functionalities such as metal-insulator transition, colossal magnetoresistance, high transition temperature (T_c) superconductivity and the emergence of ferric phases (e.g.,ferroelectricity, ferromagnetism). Furthermore, transition metal oxides are also very sensitive to small stimulation yielding a strong response to electric, magnetic or strain field applications.

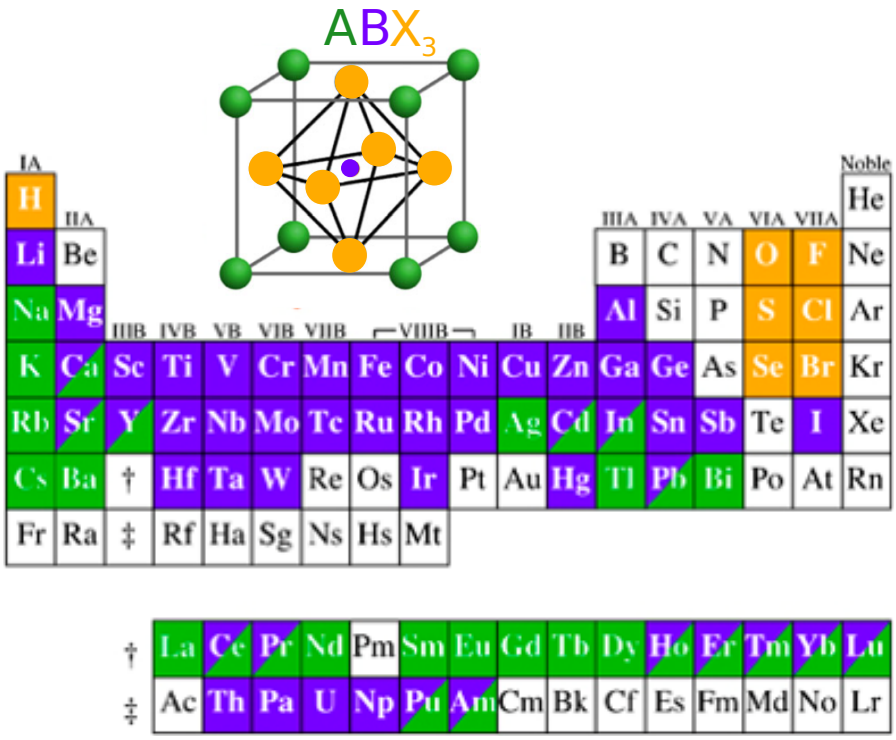

Figure 1.3 – The perovskite crystal structure. The possible elements that can occupy the three sites (A, B, and X) are indicated in green, blue and yellow on the periodic table respectively (reproduced from [8]).

1.1.2 Ternary oxides supported on metals

Ultra-thin films of ternary oxides have been prepared on metal substrates by different methods as summarized in Table 1.1. Several surface characterization techniques have been used as well to investigate the variety of structures that emerge at the surface with no counterpart in the respective bulk systems [9].

As an example of monolayers (ML) of ternary oxides prepared on metal substrates, tungstenates containing Fe or Cu were fabricated by solid state chemical

UTOx/M substrate	Film thickness	Preparation method	Investigated by	Ref
$SrTiO_3$/Pt(111)	4 Å	MBE	AES, SPALEED, STM	[10]
$BaTiO_3$/Pt(111), Pd(001)	Sub ML - 1 nm	RF magnetron sputtering	STM, LEED, XPS	[11, 12]
$BaTiO_3$/Fe(001), Pd(001), Pt(001)	1,2,3 uc	PLD	SXRD	[13, 14]
$BaTiO_3$ and $SrTiO_3$/Pt(001)	0-8 uc	PLD	LEED,MEED, stress	[15]
$CaMoO_4$/Mo(001)	1 ML	MBE	STM, LEED, AES	[16]
$BaTiO_3$/Au(111)	1 ML	MBE	STM, Monte Carlo	[17]
$CuWO_4$/Cu(110)	1 ML	MOCVD	LEED,STM, XPS, NEXAFS, HREELS, DFT	[18]
$FeWO_3$/Cu(111)	1 ML	MOCVD	LEED,STM, XPS, TPD, DFT	[19]

Table 1.1 – Summary of studies on ultrathin ternary oxide films supported on metal substrates (ML=Monolayer and uc=unit cell. Adapted from[9]).

reactions at the surface. First, clusters of $(WO_3)_3$ are deposited at low temperatures on Cu(001) or on a ML of FeO(111)/Pt(111) [18, 19]. Upon annealing, a surface chemical reaction is initiated leading to the formation of $FeWO_x$ at the Pt surface. Annealing at 900°C in UHV produces a buckled 2D honeycomb (HC) lattice, consisting in intermixed Fe^{2+} and W^{4+} ions terminated by oxygen atoms in Fe-W bridging positions as shown in Fig.1.4 [19]. This system is the first ternary compound known to form a 2D HC lattice, which is of special interest since the 2D HC geometry is the origin of many of the fascinating properties found in 2D materials, as is the case of graphene [19].

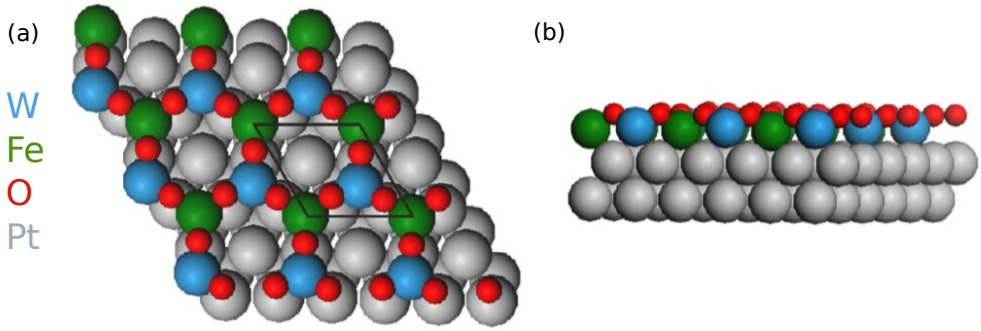

Figure 1.4 – Structure model of the (2×2)-$FeWO_3$ phase on Pt(111): (a) Top and (b) side views derived from density functional theory (DFT) calculations (reproduced from [19]).

The HC structure has been used as well as a template for the deposition of Ba atoms. A Ti_2O_3 HC lattice was grown commensurately on Au(111) where low concentrations of Ba atoms were evaporated onto this film. The UTOx consisting in $Ba_xTi_2O_3$/Au(111) display flexible structural and electronic characteristics which can be tuned by controlling the Ba coverage x [17]. Fig.1.5 (a) shows an STM image of the clean (2×2) Ti_2O_3 lattice, where the Ti atoms are assigned to the bright protrusions forming a HC pattern. O atoms sit on the bridge sites between neighbouring

Ti atoms. Fig.1.5 (b) shows an STM image of a single Ba adatom occupying the hollow site of the HC lattice. *Ab initio* calculations (Fig. 1.5(c)) confirm that the Ba atom located in the hollow site of the HC lattice is the energetically most favourable atomic arrangement. Six Ba-O bonds are formed with the neighbouring anions. The Ba-O bond length is close to those formed for bulk BaO in the rock-salt structure, meaning that upon adsorption a real ternary compound is formed. Depending on the Ba coverage x, the $Ba_xTi_2O_3$ UTOx presented several ordered phases as well as a disordered labyrinth-like phase as evidenced in the STM images in Fig.1.5(d). This structural evolution was modelled by Monte Carlo simulations showing an excellent agreement with the STM images for all coverages $0 \leq x \leq 0.62$ [17]. The charge transfer occurring between the electropositive Ba atoms and the highly electronegative support gives rise to interfacial dipole moments resulting in dipole-dipole Ba-Ba interactions, which is a key factor in understanding the Ba ordering. In this way a reduction in the work function of the system is lowered affecting significantly the reactivity of the UTOx [17].

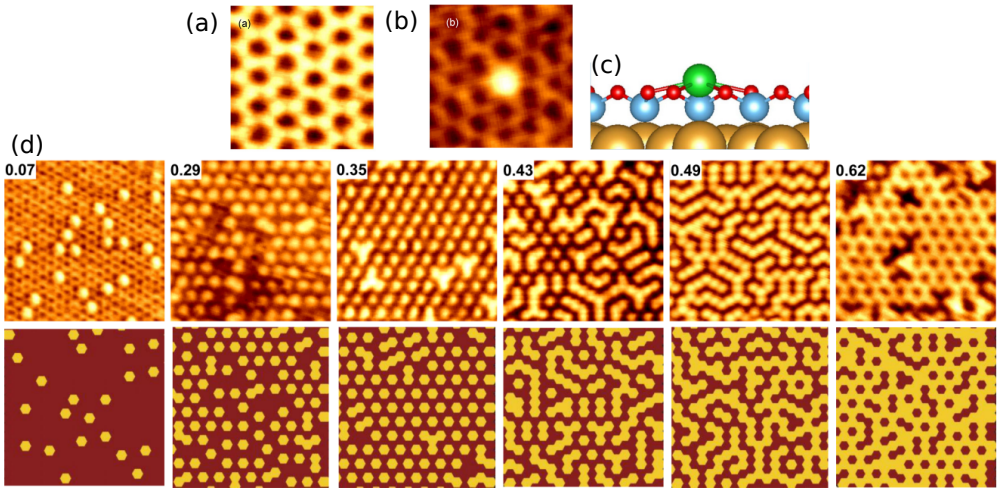

Figure 1.5 – (a) STM image of the bare Ti_2O_3 HC lattice on Au(111) (2.9×2.9 nm^2; V_s= 0.98 V; I = 0.2 nA). (b) STM image of a Ba atom adsorbed on the HC lattice (2.9×2.9 nm^2; V_s= 0.72 V; I = 0.2 nA). (c) Side view of a representation of the Ba atom (green) on the top of the Ti_2O_3 HC lattice/Au(111). O, Ti, Au atoms are represented by red, blue and yellow balls respectively. (d) (*top*) STM images (10×10 nm^2; V_s from 0.35 to 1 V; I from 0.18 to 0.28 nA) and (*bottom*) Monte Carlo simulation for different Ba coverages indicated at the left top corner. Only the adsorption sites are represented (yellow when occupied and dark red when empty) (reproduced from [17]).

The fabrication of ternary oxide layers is commonly done via pulsed laser deposition (PLD), magnetron sputtering or molecular beam epitaxy (MBE).

When growing perovskite thin films, the metal substrate needs to satisfy three important conditions: first, the lattice mismatch between the oxide and the metal must be small to facilitate an epitaxial layer-by-layer growth. Second, the metal has to be stable at high temperatures. Third, the metal has to be stable against high oxygen partial pressures, which is required for the growth of stoichiometric oxide films [5].

So far ultra-thin films of $BaTiO_3$ have been grown on Pt(111), Pt(001), Ru(0001), Pd(001) and Fe(001), [12, 13, 14, 15, 11, 20]. $BaTiO_3$ grown on Pt has been highly investigated by Förster *et al.*. Frequently they grow the oxide film in two steps: (i) $BaTiO_3$ is deposited by RF magnetron sputtering at room temperature (RT) followed by (ii) a subsequent annealing up to temperatures between 627°C and 777°C in O_2 partial pressures up to 10^{-4} mbar [12, 11]. The annealing step is important to initiate diffusion and to achieve long-range ordering in the first amorphous deposited material [5]. As a result, epitaxial $BaTiO_3$ films of bulk-like composition are formed. Upon further annealing at higher temperatures (around 850°C), the continuous oxide film turns into separated oxide islands on Pt, leading bare zones of the metal surface. This process is known as dewetting transition. Furthermore, similar annealing under UHV conditions produces a rewetting of the full metal surface by a 2D reduced oxide film [21]. In this wetting layer, various complex structures with large unit cells have been observed depending on the preparation conditions [22, 21]. One of the most interesting observations on these 2D UTOx system is that not only periodic structures with no equivalent in the bulk form have been found, but even aperiodic arrangements were discovered as will be discussed later in this chapter.

These periodic and aperiodic structures share common structural motifs which allow to study the particular surface geometry of each observed UTOx phase and its resulted properties and possible applications. This will be discussed in detail in the following section.

1.1.3 Structural motifs

In the 2D limit, UTOx presented structural and electronic phenomena quite different from the bulk oxides as discussed so far, due to the effects of 2D confinement and the UTOx/support interaction[2]. For example, several morphologies at atomic level of oxides grown on (111)-metals have been observed whose structures have no equivalent in bulk form [23, 24, 17]. The understanding of the fundamental nature of the formation of UTOx and the relationships between its local atomic structures and its physicochemical properties is still a subject of active research.

The combination of surface science characterizations and theoretical methods has provided to researchers in the UTOx field a database of UTOx with novel structural concepts and complex phases with atomic details (see e.g. Refs[17, 25, 26, 27,

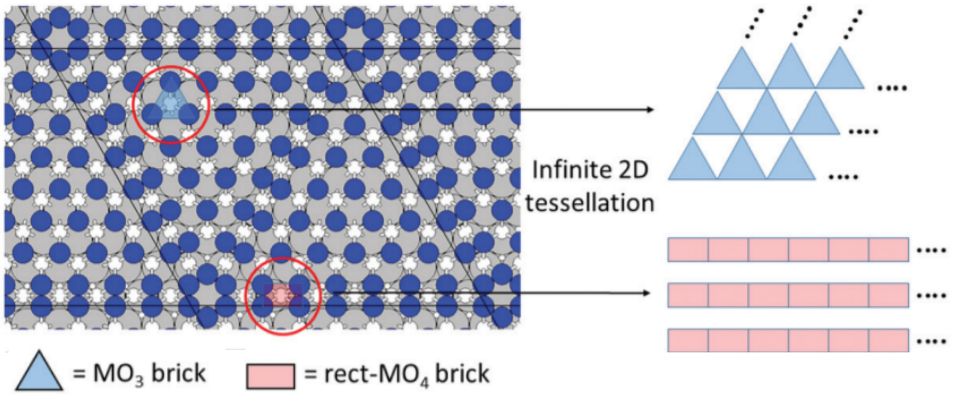

Figure 1.6 – *Left:* hexagonal $TiO_x(9\times9)$phase in which MO_3 bricks and deformed MO_4 bricks are marked in red. *Right:* tessellation of the plane by the MO_3 and MO_4 bricks (reproduced from [2]).

28]). Defining structural motifs is useful since it allows to classify and to describe a given UTOx phase. Computational modelling has played an important role in the study of UTOx supported on metals. As an example, Barcaro *et al.* derived building principles of pseudomorphic UTOx grown on (111) metal surfaces by studying TiO_x/Pt(111) phases reported in ref. [23]. The authors explain the interplay of the morphology and the stoichiometry in these phases through a combination of experimental and theoretical analysis. Spin-unpolarized density functional calculations allowed to designed and predict new phases confirmed experimentally [23].

Fig.1.6 shows the decomposition of a given TiO_x/Pt(111) UTOx phase into its constituent structural motifs indicated by the red circles. These motifs are defined as a MO_3 triangular brick and a MO_4 square brick, here deformed in a rectangular (rect-) brick. They are then replicated to cover the 2D plane (tessellation or tiling). Thus, these bricks are actually the structural motifs defined by their stoichiometry (MO_2, MO_3, MO_4, etc.) and by their epitaxial relationship with the underlying surface [2].

By combining bricks, sharing their vertex or their edges, one can obtained multiple of experimentally observed UTOx phases as presented in Fig.1.7 where some reported phases have been decorated with the MO_3 and the MO_4 bricks.

This procedure can be generalized to ternary UTOx, where multilayer phases could appeared due to the metal segregation in different layers [2]. Fig.1.8 shows the special case of the tessellation of a UTOx quasicrystalline phase derived from reduced $BaTiO_3$/Pt(111) [22] as mentioned at the end of the precedent subsection. With this example we introduce the topic of the next section, where aperiodic 2D films derived from reduced perovskite layers, supported on hexagonal metal surfaces are discussed as a particular phenomena of UTOx at the 2D limit.

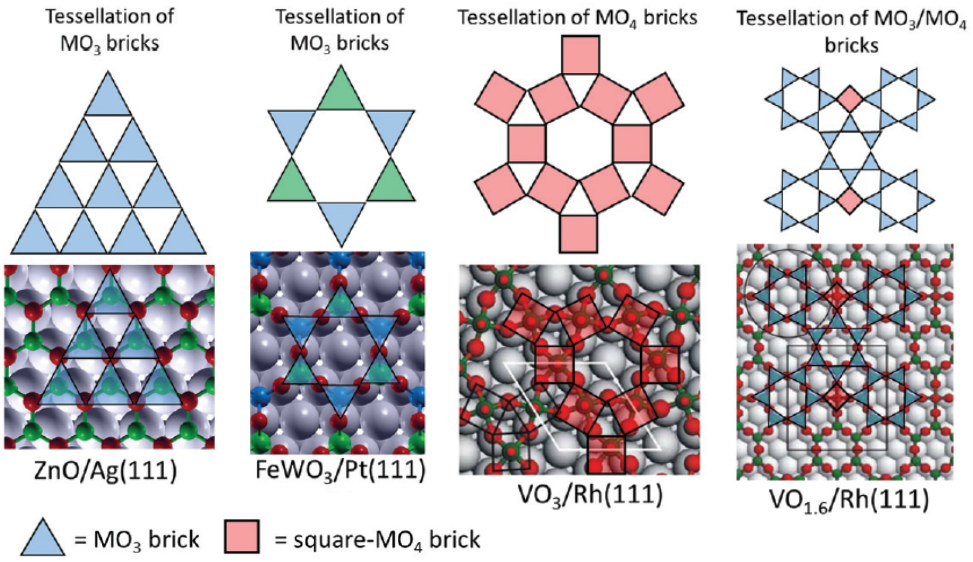

Figure 1.7 – Examples of single-layer UTOx phases and their 2D-tessellation using MO_3 bricks, MO_4 bricks and a combination of both (reproduced from [2]).

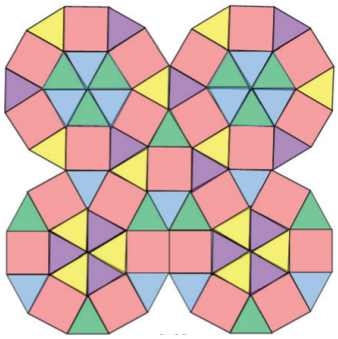

Figure 1.8 – Example of the tessellation of a ternary UTOx quasicrystalline phase, observed in $BaTiO_3$/Pt(111) (reproduced from [2]).

1.2 Aperiodic order in UTOx supported on metals

In 2013, Förster *et al.* observed for the first time an aperiodic structure formed in reduced wetting layers derived from $BaTiO_3$/Pt(111) [22], as previously mentioned in Sec.1.1.2.

This discovery was astounding for two major reasons: first, this was the very first report of aperiodic, quasicrystal (QC) phases developed in oxide materials. Second, these oxide QC (OQC) are the first example of spontaneous formation of QC-crystal heteroepitaxy [9].

But, what is exactly a quasicrystalline structure? Before going further, we will discussed in the following subsection, the generalities of QCs and some of the most important contributions to this field.

1.2.1 Quasiperiodic structures

Dan Shechtman *et al.* discovered an icosahedral alloy in 1984 [29], generating excitement as well as confusion in the scientific community (see Fig.1.9 (a), where Shechtman and his colleges were discussing about quasicrystallinity at the National Institut of Standards and Technology (NIST)). The authors reported the existence of a metallic solid which diffracts electrons like a single crystal but has a point group symmetry $m\,\bar{3}\bar{5}$, which corresponds to an icosahedral structure inconsistent with lattice translations [29]. Fig.1.9(b) shows the famous electron diffraction pattern observed by Shechtman, where an icosahedral phase is characterized by sharp diffraction spots (comparable with a diffraction pattern of a high quality crystal). However, they were located in a pentagonal geometric construction given by inflation of a basis pentagon by the golden mean number: $\tau = (1+\sqrt{5})/2$, which is incompatible with a periodic distribution of atoms. Grains up to 2 μm in size with this structure were observed in rapidly cooled alloys of Al with 10-14 at.% Mn [29]. Originally, it was called 'icosahedral phase' by the authors. Then, just after one month of Shechtman's publication, Levine and Steinhardt introduced the term 'quasicrystals' to named structures with near-neighbour orientational order and similar properties of a crystal but with quasiperiodic rather than periodic translational order [30]. In other words, QC may be defined as structures with long-range aperiodic order and crystallographically forbidden rotational symmetries (e.g., fivefold, eightfold, tenfold and twelvefold rotation axes)[31]. Quasiperiodicity is actually a very ancient concept. The famous Fibonacci sequence dates from 1202 [32], as well as the mathematical study of quasiperiodic functions has been the subject of study since last century (e.g., refs: [33, 34, 35, 36, 37]). Shechtman's discovery was the first experimental proof of quasiperiodic structures. His discovery challenged the following principles of crystallography: (i) In 1784 René-Just Haüy postulated that all crystals were made up of clusters of atoms repeated periodically in three dimensions (implying that only one-, two-, three-, four- and six-fold rotations axes, 14 Bravais lattices, 32 point groups, 51 crystal forms and 230 space groups are possible to describe any crystal in the universe)[38] For 200 years all studied crystals fulfilled this condition. Thus, periodicity became the definition of a crystal and an axiom of crystallography [39]. (ii) It was well known since the beginning of the 20th century that diffraction patterns with sharp spots arrayed on the nodes of a reciprocal lattice could only come from a periodic object [39]. At the beginning, these structural aspects caused rejection and criticism by the crystallography community. Nevertheless, other stud-

ies (e.g., Tsai *et al.* work [40, 41]) found the formation of several stable icosahedral and decagonal QCs in Al-based intermetallic systems in agreement with the first results. Since then, a vast literature on quasicrystals started to be created. Only in the beginning of the 90's there were several review articles and collections summarizing the developments and issues in this field [42, 43, 31]. This revolutionary discovery even caused the rethought of the most basic concepts in crystallography. In 1991 the International Union of Crystallography (IUCr) changed the definition of crystal accepting the term 'aperiodic crystal': *"In the following by 'crystal' we mean any solid having an essentially discrete diffraction diagram, and by 'aperiodic crystal' we mean any crystal in which three dimensional lattice periodicity can be considered to be absent. As an extension, the latter term will also include those crystals in which three-dimensional periodicity is too weak to describe significant correlations in the atomic configuration, but which can be properly described by crystallographic methods developed for actual aperiodic crystals"* [44].

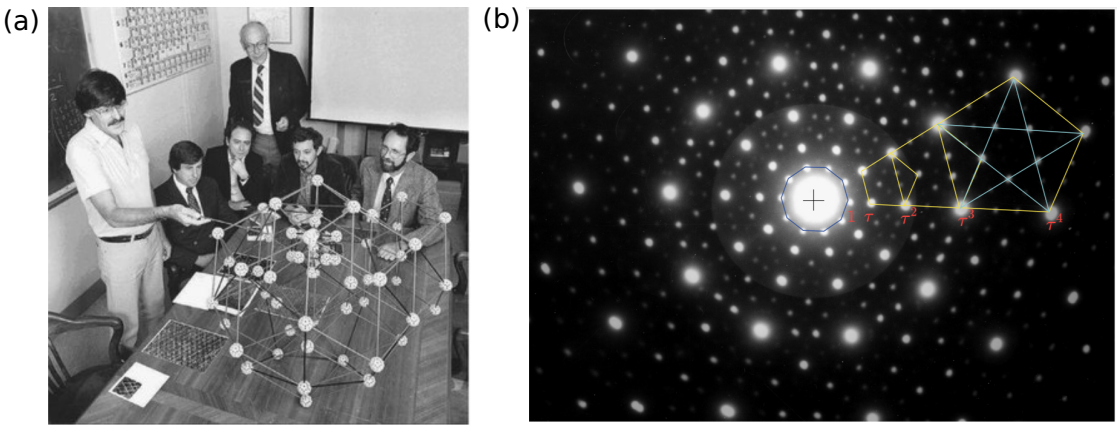

Figure 1.9 – (a) The research group on quasicrystals in early 1985 at NIST discussing about quasicrystalinity in Al_6Mn (from left to right, Dan Shechtman, Frank Biancaniello, Denis Gratias, John Cahn, Leonid Bendersky, and Robert Schaefer) [39] (b) The electron diffraction pattern observed by Dan Shechtman of the icosahedral phase in Al_6Mn comparable to those in high-quality crystals, but distributed according to an overall pentagonal symmetry constructed by the inflation of an elementary pentagon by τ, the golden mean (reproduced from [39]).

Nowadays, thermodynamically stable QC are known not only in intermetallic systems, but also in self-assembled colloidal systems [45], binary systems of nanoparticles [46], polymers [47], smectic phases [48] and more recently in oxides [22]. Naturally formed QCs have been observed in minerals stable under geological conditions[49] and accidentally synthesized in the first atomic bomb test [50].

It was only in 2011 (27 years after publishing his first results), that Dr. Shechtman

was recognized with the Nobel Prize in Chemistry *"for the discovery of quasicrystals"* [44].

1.2.2 Approximant structures

The lack of periodicity of QCs represents a problem for many ideas and methods used to describe the structure and properties of ordered solids. The concept of 'unit cell' is lost (as well as the 'Brillouin zone'), therefore calculations of electronic and vibrational properties by methods based on the periodicity of the lattice (Phonons and Bloch waves) can not be performed [31]. Nevertheless, atomic motifs or clusters with periodic arrangements are typically found to be formed along with the QC phase. These periodic structures are called approximants. They are built from the same structural units or building blocks as their parent QC, but arranged in a periodic way. Besides, approximants of various orders can exist. Low order approximants have a moderate unit cell size. With increasing order the unit cell dimensions also increase and the local order mimics that formed in the parent QC on a larger scale [31, 51].

Approximants are of special interest for the study of quasycristallinity. Since they resemble to the related QC and they are periodic, then the Bloch theorem can be applied and all the standard methods of solid-state physics can be used.

In the following we will describe the specific case of QCs and approximants recently found in ternary oxides supported on metals.

1.2.3 Quasicrystals and their Approximants in 2D Ternary Oxides

1.2.3.1 The discovery of 2D oxide QC

As mentioned at the beginning of this section, completely unexpected structures were found to be formed in the reduced wetting layers derived from perovskite oxides grown on hexagonal metal surfaces. These consist in long-range ordered structures with a sharp diffraction pattern with a 12-fold symmetry and no translational symmetry. They are known then as dodecagonal oxide QC (OQC) [9].

Fig.1.10 shows the data of the first OQC reported in 2013 by Förster *et al.* derived from an UTOx of $BaTiO_3$ grown on a single-crystal of Pt(111) [22]. The low energy electron diffraction (LEED) pattern presented in Fig.1.10 (a) reveals a 12-fold pattern (see the theoretical dodecagonal diffraction pattern in Fig.1.11 (b)) superimposed on the spots of the hexagonal substrate (marked by the black hexagons). To describe a dodecagonal structure, four lattice vectors are needed as indicated by the red arrows. This is due to the fact that dodecagonal patterns are produced by a projection from a four dimensional hyper-hexagonal lattice. Thus, using this four vectors the full diffraction pattern can be indexed [52]. Only one single domain of

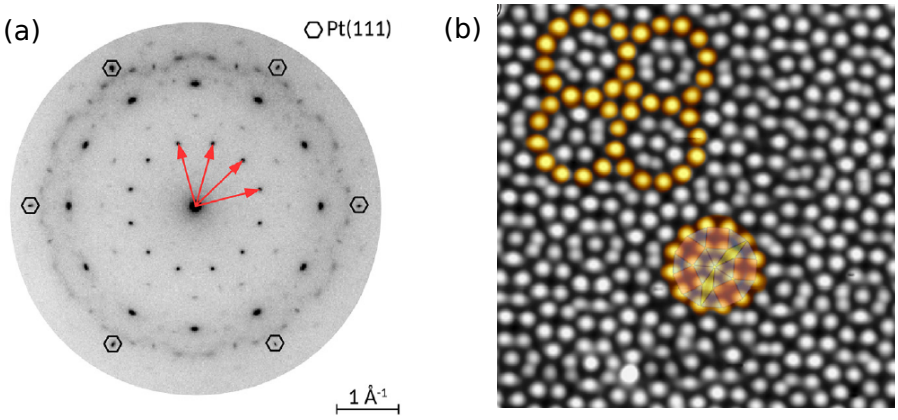

Figure 1.10 – (a) LEED pattern (at 140 eV) and (b) STM image (14×14 nm^2; 30 pA) of the 2D dodecagonal OQC derived from the $BaTiO_3$/Pt(111) system. The dodecagons are highlighted in yellow. They can be described in terms of squares, triangles and 30° rhombs motifs (reproduced from [9]).

the OQC exist, demonstrating that the OQC grows in an epitaxial alignment along the high symmetry direction of the Pt substrate [9]. The atomically resolved STM image in Fig.1.10 (b) shows the local aperiodic geometry. Authors claimed that the image contrast is given by the Ti sublattice. The Ti atoms are arranged in three different building blocks: squares, equilateral triangles, and 30° rhombs, sharing an edge length of 6.85 Å [9] . These building blocks are actually the characteristic motifs of an ideal dodecagonal tiling as described mathematically by Gälher [52] and Niizeki *et al.* [36]. This ideal tiling is known as NGT or Stampfli–Gähler tiling where a 12-fold structure can be generated from the tessellation of the mentioned motifs with a specific composition 2.73: 1: 0.37 (the number of triangles relative to the number of squares and of rhombuses) as shown in Fig.1.11 (a) [52]. The calculated diffraction pattern is shown as well in Fig.1.11 (b) generated by the four basis vectors discussed above.

Moreover, the atomic arrangement in Fig.1.10 (b) can be generated also by the recursion rule, where deflation steps generate self-similar tilings that scale with $(2+\sqrt{3})$ as exposed in Fig.1.12. The subsequent application of the recursion rule lead to the formation of characteristic dodecagons of the NGT (Fig.1.12 (b) right). By connecting the centers of these dodecagons, a triangle-square-rhomb tiling is formed on next-larger scale as emphasized in black [51].

Almost a perfect match between the OQC tiling element ratios found after the analysis of the STM images (see Fig.1.10 (b)) and the ideal NGT was observed by the authors. Ratios of 2.75:1:0.36 (for 8100 vertices positions determined from a large-scale STM image) and 2.73:1:0.37 (for 20000 vertices. An even larger dataset) were found in agreement with the NGT ratio of 2.73:1:0.37 [51]. A complete statistical

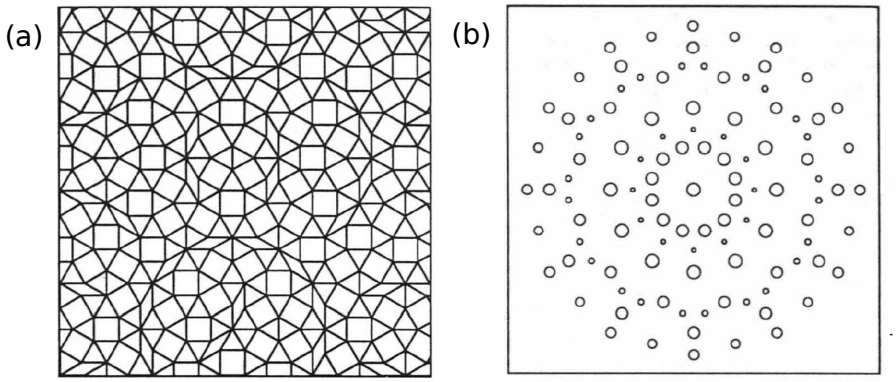

Figure 1.11 – (a) Constructed tiling using the three motifs: squares, triangles and 30° rhombs (reproduced from [52]). (b) Calculated dodecagonal diffraction pattern (reproduced from [52]).

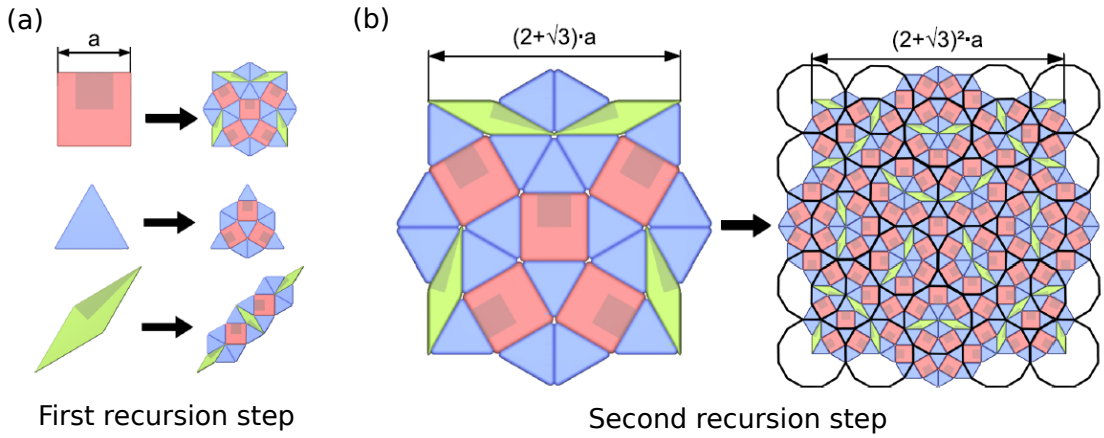

Figure 1.12 – Recursion rules for the dodecagonal NGT: (a) First recursion step. The shaded areas in the rhombs and the squares indicate a given orientation of these tiles that needs to be respected. (b) Second recursion step for the square element. After multiple interactions, a self-similar tiling is generated scaled by $(2+\sqrt{3})$. Higher hierarchical tiling forms the characteristic NGT dodecagons (marked in black) (reproduced from [51]).

analysis has been done by the authors in ref. [51] and references therein.

Surface X-ray diffraction (SXRD) has been used to obtain a reciprocal space map of the $BaTiO_3$-derived OQC [51]. This data contributed to establish a structural model of the OQC. On the other hand theoretical models based in *ab initio* calculations have been proposed by Cockayne *et al.* [53] where the NGT is formed by the Ba atoms as will be shown later in this section.

In 2017 Schenk *et al.* reported the observation of a 2D OQC derived from $SrTiO_3$

grown on Pt(111) [10]. This was the second observation of quasicrystallinity in oxides. Fig.1.13(a) shows the diffraction pattern measured by Spot Profile Analysis LEED (SPALEED) of the $SrTiO_3$ UTOx after annealing at 727°C in UHV. A dodecagonal diffraction pattern appeared suggesting the formation of an $SrTiO_3$-derived OQC. The local atomic arrangement of the $SrTiO_3$-derived OQC is shown in the atomically resolved STM image in Fig.1.13 (b). The Fourier transform (FT) of the STM image shows twelve equidistant sharp spots separated every 30° indicating the presence of a dodecagonal structure. The authors identified that two structures were formed in the wetting layer of reduced $SrTiO_3$/Pt(111): a well-ordered OQC and an approximant structure (identified in Fig.1.13(b) by the black squares as region 2 and 1 respectively). This STM image demonstrates that these structures (OQC and approximant) could coexist at the UTOx surface.

Patches of the well-ordered OQC (as in region 2 in Fig.1.13(b)) can be found locally in the STM images, allowing to identify the same dodecagonal arrangement built by the NGT motifs (squares, triangles and 30° rhombs) when bonding the bright protrusions. The measured edge length is 6.73 Å [10]. This OQC has strong similarities with the $BaTiO_3$-derived OQC. For instance, the same inflation rules can be applied and the tiling elements ratio given by: 2.79:1:0.36, close to the ideal NGT ratio [10].

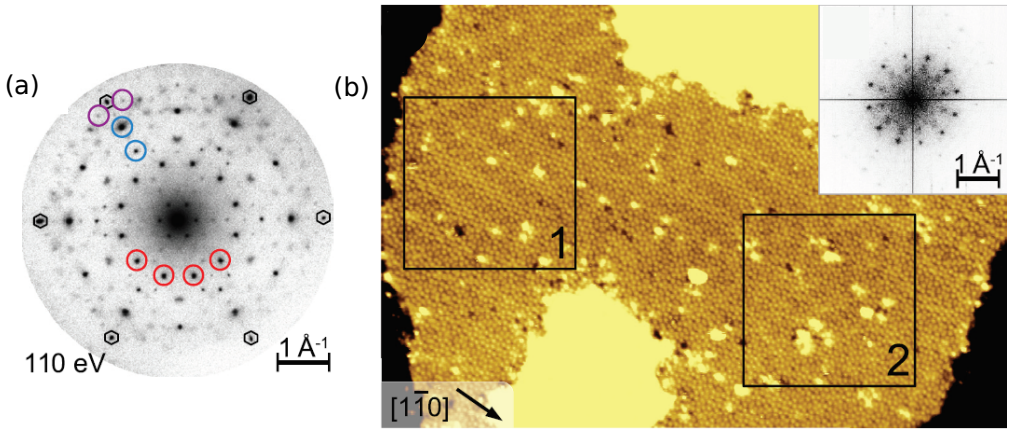

Figure 1.13 – (a) Diffraction pattern (measured by SPALEED) of the $SrTiO_3$/Pt(111)-derived OQC. First, second and third order OQC spots are marked in red, blue and magenta respectively. (b) atomically resolved large scale STM image (75×50 nm^2; -0.1 V; 20 pA) of the 2D OQC derived from the $SrTiO_3$/Pt(111) system. The regions 1 and 2 mark by black squares indicate a zone with an approximant structure coexisting with a zone where atoms arranged in a QC ordering respectively. The FT of the STM image is shown in the top-right side (reproduced from [10]).

1.2.3.2 Preparation and stability

For the preparation of OQCs, less than 1 nm of a ternary oxide needs to be depostited on the hexagonal substrate [51]. The preparation of $BaTiO_3$ on Pt(111) and its structural surface transformations have been studied in detail [11, 5, 21].

By annealing the oxide layer at temperatures above 627°C, long-ranged $BaTiO_3$(111) structure develops. Upon annealing to higher temperatures under oxidative conditions (10^{-6} mbar of O_2), the oxide film tends to reduce the interfacial contact with Pt, resulting in the formation of 3D islands. At higher oxygen concentrations, all $BaTiO_3$ segregates in islands with bare Pt(111) in between the islands. Under reducing conditions (in UHV), the annealing of a periodic or amorphous $BaTiO_3$ layer produces a rewetting of the Pt(111) surface starting at 747°C. This process starts at the step edges of the substrate, connecting the local patches with an homogeneous layer with time. At 747°C the layer is amorphous, covering completely the Pt substrate [51]. Upon higher annealing temperatures, a long-range structure is formed in the wetting layer. The OQC is typically found after annealing at temperatures between 800°C and 900°C (and pressures under 10^{-8}mbar)[21, 22, 51, 54]. At higher temperatures, the film rearanges into periodic approximant structures [51].

This wetting process can be reversed by re-oxidation as was evidenced using low-energy electron microscopy (LEEM) [21]. The complete process is shown in Fig.1.14. The OQC layer (in blue at the bottom right in Fig.1.14) is stable against dosing 10^{-6}mbar of molecular oxygen at 627°C [51]. However, with time the bright contrast of the substrate becomes visible and the wetting layer transforms into tiny islands of $BaTiO_3$ as shown in Fig.1.14 (bottom left). Moreover, by annealing further under oxygen the island density is reduced due to ripening and coalescence. In this way, the oxidation-reduction cycle is closed, fully reversible. For the case of $BaTiO_3$ on Pt(111), even upon multiple cycling, no Ba or Ti is lost by re-evaporation from the surface or diffusion into the Pt bulk [51].

For the preparation of OQC films, no special deposition technique is needed. Surface roughening as a consequence of sputter deposition or PLD and will not hinder the OQC formation. In fact, surface defects will be healed out during the high temperature treatment involved in the OQC formation process. However, the authors claimed that the highest level of precision in the preparation of OQC monolayers has been reached using MBE [51].

1.2.3.3 OQC approximants

As discussed previously, approximant structures frequently coexist with the QC phases. Fig.1.15 (a) illustrates the relationship between QC and their associated approximants. The highlighted motifs are the building blocks of the OQC tiling which could form periodic structures of different cell dimensions as shown in Fig.1.15 (b) and (c).

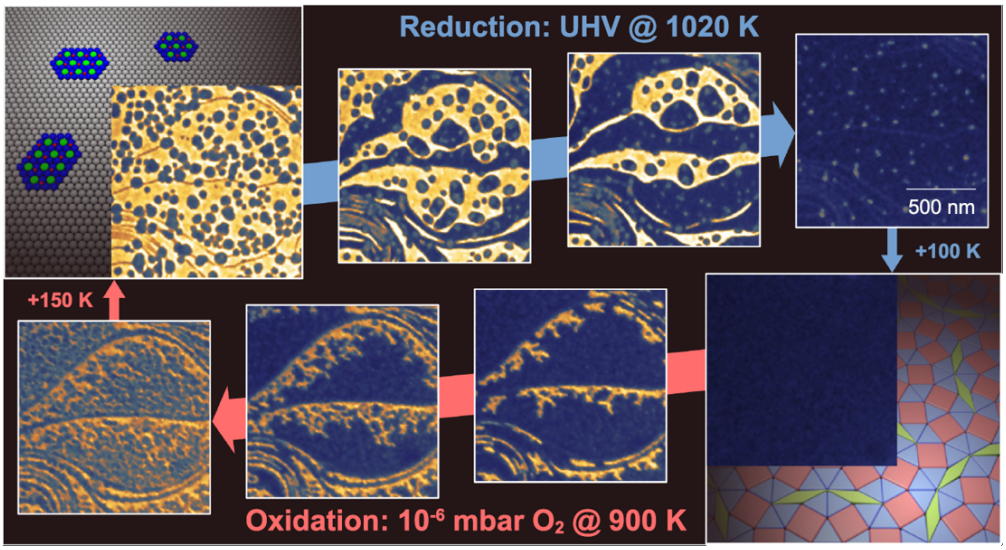

Figure 1.14 – *in situ* LEEM observation of the wetting and dewetting process of an UTOx of $BaTiO_3$ on Pt(111). At 747°C (1020 K) under UHV, $BaTiO_3$ islands (in blue) start to wet the bare Pt (top left) encapsulating the metal surface (top right). This oxide layer is a 2D film which continuously grows with time until full coverage of the Pt substrate. At 850°C (+100 K) still under UHV this wetting layer develops in an homogeneous OQC (bottom right). For high oxygen chemical potentials, the OQC decays into small $BaTiO_3$ islands (bottom left) when annealed at 627°C (900 K). At 777°C(+150 K) the small islands grow by coalescence closing the cycle (reproduced from [21]).

The small unit cell approximant in Fig.1.15 (b) has been observed in the $BaTiO_3$/Pt [55, 56] and in the $BaTiO_3$/Ru(0001) [20] systems. This square-triangle tiling is called σ-phase approximant, which include six tiling elements (two squares and four triangles) as was found for the $BaTiO_3$-derived OQC. It was first described 400 years ago by Kepler [57] and is also known as 3^2.4.3.4 Archimedean tiling (formed by regular polygons with n edges. Thus, 3 denotes an equilateral triangle, 4 a square, 5 a pentagon, etc. There are many possibilities of edge-to-edge tilings of the plane depending on the disposition of the polygons around a vertex. Therefore, a nomenclature based on the type and number of polygons around the vertex in cyclic order is used) [58] or snub-square tiling.

Taking advantage of the periodicity of this structure, DFT calculations have been performed as a complement to the experimental data in order to construct a complete structure model as mentioned above. Fig.1.16(a) shows the relaxed surface structure of the σ-phase approximant derived from DFT calculations where Ti atoms form the snub-square tiling observed by STM [55]. This model was in agreement

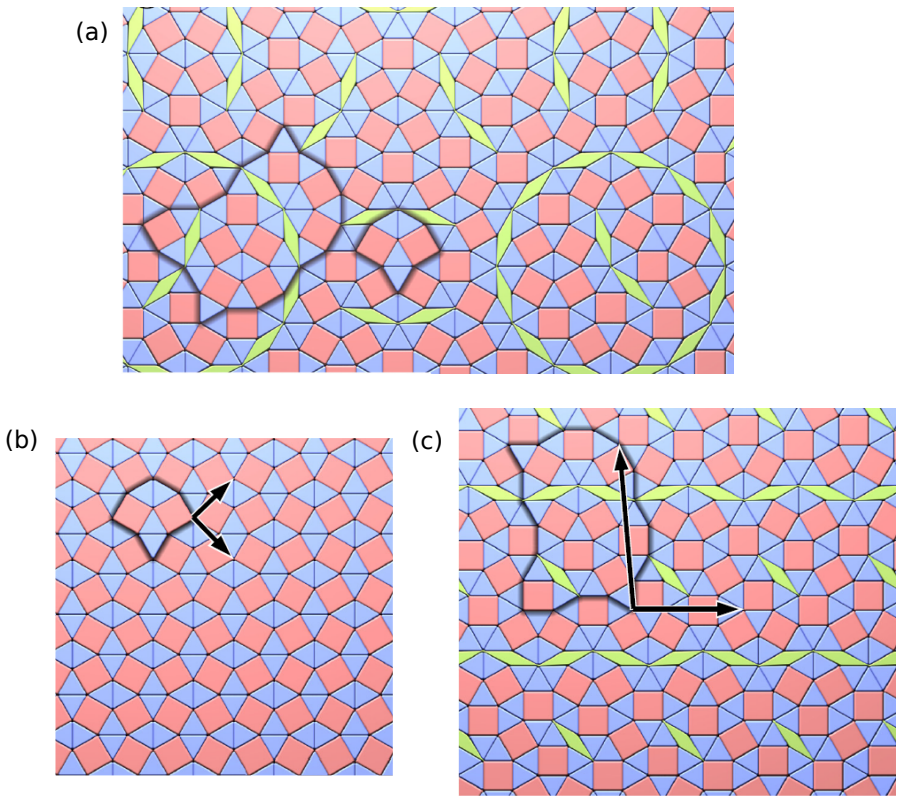

Figure 1.15 – (a) Scheme of the OQC tiling. The highlighted motifs are the building blocks of the OQC tiling which form periodic structures (approximants) of different unit cell dimentions. (b) The tessellation of the smaller approximant (on the right) in (a). (c) The tessellation of the larger approximant (on the left) in (a). The unit vectors of the periodic structures are indicated by the black arrows (reproduced from [51]).

with previous SXRD measurements where the structure analysis confirmed that Ti atoms are at the vertices of the dodecagonal motifs. The square-triangle tiling is strongly distorted, nevertheless it is in agreement with the SXRD-derived charge density plot. The total stoichiometry of the structure can be written as $Ba_4Ti_4O_{10}$ per unit cell. The side view of the structure, show that Ti atoms reside in a plane relaxing towards the Pt surface. Ba atoms relax outwards and O lead to two species with different degree of hybridization [55]. A second structural model was proposed by Cockayne *et. al* where a specific stoichiometry was assigned to each ideal NGT element as shown in Fig.1.16(b) top. In this model Ba atoms occupy the vertices of the tiles. By assuming that the bright protrusions observed in the STM images are the Ba atoms instead of the Ti atoms, and that the Ti and O atoms form a Ti-O network with threefold coordinated Ti, the authors constructed structure models

for several OQC approximants [53]. Fig.1.16(b) shows one of the structure model where the snub-square tiling is generated by the ideal NGT decorated with Ba, Ti and O atoms as building blocks for each tiling element, with edge lengths of 6.85 Å [53].

The existence of detailed structure models for the OQC approximants would contribute to the understanding of the fundamental concepts of quasicrystallinity in UTOx. For instance, how the QC structure of Ba-Ti-O is stabilized relative to approximant and other non-approximant arrangements [53]. Although the models presented here differ, they represent advances in the construction of a unique structural model which can be used for better understanding of OQCs.

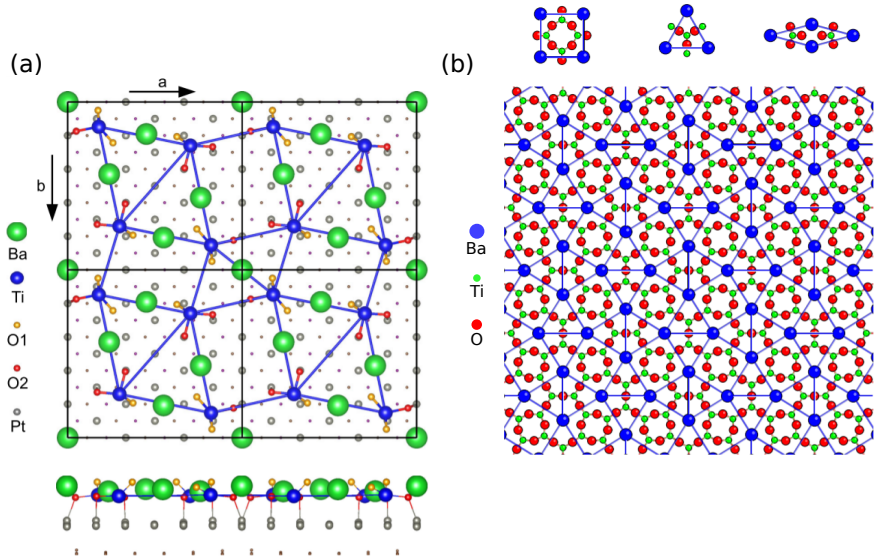

Figure 1.16 – Relaxed structures of the Ba-Ti-O σ-phase approximant structure on Pt(111) from DFT calculations (a) where Ti atoms are at the node of each tiling element (top and side views) (reproduced from [55]) and (b) where Ba atoms are at the node of the tiling elements. An specific decoration for the motifs is proposed as well (reproduced from [53]).

The large unit cell approximant illustrated in Fig.1.15(c) has been observed in the $SrTiO_3$/Pt(111) system [10]. The region 1 in Fig.1.13(b) marked a local zone where this approximant structure was found. What is special from this approximant phase is that its unit cell includes all the necessary motifs to describe the OQC tiling. Moreover, the characteristic dodecagonal motif is part of the monoclinic unit cell. The unit cell contains 36 tiling elements including nine squares, twenty four triangles, and three rhombs. The length of the shorter axis of the monoclinic rectangle is 25.1 Å . This value corresponds to the diameter of the dodecagonal unit, which is $(2+\sqrt{3})$ times the fundamental length of the OQC [10]. The long axis of the unit cell

has an angle of 95° with respect the short one, and a length of 37.7 Å . The short axis is aligned to the $< 1\bar{1}0 >$ direction of Pt [10]. Similar to the σ-phase approximant, this large unit cell monoclinic approximant forms a commensurate superstructure on the Pt(111) substrate given by the matrix $\begin{pmatrix} 9 & 0 \\ 9 & 16 \end{pmatrix}$ [59].

In addition to the discussed approximants, other approximant structures have been reported in other combinations of $BaTiO_3$ grown on metal surfaces. A wagon-wheel structure was found in the $BaTiO_3$/Pt(111) system as shown in the atomically resolved STM image in Fig.1.17 (a). A full dodecagon is contained in the hexagonal unit cell, called Wiegner-Seitz cell (WSC) [60]. The dense packing of the tiling results in a triangular cavity at the corners of the WSC as marked by the red circle. This cavities can be occupied by an additional atom as marked by the blue circle. The WSC is decorated by the NGT as follows: five squares, twelve triangles and two rhombs [60].

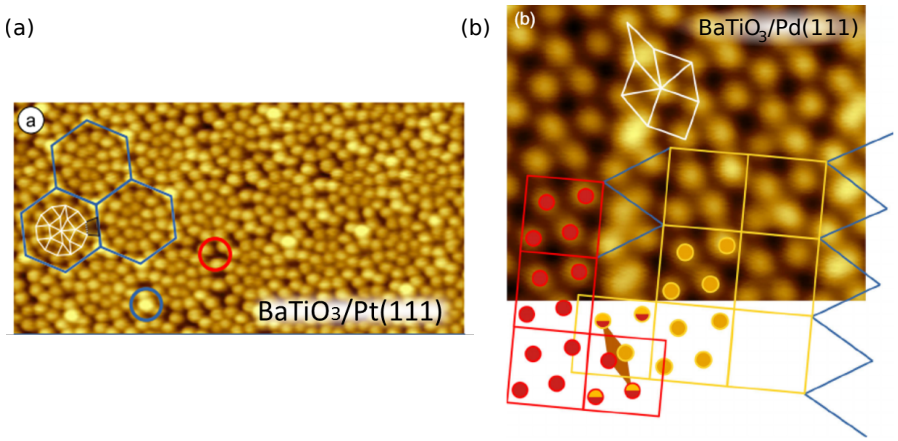

Figure 1.17 – STM images of (a)the wagon-wheel structure derived from $BaTiO_3$/Pt(111). The WSC is highlighted by the blue hexagons containing a characteristic dodecagon as indicated in white. The corner positions of the WSC can be either occupied or empty (blue and red circles) (24 ×12nm^2; 0.1 V; 0.5 nA. Reproduced from [60]. (b) The σ-phase approximant structure with incorporated row of rhombs (5×6 nm^2; 2V; 40 pA) (reproduced from [61]).

$BaTiO_3$ was deposited as well on Pd(111). After annealing under oxidation conditions, the ternary oxide tends to form 3D islands dewetting the Pd(111) surface, and then after annealing under reducing conditions a reduced 2D UTOx layer is formed between the islands. This behaviour is typical for ultrathin ternary oxide films on metal supports as was previously described for the case of $BaTiO_3$/Pt(111) (more details in the next section). On the reduced Ba-Ti-O film a σ-phase approximant structure was observed, but with local modifications in comparison with Ba-

Ti-O reduced films on other substrates. In this system, three different characteristic tiling motifs occur. These are the σ-phase, a triangle- rhombs patch, and a triangle-square-rhombs patch. The atomically resolved STM image in Fig. 1.17 (b) shows well organized rows of the σ-phase (in red and yellow) which an additional triangle-square-rhombs structure (in white) also well ordered leading to rows of vertically stacked rhombs inclined 30° and 150°. The σ-phases in two rows are shifted vertically by half of a unit cell. In fact, this phase shift in addition to the incorporated rhombs reveals the presence of 1D antiphase domain boundaries [61].

In summary, the field of aperiodic UTOx in the 2D limit has developed into a broad research area. The combination of different ternary oxides/metals is still an open possibility to continue exploring the structure and properties of OQCs. Investigations towards an understanding of the driving forces for the transition from periodic to aperiodic order are still in progress. The high level of control provided by the state-of-the-art surface science experiments and the reduced dimensionality of the OQCs, which reduces the complexity of this type of quasicrystal dramatically as compared to intermetallic or soft-matter systems, makes OQCs a perfect model system for addressing the question of the origin of aperiodic structure formation in general [9].

Bibliography

[1] F. P. Netzer and S. Surnev. Structure Concepts in Two-Dimensional Oxide Materials. In Falko P. Netzer and A. Fortunelli, editors, *Oxide Materials at the Two-Dimensional Limit*, pages 1–38. Springer International Publishing, Cham, 2016.

[2] G. Barcaro and A. Fortunelli. 2D oxides on metal materials: Concepts, status, and perspectives. *Physical Chemestry Chemical Physics*, 21:11510, 2019.

[3] C. Adamo, X. Ke, P. Schiffer, A. Soukiassian, M. Warusawithana, L. Maritato, and D. G. Schlom. Electrical and magnetic properties of $(SrMnO_3)n/(LaMnO_3)2n$ superlattices. *Applied Physics Letters*, 92(11):112508, 2008.

[4] A. Ohtomo and H. Y. Hwang. A high-mobility electron gas at the $LaAlO_3/SrTiO_3$ heterointerface. *Nature*, 427(6973):423–426, 2004.

[5] S. Förster and W. Widdra. Ultrathin Perovskites: From Bulk Structures to New Interface Concepts. In F. P. Netzer and A. Fortunelli, editors, *Oxide Materials at the Two-Dimensional Limit*, pages 361–380. Springer International Publishing, Cham, 2016.

[6] L.W. Martin, Y.-H. Chu, and R. Ramesh. Advances in the growth and characterization of magnetic, ferroelectric, and multiferroic oxide thin films. *Materials Science and Engineering: R: Reports*, 68(4-6):89–133, 2010.

[7] G. Pacchioni. Two-Dimensional Oxides: Multifunctional Materials for Advanced Technologies. *Chemistry–A European Journal*, 18(33), 2012.

[8] D. G. Schlom, L-Q. Chen, X. Pan, A. Schmehl, and M. A. Zurbuchen. A Thin Film Approach to Engineering Functionality into Oxides. *Journal of the American Ceramic Society*, 91(8):2429–2454, 2008.

[9] S. Förster and W. Widdra. Ternary Oxide Layers: Novel Crystal Structure Concepts. In *Encyclopedia of Interfacial Chemistry*. Elsevier edition, 2017.

[10] S. Schenk, S. Förster, K. Meinel, R. Hammer, B. Leibundgut, M. Paleschke, J. Pantzer, C. Dresler, F. O. Schumann, and W. Widdra. Observation of a dodecagonal oxide quasicrystal and its complex approximant in the $SrTiO_3$-Pt(111) system. *Journal of Physics: Condensed Matter*, 29(13):134002, 2017.

[11] S. Förster and W. Widdra. Growth, structure, and thermal stability of epitaxial $BaTiO_3$ films on Pt(111). *Surface Science*, 604(23-24):242163–2169, 2010.

[12] S. Förster, M. Huth, K. M. Schindler, and W. Widdra. Epitaxial $BaTiO_3$ (100) films on Pt(100): A low-energy electron diffraction, scanning tunneling microscopy, and x-ray photoelectron spectroscopy study. *The Journal of Chemical Physics*, 135(10):104701, 2011.

[13] H. L. Meyerheim, F. Klimenta, A. Ernst, K. Mohseni, S. Ostanin, M. Fechner, S. Parihar, I. V. Maznichenko, I. Mertig, and J. Kirschner. Structural Secrets of Multiferroic Interfaces. *Physical Review Letters*, 106(8):087203, 2011.

[14] H. L. Meyerheim, A. Ernst, K. Mohseni, I. V. Maznichenko, J. Henk, S. Ostanin, N. Jedrecy, F. Klimenta, J. Zegenhagen, C. Schlueter, I. Mertig, and J. Kirschner. Tuning the Structure of Ultrathin $BaTiO_3$ Films on Me(001) (Me = Fe , Pd, Pt) Surfaces. *Physical Review Letters*, 111(10):105501, 2013.

[15] J. Premper, D. Sander, and J. Kirschner. In situ stress measurements during pulsed laser deposition of $BaTiO_3$ and $SrTiO_3$ atomic layers on Pt(001). *Applied Surface Science*, 335:44–49, 2015.

[16] X. Shao, N. Nilius, P. Myrach, H-J. Freund, U. Martinez, Stefano Prada, Livia Giordano, and Gianfranco Pacchioni. Strain-induced formation of ultrathin mixed-oxide films. *Physical Review B*, 83(24):245407, 2011.

[17] C. Wu, M. R. Castell, J. Goniakowski, and C. Noguera. Stoichiometry engineering of ternary oxide ultrathin films: Ba_x Ti_2O_3 on Au(111). *Physical Review B*, 91(15):155424, 2015.

[18] M. Denk, D. Kuhness, M. Wagner, S. Surnev, F. R. Negreiros, L. Sementa, G. Barcaro, I. Vobornik, A. Fortunelli, and F. P. Netzer. Metal Tungstates at the Ultimate Two-Dimensional Limit: Fabrication of a $CuWO_4$ Nanophase. *ACS Nano*, 8(4):3947–3954, 2014.

[19] S. Pomp, D. Kuhness, G. Barcaro, L. Sementa, V. Mankad, A. Fortunelli, M. Sterrer, F. P. Netzer, and S. Surnev. Two-Dimensional Iron Tungstate: A Ternary Oxide Layer With Honeycomb Geometry. *The Journal of Physical Chemistry C*, 120(14):7629–7638, 2016.

[20] E. M. Zollner, F. Schuster, K. Meinel, P. Stötzner, S. Schenk, B. Allner, S. Förster, and W. Widdra. Two-Dimensional Wetting Layer Structures of Reduced Ternary Oxides on Ru(0001) and Pt(111). *Physica Status Solidi (B)*, 257(7):1900655, 2020.

[21] S. Förster, J. Flege, E. M. Zollner, F. O. Schumann, R. Hammer, Al. Bayat, K-M Schindler, J. Falta, and W. Widdra. Growth and decay of a two-dimensional oxide quasicrystal: High-temperature in situ microscopy. *Annalen der Physik*, 529(1-2):1600250, 2017.

[22] S. Förster, K. Meinel, R. Hammer, M. Trautmann, and W. Widdra. Quasicrystalline structure formation in a classical crystalline thin-film system. *Nature*, 502(7470):215–218, 2013.

[23] G. Barcaro, E. Cavaliere, L. Artiglia, L. Sementa, L. Gavioli, G. Granozzi, and A. Fortunelli. Building Principles and Structural Motifs in TiO_x Ultrathin Films on a (111) Substrate. *The Journal of Physical Chemistry C*, 116(24):13302–13306, 2012.

[24] C. Wu, M. S. J. Marshall, and M. R. Castell. *Surface Structures of Ultrathin TiOx Films on Au(111)*. 2011.

[25] F. P. Netzer, F. Allegretti, and S. Surnev. Low-dimensional oxide nanostructures on metals: Hybrid systems with novel properties. *Journal of Vacuum Science & Technology B*, 28(1):1–16, 2010.

[26] F. Sedona, G. A. Rizzi, S. Agnoli, F. X. Llabrés i Xamena, A. Papageorgiou, Dieter Ostermann, Mauro Sambi, Paola Finetti, Klaus Schierbaum, and Gaetano Granozzi. Ultrathin TiO_x Films on Pt(111): A LEED, XPS, and STM Investigation. *The Journal of Physical Chemistry B*, 109(51):24411–24426, 2005.

[27] N. Nilius. Properties of oxide thin films and their adsorption behavior studied by scanning tunneling microscopy and conductance spectroscopy. *Surface Science Reports*, 64(12):595–659, 2009.

[28] Falko P. Netzer. "Small and beautiful" – The novel structures and phases of nano-oxides. *Surface Science*, 604(5-6):485–489, 2010.

[29] D. Shechtman, I. Blech, D. Gratias, and J. W. Cahn. Metallic Phase with Long-Range Orientational Order and No Translational Symmetry. *Physical Review Letters*, 53(20):1951–1953, 1984.

[30] D. Levine and P. J. Steinhardt. Quasicrystals. I. Definition and Structure. *Physical Review B*, 34:596, 1986.

[31] A. I. Goldman and R. F. Kelton. Quasicrystals and crystalline approximants. *Reviews of Modern Physics*, 65(1):213–230, 1993.

[32] Leonardus and L. E. Sigler. *Fibonacci's Liber Abaci: A Translation into Modern English of Leonardo Pisano's Book of Calculation*. Sources and Studies in the History of Mathematics and Physical Sciences. Springer, New York Berlin Heidelberg, 1. softcover printing edition, 2003.

[33] Escalangon, E. *Les Fonctions Quasi-Périodiques*. Gauthier-villars edition, 1904.

[34] Berger, R. *The Undecidability of the Domino Problem*. Number 66. American mathematical soc. edition, 1966.

[35] N.G. de Bruijn. Algebraic theory of Penrose's non-periodic tilings of the plane. II. *Indagationes Mathematicae (Proceedings)*, 84(1):53–66, 1981.

[36] N Niizeki and H Mitani. Two-dimensional dodecagonal quasilattices. *Journal of Physics A: Mathematical and General*, 20(6):L405–L410, 1987.

[37] F. GahJer. Equivalence of tbe generalised grid and projection methods for the construction of quasiperiodic tilings. *Journal of Physics A*, 19:11, 1986.

[38] Haiiy. *Essai d'une Théorie Sur La Structure Des Crystaux, Appliquée à Plusieurs Genres de Substances Crystallisées*. 1783.

[39] D. Gratias and M. Quiquandon. Discovery of quasicrystals: The early days. *Comptes Rendus Physique*, 20, 2019.

[40] An-P. Tsai, A. Inoue, and T. Masumoto. A stable quasicrystal in Al-Cu-Fe system. *Japanese Journal of Applied Physics*, 26(Part 2, No. 9):L1505–L1507, 1987.

[41] A-P. Tsai, A. Inoue, and T. Masumoto. Icosahedral, decagonal and amorphous phases in Al-Cu-M (M=Transition metal) systems. *Materials Transactions, JIM*, 30(9):666–676, 1989.

[42] A. I. Goldman and M Widom. Quasicrystal Structure and Properties. *Annual Review Physical Chemistry.*, page 45, 1991.

[43] P Guyot, P Kramer, and M de Boissieu. Quasicrystals. *Reports on Progress in Physics*, 54(11):1373–1425, 1991.

[44] The Royal Swedish Academy of Sciences. The Nobel Prize in Chemistry 2011. https://www.nobelprize.org/prizes/chemistry/2011/press-release/, 2011.

[45] S. Fischer, A. Exner, K. Zielske, J. Perlich, S. Deloudi, W. Steurer, P. Lindner, and S. Förster. Colloidal quasicrystals with 12-fold and 18-fold diffraction symmetry. *Proceedings of the National Academy of Sciences*, 108(5):1810–1814, 2011.

[46] D. V. Talapin, E. V. Shevchenko, M. I. Bodnarchuk, X. Ye, J. Chen, and C. B. Murray. Quasicrystalline order in self-assembled binary nanoparticle superlattices. *Nature*, 461(7266):964–967, 2009.

[47] K. Hayashida, T. Dotera, A. Takano, and Y. Matsushita. Polymeric Quasicrystal: Mesoscopic Quasicrystalline Tiling in A B C Star Polymers. *Physical Review Letters*, 98(19):195502, 2007.

[48] Alfredo Metere, Peter Oleynikov, Mikhail Dzugutov, and Sven Lidin. A smectic dodecagonal quasicrystal. *Soft Matter*, 12(43):8869–8875, 2016.

[49] L. Bindi, P. J. Steinhardt, N. Yao, and P. J. Lu. Natural Quasicrystals. *Science*, 324(5932):1306–1309, 2009.

[50] L. Bindi, W. Kolb, G. N. Eby, P. D. Asimow, T. C. Wallace, and P. J. Steinhardt. Accidental synthesis of a previously unknown quasicrystal in the first atomic bomb test. *Proceedings of the National Academy of Sciences*, 118(22):e2101350118, 2021.

[51] S. Förster, S. Schenk, E. M. Zollner, O. Krahn, C-T. Chiang, F. O. Schumann, A. Bayat, K-M Schindler, M. Trautmann, R. Hammer, K. Meinel, W. A. Adeagbo, W. Hergert, J. I. Flege, J. Falta, M. Ellguth, C. Tusche, M. DeBoissieu, M. Muntwiler, T. Greber, and W. Widdra. Quasicrystals and their Approximants in 2D Ternary Oxides. *Physica Status Solidi (B)*, 257(7):1900624, 2020.

[52] F. Gähler. Crystallography of dodecagonal quasicrystals. *Theoretische Physik, ETH-Honggerberg,*, page 13, 1988.

[53] E Cockayne, M. Mihalkovič, and C. L. Henley. Structure of periodic crystals and quasicrystals in ultrathin films of Ba-Ti-O. *Physical Review B*, 93(2):020101, 2016.

[54] E. M. Zollner, S. Schenk, S. Förster, and W. Widdra. C_{60} adsorption on a dodecagonal oxide quasicrystal. *Physical Review B*, 100(20):205414, 2019.

[55] S. Förster, M. Trautmann, S. Roy, W. A. Adeagbo, E. M. Zollner, R. Hammer, F. O. Schumann, K. Meinel, S. K. Nayak, K. Mohseni, W. Hergert, H. L. Meyerheim, and W. Widdra. Observation and Structure Determination of an Oxide Quasicrystal Approximant. *Physical Review Letters*, 117(9):095501, 2016.

[56] S. Roy, K. Mohseni, S. Förster, M. Trautmann, F. Schumann, Eva Zollner, Holger Meyerheim, and Wolf Widdra. The Kepler tiling as the oldest complex surface structure in history: X-ray structure analysis of a two-dimensional oxide quasicrystal approximant. *Zeitschrift für Kristallographie - Crystalline Materials*, 231, 2016.

[57] Johanes Kepler. Johannes Kepler, 'Harmonices Mundi' (1619) | cabinet. https://www.cabinet.ox.ac.uk/johannes-kepler-harmonices-mundi-1619, 1619.

[58] B. Grünbaum and G. C. Shephard. Tilings by regular polygons. *Mathematics Magazine*, 50(5):227–247, 1977.

[59] S. Schenk, E. M. Zollner, O. Krahn, B. Schreck, S. Forster, and W. Widdra. Full real-space analysis of a dodecagonal quasicrystal. *Acta Crystallographica A*, A 75:7, 2019.

[60] M. Maniraj, L. V. Tran, O. Krahn, S. Schenk, W. Widdra, and S. Förster. Hexagonal approximant of the dodecagonal oxide quasicrystal on Pt(111). *Physical Review Materials*, 5(8):084006, 2021.

[61] F. E. Wührl, O. Krahn, S. Schenk, S. Förster, and W. Widdra. Antiphase Domain Boundary Formation in 2D Ba–Ti–O on Pd(111): An Alternative to Phase Separation. *Physica Status Solidi (B)*, (2100389), 2021.

Chapter 2

Experimental methods

Contents

2.1 Thin film growth methods 34
2.1.1 Description of the film stacking 35
2.1.2 The TUBE 36
2.1.3 Molecular Beam Epitaxy 38
2.1.4 Pulsed Laser Deposition 40
2.2 Surface characterization methods 42
2.2.1 ASURE platform 43
2.2.2 Surface structure characterization 45
2.2.3 Chemical analysis 54
2.2.4 Microscopy techniques 60
Bibliography 66

In this thesis, a thin film stacking configuration was developed to fabricate UTOx supported on Pt(111). This sample architecture was achieved thanks to an ensemble of epitaxial growth techniques such as MBE and PLD. Every deposition process is monitored by Reflection High Energy Electron Diffraction (RHEED). Other surface characterization techniques such as X-ray Photoelectron Spectroscopy (XPS), Scanning electron microscopy (SEM) and Scanning Auger microscopy (SAM), scanning tunnelling microscopy (STM) or low Energy Electron Diffraction (LEED) were performed as well to characterize the evolution of the chemistry and the structure at the surface. These growth and characterization techniques require UHV conditions to minimize the contaminants adsorption on the substrate prior to epitaxial growth, the incorporation during the growth of the thin films and the final adsorption on the resulting surface after growth of the oxide.

This chapter presents a description of the UHV techniques used in this work. The first section is dedicated to the presentation of the large UHV facility available at the Jean Lamour Institute (IJL) known as the TUBE, where the samples were fabricated and characterized *in situ*. The second section explains the basic principles of the growth techniques used. Finally, the third section exposes the surface characterization techniques used to study the structure, the composition and the morphology of the obtained films.

2.1 Thin film growth methods

Understanding the surface of materials has been an important challenge for humanity since ancient times. For instance, solid materials found in the everyday life objects have different characteristics at their external side (such as polishing or brilliance) [1]. Nevertheless, it is only in the past decades that an improved understanding of surfaces has been developed and a complete branch of materials science has been dedicated to the study of the properties and possible technological applications of surfaces [2]. But why are they so interesting? And moreover, what is the definition of a surface?

With the development of condensed matter physics, it was better understood that the properties of a material depend completely on its atomic structure and chemistry. The amount of atoms located at the surface of a material could be negligible with respect to the number of atoms in the bulk material. Nevertheless, the surface effects are not negligible at all. The surface is the exchange place between the material and its environment. Besides, the translational symmetry of the bulk is broken at the surface, which means that its atomic and electronic structures differ from those of the volume leading to the possibility of finding completely different properties.

For these reasons, one of the primary aims of surface science and engineering is

to create structures or components at the nanoscale where surface properties have a higher relevance (for instance, consider a cube of $1cm^3$ and on the other hand a cubic arrangement of 10^3 atoms. The ratio between surface atoms and bulk atoms is on the order of 10^{-8} for the former cube while it is equal to 0.6 for the latter case!) [1].

Thin film engineering at the nanoscale has been developed in the last decades, allowing the synthesis of a wide range of materials, from simple metals to more complex intermetallics as well as functional oxides. This is the case of UTOx grown on metal surfaces. In particular, when approaching the 2D limit, the structure of an UTOx grown on (111) metal surfaces changes, leading, for example, to the formation of quasicrystaline structures as mentioned in the previous Chapter [3, 4, 5].

2.1.1 Description of the film stacking

For this project, a thin film of $SrTiO_3$(111) was epitaxially grown on a 10 nm thick Pt(111) buffer layer following the sample architecture presented in Fig. 2.1. We chose to use a thin film of a (111)-oriented metal grown by MBE rather than a commercial single crystal. This approach may be more versatile to explore various perovskites on metal substrates, allowing the investigation of physico-chemical properties of new complex 2D oxide phases. In addition, the use of the metal as thin film reduces costs in the sample fabrication. As we are interested in the interaction of the Pt topmost layer with the UTOx, we believe that 10 nm could be an optimal thickness for the buffer layer, since it is thick enough to avoid any contribution of the Pt/α-Al_2O_3(0001) interaction at the surface.

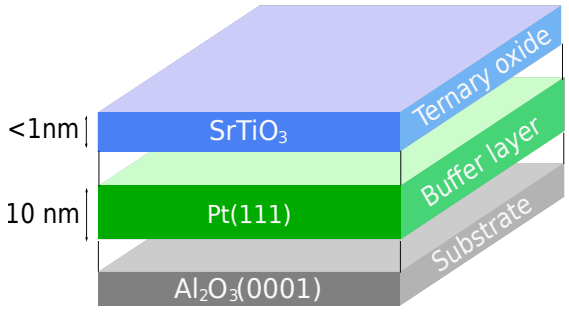

Figure 2.1 – Schematic of the sample architecture.

In the following, a description of the different growth techniques will be given, followed by a description of the surface characterization methods used in the development of this work.

2.1.2 The TUBE

In 2016, IJL inaugurated a large UHV platform unique in Europe known as the TUBE. This acronym comes from the given name "inTerconnection under Ultra-high vacuum of chamBers for Elaboration and characterization for novel material" which describes perfectly the purpose of this equipment created in response to the need of integrate diverse thin films growth systems and *in situ* analysis. Figure 2.2 shows a picture of this exceptional set of UHV tools. It is composed by 28 UHV instruments (24 deposition or/and analysis chambers plus 4 introduction load-locks) interconnected along a 70 meters long UHV tube. In total 14 chambers are dedicated to the thin films elaboration (7 MBE, 1 PLD, 3 sputtering, 1 atomic layer deposition (ALD) system, 1 lithography and 1 semi industrial physical vapour deposition (PVD)) and 10 chambers are available for structural (STM, AFM, SEM, RHEED and LEED), chemical (XPS, Auger, Nano-SAM) and physical characterization (such as Angle-resolved photoemission spectroscopy (ARPES), Magnetic optical Kerr effect microscopy or ellipsometry) [6]. 40 metres of the TUBE are dedicated to research

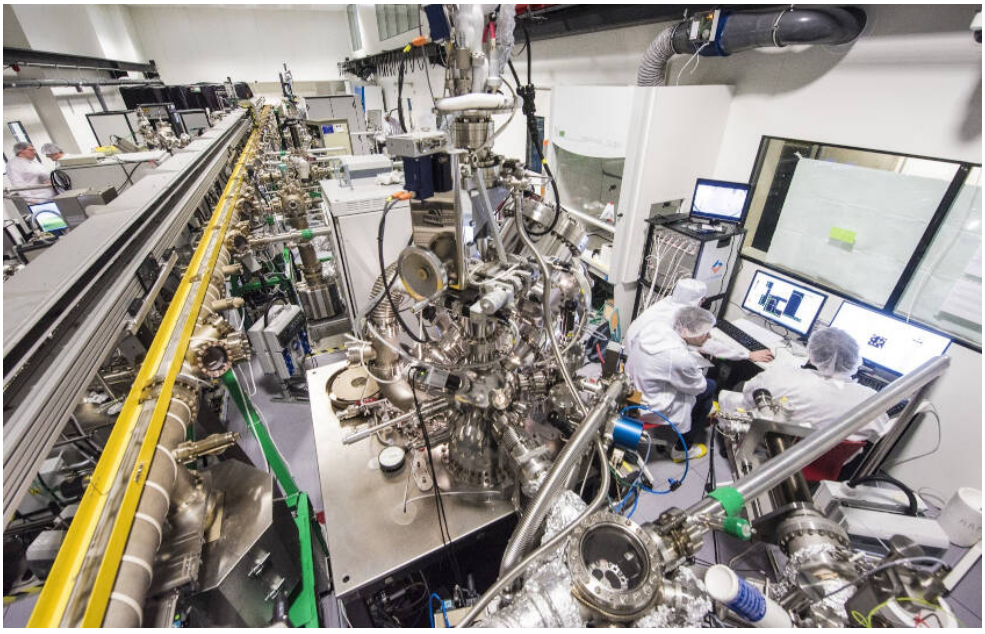

Figure 2.2 – The TUBE: A large UHV facility for the fabrication and characterisation of novel nanomaterials at IJL. ©Hubert Raguet - IJL - CNRS

work performed at the institute. The remaining 30 meters are available for industrially oriented research and the development of new technologies. This large facility is open to the international scientific community as well as to collaboration with private companies [6].

Figure 2.3 shows a schematic of the various chambers assembled along the TUBE. The circles highlight the different chambers (and techniques) employed during the development of this thesis. In fact, this project tested the functionality of this impressive platform by using in total eight different UHV chambers. For the sample fabrication, two MBE systems plus a chamber used for substrate preparation (the Auger analysis chamber) and a PLD system were used (see red circles in Figure 2.3). For chemical and structural surface characterization, two XPS and Auger spectroscopy systems (Surface 1 and 2), a STM and a SEM and Nano Auger assembly (SCAN) were used (as marked in Figure 2.3 by the blue circles). The transfer between chambers is possible thanks to an automatic mobile plate which travels along the UHV tube transporting a trolley containing up to twelve samples. A good control of the vacuum in the platform is ensured due to the segmentation of the Tube in several zones delimited by 16 valves which are opened and closed when the trolley is crossing. Besides, UHV conditions inside the chambers are controlled by a set of valves located at the intersection of the transfer rods and the chambers entrance as well as in between the pumps and the chambers. In total, more than 60 valves and 40 pressure gauges across the TUBE guarantee good UHV everywhere along the platform. Figure 2.4 (left) shows one of the zones of the Tube with a zoom (right) to the inside allowing to see the trolley attached to the mobile plate by the magnets. The TUBE is equipped with eight trolleys in total, each one with a capacity to carry twelve sample holders. This instrument is managed by the competence centre of the IJL called CC Davm (acronym from the French "Dépôt et Analyse sous Ultravide de nanoMatériaux").

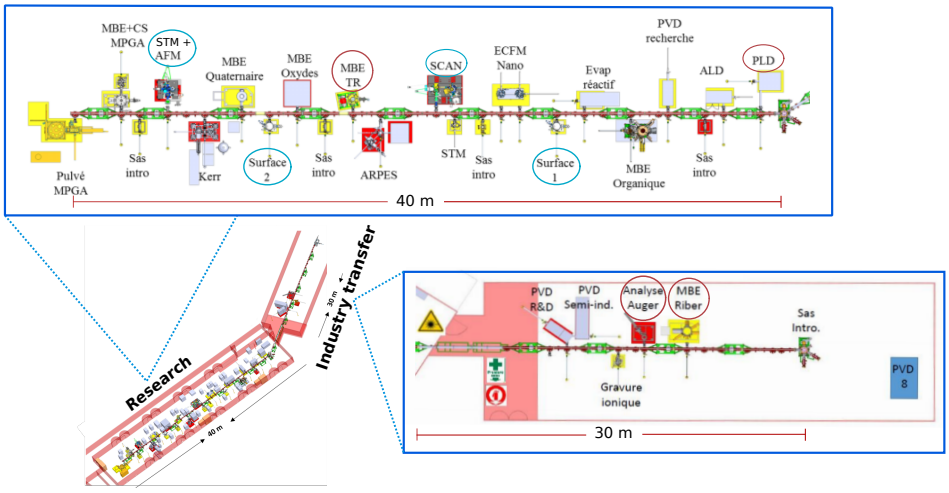

Figure 2.3 – Schematic of the 24 instruments and 4 introduction load-locks connected to the 70 m UHV TUBE. In blue and red circles are highlighted the 8 chambers used during this thesis.

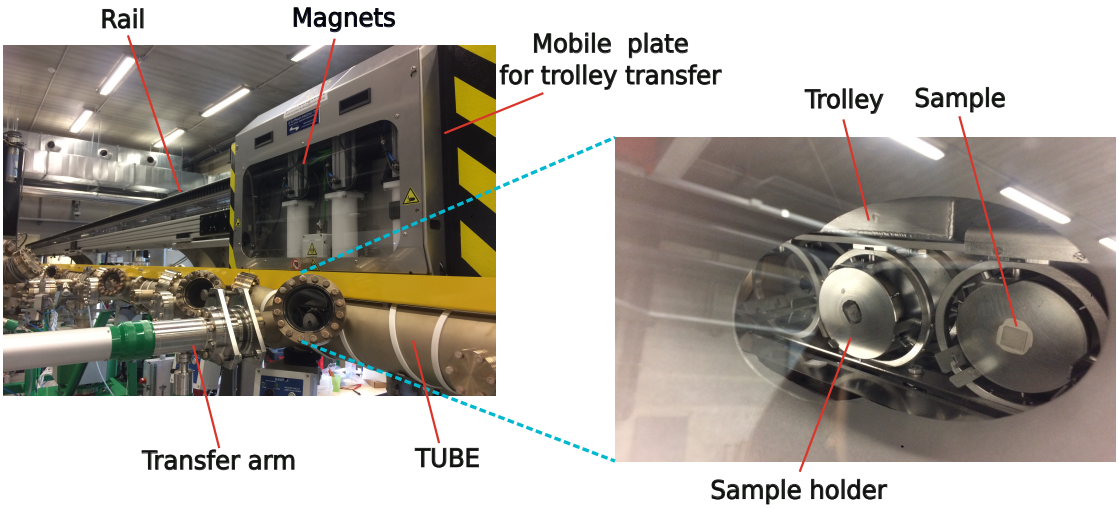

Figure 2.4 – *Left:* The mobile plate transporting the samples through the TUBE. *Right*: view inside the TUBE of one of the trolleys carrying the samples.

In Fig.2.4 (right) the samples holders used during the sample fabrication inside the TUBE are visible. These are made of Inconel (a nickel-chromium superalloy), cooper or tantalum, with a very precise shape allowing the transfer in the different systems interconnected to the TUBE. For this project, substrates were fixed to the sample holders using silver paint with subsequent annealing at around 100°C for 1 hour (as described in Chap.3).

2.1.3 Molecular Beam Epitaxy

Molecular beam epitaxy (MBE) is an UHV epitaxial growth technique based on the interaction of a crystalline substrate and the species adsorbed from a molecular beam of thermal energy coming from a high purity material. The development of this technique started at the end of the 1960's from the convergence of studies on the deposition by thermal evaporation of compounds from the III-IV group and the improvement of techniques operating under UHV conditions [7]. Molecular beams are generated by the evaporation of the desired material contained in a crucible inside the effusion cells heated (in the case of our MBE system) by an electron beam. The substrate is located at a distance d of the crucible as presented in Fig.2.5. If the substrate is perpendicular to the beam, the flux per unit surface and time is given by:

$$\varphi_{beam} = \left(\frac{AP}{\pi d^2}\right)\left(\frac{N_A}{2\pi M k_B T}\right)^{1/2} \tag{2.1}$$

Where P is the pressure in the cell, N_A is Avogadro's number, M is the molecular weight of the element, A is the aperture area of the cell and T is the absolute tem-

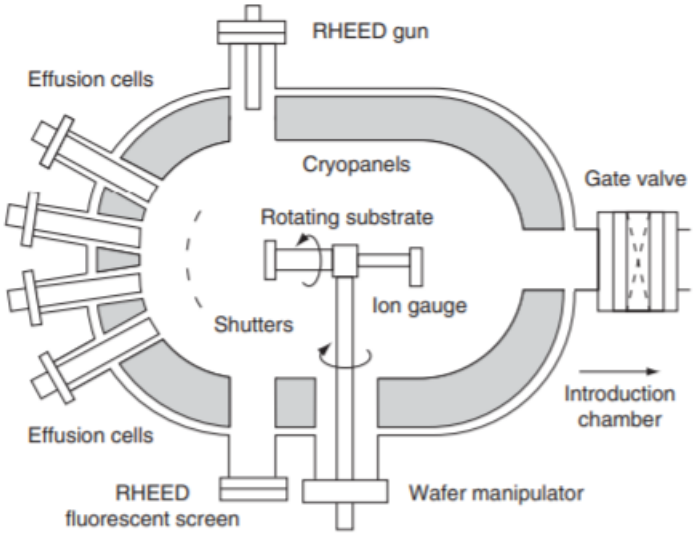

Figure 2.5 – Schematic of a MBE chamber (reproduced from [7]).

perature. UHV conditions are required to minimize the incorporation of contaminants at the growth surface and in the epitaxial layer. In order to obtain an efficient growth rate, the cells are constituted by large-aperture crucibles resulting in rates of tenths of several nanometres per second. The flux generated depends on several parameters such as the cell geometry and its position with respect to the substrate. In order to guarantee a homogeneous flux on the substrate, it is usually azimuthally rotated during the growth [7].

One of the MBE systems connected to the TUBE is shown in Fig. 2.6. The chamber is equipped with a RHEED set-up allowing to monitor *in situ* the growth process, providing a real-time feedback on the influence of the growth conditions on the structure of the epitaxial layers. The flux is controlled during the growth by a quartz crystal microbalance (QCM). However, as this QCM is located close to the electron beam gun and about 30 cm under the sample (bottom left in Fig.2.6), the recorded value would be higher than the real flux arriving to the substrate surface. To correct this issue, a second QCM (top right) can be inserted almost at the sample position, allowing to calibrate the electron beam power (recorded with the first QCM) needed to obtain the desire flux in the second QCM.

This MBE system is equipped with two electron guns connected to two groups of cells containing crucibles with different metals (such as Ni, Co, and Mg). A set of turbo-molecular, ionic and titanium sublimation and primary pumps, allows to obtain a base pressure in the chamber of about 5×10^{-11} mbar.

For this project two independent MBE set ups connected to the TUBE (see Fig.2.3) were used for the growth of the metal buffer layer (see Fig.2.1). Pt and Ti/Pt bilayer

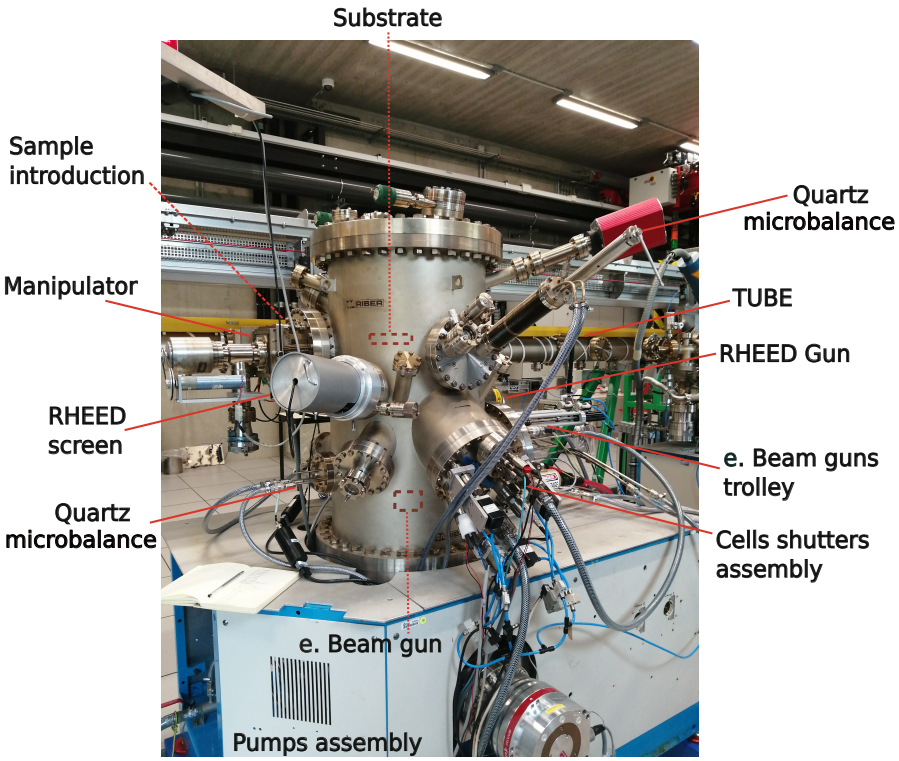

Figure 2.6 – The MBE chamber connected to the TUBE.

were selected as the supported metals for the $SrTiO_3$ thin films. Since Ti was not available in the same MBE system where Pt was grown, Ti deposition was performed in another MBE system.

2.1.4 Pulsed Laser Deposition

Pulsed laser deposition (PLD) is today a well known technique for the growth of complex oxides thin films due to its success in growing *in situ* epitaxial high temperature superconducting films [8]. This technique was developed in the late 1980's after studies in the applicability of lasers (discovered in the early 1960's) as a directed energy source for evaporation of a desired material. Nowadays, this technique is used in the deposition of insulators , semiconductors, superconductors, metals, polymers and even biological materials [9, 10, 11, 12, 13]. PLD is a physical vapour deposition process carried out under vacuum conditions. Here, a pulsed laser is focussed onto a target. If the laser energy is sufficiently high, a small amount of material is vaporized and ejected away from the target's surface. This vapour is made of atoms, molecules, ions and electrons which constitute a plasma called plume. This stage is known as ablation. The ablated material is ejected from the target in a

highly forward-directed plume. This ablation plume provides the material flux for film growth. PLD is a very attractive method for the growth of complex oxides since it guarantees a nearly stoichiometric transfer of material from the target to the substrate. Besides it can be operated either in UHV environment or in the presence of a background gas, such as oxygen which is commonly used when depositing oxides to fully oxygenate the deposited films [8]. This process is schematically shown in Fig.2.7.

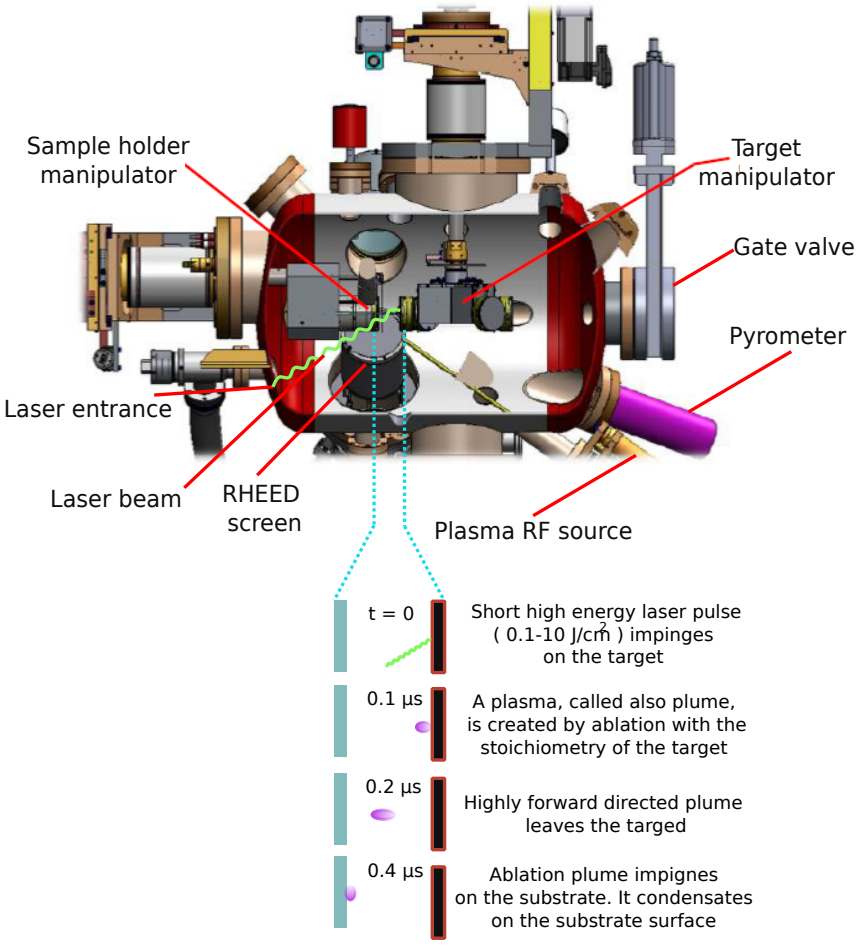

Figure 2.7 – *Top*: Schema of the inside of the PLD chamber connected to the TUBE. *Bottom*: Sequence of the PLD process (adapted from ref [8]).

Typically, the deposition rate ranges from 0.001 to 1 Å per laser pulse [8], allowing a controlled deposition process in multilayer systems with good interface properties. This degree of control can be achieved using RHEED as a surface technique that helps to determine the crystallinity and smoothness of the grown film. The oscillations in the intensity of diffraction pattern during the film growth are correlated to the layer-by-layer growth as detailed in the next section. Fig. 2.8 shows the PLD system connected to the TUBE, which possess a KrF excrimer laser (248 nm), a RHEED instrument and a radio frequency (RF) O_2 plasma source. The pumps assembly guarantees a base pressure inside the deposition chamber on the order of 10^{-9}mbar.

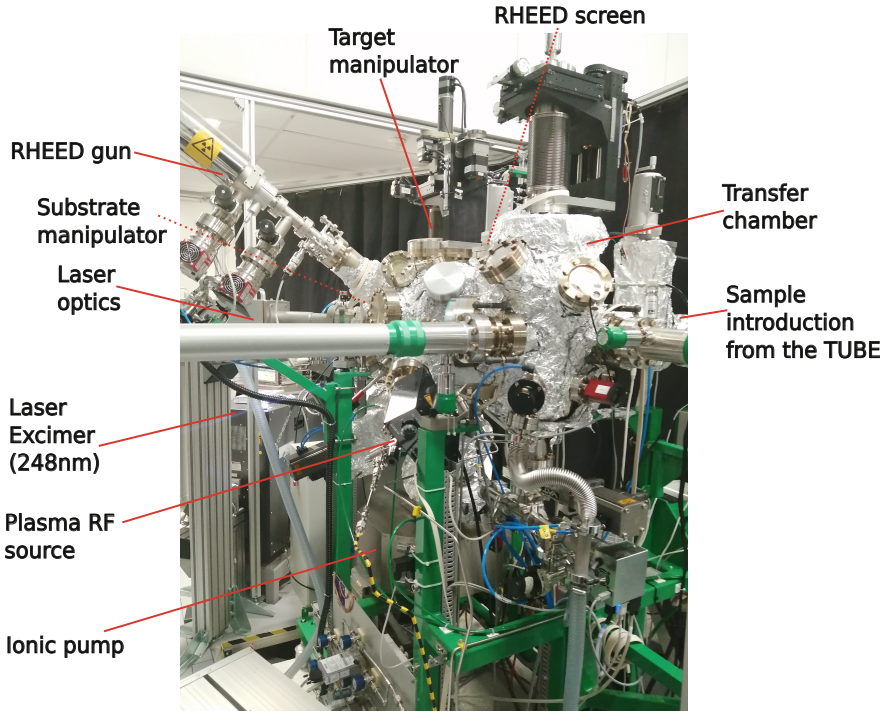

Figure 2.8 – The PLD chamber connected to the TUBE.

2.2 Surface characterization methods

After sample fabrication, different surface characterization methods were used to obtain information about the structure, the chemical composition and the topography of the final surface. Besides, quasicrystallinity in oxides is the result of annealing at high temperatures under very specific conditions. Which means that, all

changes (structural, compositional and in morphology) at the surface need to be monitored and analysed.

In this section, a description of the many different surface characterization techniques that were used during this project will be given. Several characterizations were performed *in situ* at the TUBE, while others were done on a stand-alone UHV system called ASURE platform, which is briefly described here as well.

2.2.1 ASURE platform

The formation of an UTOx requires exigent experimental conditions, such as high annealing temperature (> 1000 K or 730 °C) and low pressure (< 10^{-8} mbar).

For the present work, ensuring these conditions was essential. After sample fabrication, the specimens were transferred from the TUBE to a second UHV system called platform ASURE from its acronym in French: Alliage SUrface et REactivite. In particular, this system possess a special chamber dedicated to high temperature annealing (up to 1110°C depending on the sample mounting) under various gases, called reactivity chamber. Fig. 2.9 shows the ASURE platform, consisting in three UHV interconnected chambers: the reactivity chamber, equipped with an e-beam heater and a mass spectrometer, a LEED system and an ion bombardment gun; a preparation chamber, equipped with a resistive heater, a mass spectrometer, a LEED system and evaporation sources for metallic and molecular deposition; and an analysis chamber, equipped with a X-ray and UV photoemission system with an hemispheric analyser and a variable temperature Omicron STM.

The base pressure inside the preparation, the analysis and the reactivity chambers are in the order of 10^{-11}, 1×10^{-10} and 5×10^{-10}mbar respectively. These low pressures are possible thanks to the pumping assembly consisting in ionic, turbo, Ti sublimation and primary pumps as shown in Fig. 2.9. The temperature in the chambers is controlled by thermocouples located on the heater close (but not connected) to the sample holders. Besides, a bichromatic pyrometer was used as well to directly measure the temperature on the sample surface.

Samples coming from the TUBE after fabrication were detached from the sample holder in order to be fixed on an Omicron Ta plate compatible with the ASURE platform. The silver painting was carefully removed from the back of the sample before fixing it with Ta wires by spot welding. Fig. 2.10(a) shows one of the samples used in this project, fixed with three Ta wires inside the reactivity chambers of the ASURE platform. The sample plates used for samples ***A*** and ***B*** reported in Chap.4 had a rectangular window as shown in Fig. 2.10(b), allowing to achieve higher annealing temperatures at the surface of the sample, since the electron beam impinge directly on the back side of the sample and not on the Ta plate (as it is the case when using a normal plate).

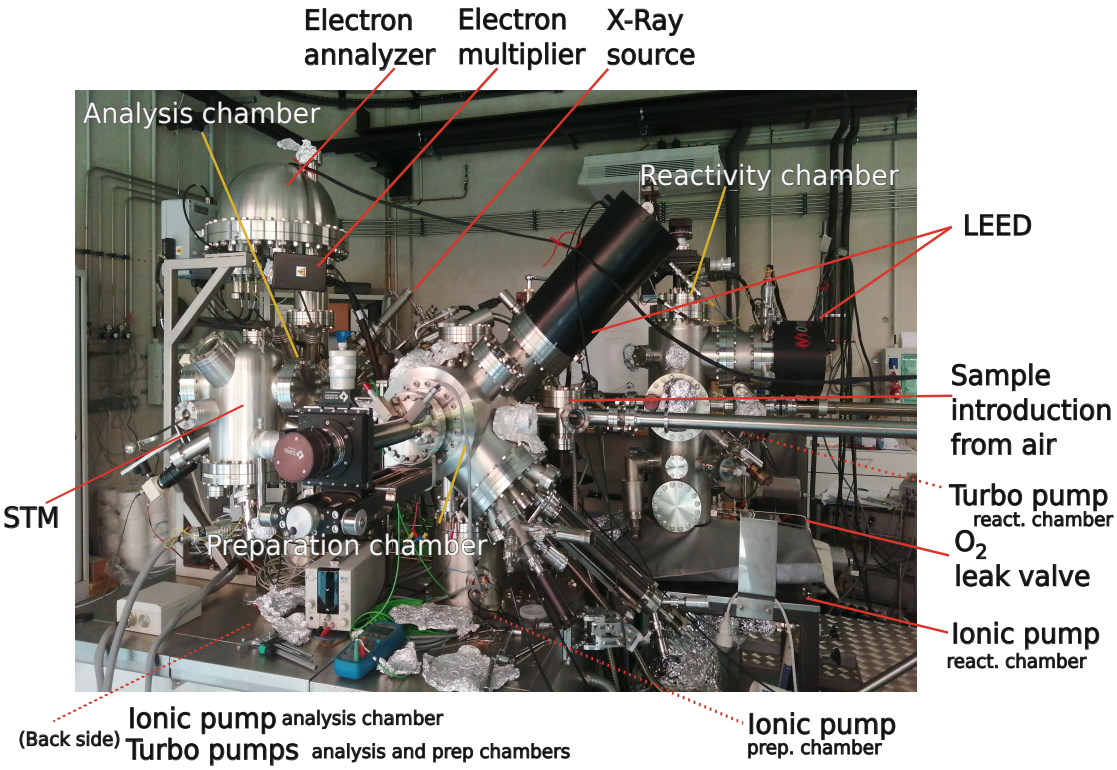

Figure 2.9 – ASURE platform composed by three interconnected UHV chambers. *(rigth)* A reactivity chamber, *(middle)* a preparation chamber and *(left)* an analysis chamber.

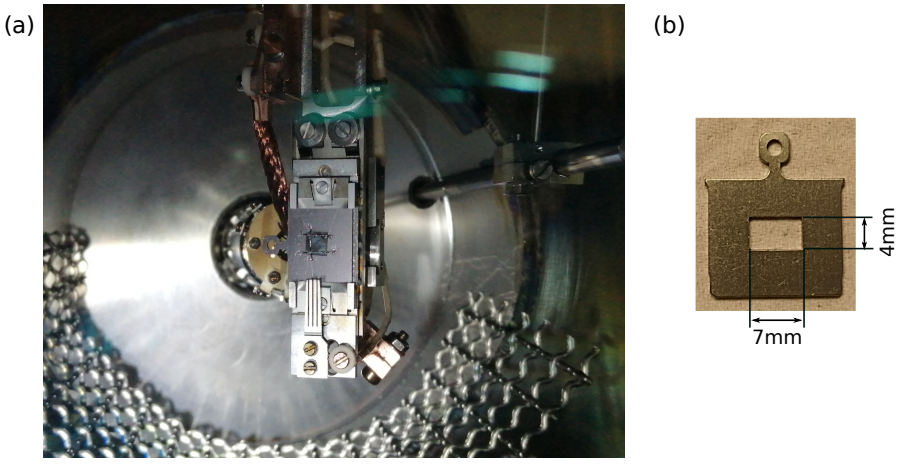

Figure 2.10 – (a) Sample of 5×5 mm^2 inside the reactivity chamber, fixed by three Ta wires on an Omicron plate. (b) Ta plate with a rectangular 7× 4 mm^2 window.

2.2.2 Surface structure characterization

2.2.2.1 Reflection high-energy electron diffraction

Reflection high energy electron diffraction (RHEED) is a highly used technique to analyse the structure of crystal surfaces. Although RHEED is a surface characterization method, it is a tool of great importance used to monitor *in situ* the growth of thin films. Surface reconstruction and surface roughness can be followed during MBE or PLD deposition, for example. RHEED instruments use a finely collimated electron beam of 10-100 keV which impinges the sample surface at a grazing angle producing a forward scattered diffraction pattern [14]. This pattern corresponds to a projection of the 2D reciprocal lattice of the sample surface. Numerous are the structural informations that can be obtained by analysing the RHEED patterns. For instance:

- Surface periodicity. The real space lattice can be established.
- Flatness of the surface.
- Epitaxial relationships between the grown films or islands with respect to the substrate.
- Sizes of grains or domains of the grown surface.
- Growth mode of the thin films and number of grown atomic layers

Fig. 2.11 shows the scheme of a RHEED apparatus. An electron beam is produced generally from a tungsten filament and then accelerated toward the sample surface by a voltage. The electron beam passes through a small aperture to be focused on the sample by magnetic focusing lens. The beam will irradiate the sample surface with a grazing angle ϑ_g between 0.5° and 6°, after being deflected by the deflection coils 1 and 2. The size of the irradiated zone is about 1-3 mm along the beam, which means that the final RHEED pattern will give an average information of the macroscopic radiated area. The RHEED pattern is observed on the fluorescent screen and can be recorded by a CCD camera from the outside of the UHV setup [14].

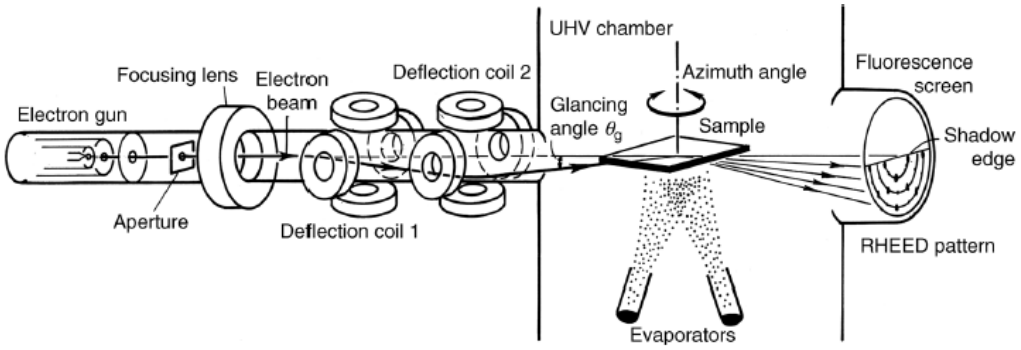

Figure 2.11 – Schematic of a RHEED system (reproduced from [14]).

Formation of a RHEED pattern

Fig. 2.12 represents the geometric configuration of a diffraction experiment in the real (or direct) space and its construction in the reciprocal space. If the electron beam arrives parallel to the sample (described by a vector $\mathbf{k}_i$), it will be diffracted (vector $\mathbf{k}_f$) with an angle α with respect the direction of the incident beam. If we restrict the diffraction phenomena to only elastic scattering, for a wave-vector $\mathbf{k}_i$ coming from the incident electron wave the diffracted waves, for instance k_f, will have the same magnitude as $\mathbf{k}_i$. Therefore, when these vectors are drawn from a common origin, as illustrated in Fig. 2.12 (*right*), their end points will be on a sphere with radius $|\mathbf{k}_i|$ given by:

$$|\mathbf{k}_i| = \sqrt{2mE}/\hbar \tag{2.2}$$

where m is the mass of an electron, E is the energy of the electron, and $\hbar$ is the Planck constant divided by 2π. This sphere is known as the *Ewald sphere*. Here, both the elastic scattering and the diffraction conditions are fulfilled simultaneously. Consequently, the RHEED patterns observed on the fluorescence screen, come from the intersection between the reciprocal lattice planes and the Ewald sphere.

From Fig. 2.12(*left*), one can write:

$$\tan\alpha = \frac{e(hkl)}{D}$$

where $e(hkl)$ is the distance on the screen between the incident beam and the point corresponding to the plane *(hkl)* and D is the distance between the detection screen and the spot given by the incident and the diffracted beams. If we take a vector in the reciprocal space $\mathbf{G}(hkl)$ which satisfies the Bragg condition $2d(hkl)\sin\vartheta = \lambda$, where d(hkl) is the interplanar distance and λ is the wavelength coming from the incident beam. With $2\vartheta = \alpha$ (as in Fig. 2.12(right)), this vector can be expressed by:

$$|\mathbf{G}(hkl)| = \frac{2\pi}{d(hkl)} \tag{2.3}$$

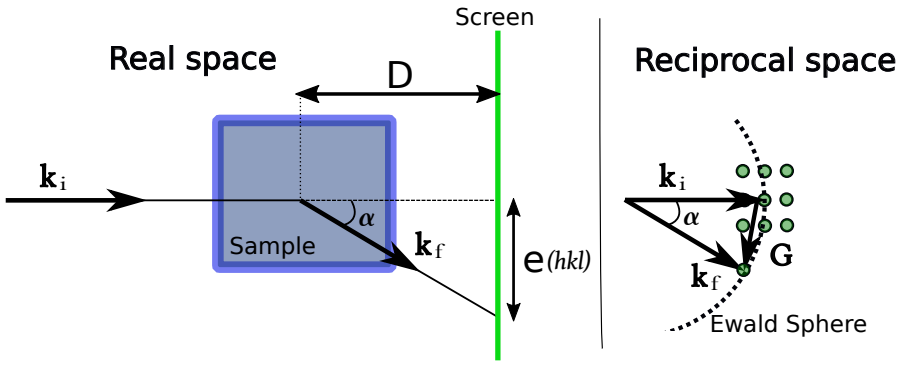

Figure 2.12 – Schematic of a diffraction experiment in the real (*left*) and in the reciprocal (*right*) space (adapted from [1]).

By simple application of trigonometry relations, one can obtain the relation between the order of magnitude of the real and reciprocal space:

$$1+\left(\frac{\mathrm{D}}{\mathrm{e}(hkl)}\right)^2=\frac{1}{\left(\frac{\lambda}{\mathrm{d}(hkl)}\right)^2\left(1-\left(\frac{\lambda}{2\mathrm{d}hkl}\right)^2\right)} \tag{2.4}$$

Moreover, if $\lambda \ll \mathrm{d}$, which is the case in RHEED, then Eq. 2.4 simplifies in:

$$\frac{\mathrm{e}(hkl)}{\mathrm{D}} \cong \frac{\lambda}{\mathrm{d}(hkl)} \tag{2.5}$$

Eq.2.5 has important consequences for geometric considerations. Considering that the typical size of a fluorescence screen is about 10 cm and the distance between atoms is in the order of 0.2 nm, then, λ will constraint the distance between the sample and the screen. From Eq.2.2 one can calculate λ knowing that $\lambda = 2\pi/\mathrm{k}$ and $\mathrm{E} = e\mathrm{V}$ with V the voltage used to accelerate the electrons (which could vary from 10 to 40 kV). Therefore, for $\lambda = 0.01$nm, for example, D is 20 times larger than e*(hkl)*!

This means that in a RHEED set-up, the electron gun and the screen can be spaced far apart from the sample, leaving the front of the sample open for deposition sources. This implies that RHEED can be used as an *in situ* technique to control the structure of the growing surface directly during the growth process.

Possible RHEED patterns

As mentioned above, the observed RHEED patterns come from the intersection between the reciprocal lattice planes and the Ewald sphere. For an ideal case, where the surface is perfectly flat (2D), the reciprocal space is a 2D lattice formed by thin

lines, perpendicular to the real surface. The intersection of this streaks with the Ewald sphere forms a pattern made up of a set of diffraction spots on concentric circles (also observed) called Laue zones as illustrated in Fig.2.13(a). The left column represents the real surface morphology, the middle column the corresponding pattern in reciprocal space and in the right column the observed RHEED pattern.

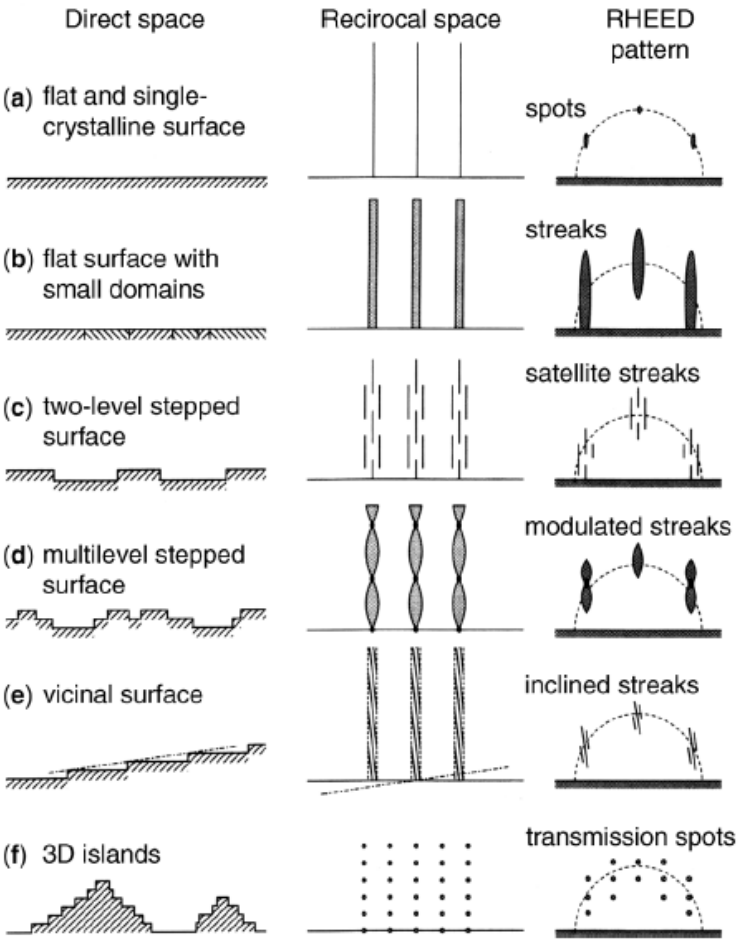

Figure 2.13 – Schematic of different imperfect surfaces and their corresponding pattern in reciprocal space and in RHEED measurements (reproduced from [14]).

Nevertheless, real samples are not always ideal. Fig.2.13(b-f) represents RHEED patterns observed for surfaces with imperfections (such as domains, steps, vicinal surfaces and islands). In practice, the observed RHEED pattern of a flat surface will frequently be a set of streaks as presented in Fig. 2.13(b). This is due to the fact that, as the surface is never ideally 2D, the reciprocal space is no longer a thin line, but a rod with a finite diameter as exemplify in Fig. 2.14(a). Thus, the intersection of

these rods with the Ewald sphere is no longer a spot, instead the Ewald sphere will have a certain thickness given by an uncertainty $\Delta\vartheta$. Besides, in reality, the electron beam penetrates more than the first atomic layer, which means that the intensity will be modulated along the reciprocal rods. Then, a surface with small out of phase domains (smaller than the coherence length of the beam), will produce a RHEED pattern formed by elongated diffraction streaks.

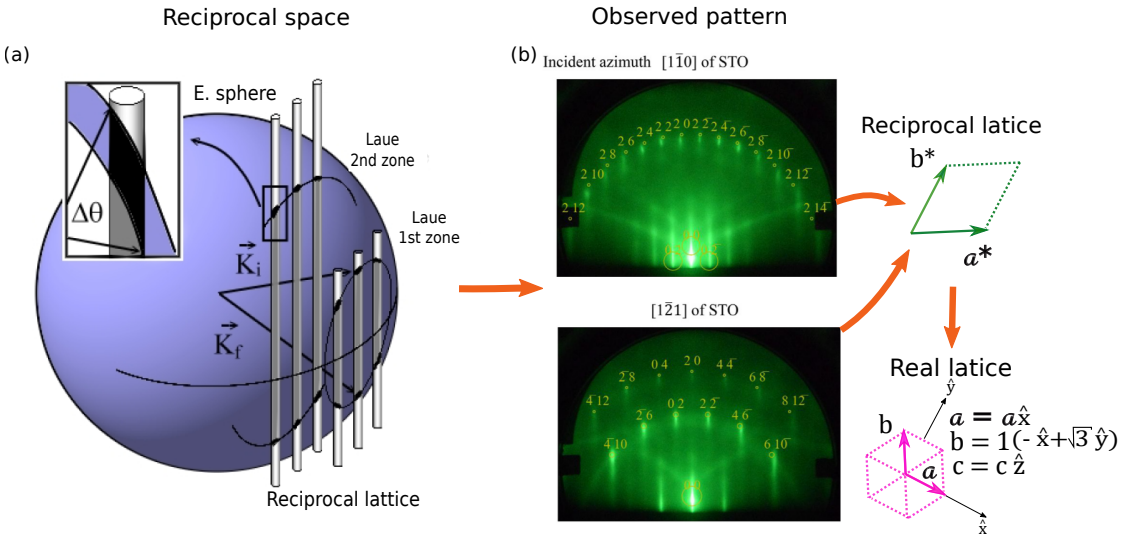

Figure 2.14 – (a) Schematic of the formation of a RHEED pattern by the intersection of the Ewal sphere and the reciprocal rods coming from a real surface (adapted from [15]). (b) RHEED pattern of a Pt film grown on $SrTiO_3(111)$. The observed pattern gives information of the reciprocal lattice, which can be transformed in the real lattice parameters (adapted from [16]).

Another practical aspect of this method (more related to the surface structure analysis), is that a reciprocal lattice map can be obtained from the RHEED patterns as presented in Fig.2.14(b) for the case of a Pt film grown on $SrTiO_3(111)$ where the diffraction patterns go up to the 2nd Laue zone indicating good crystallinity. Note that the pattern consist in streaks rather than spots. The separation of the streaks for the [1$\bar{1}$0] direction corresponds to the reciprocal lattice parameters. Then, the reciprocal vectors $\boldsymbol{a}^*$ and $\boldsymbol{b}^*$ can be determined, which means that the real space vectors $\boldsymbol{a}$ and $\boldsymbol{b}$ can be deduced along with the real space unit cell parameters along the three dimension space directions $\hat{x}, \hat{y}, \hat{z}$. For the hexagonal case, the reciprocal

lattice vectors are given by the relations:

$$\boldsymbol{a}^* = \left(\frac{2\pi}{\mathrm{a}}\right)\frac{\sqrt{3}\hat{\mathrm{x}}+\hat{\mathrm{y}}}{\sqrt{3}} \tag{2.6}$$

$$\boldsymbol{b}^* = \left(\frac{2\pi}{\mathrm{a}}\right)\frac{2\hat{\mathrm{y}}}{\sqrt{3}} \tag{2.7}$$

$$\boldsymbol{c}^* = \mathrm{c}\hat{\mathrm{z}} \tag{2.8}$$

In this way, the periodicity or unit cell of the surface reconstruction is known simply from the arrangement of the superlattice spots in RHEED pattern.

RHEED oscillations

In the case of a layer-by-layer growth, RHEED can be also used as an excellent tool to determine the growth rate of a monolayer. By measuring the changes in the intensity of a specular spot, one can relate the period of the oscillations to the time that is necessary to deposit one monolayer.

Fig. 2.15 shows a layer-by-layer growth where atomic layer grows by making 2D islands at different places on the surface, then the islands grow and eventually connect each other to complete the new atomic layer. Consequently, the surface temporally becomes a stepped surface during the growth. During this process the intensity of a specular spot oscillates as shown in the right of Fig. 2.15. The period of the oscillation corresponds to the completion of a single atomic layer, therefore it is possible to determine the number of atomic layers grown by counting the number of intensity oscillations of the specular spot in RHEED. This measurement could be done in the course of a PLD growth, for example.

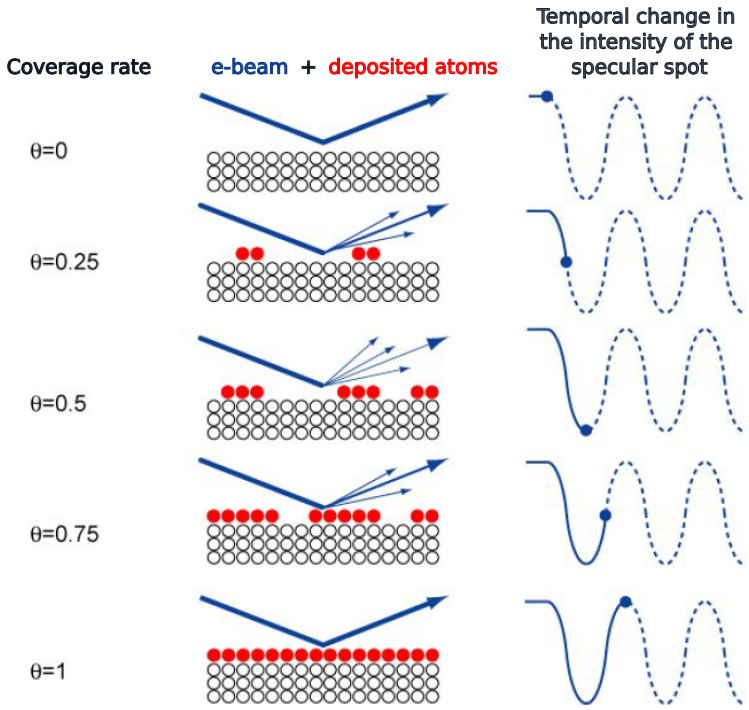

Figure 2.15 – RHEED oscillations at the different stages of a film growth. *(left)* Growth is initiated and the coverage rate ϑ increases. The intensity of a specular reflection *(rigth)* is proportional to the surface roughness (reproduced from [17]).

2.2.2.2 Low energy electron diffraction

One of the most powerful techniques available for surface structural analysis is low energy electron diffraction (LEED). This technique is widely used in materials science research to study surface structure. It has many similarities to X-ray and neutron diffraction but due to the short mean free path of low energy electrons in solids, it is highly surface sensitive [2]. Upon penetrating the crystal, primary electrons will lose kinetic energy, due to inelastic scattering processes, leading to a decay commonly treated as an exponential function. Thus, the decay of the primary electron beam intensity I_0 in the direction of the propagation is given by:

$$I(d) = I_0 e^{-d/\Lambda(E)} \tag{2.9}$$

where d is the penetration depth and $\Lambda(E)$ is the inelastic mean free path, defined as the average distance that an electron with a given energy travels between successive inelastic collisions. The mean free path is minimal (5-10Å) in the energy range of LEED measurements, where the electron beam is directed onto a single-crystalline surface with energies typically in the range of 10 to 500 eV.

Fig.2.16 illustrates a LEED set-up where the electrons are generated by a cathode filament (tungsten or LaB_6 crystal) with energies in the range of 0 to 1000 eV. The effective diameter of the electron beam is about 1 mm and the angular spread is typically about 0.5 °. This implies that steps and surface imperfections are not generally visible but can manifest themselves as background noise. More sophisticated techniques, such as the Spot Profile Analysis of electron diffraction (SPA-LEED) allow to obtain the surface roughness and average terrace size.

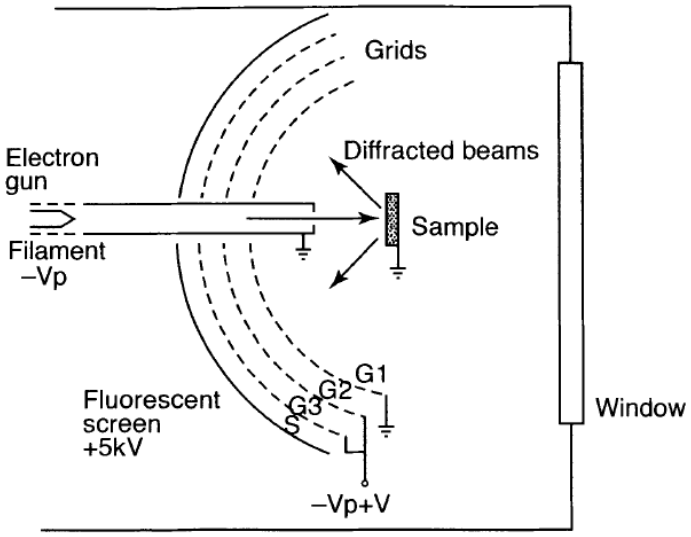

Figure 2.16 – Scheme of a typical LEED system (reproduced from [2]).

Electrons are accelerated through a potential difference V, then they impinge on the surface, where they are diffracted. The elastically backscattered electrons travel to the grid G1. A small negative voltage between G1 and G2 rejects most of the inelastically scattered electrons while the elastically scattered electrons reach G3. A large positive voltage between G3 and the fluorescent screen accelerates the electrons producing fluorescence when they impact on the screen, leading to bright spots forming the LEED pattern which can be collected by a CCD camera. In contrast to X-ray diffraction in which the wavelength is usually held fixed, in LEED there is this extra degree of freedom of changing the electron wavelength via changing the energy (see Eq.2.2). Different software allow to record the LEED patterns at different energies, allowing to determine the structure of the surface.

If we consider Eq.2.5 this time for a LEED experiment, as the energy of the electrons is lower than for the RHEED method, a typical value for λ could be between 0.2 and 0.006 nm (for a potential between 50V and 40 kV). This lead to a distance D about the order of magnitude of e*(hkl)* typically in the order of 0.2 nm. This is one

	Energy	λ (nm)	Beam diameter	D
LEED	10-500 eV	0.2	0.2-1 mm	in the order of e
RHEED	10-40 kV	0.01	50-100 μm	almost 20 times e

Table 2.1 – Comparison between the characteristics of the electron diffraction techniques discussed in this chapter (adapted from [2, 1]).

of the greatest differences between RHEED and LEED techniques. In a LEED set-up it is not possible to monitor the growth of a material. The detector needs to be close to the sample [1].

Table 2.1 summarizes the main characteristics of both electron diffraction techniques discussed so far, exposing their differences in the incident beam energy and its consequences in terms of wavelength λ, beam diameter and the distance between the sample and the fluorescent screen D.

Formation of a LEED pattern

The distance between the sample and the screen represents a limitation for this technique. Nevertheless this problem was smartly solved by a set-up, as previously described above, where electrons are send perpendicular to the sample surface as shown in Fig. 2.16 (in contrast with RHEED) and the backscattered electrons are recovered on an hemispherical fluorescent screen. In this case, the diffraction rods are parallel to the incoming beam ($\mathbf{k}_i$) as shown schematically in Fig. 2.17. Therefore, the intersection between these rods and the Ewald sphere is directly the reciprocal lattice as represented by the green dots in Fig. 2.17 [1].

Fig. 2.18 presents examples of LEED patterns from different phases of $SrTiO_3$. Fig. 2.18(a) shows the diffraction pattern of a (111)-oriented $SrTiO_3$ surface. Crystal symmetry and lattice dimensions can be obtained using the proper calibration of the instrument. Fig.2.18(b) shows a surface reconstruction of $SrTiO_3$, where the reciprocal lattice is six times smaller than the $SrTiO_3$(111) lattice. Therefore, in real space, following the relations given by Eq. 2.10, this LEED pattern corresponds to a surface reconstruction where $SrTiO_3$(111) lattice parameters are six times larger (a (6×6) surface reconstruction)

$$\boldsymbol{a} = \frac{1}{\boldsymbol{a}^* \sin 60^\circ} \tag{2.10}$$

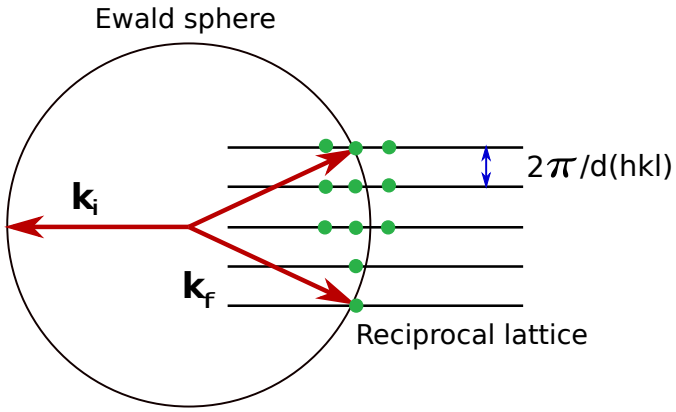

Figure 2.17 – Schematics of the LEED pattern construction from the intersection of the Ewald sphere and the reciprocal lattice rods. $\mathbf{k_i}$ is the wave vector of the incident beam perpendicular to the sample, and $\mathbf{k_f}$ represents the possible vectors of the the backscattered electrons. A LEED pattern image directly the reciprocal lattice (green spots) (adapted from [1]).

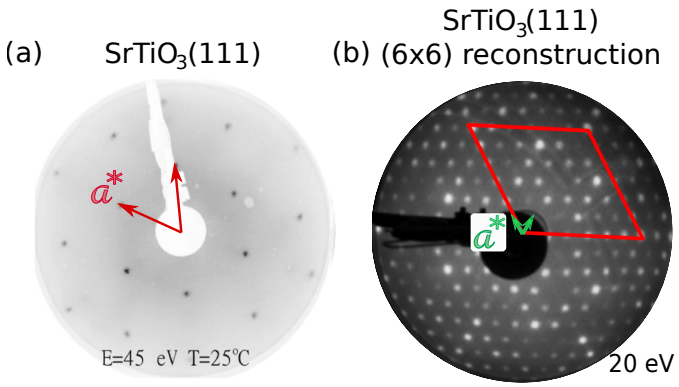

Figure 2.18 – LEED patterns of (a) $SrTiO_3(111)(1\times1)$ (reproduced from [18]) (b) Reconstructed (6×6)$SrTiO_3(111)$ (reproduced from [19]).

2.2.3 Chemical analysis

Chemical analysis of solid materials with electron spectroscopy is based on energy analysis of secondary electrons emitted as a result of excitation of the surface by photons, electrons, ions, or neutrons.

The most important methods that are employed in commercial surface analytical instruments are X-ray photoelectron spectroscopy (XPS), also known as electron spectroscopy for chemical analysis (ESCA), and Auger electron spectroscopy (AES). These techniques are highly important in surface science since they allow to:

- Detect all elements present at the surface of a specimen (except hydrogen and

helium)

- Detect chemical bonding states
- Obtain information depth in the nanometre region (up to 10 nm)

The reason for the surface specificity of electron spectroscopy is the small information depth of typically some nanometers due to the inelastic mean free path of electrons of energy between typically 40 and 2500 eV [20].

2.2.3.1 X-ray photoelectron spectroscopy

Based on the photoelectric effect, XPS uses photons to irradiate the surface of a sample producing the emission of electrons, which can be detected and the atomic core level binding energy E_b can be determined. When an X-ray of a known energy $h\nu$, generally Mg Kα (1253.6 eV) or Al Kα (1486.6 eV), interacts with an atom, excited states are created and electrons, called photoelectrons, are emitted with a kinetic energy E_k given by:

$$E_k = h\nu - E_b - \varphi_s \tag{2.11}$$

where, φ_s is the work function of the spectrometer (typically 4 to 5 eV). Fig. 2.19 shows the schematics of the photoemission process. In addition to photoelectrons, Auger electrons may be emitted because of the relaxation of the excited ions remaining after photoemission. This Auger electron emission occurs approximately 10^{-14} seconds after the photoelectric event (this is the subject of the next section) [20, 21].

In an XPS experiment, the E_k is measured, thus it is possible (by Eq.2.11) to obtain the binding energies of various core electrons, as well as those of the outer (or valence) electrons that are involved in chemical bonding [22]. This information can be used to identify all the elements of the periodic table (except H and He) and the chemical environments of the atom of interest.

Fig. 2.20 shows the work principle of an XPS apparatus, where the sample can be rotated and photoelectrons are detected by the electron energy analyser according to their E_k. The analyser is usually set with a pass energy E_{pass} which is an energy window that accepts only those electrons with an energy in the range of this window. To maintain a constant energy resolution the E_{pass} is fixed and a positive bias is apply to slow the incoming photoelectrons. In this way, they are adjusted to the E_{pass} at the entrance of the analyser. Electrons are detected as discrete events, the number of counts for a given detection time and energy is stored and displayed as an energy spectra [21].

As an example, Fig.2.20 (right bottom) shows typical XPS survey spectra for Rh, Ag, Ir and Pt. This spectra is a plot of the number of electrons detected at a specific

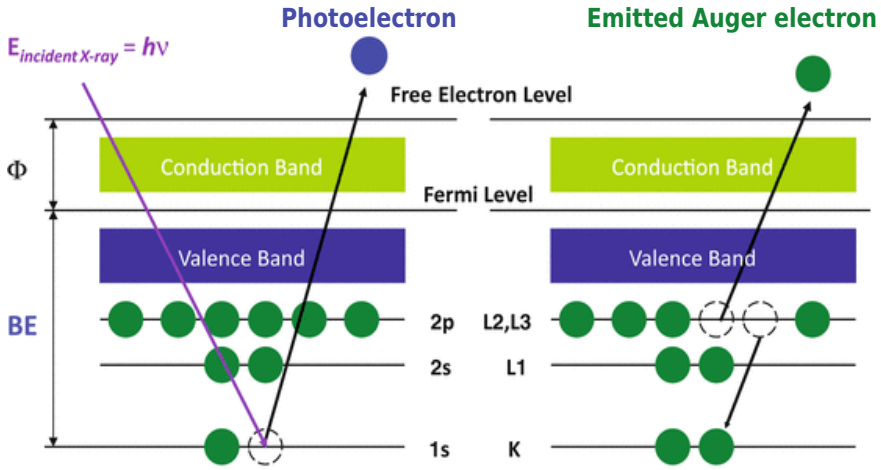

Figure 2.19 – Schematics of the photoelectron emission. An Auger electron may also be emitted after relaxation (reproduced from [23]).

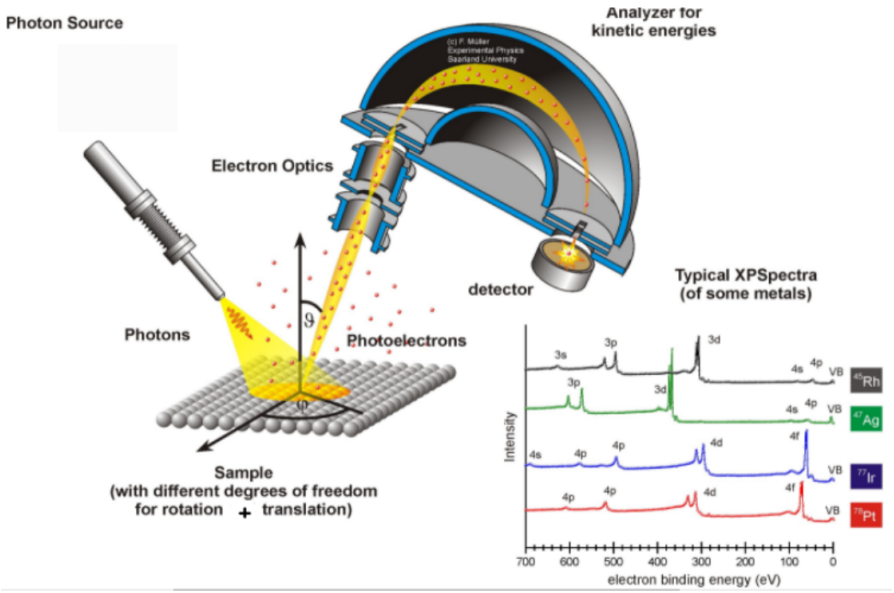

Figure 2.20 – Schematics of the XPS system (reproduced from [24])

binding energy. As most elements produce more than one peak in XPS, corresponding to the electron configuration of the electrons within the atoms (e.g., 1s, 2s, 2p, 3s, etc.), it is convenient to obtain a survey spectrum from 0 eV (the Fermi level) to binding energies around 1200 eV (≈the source energy when using Al Kα or Mg Kα X-rays). This is a good starting point, allowing to set up subsequent high resolution

XPS measurements in the range of binding energies corresponding to peaks of the core levels of interest [25].

In this thesis, XPS measurements were performed in three different UHV chambers. Two of them connected to the TUBE and a third one belonging to the ASURE platform presented before. Fig. 2.21 shows one of the XPS systems connected to the TUBE where most of the measurements reported here were performed. This system consists in a CMA unit (Cylindrical Mirror Analyser) with an integrated electron gun with a beam energy from 20 eV to 5 keV. A beam diameter < 100μm at 5 keV and a maximum beam current of 20μA. The X-ray source is a DAR400 with an energy resolution of 0.6 eV for Mg K_α and 0.8 eV for Al K_α. The XPS system connected to the analysis chamber of the ASURE platform (Fig. 2.9) has an Omicron hemispherical electron analyser EA125. The detected signal is amplified using a 7-channel electron multipliers also called channeltron.

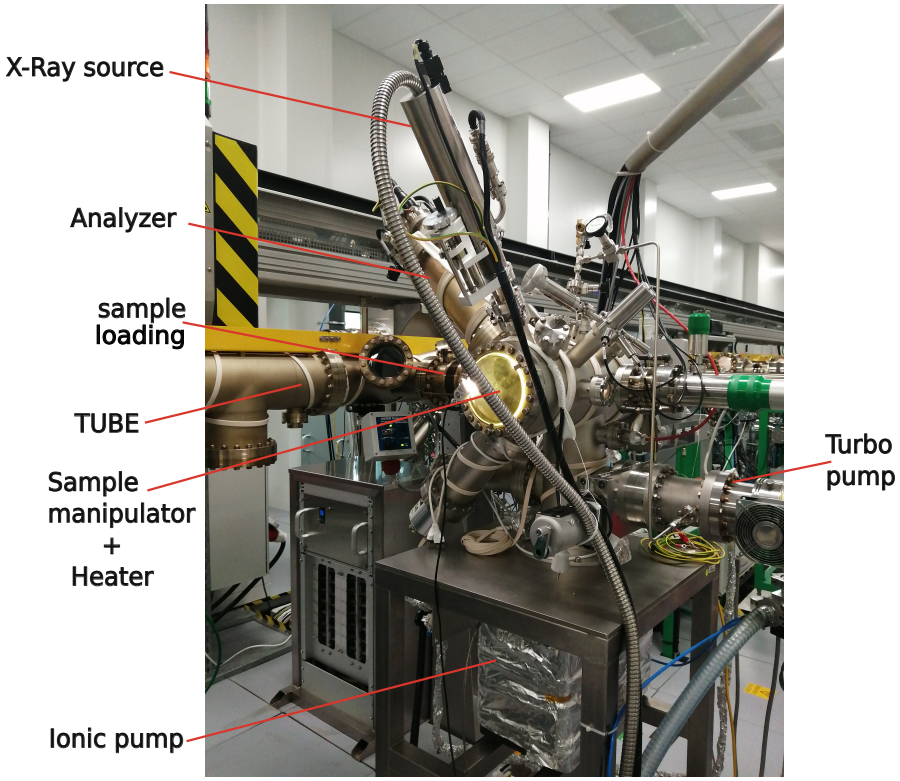

Figure 2.21 – XPS system connected to the TUBE

The software CasaXPS was used in this thesis to treat all the XPS measurements. XPS quantification in terms of peak intensities is performed by measuring the peak areas of specific core lines (I) and by applying appropriate relative sensitivity factors (RSF) [26]. The CasaXPS software provides a library where the RSF and peak posi-

tions from standard samples are considered (along with other corrections to the raw peak area) allowing to determine the atomic concentration (C) of an element X in a sample given by:

$$C_x = \frac{I_x/RSF_x}{\sum I_i/RSF_i} \tag{2.12}$$

Peak areas are determined after removal of background (BG) corrections across the binding energy range of the peak of interest. The most common BG used are [27]:

- Simple straight line or linear BG.
- Shirley BG, where the BG intensity goes up in proportion to the total number of secondary photoelectrons below its binding energy position
- Tougaard BG, which offers practical BG computation based on electron energy losses with more control over the BG shape.

The spin-orbit coupling of the orbital and spin angular momentum are detected by XPS, since all orbital levels (except the s level) give rise to an energy doublet. This doublet corresponds to the two possible states given by the principal quantum number n_{lj} (where l is the angular momentum quantum number, s is the spin angular momentum ($\pm 1/2$) and $j = l+s$). Fig. 2.22 illustrates the splitting of the energy levels where, instead of a single energy level for a final state, the final state splits into two states producing a XPS spectra as doublet pairs [26]. The peaks will also have specific area ratios based on the degeneracy of each spin state. For example, for the 2p spectra, where n is 2 and l is 1, j will be 1/2 and 3/2. The area ratio for the two spin orbit peaks (2p1/2:2p3/2) will be 1:2 (corresponding to 2 electrons in the 2p1/2 level and 4 electrons in the 2p3/2 level). These ratios must be taken into account when analysing spectra of the p, d and f core levels. Spin-orbit splitting values (eV) can be found in a variety of databases (such as NIST Database [28] or XPS Reference Pages [25]). These values will be needed when fitting spectra in order to properly identify the species present.

2.2.3.2 Auger electron spectroscopy

Presented schematically in Fig. 2.19, XPS involves the removal of a single core electron, while Auger electron spectroscopy (AES) is a two-electron process subsequent to the removal of the core electron, with the Auger electron ejected following reorganisation within the atom [2]. The kinetic energy of the emitted electron is equal to the measured Auger electron energy, E_{WXY}, and is given by the difference between the binding energies of electron levels W, X, Y, given by

$$E_{WXY} = E_W - E_X - E_Y - \Phi_s \tag{2.13}$$

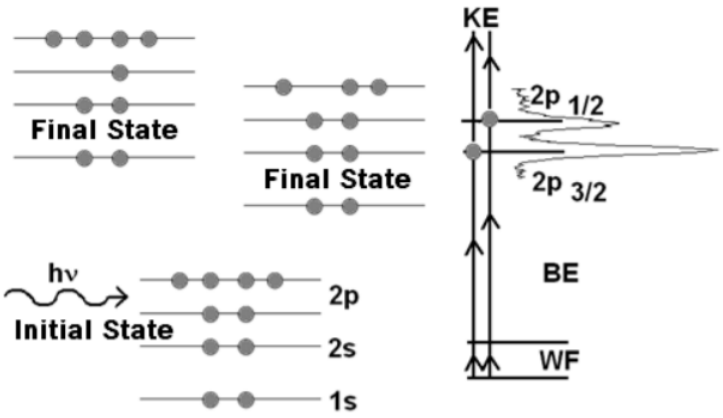

Figure 2.22 – Spin-orbit doublet for a p-orbital (reproduced from [26]).

where Φ_s is the analyser work function (a small correction as in the XPS measurement). Eq.2.13 neglects the ionization and relaxation effects which accompany any Auger transition. In general, E_W and E_X are the binding energies for the single ionized atom, and E_Y is that of the doubled ionized state. In fact, two electrons have left the atom. E_{WXY} can be determined from X-ray tables of electron energies E_W, E_X, E_Y. All possible Auger transitions can be calculated, thus the direct identification of the species in a multi-element sample can be done by using tabulated energies. In addition, an energy spectra is recorded where the intensity of the main peak related to a specific element, is accompanied by neighbouring peaks resulting in a characteristic pattern of a specified "family" of transitions (KLL, LMM, and MNN) [20].

In a typical AES experiment, the sample is irradiated with a focused beam of primary electrons of sufficiently high energy (l–20 keV). Auger electrons possess characteristic energies of the analysed elements. Their inelastic mean free path is strongly dependent on the Auger electron energy, typically between 0.3 and 3 nm. Auger electrons are superimposed on a large and smoothly varying background consisting of inelastically scattered primary and secondary electrons. Because of this fact, Auger spectra are usually presented in the differentiated mode d(N(E)/dE) where N(E) is the counts per second as a function of the kinetic energy E [20].

XPS is more popular in chemical analysis whereas the foremost feature of AES is its highly focused electron beam that allows spatially resolved investigations similar to scanning electron microscopy and is therefore often called scanning Auger microscopy (SAM).

Most of the AES instruments operate in a pulse counting mode which directly acquires the intensity (counts per second), N, as a function of the kinetic energy N(E). Frequently, the first derivative of the direct spectra, d(N(E))/dE is measured or obtained from the N(E) data [20]. Fig.2.23 shows as an example the derivate AES

spectra in the of Al in Al_2O_3 obtained at an excitation energy of 3 keV. The strongest Al peaks are at 35 eV, 51 eV and 1378 eV. At 500 eV the oxygen peaks can be identified as well.

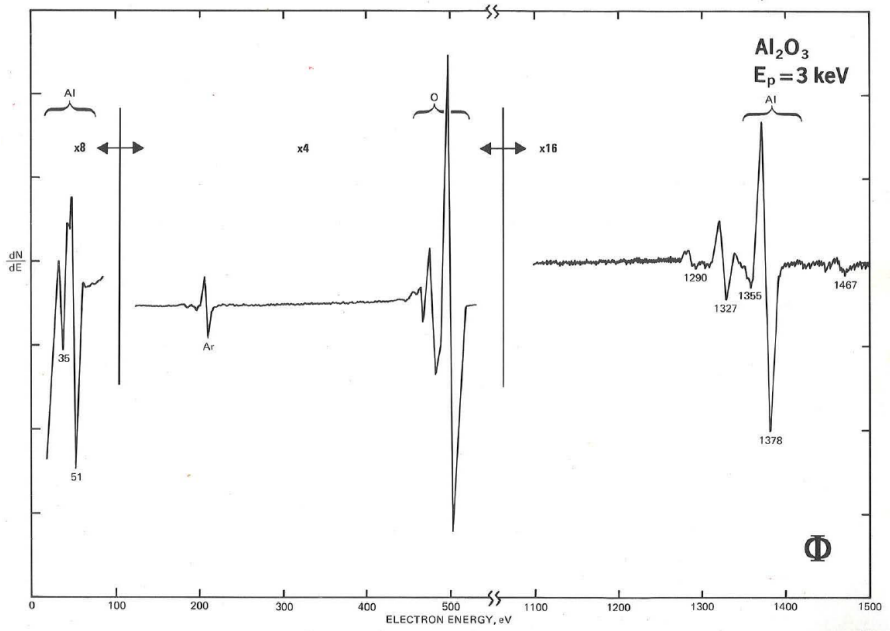

Figure 2.23 – AES spectra of Al in Al_2O_3 at an excitation energy of 3 keV (reproduced from [29]).

2.2.4 Microscopy techniques

2.2.4.1 SCAN platform

During this thesis, AES and Nano-Scanning Auger Microscopy (Nano-SAM) characterizations were performed at the Structural and Chemical Analysis at the Nanoscale (SCAN) platform connected to the TUBE presented in Fig. 2.24. This platform allows the structural and chemical analysis of surfaces down to the nanometre scale with high spatial resolution. The chambers are equipped with an electronic microscope adapted to UHV conditions (Gemini electron column), two secondary electrons detectors, an hemispherical multichannel analyser for Auger microscopy and a Electron backscattered diffraction (EBSD) detector. The spatial resolution of the electronic microscope is 3 nm and 6 nm for Auger microscopy. In addition, samples can be annealed *in situ* up to 477°C. The preparation chamber is equipped with an evaporation source allowing *in situ* thin films deposition and sample cleaning facility by ion bombardment or simple annealing with an e-beam heater. The pumps

assembly guarantees a base pressure inside the chambers of about 5×10^{-11}mbar.

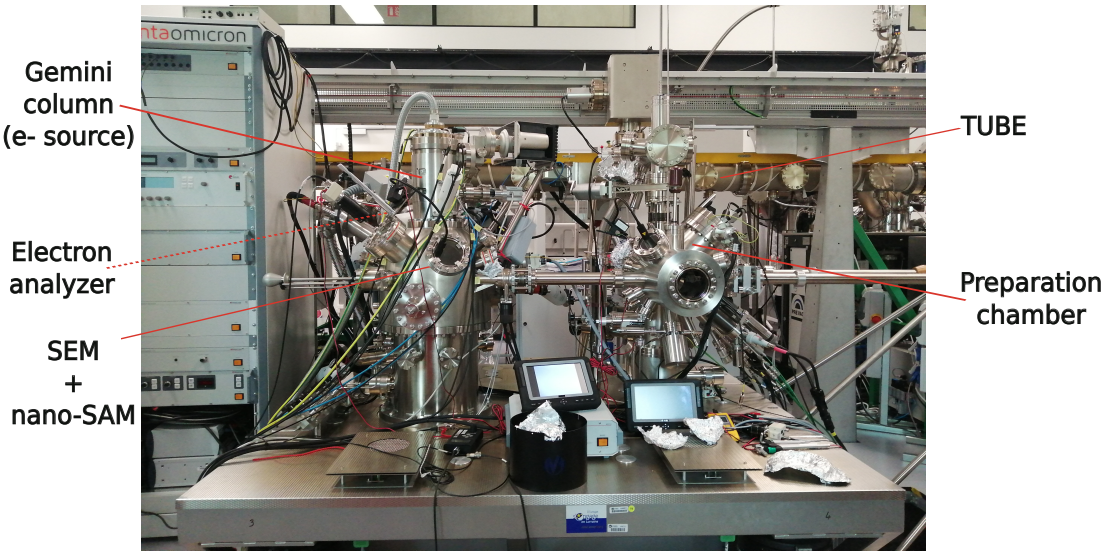

Figure 2.24 – SCAN platform connected to the TUBE.

2.2.4.2 Nano-Scanning Auger Microscopy

Scanning Auger microscopy (SAM) is a powerful technique in surface analysis, which combines physical imaging of the surface as in Scanning electron microscopy (SEM), with chemical analysis of individual areas coming from the Auger spectroscopy element identification. In the following, a brief presentation of SEM will be given followed by the description of the SAM technique.

Scanning electron microscopy: One of the ways in which surface images can be obtained using electron beams is through a scanning electron microscope (SEM). This is one of the most versatile instruments that is available for the examination and analysis of the microstructure morphology and chemical composition of a surface [30]. Due to the very narrow electron beam, SEM micrographs have a great depth of field to obtain a characteristic three dimensional appearance useful to study the surface structure of different kind of specimens. In a typical SEM, as presented in Fig. 2.25, the electron beam is produced by an electron gun (W or LaB_6) and then, it is accelerated through high voltage (up to 30 kV). After passing through the condensator and the objective lens, the beam is focussed on the sample surface for a specific working distance. Afterwards, the beam scans the specimen surface using the (x,y) deflection coils. Various signals are produced from the electron

beam-surface interaction [2, 30]. The backscattered (BSE) and secondary electrons (SE) that are emitted from the specimen are collected by a detector. Information such as topography, composition (if an EDX detector is available), crystal orientation, electrical fields and even magnetic field can be obtained from the detected signals.

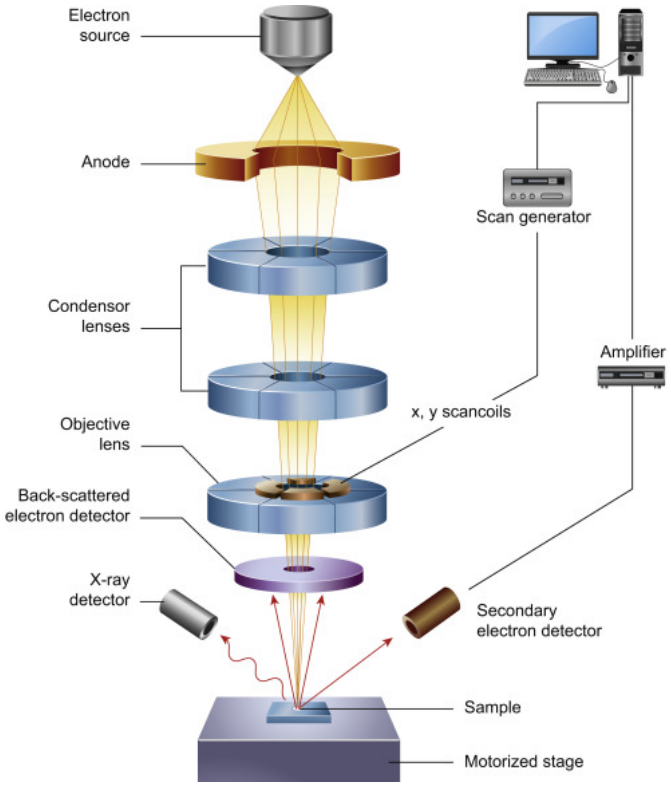

Figure 2.25 – Schematics of a SEM system (reproduced from [31]).

Scanning Auger microscopy: Beyond the surface morphology, a surface compositional map can be obtained by performing AES in the scanning mode. In this mode, the electron beam rasters over a selected area of the surface. By tuning the analyser to detect Auger electrons from the elements of interest a compositional map of the surface elemental concentrations can be obtained [2].

The special feature of the SAM system present at the SCAN platform, is that it counts with a NanoSAM lab system. In contrast with conventional Auger microscopy systems, Nano-SAM has an extremely good spatial resolution. The UHV Gemini electron column achieves the highest resolution available for UHV operation. It has the smallest e-beam spot size (< 10 nm) [32]. The NanoSAM lab enables

the direct acquisition of a AES spectra at the live SEM image, which results in a microscopic image of the chemistry of a surface. Fig. 2.26 gives an example of how a NanoSAM spectra can be obtain from a specific region on the sample surface previously imaged by SEM. The NanoSEM spectra corresponds to a $Mg_{0.75}Zn_{0.25}Al_2O_4$:Tb surface coming from various positions on the rough surface as indicated on the inset SEM image.

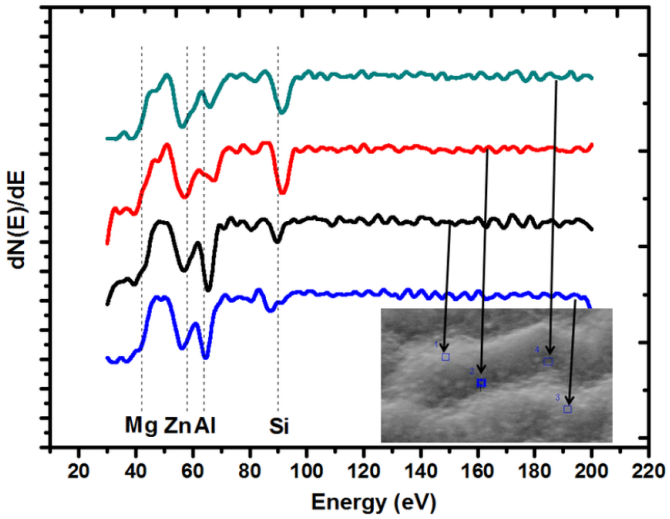

Figure 2.26 – High resolution NanoSAM spectra of the low energy region of a thin film of $Mg_{0.75}Zn_{0.25}Al_2O_4$:Tb. The inset shows a SEM image of the surface indicating the regions on the rough surface where the electron beam was scanned to collect the NanoSAM spectra (reproduced from [33]).

2.2.4.3 Scanning tunnelling microscopy

The final aim of nanotechnology is the control of matter at the atomic and molecular levels. Scanning tunneling microscopy (STM) has proven to be the "eyes and fingers" of nanotechnology (along with other scanning probe microscopy techniques). STM shows impressive performance resolving structures with sub-nanometer details [34]. This technique was introduced in 1982 by Binning and Rohrer, who based on vacuum tunnelling, developed a microscope capable to obtain the topography of surfaces in real space with a lateral resolution in the sub-Å range and a depth resolution of a $\simeq$ 10 pm [35].

An STM consist essentially in a sharp metallic tip which scans the surface of an electrically conducting sample. The tip acts like one of the electrodes of a tunnel junction, while the surface of the sample acts like the second electrode. Fig 2.27

shows the working principle of STM. Both tip-sample separation and lateral position can be varied with sub-Å precision by means of a piezoelectric scanner. The tunnel current J_T is a sensitive function of the gap width s as expressed Eq. 2.14:

$$J_T \propto V_{app} \exp\left(-A\Phi^{1/2}s\right) \tag{2.14}$$

Where φ is the average barrier high and $A = 1$ if Φ is measured in eV and s in Å . With Φ of some eV, J_T changes by an order of magnitude for every Å of s. When a negative bias voltage is applied to the sample, electrons in occupied states of the sample will tunnel through the vacuum barrier to empty states of the tip, resulting in a measurable tunnel current [35]. If a positive bias voltage is applied, electrons will tunnel from the tip to the sample. In a constant-current mode, the tunnelling current is kept constant while the tip scans the surface, giving a contour of the density of states (DOS), which in the case of homogeneous elemental metals, corresponds to the topography of the sample surface. If the local DOS varies spatially, the resulting image contains a mixture of DOS and topographic information. With the appropriate tunnelling parameters, however, the contribution of the topography dominates the image [36].

STM can also measure the sample DOS as a function of energy, up to several eV from the Fermi level ε_F in occupied and unoccupied states. This is usually done by sweeping the bias voltage and measuring the tunnelling current J_T while maintaining constant tip-sample separation s.

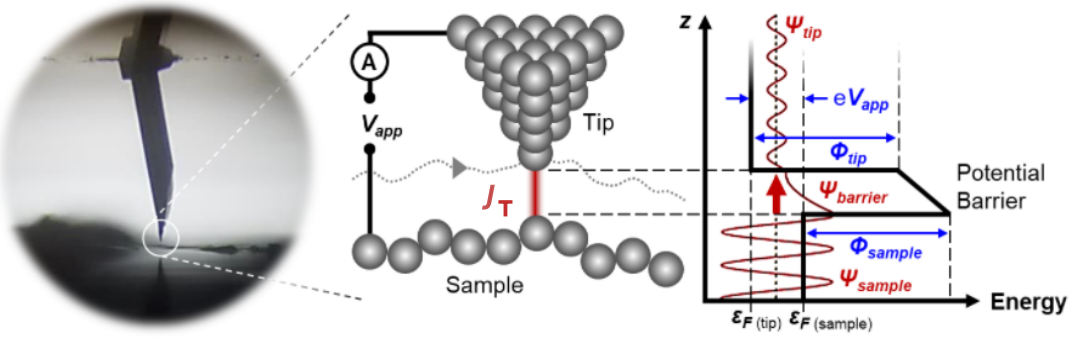

Figure 2.27 – *left* A magnified view of a STM probe. *rigth*: A schematic of the work principle of a STM. e is the elementary charge, V_{app} is the applied bias voltage, ε_F is the Fermi level and ψ is the electron wave function (reproduced from [37]).

STM has been used successfully to the study of oxide ultra-thin films. Specially, STM measurements have been crucial in the identification of quasicrystalline order or labyrinth phases in ultra-thin ternary oxide films [38]. In this thesis, STM measurements were performed in the ASURE platform (Fig. 2.9), where STM images

were obtained at constant-current mode, at room temperature and at low temperature (∼ 20 K). The tip used consists in a tungsten wire with a sharp tip formed by chemical etching. Omicron Matrix SPM control system was used for the image acquisition. The images obtained were treated with the software WxSM solutions [34].

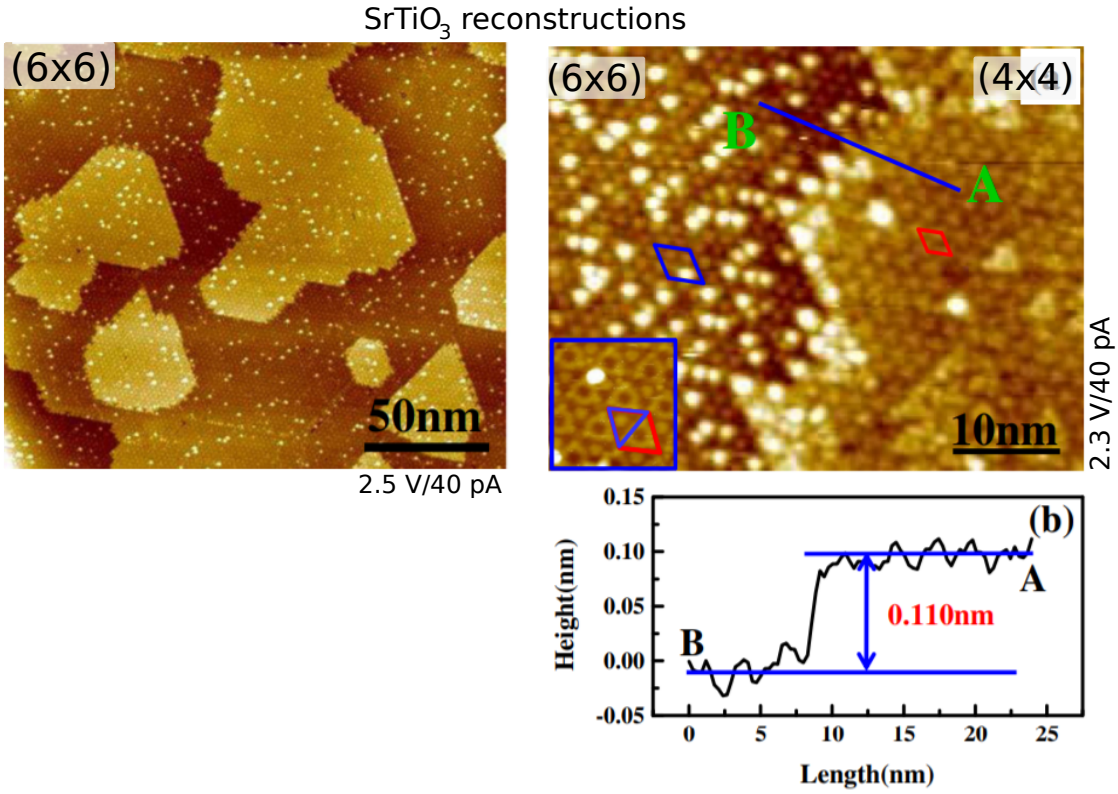

Figure 2.28 – High resolution STM images of a (6×6) and (4×4) surface reconstructions of $SrTiO_3$. Left image corresponds to the LEED pattern showed in Fig2.18(b) from a (6×6) reconstruction. Right image show how both reconstructions coexist with each other. Unit cells are marked in blue an red respectively. A line profile along the line AB is shown above, indicating the size of the step (reproduced from [19]).

Fig. 2.28 shows examples of atomic resolution STM images from two $SrTiO_3(111)$ surface reconstructions. The image on the left is the corresponding STM image of the LEED pattern previously presented in Fig. 2.18(b) [19]. Here one can see how these two techniques are complementary and of great importance for determining the atomic surface structure. Furthermore, profiles can be traced (as in the right image), in order to measure the heigh of the steps present at the surface.

Bibliography

[1] A. Stephane and P. Muller. *Les surfaces solides : concepts et methodes*. Savoirs actuels Physique. EDP Sciences CNRS editions, Les Ullis Paris, 2005.

[2] D. J. O'Connor, B. A. Sexton, and R. St. C. Smart. *Surface Analysis Methods in Materials Science / D.J. O'Connor, B.A. Sexton, R.St.C. Smart (Eds.)*. Springer Berlin ; London, 2nd ed. edition, 2003.

[3] G. Barcaro and A. Fortunelli. 2D oxides on metal materials: Concepts, status, and perspectives. *Physical Chemestry Chemical Physics*, 21:11510, 2019.

[4] S. Förster, K. Meinel, R. Hammer, M. Trautmann, and W. Widdra. Quasicrystalline structure formation in a classical crystalline thin-film system. *Nature*, 502(7470):215–218, 2013.

[5] S. Schenk, S. Förster, K. Meinel, R. Hammer, B. Leibundgut, M. Paleschke, J. Pantzer, C. Dresler, F. O. Schumann, and W. Widdra. Observation of a dodecagonal oxide quasicrystal and its complex approximant in the $SrTiO_3$-Pt(111) system. *Journal of Physics: Condensed Matter*, 29(13):134002, 2017.

[6] Daum : Plateforme de Dépôts et d'Analyses sous Ultravide de nanoMatériaux. https://wiki.ijl.univ-lorraine.fr/doku.php?id=wikiijl:cc:daum:accueil.

[7] P Frigeri, L Seravalli, G Trevisi, and S Franchi. 3.12 Molecular Beam Epitaxy: An Overview. page 43, 2011.

[8] D. P. Norton. Pulsed Laser Deposition of Complex Materials: Progress Toward Applications. In *Pulsed Laser Deposition of Thin Films*, chapter 1, pages 1–31. John Wiley & Sons, Ltd, 2006.

[9] H. S. Kwok, J. P. Zheng, S. Witanachchi, P. Mattocks, L. Shi, Q. Y. Ying, X. W. Wang, and D. T. Shaw. Growth of highly oriented CdS thin films by laser-evaporation deposition. *Applied Physics Letters*, 52(13):1095–1097, 1988.

[10] L. Shi, Y. Hashishin, S. Y. Dong, J. P. Zheng, and H. S. Kwok. Laser deposition of CdS/Y-Ba-Cu-O heterostructures. *Applied Physics Letters*, 59(11):1377–1379, 1991.

[11] J. P. Zheng and H. S. Kwok. Low resistivity indium tin oxide films by pulsed laser deposition. *Applied Physics Letters*, 63(1):1–3, 1993.

[12] D. H. Kim and H. S. Kwok. Pulsed laser deposition of VO $_2$ thin films. *Applied Physics Letters*, 65(25):3188–3190, 1994.

[13] D. B. Chrisey, A. Piqué, R. A. McGill, J. S. Horwitz, B. R. Ringeisen, D. M. Bubb, and P. K. Wu. Laser Deposition of Polymer and Biomaterial Films. *Chemical Reviews*, 103(2):553–576, 2003.

[14] S. Hasegawa. Reflection High-Energy Electron Diffraction. In *Characterization of Materials*, pages 1–14. American Cancer Society, 2012.

[15] Guyard, S. *Epitaxie par ablation laser pulsé du titane de strontium : Application aux dispositfs agiles hyperfrécuence*. PhD thesis, Université de Paris 6, 2007.

[16] M. Kasai and H. Dohi. Growth temperature and relaxation of lattice strain in epitaxial Pt films exhibiting diffraction fringes. *Surface Science*, 689:121461, 2019.

[17] Devillers, T. Ferromagnetic phases of $Ge_{(1-x)}Mn$_x$ for spintronics applications. 2008.

[18] M. Saghayezhian, L. Chen, G. Wang, H. Guo, E. W. Plummer, and J. Zhang. Polar compensation at the surface of $SrTiO_3(111)$. *Physical Review B*, 93(12):125408, 2016.

[19] J. Feng, X. Zhu, and J. Guo. Reconstructions on $SrTiO_3(111)$ surface tuned by Ti/Sr deposition. *Surface Science*, 614:38–45, 2013.

[20] S. Hofmann. *Auger- and X-Ray Photoelectron Spectroscopy in Materials Science: A User-Oriented Guide*. Springer Series in Surface Sciences 49. Springer-Verlag Berlin Heidelberg, first edition, 2013.

[21] J. F. Moulder, W.F. Stickle, P. E. Sobol, and K. D. Bomben. *Handbook of X Ray Photoelectrfon Spectroscopy: A Reference Book of Standard Spectra for Identification and Interpretation of Xps Data*. Physical Electronics, 1992.

[22] C. S. Fadley. X-ray photoelectron spectroscopy: Progress and perspectives. *Journal of Electron Spectroscopy and Related Phenomena*, 178–179:2–32, 2010.

[23] R. T. Haasch. X-ray photoelectron spectroscopy (XPS) and auger electron spectroscopy (AES). In M. Sardela, editor, *Practical Materials Characterization*, pages 93–132. Springer New York, New York, NY, 2014.

[24] Rob. X-Ray Photoelectron Spectroscopy, 2021.

[25] M. Biesinger. X-ray Photoelectron Spectroscopy (XPS) Reference Pages. http://www.xpsfitting.com/, 2020.

[26] Casa Software Ltd Neal, F. CasaXPS manual 2.3.15: Introduction to XPS and AES, 2009.

[27] N. Fairley. Peak Fitting in XPS. page 29, 2006.

[28] A. V. Naumkin, C. J. Powell, A. Kraut-Vass, and S. W. Gaarenstroom. NIST X-ray Photoelectron Spectroscopy Database, 2012.

[29] L. E. Davis, N. C. MacDonald, P. W. Palmberg, G. E. Riach, and R. E. Weber. Handbook of Auger Electron Spectroscopy, 1976.

[30] J Goldstein, J.R. Michael, D. E. Newbury, D. C. Joy, C E. Lyman, Patrick Echlin, Eric Lifshin, and Linda Sawyer. *Scanning Electron Microscopy and X-ray Microanalysis*. Springer, 3rd edition, 2003.

[31] B. J. Inkson. 2 - Scanning electron microscopy (SEM) and transmission electron microscopy (TEM) for materials characterization. In G. Hübschen, I. Altpeter, R. Tschuncky, and H. G. Herrmann, editors, *Materials Characterization Using Nondestructive Evaluation (NDE) Methods*, pages 17–43. Woodhead Publishing, 2016.

[32] NanoScan Lab - Scienta Omicron. https://scientaomicron.com/en/system-solutions/electron-spectroscopy/NanoScan-Lab.

[33] R. Kroon, W. Tabaza, and H. Swart. Luminescence of (Mg,Zn)Al_2O_4:Tb mixed spinel thin films prepared by spin-coating. *Proceedings of SPIE - The International Society for Optical Engineering*, 9359, 2015.

[34] I. Horcas, R. Fernández, J. M. Gómez-Rodríguez, J. Colchero, J. Gómez-Herrero, and A. M. Baro. WSXM: A software for scanning probe microscopy and a tool for nanotechnology. *Review of Scientific Instruments*, 78(1):013705, 2007.

[35] G. Binnig and H. Rohrer. Scanning Tunneling Microscopy. *Reviews of Modern Physics, Part*, pages 59–3, 1987.

[36] Yi Yin, M. Zech, T. L. Williams, and J. E. Hoffman. Scanning tunneling microscopy and spectroscopy on iron-pnictides. *Physica C: Superconductivity*, 469(9):535–544, 2009.

[37] Spectra Research Corporation. APRIL CURRENT AMPLIFIERS BRING MAY ULTRA-LOW-CURRENT STM, 2021.

[38] M.R. Castell. STM and STS of Oxide Ultrathin Films. In *Encyclopedia of Interfacial Chemistry*, pages 332–337. Elsevier, 2018.

Chapter 3

Growth of $SrTiO_3$ on Pt(111)/ α-Al_2O_3(0001)

Contents

3.1 Measurements of the sample temperatures 70
3.2 Pt(111) grown on α-Al_2O_3(0001): state of the art 71
3.2.1 Substrate preparation 74
3.2.2 10 nm of Pt(111) grown on Al_2O_3(0001) by MBE 75
3.3 Growth of Ti/Pt(111) buffer layer on α-Al_2O_3(0001) 81
3.3.1 1 nm of Ti grown on Pt(111)/Al_2O_3(0001) by MBE 81
3.4 $SrTiO_3$ thin films deposited on Pt(111) by PLD 90
3.4.1 Crystal structure and epitaxial relationships:state of the art 90
3.4.2 Thin films of $SrTiO_3$ on (Ti/)Pt(111) by PLD results 92
3.5 TEM investigations 96
Bibliography 100

The growth of multilayer systems is a very active field in material science, specially attractive for functional oxides in perovskite systems (e.g., see ref. [1] and references therein). The goal is to combine different thin film materials with different thickness and strain dependence with physical properties to create new heterostructures with novel properties [2].
In the present work, a thin film stacking was used to investigate the structural and chemical changes of ultrathin films of $SrTiO_3$ grown on a metal surface. In particular, we would like to study the interface frustration that might drive the oxide film to form aperiodic structures when approaching the 2D limit [2]. We chose a film-stacking approach (instead of using single crystal metal substrates [3, 4, 5, 6]) since it allows the exploration of different oxide/metal combinations, if materials with small deviations in the lattice parameter are found. Thus, materials with tunable properties could be synthesized. To test this method we decided to start with an already studied combination: $SrTiO_3$/Pt(111) [6]. Here, thin films (< 30 nm) of $SrTiO_3$ were deposited by PLD on a 10 nm layer of Pt(111) with or without an additional nm of Ti. The metals were deposited by MBE on an α-Al_2O_3(0001) substrate.

This chapter is divided in five sections. The first one gives an explanation of the temperature measurement methods used during the sample fabrication and characterizations. The second and the third ones, expose the epitaxial growth of Pt(111) and Ti/Pt(111) on Al_2O_3(0001) by MBE. The forth one is dedicated to the results of the deposition of $SrTiO_3$ thin films by PLD. The structural characterizations of the surface by means of RHEED and X-ray diffraction are discussed here, as well as the chemical characterization performed by XPS, AES and Nano-SEM. Finally, the fifth section is committed to the results of the transmission electron microscopy (TEM) studies of the film stacking performed in collaboration with the Jožef Stefan Institute in Slovenia.

3.1 Measurements of the sample temperatures

Two instruments were used to measure the temperature of the samples: Thermocouples (Th), installed inside the UHV chambers, and a bichromatic pyrometer (T_{Pyro}). As various UHV systems were used to grow and characterize the samples, temperature measurements could vary since the thermocouples are placed differently with respect the sample's position in the different chambers. For instance, in the PLD, XPS and MBE chambers the thermocouple is located in the back of the sample holder, almost in contact with it, while in the SCAN platform it is located on the manipulator next to the e-beam heater and the sample plate, therefore it is normal to measure lower temperature values. On the other hand, the bichromatic pyrometer can be pointed directly on the sample surface, thus the temperature measurement could be higher than for the one rerecorded with the thermocouple in the

SCAN chamber, or lower than the one rerecorded when the thermocouple is closer to the sample holder. A considerable shift (even about 200°C) could be present between the thermocouple and the pyrometer measurements.

To avoid discrepancies in temperature measurements across the different chambers, we chose to rely on the temperature measured by the bichromatic pyrometer. Nevertheless, not always was possible to obtain a temperature reading with this instrument (due to geometric constrains or availability of the pyrometer, for instance). Therefore, the reader will find throughout this chapter a clarification of the instrument used to measured the reported temperature (Th or T_{Pyro}).

3.2 Pt(111) grown on α-Al_2O_3(0001): state of the art

The growth of Pt thin films is of considerable interest in different fields of science and technology due to its remarkable physicochemical properties such as low resistivity, high thermal stability, and high stability in oxygen environments at high temperatures [7, 8]. The main disadvantage of using Pt is related to its high cost due to its rarity. Therefore, applications where Pt is used as a thin film are preferable. One of the most common substrates for Pt films is α-Al_2O_3(0001) since the lattice mismatch between these two materials is small, only 0.9% [9, 10]. Bulk Pt has a *fcc* crystal structure (space group: $Fm\bar{3}m$) while the bulk crystal structure of α-Al_2O_3 is a corundum, which has rhombohedral symmetry (space group: $R\bar{3}c$) [11]. The crystal structure of Pt is presented in Fig.3.1(a) consisting on a *fcc* cell with a lattice parameter of 3.98 Å [12]. In the (111) plane (highlighted in red and reproduced in Fig. 3.1(b)), the in-plane lattice parameter is 2.81 Å. Fig.3.1 (c) shows the crystal structure of α-Al_2O_3, which is formed by Al^{3+} and O^{2-} ions. If the O^{2-} anions are depicted as balls, the crystal lattice takes the form of their closest hexagonal packing. The Al^{3+} cations are located in a crystalline field that has no symmetry centre (due to crystal lattice distortions). These cations lie in the octahedral hollows between the closely packed O^{2-} ions, filling two thirds of these hollows [13]. Fig.3.1(d) illustrates the Al_2O_3(0001) basal plane, with an hexagonal structure described by an in-plane lattice parameter of 4.75 Å. The positions of the Al and the O atoms from the outermost layer to the 6th layer are indicated.

During the last decades various authors have studied the growth of Pt(111) on Al_2O_3(0001) by different fabrication methods such as evaporation [14, 15], metalorganic chemical vapour deposition (MOCVD)[15], sputtering [10, 16, 8, 17, 7, 18] and molecular beam epitaxy (MBE) [19, 9]. These studies show mainly by means of XRD and electron diffraction, that the growth of Pt on Al_2O_3(0001) is well (111)-oriented for every growth technique at temperatures close to 600°C.

For Pt films grown by MBE, Farrow *et al.* showed that for thickness of 15 Å and 30 Å deposited at a substrate temperature of 600°C [9], the films presented RHEED

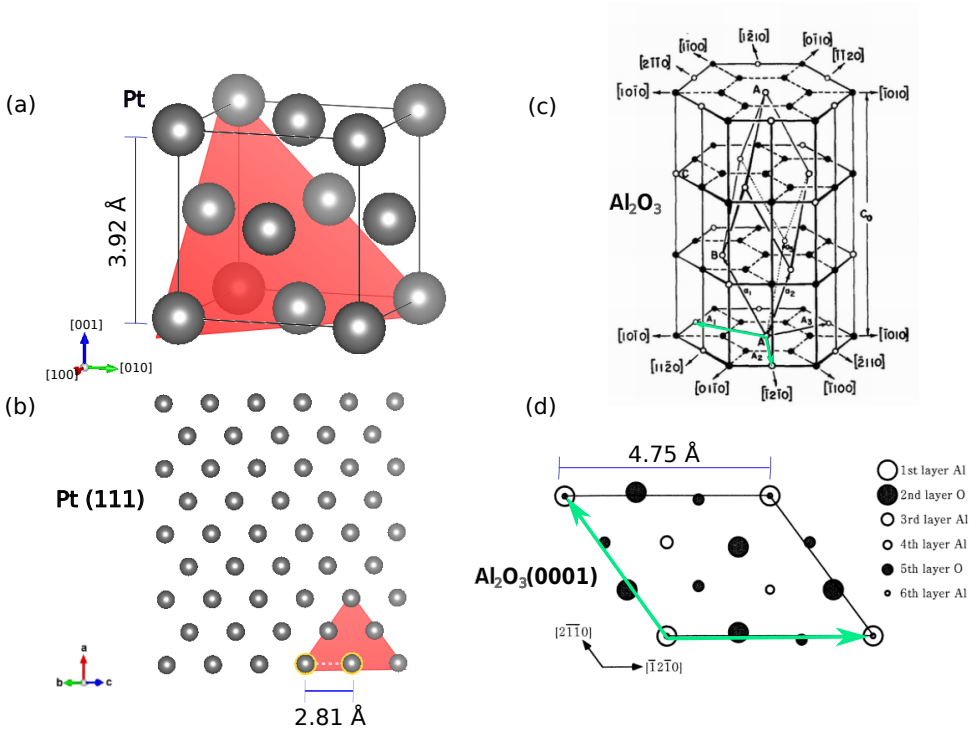

Figure 3.1 – (a) Schematics of the Pt *fcc* crystal structure. The (111) plane is highlighted in red. (b) The [111]-oriented Pt layer. (c) The Al_2O_3 hexagonal crystal structure. Black and white dots represent the Al^{3+} ions and the octahedral hollows between two layers of O^{-2} respectively. $\mathbf{A}_1$, $\mathbf{A}_2$ and $\mathbf{A}_3$ are the $< 11\bar{2}0 >$ translational vectors of the hexagonal cell for the basal plane. $\mathbf{A}_1$ and $\mathbf{A}_2$ are highlighted in green (reproduced from [13]). (d) The top view of the hexagonal atomic arrangement of the Al_2O_3(0001). The stacking of the Al and O atoms are indicated from the surface to the 6th layer (reproduced from [11])

patterns replicated on a 60° rotation of the substrate, which means that Pt growth axis is [111] preserving a 6-fold symmetry. The thicker film presented sharp elongated RHEED streaks, while the thinner one showed a tendency to form shorter and diffuse streaks with a distribution typical of island growth [9]. Besides, RHEED and X-ray photoelectron diffraction (XPD) results suggest that twinning occurs at the initial island nucleation stage. The reported epitaxial relationships determined by LEED are: Pt[111]||Al_2O_3[0001] and Pt(110)||$Al_2O_3(10\bar{1}0)$.
Growth temperatures above and below 600°C were also explored by the authors. It was found that for substrate temperatures $\gtrsim$ 650°C films of 30 Å were not continuous. For temperatures $\lesssim$ 550°C it was observed that films were continuous but the RHEED streaks became significantly more diffuse when temperature was de-

creased, indicating reduced in-plane coherence [9].

Films of 14 nm were deposited by Zhou *et al.* at substrate temperatures between 550°C and 730°C. RHEED patterns taken at different deposition times showed how a change from a three dimensional growth mode into a two dimensional growth mode after the nucleation stage occurs [19]. To know the in-plane structural information, XRD measurements were performed along with TEM measurements. The epitaxial relationships are: Pt(111)||Al_2O_3(0001) and Pt[01$\bar{1}$]||Al_2O_3[10$\bar{1}$0]; Pt[$\bar{1}$21]||Al_2O_3(11$\bar{2}$0).

These relationships are illustrated schematically in Fig. 3.2(a) where the basal hexagonal plane of α-Al_2O_3(0001) and the arrangement of the Pt atoms in Pt(111) in the real space, are represented by white and blue circles respectively. The unit cell vectors, $\boldsymbol{a}_1$ and $\boldsymbol{a}_2$, of the α-Al_2O_3(0001) lattice are indicated by green arrows. Using the Eqs.2.6-2.8 introduced in Chap.2, one can construct the reciprocal lattice which is also hexagonal but with a rotation about the $\hat{z}$ axis by an angle of 30° as represented in Fig. 3.2(b). The reciprocal lattice vectors, $\boldsymbol{a}_1^*$ and $\boldsymbol{a}_2^*$, are marked in green as well. Fig. 3.2(c) represents, in the reciprocal space, the diffraction nodes for the initial α-Al_2O_3 substrate (green rods) and the expected variation after the Pt deposition (magenta rods). Along the same directions in (a), epitaxial Pt(111)//α-Al_2O_3(0001) leads to rods appearing one out of three in the Pt<$\bar{1}$21> direction, while in the Pt<01$\bar{1}$> direction they appear at the same position of the α-Al_2O_3 rods.

In summary, literature shows that epitaxial thin films of Pt(111) are grown by MBE on α-Al_2O_3(0001) in a 2D mode resulting in a smooth surface, for temperatures between 550°C and 650°C. The growth is (111)-oriented for every reported deposition technique.

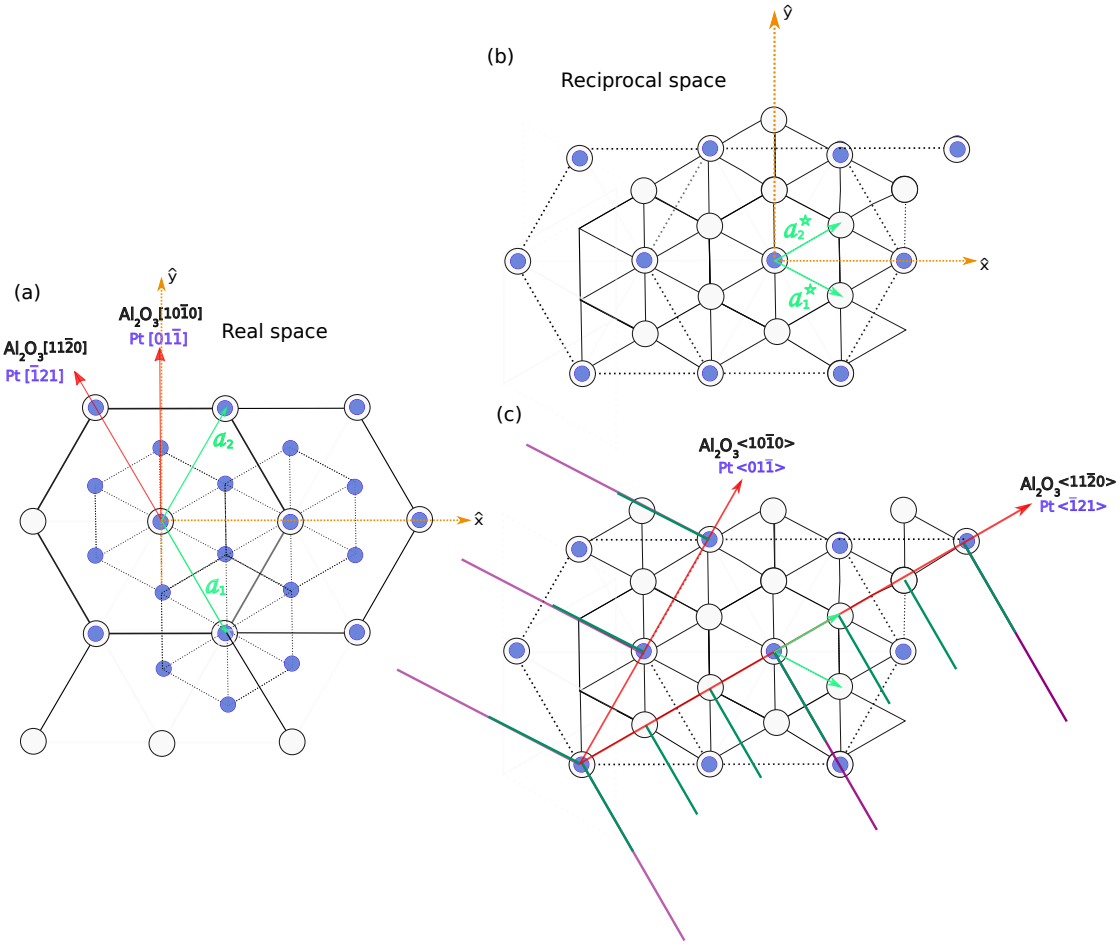

Figure 3.2 – (a) Schematic diagram of the epitaxial relationships between Pt(111)(blue circles and doted lines) and the basal plane of α-Al_2O_3 (white circles and full lines) in the real space. The unit cell vectors of α-Al_2O_3 $\boldsymbol{a}_1$ and $\boldsymbol{a}_2$ are indicated by the green arrows. (b) Schematic representation of the reciprocal space construction of the α-Al_2O_3(0001) and the Pt(111) hexagonal lattices. The reciprocal lattice vectors $\boldsymbol{a}_1^*$ and $\boldsymbol{a}_2^*$ are indicated by the green arrows. (c) The diffraction nodes of the α-Al_2O_3 in the Pt[$\bar{1}$21] and the Pt[01$\bar{1}$] directions shown by the green rods. After Pt deposition, the rods in the Pt[$\bar{1}$21] direction are expected to appear one out of three Al_2O_3 rods, while in the Pt[01$\bar{1}$] direction they are expected to appear at the same position of the Al_2O_3 rods, as pointed by the magenta rods.

3.2.1 Substrate preparation

First, α-Al_2O_3(0001) substrates (SurfaceNet GmbH) were cleaned in an ultrasonic bath in acetone for 5 minutes followed by a second ultrasonic bath in ethanol for 5

minutes. Then, the substrates were pasted on the sample holders using silver paint and subsequently annealed at around 100°C for 1 hour. Substrates with dimensions either 5 ×5 mm^2 or 10 × 10 mm^2 where used, with a thickness of 1 mm or 0.5 mm. Samples were also fabricated with substrates cut from a α-Al_2O_3(0001) wafer with a thickness of 0.3 mm. After the substrates were mounted, they were annealed at 900°C (T_h) under UHV for 15 minutes in the analysis chamber interconnected to the MBE system by the TUBE (see Chap. 2 for more details concerning the TUBE). Once the substrates were degassed, they were transferred under UHV to the MBE chamber where the Pt growth was performed.

3.2.2 10 nm of Pt(111) grown on Al_2O_3(0001) by MBE

Considering the literature results discussed in the previous section, we used α-Al_2O_3(0001) as a substrate for the growth of 10 nm of Pt by MBE. Our objective at this stage is to obtain a smooth, well oriented Pt(111) layer with a high crystalline quality.

The Pt deposition was performed at substrate temperature of 400°C (T_h) at a rate of 0.1 Å/s under a typical pressure of about 10^{-9} mbar. Although literature reports higher substrate temperatures as mentioned above, it was determined by previous experiments preformed in our MBE system, that 400°C is the ideal measured temperature to growth smooth layers of Pt on Al_2O_3(0001) substrates. The discrepancy with the literature is probably due to the fact that the T_h measured is possibly lower than the actual sample temperature.

The film structure was probed *in situ* during the different stages of the sample fabrication by RHEED. Fig.3.3 (a) presents the RHEED patterns along the $Al_2O_3[10\bar{1}0]$ and $Al_2O_3[11\bar{2}0]$ directions, starting with the diffraction pattern of the clean substrate. After Pt growth and cooling, the RHEED patterns recorded at room temperature (RT) exhibit sharp elongated streaks indicating a smooth surface. Besides, the same pattern is repeated every 60° confirming a 6-fold surface symmetry of the thin film. As shown above in Fig.3.2(c), if the growth is epitaxial, additional diffraction streaks are expected to be observed in the RHEED patterns taken along the $Al_2O_3[11\bar{2}0]$ direction with respect the $Pt[\bar{1}21]$ direction, while diffraction streaks in the patterns taken along the $Al_2O_3[10\bar{1}0]$ and the $Pt[01\bar{1}]$ directions should be observed at the same positions. Fig.3.3 (b) shows the line profiles of the RHEED patterns in (a) in the $Al_2O_3[10\bar{1}0]$ (bottom) and $Al_2O_3[11\bar{2}0]$ (top) directions, confirming the expected positions of the diffraction streaks of the clean substrate (red curve) and after the Pt(111) deposition (black curve). In the $Pt[01\bar{1}]$ direction, Pt peaks are present one out of three of the Al_2O_3(0001) peaks. In the $Pt[\bar{1}21]$ direction, Pt peaks are at the same positions of the Al_2O_3(0001) peaks, reflecting epitaxial growth of the Pt film. The profile is measured along the yellow path. Here and in all the following

RHEED patterns the path consists of a single line segment whose width is indicated by the top and bottom yellow lines.

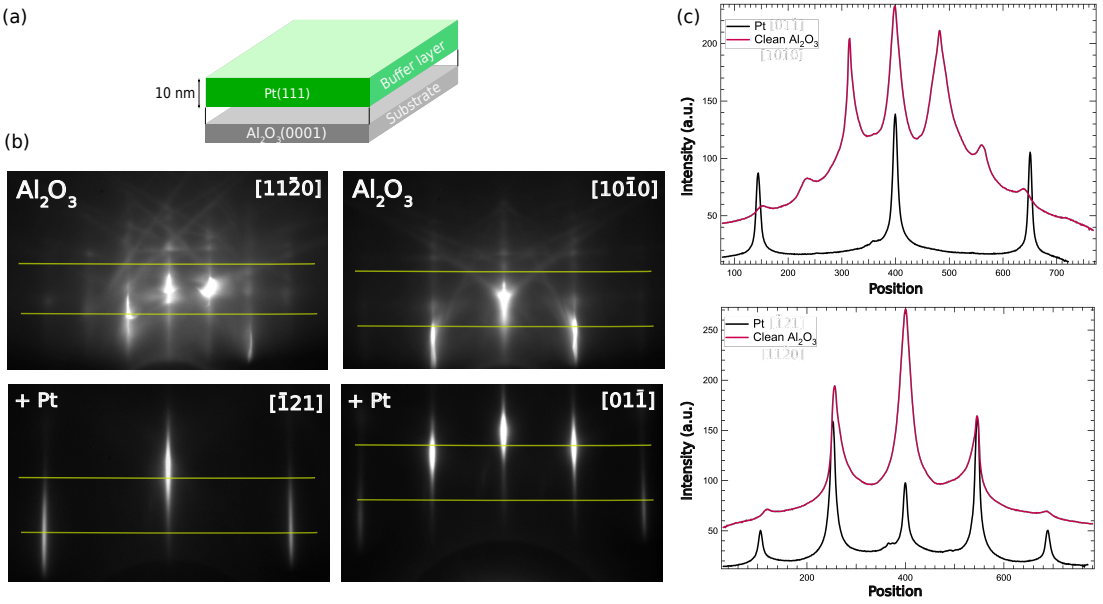

Figure 3.3 – (a) Schematic of the 10 nm Pt(111) buffer layer grown on the α-Al_2O_3(0001) substrate. (b) RHEED patterns of the Al_2O_3(0001) substrate (top) and the 10 nm Pt(111) buffer layer (bottom) after deposition and subsequent cooling. (c) Corresponding line profiles taken along the yellow lines in (b), showing an epitaxial growth of Pt (111) on the Al_2O_3(0001) substrate.

High resolution X-ray diffraction (HRXRD) $\omega - 2\vartheta$ measurements of the 10 nm Pt film grown on an Al_2O_3 (0001) substrate are shown in Fig.3.4. XRD characterizations were performed with a MRD X'Pert Pro diffractometer in a Bragg-Brentano configuration, by using Cu K_{α_1} radiation ($\lambda = 1.54056$ Å). The substrate reflections are clearly observed along with the *hhh* reflections of Pt. No reflections from other planes are present indicating that Pt is well (111)-oriented. Laue oscillations around the Pt Bragg's peaks indicate good crystallinity and high interface and surface quality. The upper graph in Fig 3.4 shows the φ-scan of the Pt film and substrate measured using the reflection planes {220} and {119} respectively. Six peaks separated by 60° for both, substrate and film, are evidence of the six-fold symmetry and moreover the epitaxial growth of Pt(111) on the α-Al_2O_3 (0001) substrate. These results confirm the epitaxial relationships:

$$\mathrm{Pt(111)||Al_2O_3(0001)}$$
$$\mathrm{Pt[01\bar{1}]||Al_2O_3[10\bar{1}0]\ and\ Pt[\bar{1}21]||Al_2O_3[11\bar{2}0]}$$

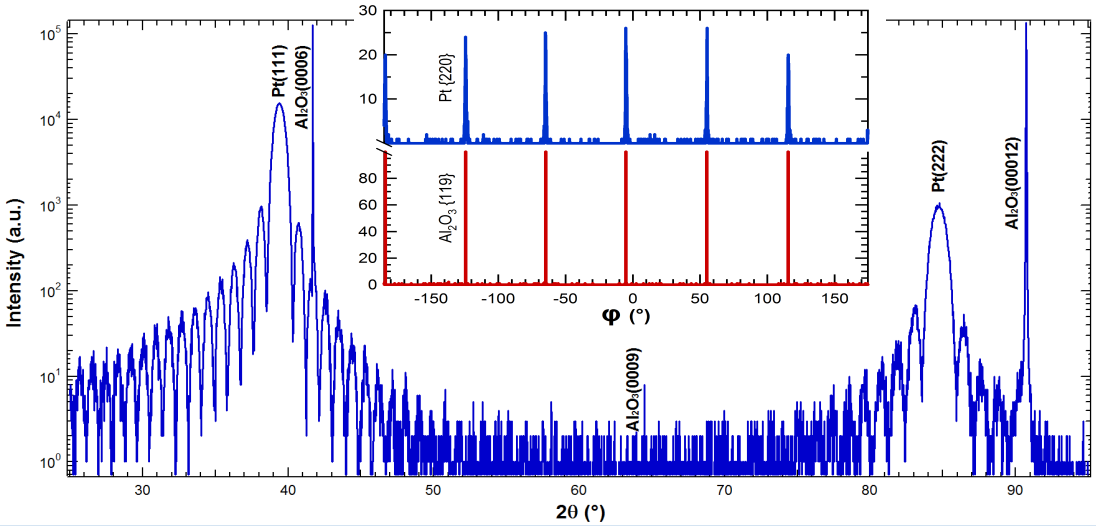

Figure 3.4 – HRXRD $2\vartheta-\omega$ scan of the 10 nm Pt layer grown on Al_2O_3(0001) and the XRD φ-scans (inset) along the the reflection planes {220} (in blue) and {119} (in red) of the Pt film and the substrate respectively.

Evolution of the buffer layer surface upon annealing: XPS, Auger and nano-SEM characterization

After the buffer layer growth, the samples will be exposed to high temperatures: > 800°C during the preparation of the $SrTiO_3$ film (see section 3.4) and ∼ 1000°C during the heat treatment necessary to obtain an UTOx (see Chap.1). Therefore, a study of the behaviour of the buffer layer at high annealing temperatures seemed pertinent. Specifically, we would like to see if a dewetting of the buffer layer occurs when annealing at high temperatures. Guaranteeing an homogeneous buffer layer, completely covering the substrate surface is important in order to provide a continuous metal film where the oxide will be deposited afterwards. Nano SAM and AES characterizations were performed (in the SCAN platform. See Chap.2) in order to identify the possible chemical changes on the surface when annealing. If the Pt buffer layer dewets, O peaks and Al peaks coming from the Al_2O_3 substrate should be observed in the spectra recorded after annealing.

One sample was removed from UHV, detached from the sample holder, then cleaned from the excess of silver paint and afterwards fixed on an Omicron plate using Ta wires. Samples were introduced in the preparation chamber of the SCAN platform under a pressure of about 1×10^{-10}mbar.

Fig.3.5 shows from bottom to top, the SEM images of the Pt/α-Al_2O_3(0001) surface in the as loaded state and after annealing at various temperatures up to 690°C (T_{Pyro}). The beam energy and current used for each image is indicated, as well as

the magnification factor. Blue arrows specify the zone where the subsequent image comes from. Red images at 600°C and at 690°C, correspond to the SEM images where Auger spectra were obtained. Two close areas where selected (denoted by the blues squares A1, A2, A3 and A4) in order to compare the chemical composition inside and outside an observed defect. Images and AES measurements were performed at an initial pressure of 4.2×10^{-11}mbar and at 3×10^{-9}mbar for higher temperatures.

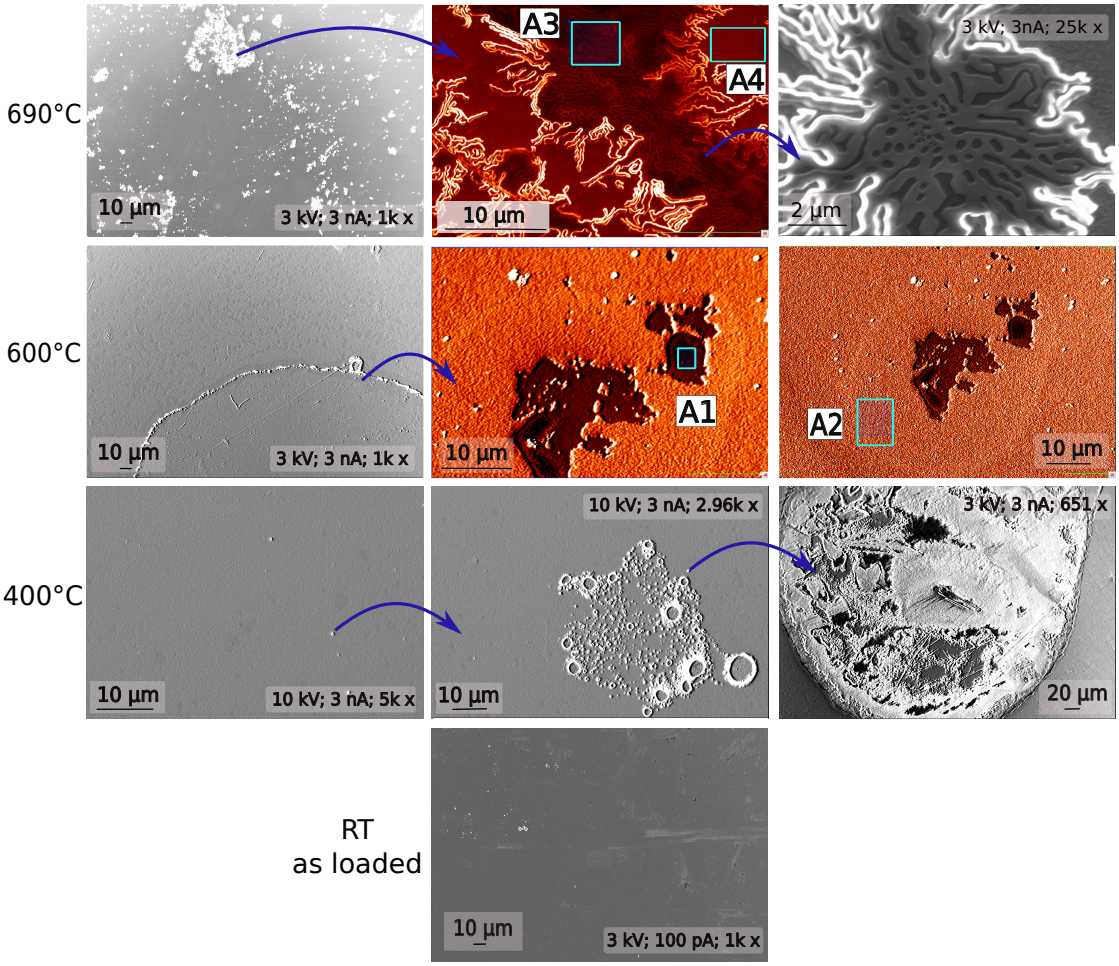

Figure 3.5 – SEM images of the Pt layer growth on α-Al_2O_3(0001) at different temperatures. Electron beam energy and current are indicated followed by the magnification power in each image. Blue arrows specify the zone of magnification of the subsequent image. Red images correspond to the SEM images where AES was performed. Blue squares mark the area of AES measurement denoted by A1 (inside a defect), A2(outside a defect), A3(inside a defect) and A4 (outside a defect).

SEM images at lower magnification were taken on different, random zones on

the surface (only one representative image is presented here). At RT, measurements reveal an homogeneous topography of the surface with some defects evidenced in lighter grey. When annealing at 400°C, surface morphology remains smooth and homogeneous. A few defects can be detected. At higher annealing temperatures, the defect density increases slightly. A few examples are shown in Fig. 3.5. At higher annealing temperatures (690°C) the number of defects increase on the surface, although they seem concentrated in clusters surrounded by smooth zones. Defaults adopt a special morphology evidenced at higher magnification as shown in Fig. 3.5.

Surface element composition at RT, and after annealing at 400°C, 600°C and 690°C corresponding to the SEM characterization in Fig. 3.5 is presented in the AES spectra in Fig. 3.6. Measurements at RT and after annealing at 400°C were performed on a surface averaged mode. On the other hand, spectra at 600°C and 690°C were obtained from measurements on two specific zones (A1 and A2 at 600°C; A3 and A4 at 690°C) as mentioned previously.

At RT, a peak at 69 eV evidences the presence of Pt on the surface. A strong peak of C at 273 eV is also observed coming from surface contamination through the air transfer. At 400°C Pt and C peaks are identified with a shift of 9 eV and 7 eV to smaller energies respectively due to charge effects. A small peak around 505 eV can be observed attributed to O. After annealing at 600°C AES on zones specified as A1 and A2 in Fig.3.5 show different composition. Inside the defect, A1 in Fig.3.5, there is a clear presence of O and C. No peak of Pt is detected (expected at 68 eV [20]) while a less intense peak detected at 55 eV could be attributed to oxidized Al (which is expected at 51 eV for Al in Al_2O_3 [20]). Outside the defect, A2 in Fig.3.5, no peak of O is visible, instead the Pt peak at 60 eV is clear along with a smaller C peak meaning that at 600°C C is not completely desorbed. These differences in both spectra is a signal of a dewetting of Pt at a particular zone of the surface. At 690°C AES inside the feature, A3 in Fig.3.5, shows still the presence of C on the surface accompanying the Pt peak at 70 eV. Outside the feature, A4 in Fig.3.5, no C peak is detected at all, while an O peak is present at 507 eV along with a modified Pt peak at 70 eV. Shapes of peaks at lower energies change, possible due to the detection of less intense Al peaks (at 51 eV and 35 eV for Al in Al_2O_3 [20]) that could overlap the main Pt peak coming from remaining Pt on that specific zone. The presence of O for certain zones in addition to the absence or modified Pt peak could correspond to bare zones of Al_2O_3, where Pt dewetted partially the substrate.

In summary, annealing the 10 nm Pt(111) film deposited on α-Al_2O_3(0001) at temperatures above 600°C (T_{Pyro}) could lead to a localized dewetting of the film, but most of the surface area remains covered by the Pt buffer layer which we believe is acceptable for the subsequent deposition of $SrTiO_3$ thin films and the obtention of UTOx/metal phases by high temperature annealing.

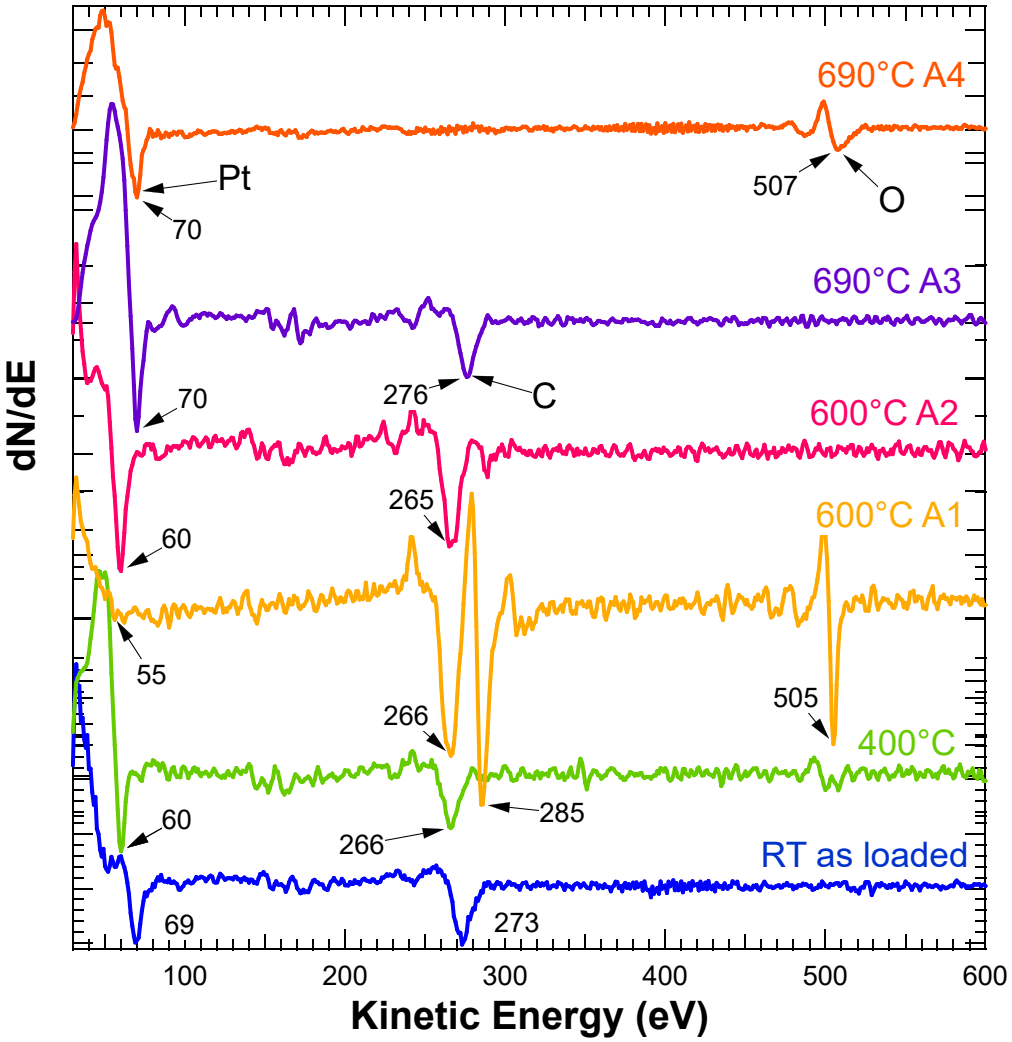

Figure 3.6 – Auger spectra of the Pt(111)/α-Al_2O_3(0001) as loaded and after annealing at the indicated intermediate temperatures up to 960°C (bichromatic measurement). Spectra at 600° and 690°C were performed on specific areas A1, A2, A3 and A4 marked in Fig.3.5. Excitation energy: 3 keV

3.3 Growth of Ti/Pt(111) buffer layer on α-Al_2O_3(0001)

One of the goals at this stage of the project, as it was mentioned previously, was to grow an ultra-thin, smooth, well (111)-oriented $SrTiO_3$ film on Pt(111). Our first attempts lead to a rough oxide film with a mixture of orientations, as it will be discuss in the next section (Sec. 3.4). For that reason we looked for a way to favour the (111)-orientation of $SrTiO_3$ thin films. Literature shows that an additional Ti layer between 1 and 3 nm before or after Pt growth on α-Al_2O_3(0001), promotes (111)-orientated $SrTiO_3$ films when grown on Pt(111) by dc sputtering [21] or by ion beam sputter deposition (IBSD) method [22]. It has been suggested that either the formation of a Pt–Ti intermetallic or a TiO_2 on the Pt surface provide a templating layer for (111) epitaxial perovskite growth [21, 22, 23].

Fig.3.7 shows the schematics of the Ti hexagonal close package crystal structure. The distance between atoms on the basal plane is 2.95 Å (only 4.7% larger than Pt(111) in plane lattice parameter).

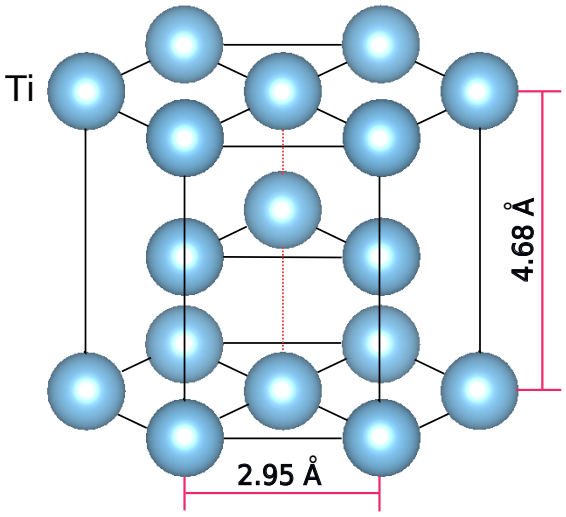

Figure 3.7 – Schematics of the *hcp* crystal structure of Ti

3.3.1 1 nm of Ti grown on Pt(111)/Al_2O_3(0001) by MBE

After epitaxial growth of Pt(111) on the Al_2O_3(0001) substrate, the sample was transferred under vacuum ($\sim 10^{-10}$mbar) to a second MBE system interconnected to the TUBE (see Chap.2). 1 nm of Ti was deposited at RT under UHV conditions. Two batches of samples were made depending on the availability of Ti in the MBE chambers connected to the TUBE. For the first batch, Pt and Ti were grown in two dis-

tinct chambers meaning a UHV transfer was necessary. For the second batch, Pt and Ti were deposited subsequently in the same chamber. Both were grown with a pressure of 10^{-9}mbar during deposition. Fig.3.8 shows the RHEED patterns of the Al_2O_3(0001) substrate at RT in the $Al_2O_3[11\bar{2}0]$ and $Al_2O_3[10\bar{1}0]$ directions after degassing, followed by the RHEED patterns in the Pt$[\bar{1}21]$ and Pt$[01\bar{1}]$ directions of the Pt film after cooling at RT and the Ti just after deposition at RT as well. These last show a blurred streaky pattern, reflecting lower surface quality and more roughness than the as-grown Pt layer. In addition, intermediate diffraction rods in the Pt$[\bar{1}21]$ direction are observed as marked by the blue arrows.

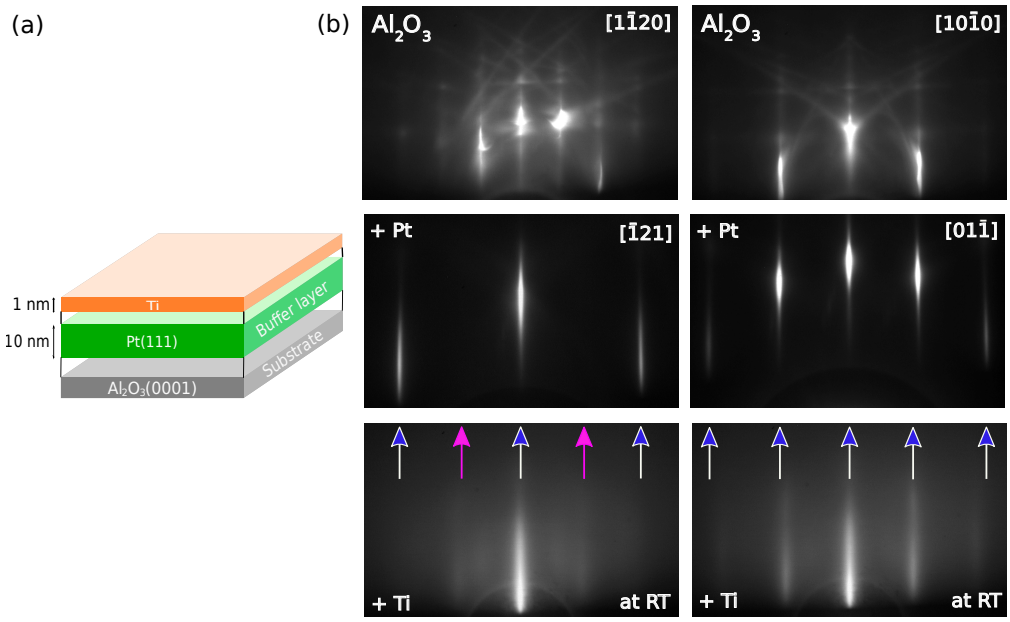

Figure 3.8 – (a) Schematics of the film stacking with the additional 1 nm of Ti. (b) RHEED patterns of the Al_2O_3(0001) substrate (top), the 10 nm Pt(111) buffer layer (middle) and the 1 nm additional Ti layer as-deposited at RT (bottom). The blue and magenta arrows indicate the expected and the extra diffraction streaks after Ti deposition respectively. All patterns were taken at RT

As mentioned previously, samples will be exposed to high temperatures (> 800°C during the preparation of the $SrTiO_3$ and ~ 1000°C (T_{Pyro}) during the heat treatment necessary to obtain an UTOx), therefore, we performed a study of the compositional and structural changes of the Ti/Pt(111) buffer layer when temperature increases. Specifically, we would like to know if the interdiffusion of Ti into the Pt layer leads to the formation of an intermetallic phase [23, 24]. The next sections of this chapter are dedicated to the study of the chemical and the structure evolution of the Ti/Pt(111) buffer layer upon annealing.

3.3.1.1 Chemical evolution of the buffer layer upon annealing

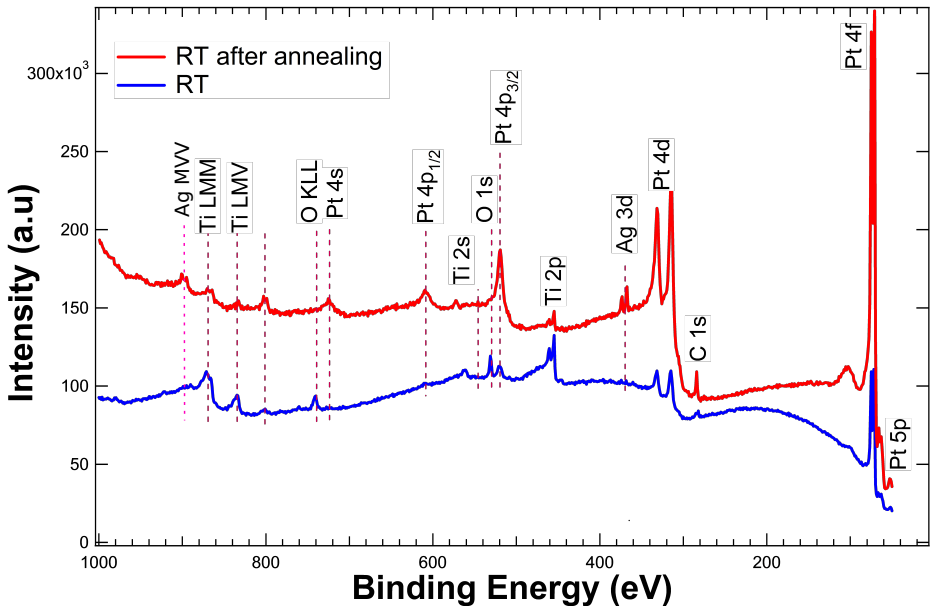

Figure 3.9 – XPS survey spectra (Mg K_α) at RT (in blue) and after annealing at 500°C (Th measured, in red) of the Ti/Pt buffer layer.

Samples were transferred to the XPS chamber connected to the TUBE where they were annealed and characterized *in situ*. Fig.3.9 shows the XPS survey spectra (Mg K_α source) of the Ti(1 nm)/Pt(10 nm) buffer layer before and after annealing at 500°C (T_{Th}) in UHV (the highest temperature that can be achieved in the XPS chamber). At RT a small C 1s is present, along with O 1s indicating contamination on the sample surface. This could be explained by the fact that the sample was stored for a couple of days at a pressure of 4×10^{-9}mbar. This delay before XPS characterization can be justified by the unavailability of the instrument just after sample preparation. Characteristic peaks from Ti and Pt are well identified. After annealing, Pt peaks are more intense compared with the Ti peaks. This indicates intermixing between the Ti layer and the Pt buffer. C 1s peak is more visible, along with Ag 3d peaks coming from the silver paint residuals surrounding the sample. No O peak was detected. The reduction in the intensity of the Ti 2p and the O 1s peaks, as well as the increasing of the Pt 4d peaks will be discussed as follows.

The binding energies of Ti 2p, Pt 4d and O 1s+Pt $4p_{3/2}$ core levels were measured *in situ* by XPS before and after annealing at 500°C. Fig.3.10 (a) shows the Ti 2p XPS spectra before annealing. A peak at 454.1 eV, assigned to Ti $2p_{3/2}$, with its spin doublet at 460.1 eV, assigned to Ti $2p_{1/2}$, separated by 6 eV, indicates that Ti is in a metallic phase [25]. The Pt 4d spin doublet is shown as well in Fig.3.10 (b). The

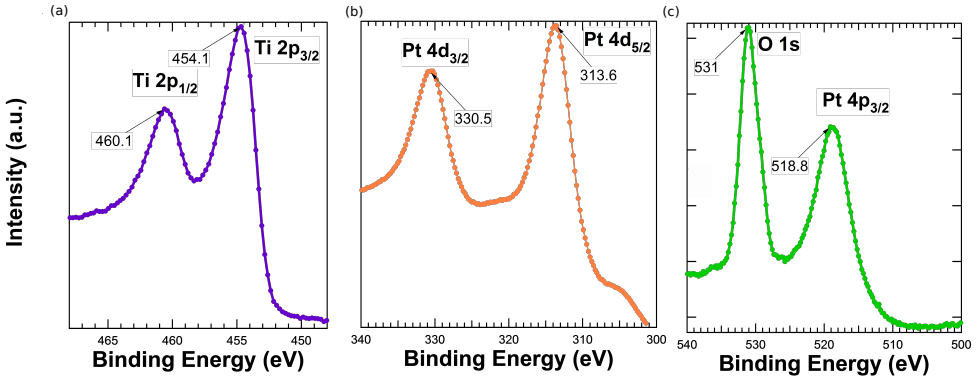

Figure 3.10 – XPS spectra at RT for (a) Ti 2p, (b) Pt 4d and (c) O 1s + Pt $4p_{3/2}$ core levels of the Ti/Pt buffer layer after growth.

Pt $4d_{3/2}$ and Pt $4d_{5/2}$ peaks are detected at 330.5 eV and at 313.6 eV respectively. This values are shifted by around 2 eV to lower binding energies with respect the values reported in ref. [26] for metallic Pt. Typical O 1s peak [26] at 531 eV is detected next to the Pt $4p_{3/2}$ peak at 518.8 eV respectively. As the binding energy of TiO_2 is 531 eV and Ti is still in metallic state, we can conclude that oxygen comes from contamination and adsorbs on the surface.

Fig.3.11 shows the XPS spectra at different temperatures, from RT up to 500°C (T_{Th}) for the previously described core levels. Fig.3.11(a) reveals no considerable shift in the binding energies of the Ti $2p_{3/2}$ and the Ti $2p_{1/2}$ peaks after annealing, suggesting that Ti remains in a metallic state. Nevertheless, the peaks intensity has considerably decreased during annealing, along with the intensity of the O 1s peak presented in Fig.3.11(c). At 450°C almost no oxygen is present at the surface, indicating that oxygen desorbs the surface upon annealing. On the other hand, the intensity of Pt 4d (Fig.3.11(b)) and the Pt $4p_{3/2}$ has increased with annealing. Fig3.12 displays the relation between the peak area of Ti $2p_{3/2}$ and Pt $4d_{3/2}$ with respect temperature. At temperatures higher than 250°C an interdiffusion process of Ti in Pt is evident.

Our results are in agreement with the literature, where interdiffusion of Ti in Pt has been observed at temperatures close to 400°C [27]. Moreover, other studies have shown that annealing a Ti/Pt film at temperatures up to 500°C (and higher), a formation of a Pt_3Ti or Pt_8Ti alloy could occur evidenced by a shift in the Ti 2p peaks to higher binding energies (of about 1.3 eV [24, 28] or 0.4 and 0.5 eV [29]). Fig. 3.11 exhibit small shifts to higher binding energies after annealing for the Ti 2p, Pt4d and Pt $4p_{3/2}$ core levels. However, the resolution of our data does not allow us to determine a exact value of the shift or a fit where the formation of a Ti-Pt surface alloy could be evidenced.

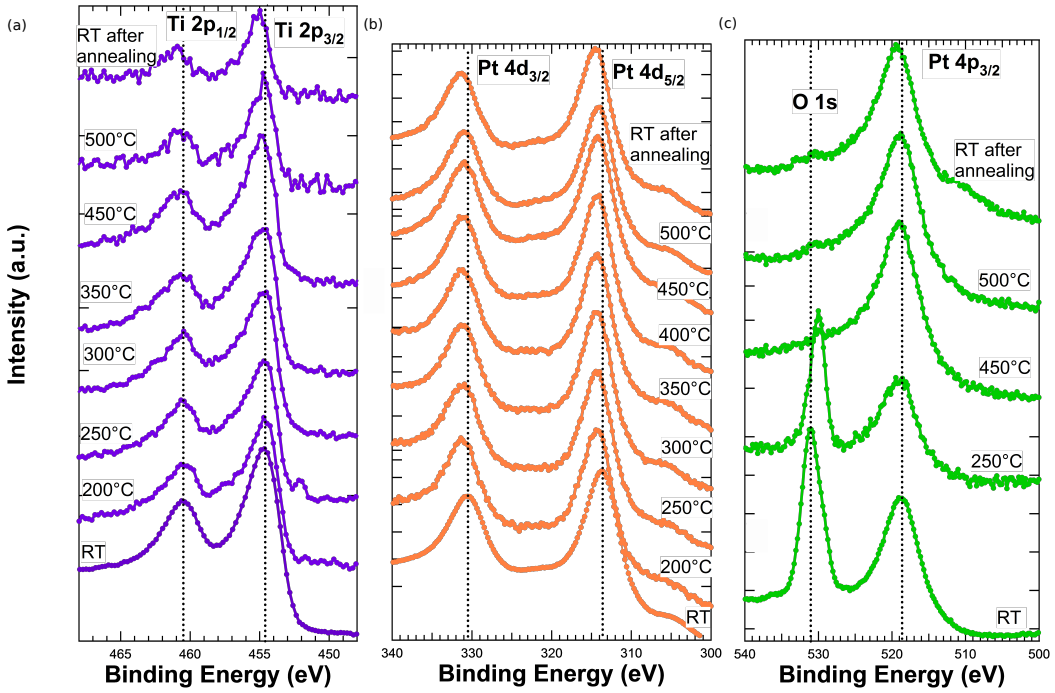

Figure 3.11 – XPS spectra at different annealing temperatures of the (a) Ti 2p, (b) Pt 4d and (c) O 1s + Pt $4p_{3/2}$ core levels.

To verify the idea of a possible formation of a Ti-Pt alloy after annealing other studies were performed as it will be discussed in the following of this chapter.

3.3.1.2 Structural evolution of the buffer layer upon annealing

RHEED patterns along the Pt[$\bar{1}$21] and Pt[01$\bar{1}$] directions were taken during annealing of the Ti/Pt buffer layer (sample architecture presented in Fig.3.13 (b)(top)). Fig. 3.13 (a) shows the diffraction patterns from the Pt layer at RT (top) followed by the patterns corresponding to the as-grown Ti film at RT, and after annealing at different temperatures up to 1050°C (T_{Th} equivalent to 875°C T_{Pyro}). RHEED patterns just after Ti deposition evidence low surface quality (blurred pattern and unsharpened streaks), specially in the Pt[$\bar{1}$21] direction. The position of the Pt diffraction streaks are indicated by the blue arrows. During annealing, patterns exhibit sharper elongated streaks repeated every 60° confirming a 6-fold surface symmetry of the epitaxial Pt thin film. Additional diffraction streaks are present (indicated by the magenta arrows) as confirmed by the line profiles in Fig.3.13 (b) (bottom) clearly visible in both directions at temperatures between 530°C and 820°C. After further annealing an improvement of the surface crystallinity of the Ti/Pt layer is observed, leading to very sharp diffraction patterns. Besides, the additional diffraction streaks are not

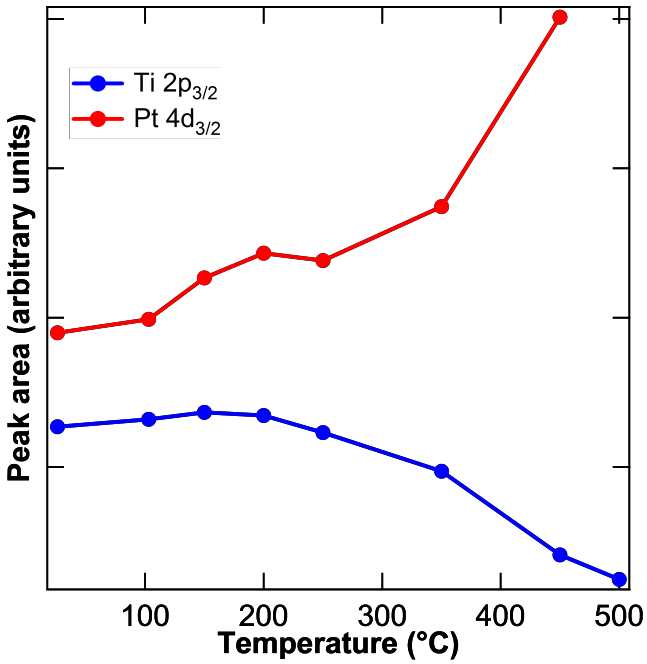

Figure 3.12 – Peak area of the Ti $2p_{3/2}$ (blue) and Pt $4d_{3/2}$ (red) in function of the annealing temperature.

present after 900°C leading only streaks at the same position of the initial Pt surface diffraction pattern as indicated by the blue arrows. These could be explained by the possible formation of a Pt-Ti alloy during annealing which modifies the surface structure. Then, when the temperature increases, Ti interdiffuses deeper into the Pt layer in a solid solution, showing up again a diffraction pattern very close to the initial one (confirmed by the line patterns in red in Fig. 3.13 (b)).

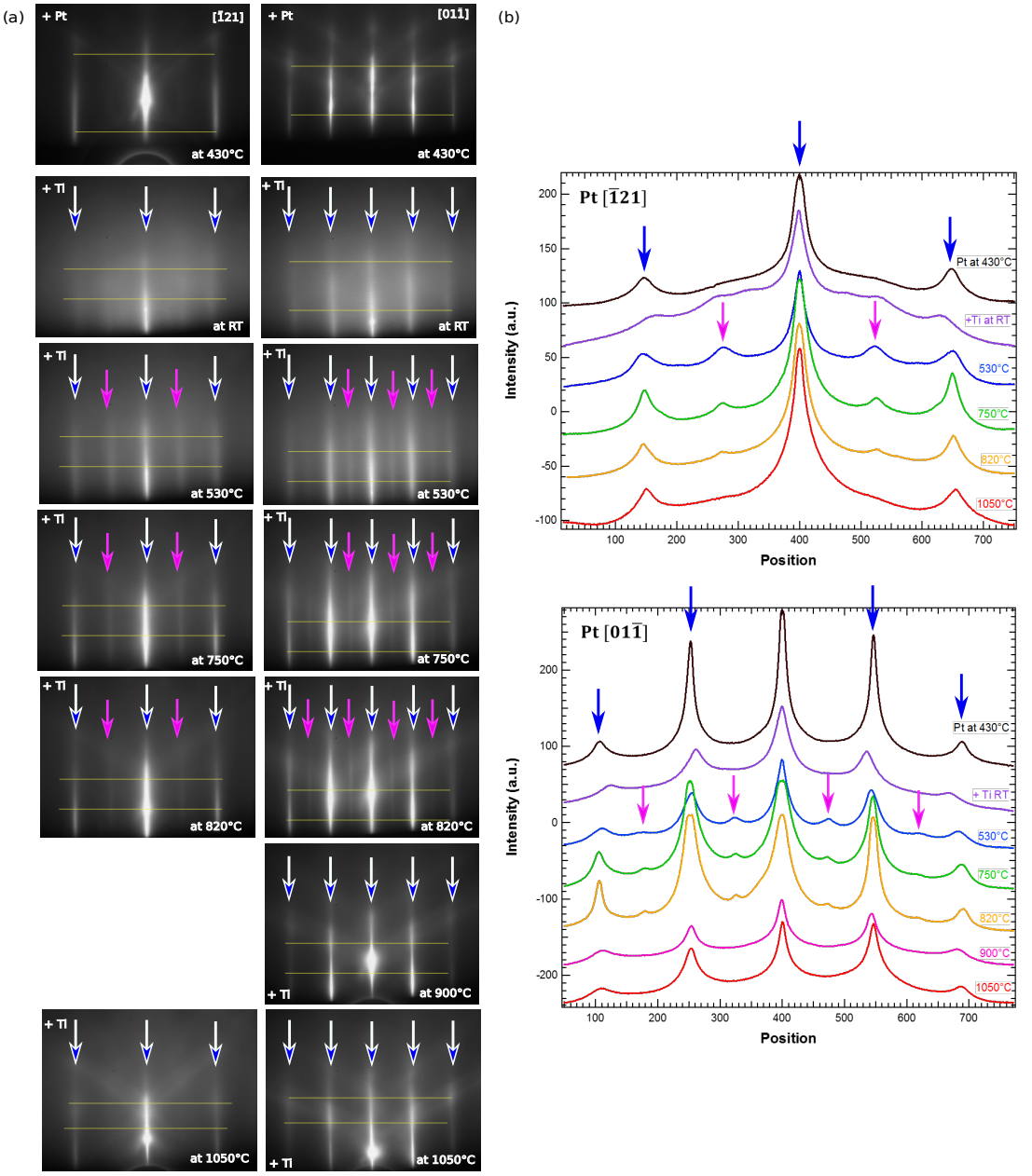

Figure 3.13 – (a) RHEED patterns of the (1nm)Ti/Pt(111)(10 nm) buffer layer as a function of the annealing temperature. The blue arrows indicate the expected diffraction streaks following the Pt diffraction pattern. The magenta arrows indicate the additional streaks observed after Ti deposition at RT and during annealing up to 900°C. (b) The line profiles of the RHEED patterns in (a) along the yellow line.

HRXRD 2ϑ scan presented in Fig.3.14 shows the strong (111) and (222) reflections of Pt along with the substrate 000m reflections. The Laue oscillations are clearly observed on both sides of the Pt (111) peak indicating high crystallinity after the deposition and subsequent annealing of the Ti/Pt(111) buffer layer. Inside the circle in blue, the fit function of the Pt(111) peak is shown. The fit was done using a pseudo-Voigt function considering the Laue oscillations. This fit help us to determine the diffraction angle of the scanned buffer layers. Thus, the spacing between the planes (d_{111}) can be calculated from the Bragg's law :

$$n\lambda = 2d\sin\vartheta \tag{3.1}$$

where n is the diffraction order, λ is the X-ray wavelength (1.54 Å Cu K_α radiation), d is the inter-plane spacing and ϑ is the diffraction angle. Therefore, the lattice parameter (a) can be deduced from the spacing relation of a cubic system, given by:

$$d_{hkl} = \frac{a}{\sqrt{h^2+k^2+l^2}} \tag{3.2}$$

where hkl are the Miller index. Then, the structure information of the Pt and the Ti/Pt buffer layer can be obtained and compared as summarized in Table 3.1. The lattice parameter of the buffer layer slightly decreases after the Ti addition on Pt and its subsequent annealing in UHV (about 0.23% and 1.26%) respectively. After annealing, the resulting thin film exhibits reduced lattice parameter in comparison with the one of pure Pt(111). This could favour the $SrTiO_3$(111) epitaxial deposition due to a smaller lattice mismatch. As a result, the 0.4% lattice mismatch between $SrTiO_3$ and Pt reduces to 0.1% for $SrTiO_3$ on the annealed Ti/Pt film.

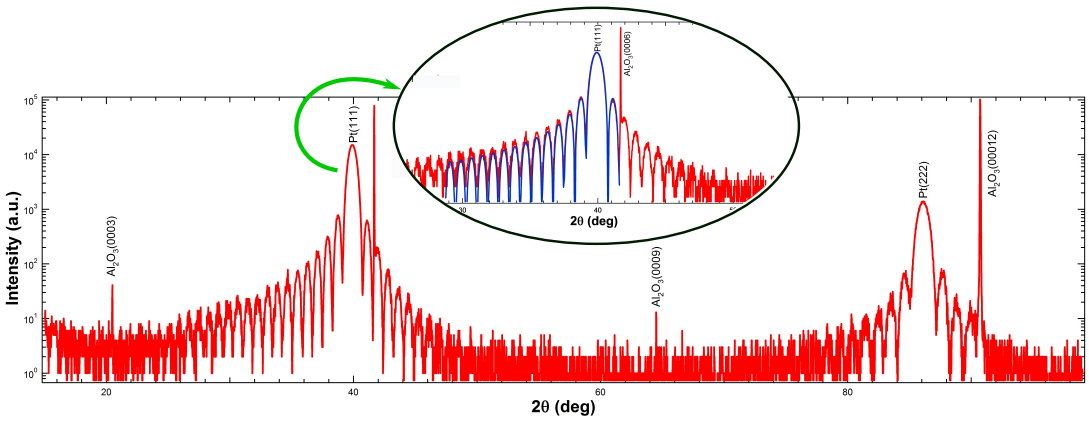

Figure 3.14 – HRXRD 2ϑ – ω scan of the Ti(1 nm)/Pt(10 nm) buffer layer grown on Al_2O_3(0001) after annealing at 630°C. The Pt(111) peak fit considering the Laue oscillations is highlighted in blue (inset figure).

A shift to higher diffraction angles is observed after the deposition of 1 nm of Ti and its subsequent annealing as shown in the HRXRD scans in Fig.3.15. Three different samples were prepared under the same conditions (Pt and Ti growth at 400°C and RT respectively). From bottom to top, the diffractograms in Fig. 3.15 show the structure evolution of the buffer layer starting with the scan corresponding to the Pt film (in blue), then the scan of the Ti/Pt film (in green) and finally,the scan of the Ti/Pt film annealed at 600°C (T_h) in UHV. The strong Pt(111) reflections are clear along with the (0006) reflections of the substrate. Comparing the Pt(111) peaks of the three samples, a shift of about 0.1° and 0.5° to higher diffraction angles is observed for the Ti/Pt and the Ti/Pt annealed film respectively, comparing with the Pt film. These shifts could indicate the formation of a Ti/Pt alloy as reported by Weng *et al.* [29]. Besides, Chen *et al.* found a lattice parameter of 3.906 Å for a Pt_3Ti alloy [30], very close to our deduced lattice parameter value after annealing of 3.908 ± 0.0002 Å (see Table 3.1) suggesting as well, the possible formation of a Pt-Ti alloy.

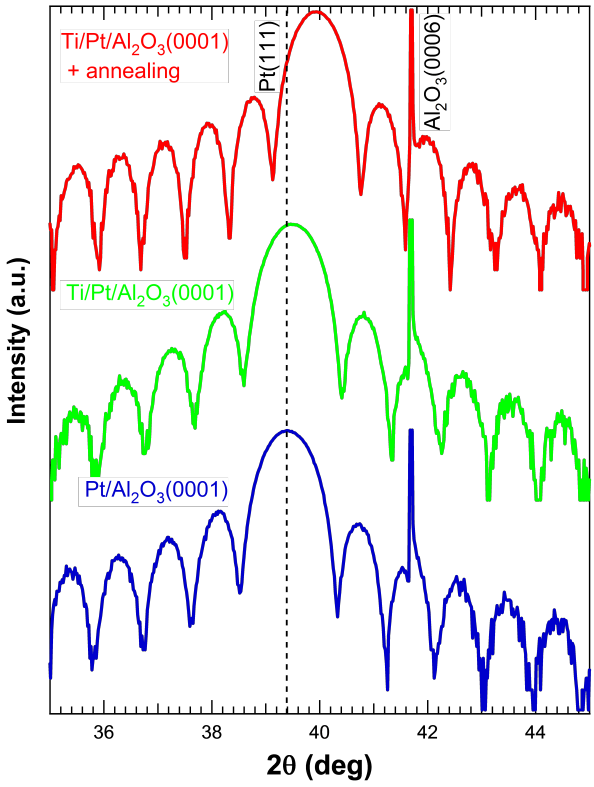

Figure 3.15 – HRXRD $2\vartheta-\omega$ scans of the 10 nm Pt(111) buffer layer (blue); the buffer layer with an additional nm of Ti (green); and the Ti/Pt(111) buffer layer annealed at 630°C (T_h) in UHV (red).

Structure information of the Ti/Pt buffer layer				
	2ϑ [°]	d_{111} [Å]	a [Å]	thickness [Å]
Pt	39.397±0.0046	2.285±4.54 × 10^{-5}	3.958±7.86 × 10^{-5}	105.123±0.002
Ti/Pt	39.489±0.005	2.280±0.001	3.949±0.002	102.607±0.040
Ti/Pt annealed	39.925±0.0002	2.256±0.0001	3.908±0.0002	115.069±0.006

Table 3.1 – Structure information of the Ti/Pt buffer layer based on HRXRD measurements of Fig.3.15.

3.4 $SrTiO_3$ thin films deposited on Pt(111) by PLD

3.4.1 Crystal structure and epitaxial relationships:state of the art

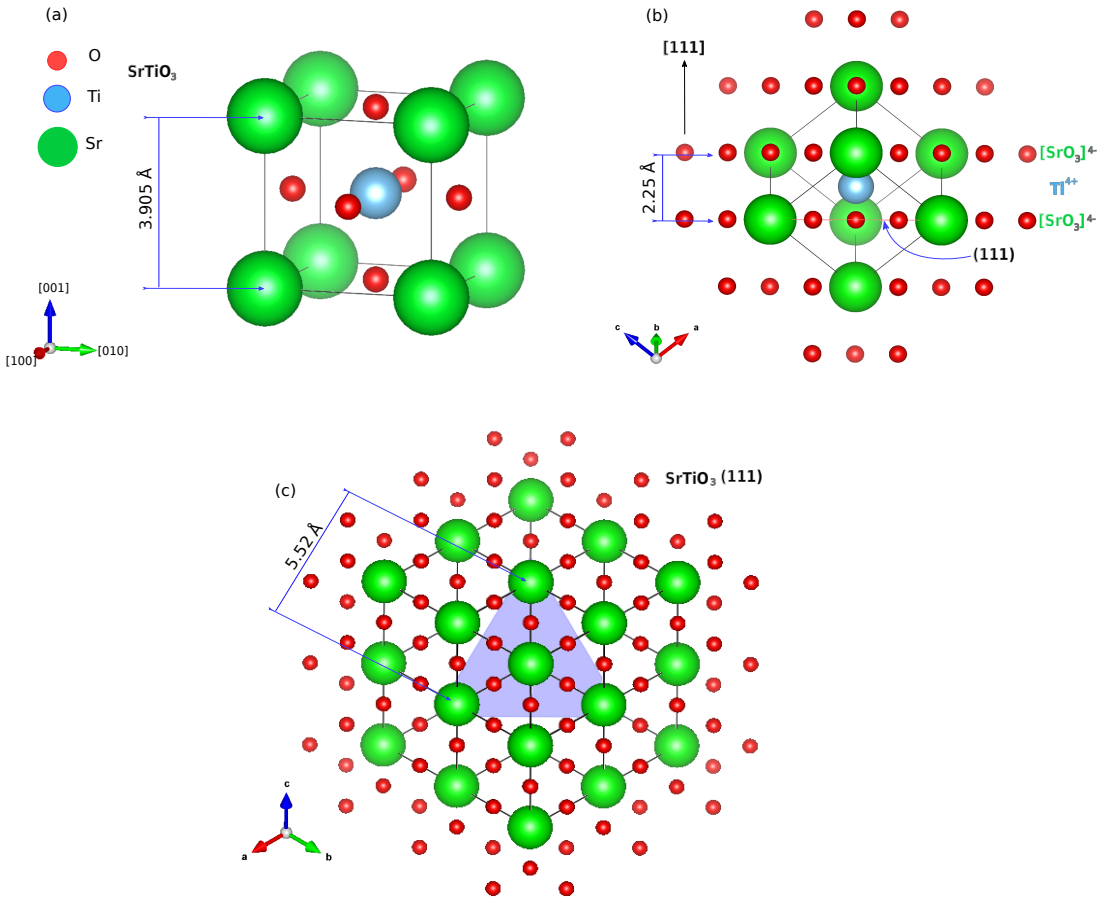

Figure 3.16 – (a) Schematic representation of the $SrTiO_3$ cubic perovskite crystal structure. (b) The $SrTiO_3$ unit cell [111]-oriented. (c) Top view of the (111) plane.

$SrTiO_3$ is a ternary complex oxide with a cubic perovskite crystal structure with a lattice parameter of 3.905 Å as represented in Fig.3.16 (a). Fig.3.16(b) represents the $SrTiO_3$ unit cell [111]-oriented, showing the stacking of the $(SrO_3)^{4-}$ and the Ti^{4+} planes. The adjacent $(SrO_3)^{4-}$ or Ti^{4+} planes are separated by a distance of 2.25Å. Fig. 3.16(c) shows the top view of the $SrTiO_3$(111) with the in-plane hexagonal lattice parameter of 5.52Å .

As mentioned before, epitaxial $SrTiO_3$(111) films are expected to form on Pt(111) surfaces due to their small lattice mismatch (only 0.4% at RT) [21, 22]. However, the growth mechanism of thin films of $SrTiO_3$ on Pt(111) involves complex phenomena such as in- and out-of-plane strains or surface and interface surface energy anisotropies, producing a thin film growth in random orientations instead of the expected (111) orientation [18, 22, 31, 32, 33]. This mixture of orientations have been observed in deposition methods such as radio-frequency sputtering [18, 22, 21, 32, 34] metal organic deposition [35], sol-gel process [36] and PLD (deposited on MgO(001) substrates) [37].

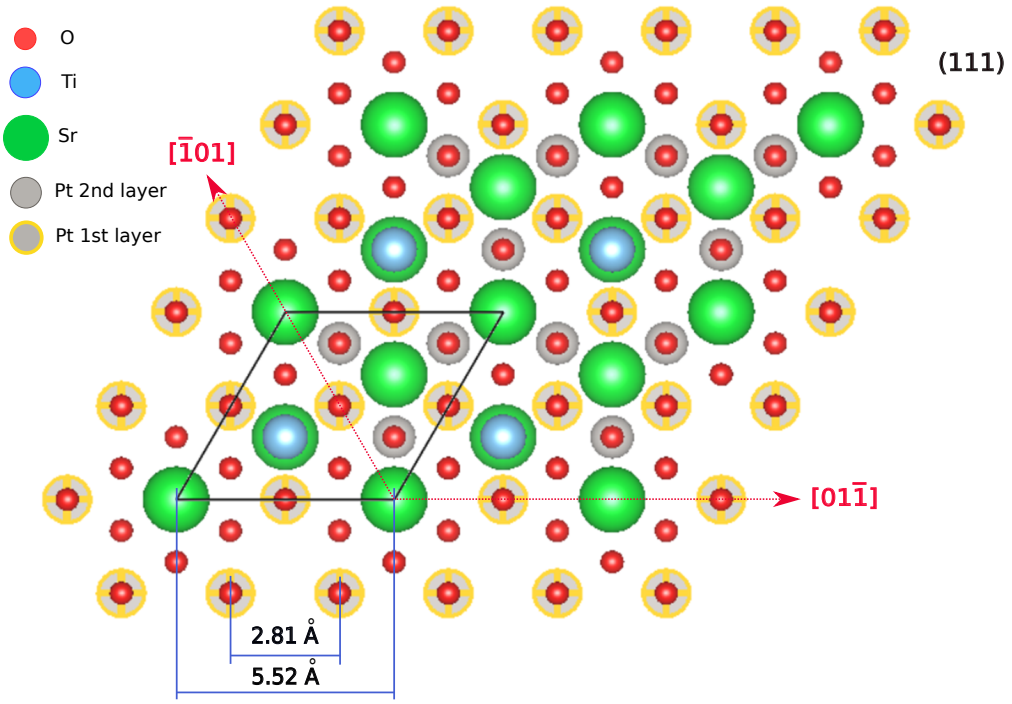

Figure 3.17 – Schematics of $SrTiO_3$ (111) on Pt(111). A SrO_3^{4-} layer is located on the first Pt layer (gray spots contoured in yellow). The hexagonal unit cell is indicated in black formed by the Sr atoms posed on the Pt atoms.

Fig. 3.17 shows the schematics of a (111)-oriented $SrTiO_3$ film on a Pt(111) surface. For most of the perovskite oxides, the (111) plane has the highest surface en-

ergy in comparison with the (100) and (110) planes [32, 38], implying that (111)-oriented films (with thickness in the nm order) are difficult to grow, even though (111)-oriented $SrTiO_3$ has a good lattice match with Pt(111). The Pt[$01\bar{1}$] and Pt[$\bar{1}01$] directions are indicated in the figure as well as the in-plane Sr atoms. These ones form a structure with 3-fold symmetry with a distance between atoms of 5.52Å following the 3-fold symmetry of the Pt buffer layer (with a smaller in-plane atom separation of 2.81 Å). The reported epitaxial relations are: $SrTiO_3$(111)||Pt(111) and $SrTiO_3$[$01\bar{1}$]||Pt[$01\bar{1}$] [21] .

3.4.2 Thin films of $SrTiO_3$ on (Ti/)Pt(111) by PLD results

$SrTiO_3$ thin films of several thickness (from 4 to 300 Å) were deposited under different pressure and temperature conditions on the Pt(111) or Ti/Pt(111) surface by PLD. $SrTiO_3$ target was ablated using a KrF excimer laser (248 nm) at 1Hz pulse repetition and fluency of 0.4 J/cm^2. As a reminder for the reader, OQCs are 2D structures derived from UTOx films supported on metals [5, 6]. Therefore, the aim at this stage of the sample fabrication, is to deposit a smooth, homogeneous ultra-thin film (few atomic planes) of $SrTiO_3$ on Pt(111).

Parameters such as thickness of the film, deposition temperature and pressure, annealing after deposition and cleaning of the buffer layer surface, were modified during the PLD process in order to improve the quality of the $SrTiO_3$ film surface. The growth was monitored by RHEED.

Fig. 3.18 shows the deposition of a smooth, ultra-thin film of about 4 Å of $SrTiO_3$ on the Pt and the Ti/Pt layers surface. The deposition was performed for both cases at RT, under vacuum at 8×10^{-9} mbar. The surface was then annealed (10°C/min) at 800°C (T_{Th}, equivalent to 660°C T_{Pyro} measurement) in an oxygen atmosphere (1×10^{-6}mbar) for few minutes to recrystallize these oxide films. Fig. 3.18 (a) corresponds to the RHEED patterns of 4 Å of $SrTiO_3$ deposited on Pt(111) starting with the Pt pattern along the Pt[$01\bar{1}$] and Pt[$1\bar{2}1$] directions. After $SrTiO_3$ deposition and during annealing, the observed pattern is more blurry. The corresponding line profiles presented in Fig 3.18 (b) show less defined peaks during these stages. After cooling to RT sharper peaks are obtained coming from the elongated and sharp streaks repeated every 60°, which confirm a 6-fold smooth surface symmetry following epitaxially the Pt(111) structure. Ultra-thin films of 4 Å of $SrTiO_3$ were deposited on the Ti/Pt(111) buffer layer as well under the same conditions previously mentioned. Fig.3.18 (c) shows the characteristic RHEED pattern of the oxide film, on the Ti/Pt layer, at RT after cooling. The spotty pattern indicates that $SrTiO_3$ grows in a 3D mode. Besides additional streaks appear as highlighted by the magenta arrows (blue arrows indicate the main diffraction streaks in agreement with the film deposited on the Pt layer). This could be an insight that the resulted surface is cov-

ered by $SrTiO_3$ islands mainly (111)-oriented.

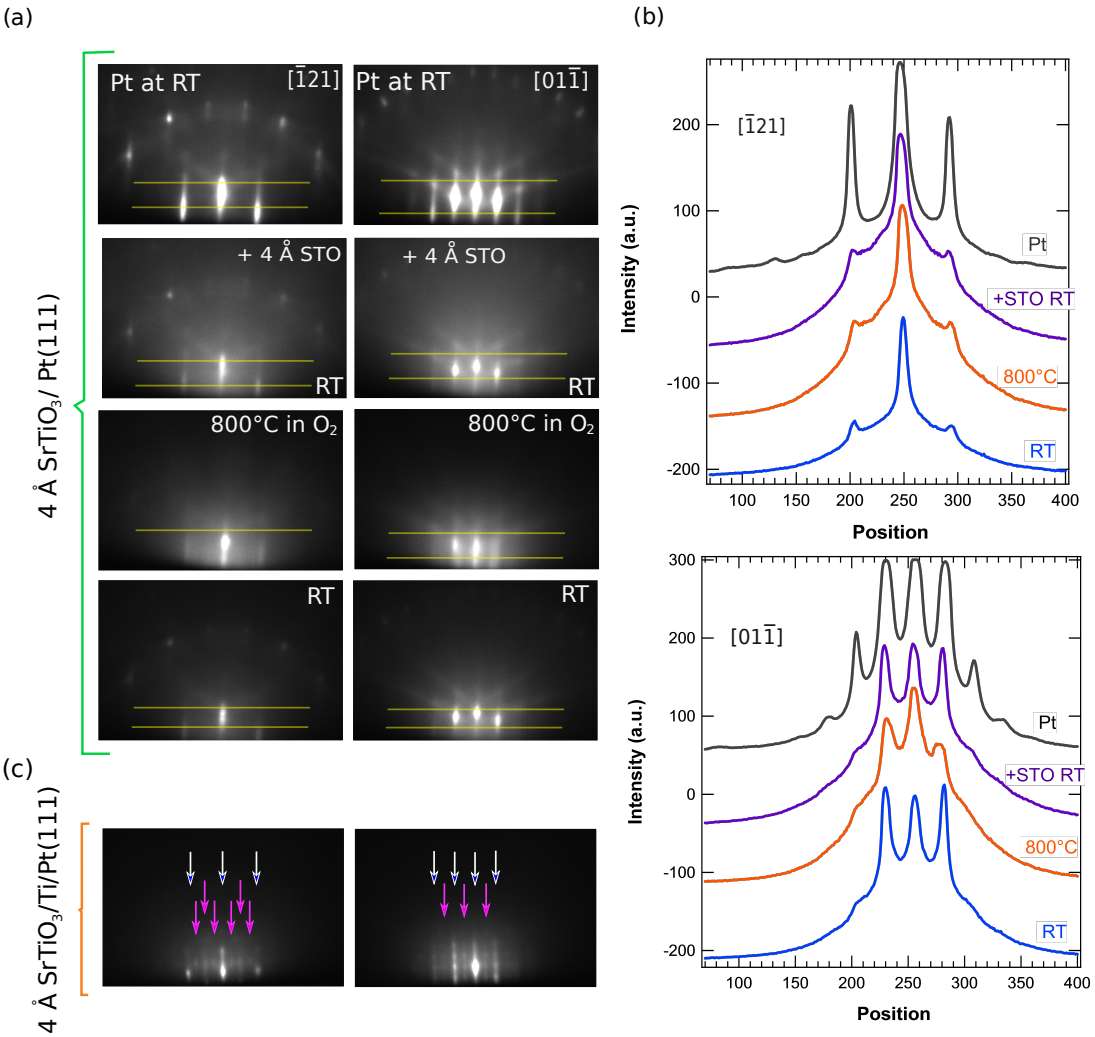

Figure 3.18 – (a) RHEED patterns of the 4Å of $SrTiO_3$ film deposited on Pt(111)/α-Al_2O_3(0001). (b) Line profiles of the RHEED patterns along the yellow lines in (a). (c) RHEED patterns of 4Å of $SrTiO_3$ film deposited on Ti/Pt(111)/α-Al_2O_3(0001). Blue arrows indicate the streaks in agreement with a (111)-oriented film; magenta arrows indicate additional observed streaks.

In order to perform structure studies, such as XRD or TEM, thicker oxide films were deposited. As mentioned previously, to preserve the (111)-orientation of $SrTiO_3$ on Pt(111) could be difficult. In addition, it was thought that the (111)-orientation of the oxide surface was important to obtain an OQC. Therefore, to favour the desired orientation, $SrTiO_3$ films of 100 Å, 20 Å, and 50 Å, were deposited on Ti/Pt(111) layers. Before the oxide deposition, the metal surfaces were annealed and monitored

by RHEED. At 600°C (T_{Th}) a smooth surface was obtained as evidenced by the sharp streaks in Fig. 3.19(a). Fig. 3.19(b) and (c) show the RHEED patterns (along a random, representative direction) of the 20 Å and 50 Å films of $SrTiO_3$ deposited at RT in UHV (10^{-9}mbar) subsequent annealed in 10^{-5} mbar of oxygen at 750°C (T_{Th}). Both RHEED patterns tend to be spotty and blurry, which means that these surfaces present larger roughness and are less well oriented than the 4 Å $SrTiO_3$ films in Fig.3.18 (a).

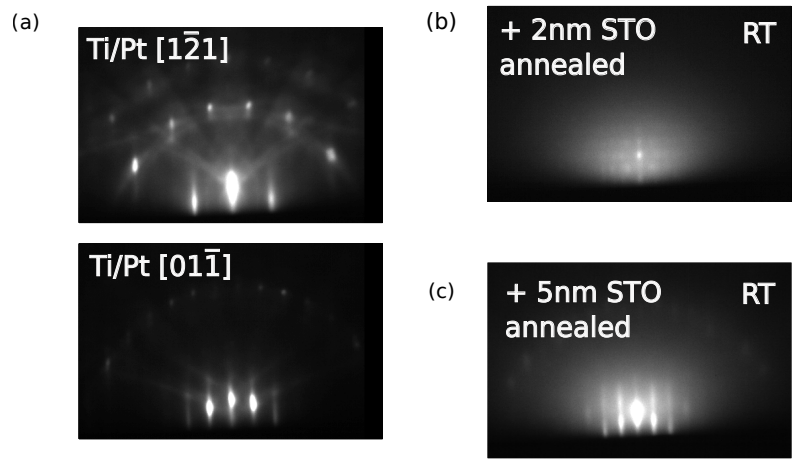

Figure 3.19 – (a) RHEED patterns of the Ti/Pt(111)/α-Al_2O_3(0001) surface, after annealing at 600°C (T_{Th}) in UHV. A smooth surface is evidenced by the sharp streaks. RHEED patterns of (b) 20 Å and (c) 50 Å $SrTiO_3$ film deposited on Ti/Pt(111).

At that point in time, thanks to a careful reading of the literature on the subject and the fruitful communications with professor Widdra's team, we learnt that (111) orientation of $SrTiO_3$ is not a prerequisite to obtain an OQC. Therefore, we decided to remove the Ti layer from the film stacking to make it as simple as possible. Nevertheless, the study on the Ti/Pt growth will probably be useful in the future. Indeed, the change of surface composition and the lattice parameter reduction may be used to epitaxially grow other oxides with a smaller in plane lattice parameter as a starting point for new OQCs. The following RHEED patterns correspond to a $SrTiO_3$ film of 8 Å grown on Pt(111) under different conditions of the samples reported so far in this section. 8 Å of $SrTiO_3$ were deposited at 800°C (Th measured, equivalent to 665°C T_{Pyro}) in an oxygen atmosphere (1×10^{-5}mbar). Fig. 3.20 shows the RHEED patterns of the clean substrate (top), after Pt growth (middle), the RHEED pattern exhibits sharp elongated streaks repeated every 60° confirming a 6-fold surface symmetry of the epitaxial Pt thin film. Blue arrows indicate the matching of the streaks after the films deposition. The spotty pattern coming from the $SrTiO_3$ film after deposition at 800°C and at RT after cooling, indicates that the ultra thin film

presents surface islands when grown on the Pt(111) surface and possible orientations different from the (111). Additional rods are observed at approximately half of the spacing of the Pt pattern, which correspond to the larger $SrTiO_3$(111) lattice parameter. Line profiles of the RHEED images help to see the change in the surface structure. A reduction in the separation of the streaks in the Pt[$\bar{1}$21] direction are evident even after cooling probably due to a mixture of orientations.

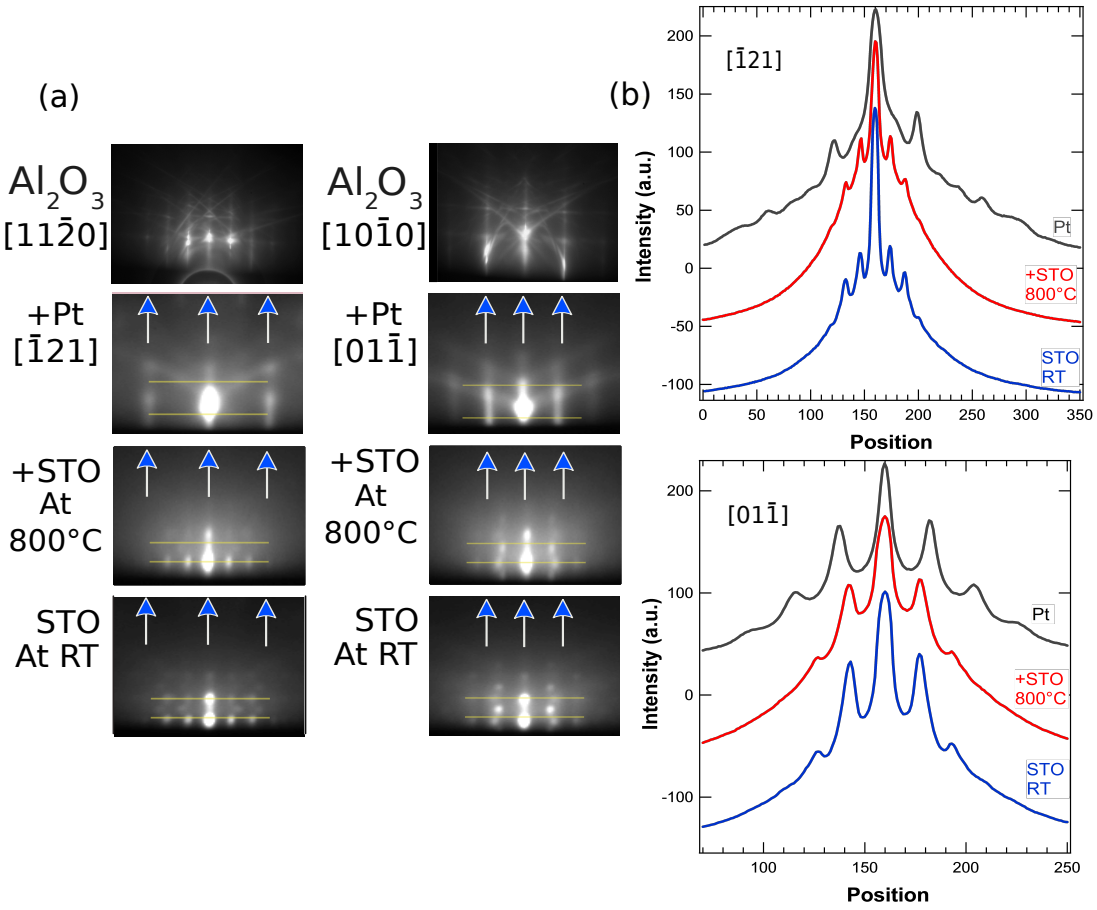

Figure 3.20 – (a) RHEED patterns of the full film stacking (from top to bottom): the clean substrate, after the deposition of 10 nm of Pt, after deposition of 8Å of $SrTiO_3$ at 800°C and of the $SrTiO_3$ film at RT. Blue arrows indicate the six-fold symmetry diffraction pattern of the Pt layer. (b) Line profiles of the RHEED patterns in (a) along the yellow lines.

In summary, we succeed in the deposition of smooth ultra-thin films of 4 Å of $SrTiO_3$ on (Ti/)Pt(111)/Al_2O_3(0001) (see Fig. 3.18). For thickness higher than 8Å the growth was observed to become 3D and probably with different orientations (not only $SrTiO_3$(111)). In the next chapter, the reader will notice that approximants and

other UTOx complex phases were observed on samples with an oxide film of 8 Å 20 Å and 50 Å (whose RHEED patterns were presented here in this section).

Besides, different oxide preparation conditions were tested, demonstrating that deposition performed at RT under UHV or at high temperature under O_2, could lead to exploitable $SrTiO_3$ surfaces where complex 2D structures could be formed.

3.5 TEM investigations

To obtain further information of the film stacking, high resolution transmission electron microscopy (HRTEM) investigations were performed in collaboration with the Jožef Stefan Institute in Slovenia.

Schmidt *et al.* investigated the interface atomic structure of epitaxial $SrTiO_3$(111) grown on Pt electrodes grown on Al_2O_3(0001) by atomic resolution high-angle annular dark field (HAADF) imaging in scanning transmission electron microscopy [21]. HAADF images showed an atomically abrupt $SrTiO_3$/Pt interface with no interfacial layers. The $SrTiO_3$ films contained two twin variants that were related by a 180° rotation about the [111] surface normal [21]. With respect to the role of Ti promoting epitaxial [111] growth, the images did not show any evidence for templating by either an interfacial TiO_2 or a Pt–Ti intermetallic layer [21].

Fig.3.21 shows a high-angle annular dark-field scanning transmission electron microscopy (HAADF-STEM) image of a thin film stacking made up of $SrTiO_3$ (10 nm)/Ti (1nm)/Pt(111) (10 nm)//Al_2O_3 (0001). The focus ion beam (FIB) lamella was cut perpendicular to the $Al_2O_3[10\bar{1}0]$ direction. The measured thickness of the buffer layer is about 12 nm and that of the $SrTiO_3$ film is 10 nm, in agreement with expected values for this particular sample. The interfaces at both Pt/Al_2O_3 and Pt/$SrTiO_3$ are relatively sharp. Due to the slight thickness difference of the projected layers along the viewing direction and the resulting variation in corresponding focal planes, the atomic structure of each layer could not be observed simultaneously in one image. Instead, atomically resolved average background subtraction filtering (ABSF-filtered) HAADF-STEM images are shown as insets on the raw image at their corresponding zone axes $Al_2O_3[10\bar{1}0]$, Pt[110] and $SrTiO_3$[110] respectively. As can be seen in the raw image, various crystalline grains are present in the $SrTiO_3$ layer, whose average grain size lies at around 15 nm. For determining the orientation relationship between the Pt and $SrTiO_3$ layers and inspecting the interface at a higher end, the STEM imaging was carried out at the interfacial region at an atomic resolution. Fig. 3.22(a) presents an atomically-resolved HAADF-STEM image of the Pt/$SrTiO_3$ interfacial region. The Pt and $SrTiO_3$ layers are viewed along the Pt[110] and $SrTiO_3$[110] zone axes, respectively. The corresponding superimposed structural models of Pt and $SrTiO_3$ are in good agreement with the underlying atomic-resolution STEM image. The atomically-sharp interface is present between the Pt

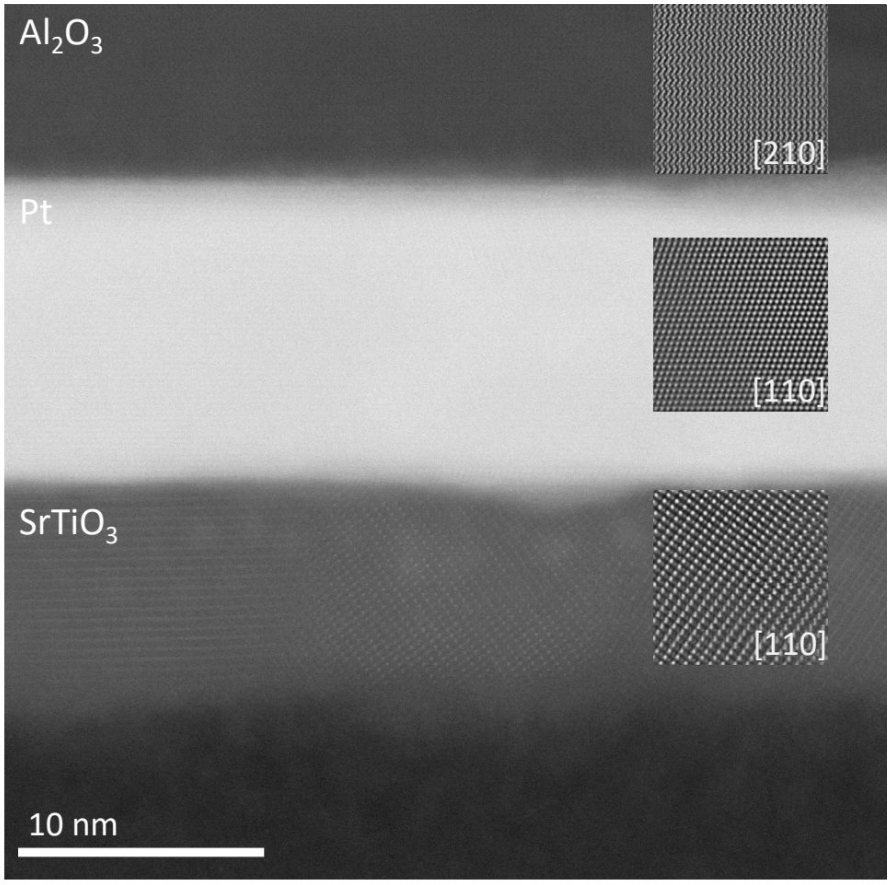

Figure 3.21 – HAADF-STEM image showing the thin film stacking consisting of Al_2O_3(0001) substrate, approx. 12 nm of Ti/Pt buffer layer and 10 nm of $SrTiO_3$. The matching atomically-resolved HAADF-STEM images are shown as inserts on the raw image at their corresponding zone axes of Al_2O_3[210], Pt[110] and $SrTiO_3$[110] respectively.

layer and the $SrTiO_3$ thin film in agreement with the investigations performed by Schmidt *et al.*[21]. The fast-Fourier transform (FFT) pattern formed from the dotted marked region on the HAADF-STEM image is shown in Fig.3.22(b). Some of the spots on the FFT pattern are assigned to the Pt and $SrTiO_3$ atomic planes. The analysis confirms that the Pt(111) lattice planes are parallel to (111)$SrTiO_3$ planes. The orientation relationship deduced from the FFT pattern is Pt(111) Pt[110] $\|$ $SrTiO_3$(111) $SrTiO_3$[110].

Fig. 3.23 presents an STEM-HAADF image presenting three layers (Al_2O_3, Pt and $SrTiO_3$), and the corresponding energy dispersive X-ray spectroscopy in STEM mode (EDXS) elemental maps of Al, O, Pt, Ti and Sr. There is a 2 nm thick Ti-rich

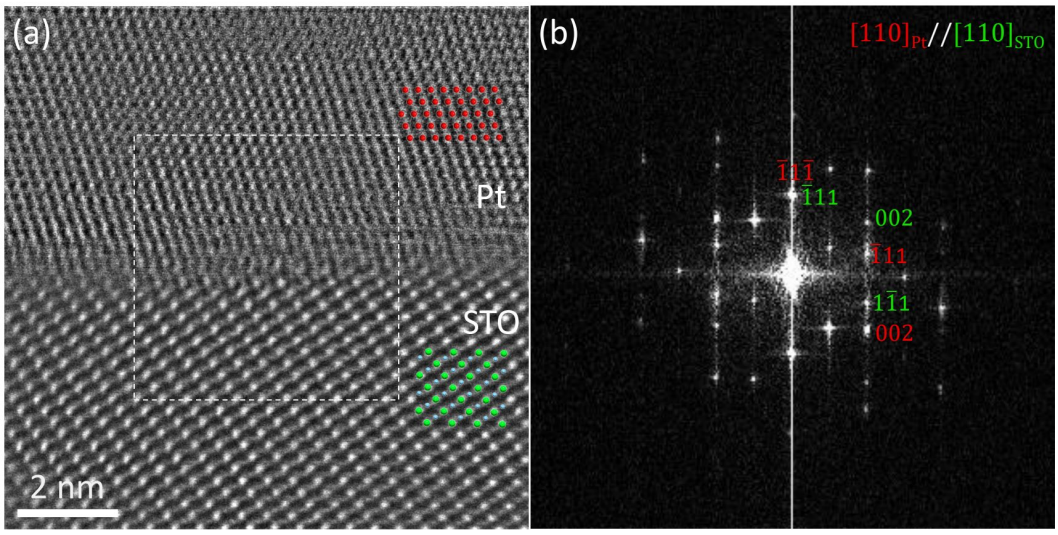

Figure 3.22 – (a) Atomically resolved ABSF-filtered HAADF-STEM image of the $Pt/SrTiO_3$ interfacial region with the superimposed structural models viewed in the Pt[110] and $SrTiO_3$[110] zone axes, respectively. Pt, Sr and Ti atoms are shown in red, green and blue, respectively. (b) The corresponding FFT pattern obtained from the marked area at (a).

layer present at the interface between Pt buffer layer and $SrTiO_3$ thin film. This Ti-rich layer is clearly distinguishable from the $SrTiO_3$ layer, since there is no Sr present at this layer, as shown by the EDXS maps. Note that the sample prepared for TEM analysis has a 10 nm Pt buffer enriched with 1 nm Ti layer on top indicating that the Ti/Pt buffer layer after annealing, forms a Pt-Ti solid solution with slightly modified lattice parameter compared to pure Pt. The observation of the Ti-rich layer indicates that this additional Ti did not intermixed homogeneously with the Pt over the whole buffer thickness. No Ti-Pt alloy is formed in agreement with Schmidt *et al.* as mentioned above [21]. As seen in the EDXS maps, the Ti-rich layer has a sharp interface with the Sr layer, which is in an agreement with the atomically-resolved HAADF-STEM image of the Pt-$SrTiO_3$ interface (Fig. 3.22 (a)).

These results lead us to conclude that annealing the Ti/Pt(111) buffer layer up to 800°C (T_{Th}) during the deposition of $SrTiO_3$ films, does not lead to the formation of a Pt-Ti compound but to a solid solution!. Nevertheless, XPS and XRD measurements suggested that chemical and structural changes occur when the Ti/Pt buffer layer was annealed, indicating the possible formation of a Pt_3Ti alloy (see Secs.3.3.1.1 and 3.3.1.2). In fact, as mentioned previously, the annealing temperature in the XPS chamber was a limitation since it is lower than the temperatures achieved in the PLD chamber. Thus, a possible explanation could be that at tem-

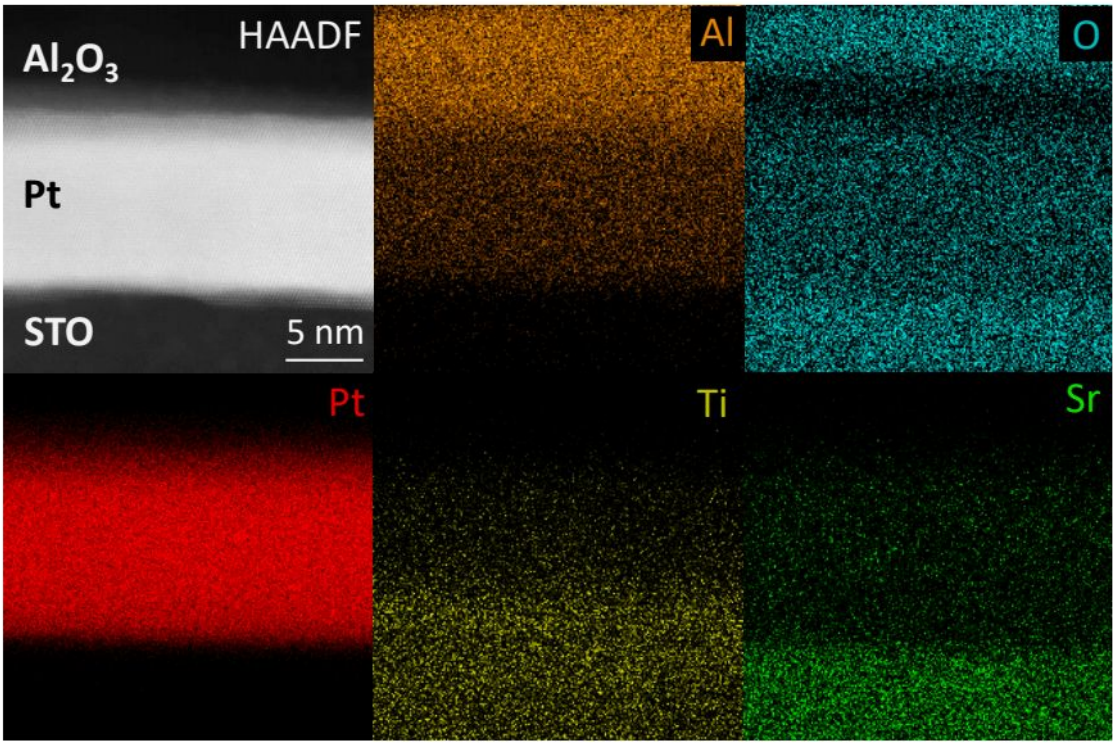

Figure 3.23 – *top left:*STEM-HAADF image presenting all three layers (Al_2O_3, Pt and $SrTiO_3$), and EDS elemental maps of Al, O, Pt, Ti and Sr.

peratures above 250°C Ti starts to interdiffuse the Pt layer. At around 500°C a Pt-Ti alloy is formed, but at further annealing, around 900°C (T_{Th}), Ti interdifuses the Pt layer as a solid solution. This could be as well, the explanation of the variation of the RHEED patterns observed for the Ti/Pt(111) buffer layer upon annealing at 1050°C presented in Fig.3.13. The additional diffraction streaks (indicated by the magenta arrows) between 530°C and 820°C could be the consequence of the formation of a transient Pt-Ti alloy. At 900°C they disappear leading a diffraction pattern with sharp streaks at the same position as the Pt pattern as expected for a solid solution.

In conclusion, ultra-thin films of $SrTiO_3$ were deposited by PLD on epitaxial Pt(111) grown on α-Al_2O_3(0001) by MBE. Some samples had an additional nanometre of Ti deposited on the top of the Pt(111) buffer layer. The film stacking was fully characterized by a combination of RHEED, XRD, XPS and HRTEM revealing that the final $SrTiO_3$ surface is rough for films with thickness $\geq$ 8Å. Concerning the behaviour of the buffer layer at high temperature, we observe that Pt dewets locally the substrate at temperatures higher than 600°C (T_{Pyro}). Besides, for the Ti/Pt buffer layers it was found that Ti interdiffuses the 10 nm Pt layer in a solid solution when annealed at temperatures above 800°C (T_{Pyro}).

Bibliography

[1] I. Vrejoiu, M. Alexe, D. Hesse, and U. Gösele. Functional Perovskites – From Epitaxial Films to Nanostructured Arrays. *Advanced Functional Materials*, 18(24):3892–3906, 2008.

[2] S. Förster and W. Widdra. Ultrathin Perovskites: From Bulk Structures to New Interface Concepts. In F. P. Netzer and A. Fortunelli, editors, *Oxide Materials at the Two-Dimensional Limit*, pages 361–380. Springer International Publishing, Cham, 2016.

[3] S. Förster, K. Meinel, K-M Schindler, and W. Widdra. Oxygen-deficient ordered phases of ultrathin $BaTiO_3$ films on Pt(111). *Surface and Interface Analysis*, 44(6):628–634, 2012.

[4] S. Förster and W. Widdra. Growth, structure, and thermal stability of epitaxial $BaTiO_3$ films on Pt(111). *Surface Science*, 604(23-24):242163–2169, 2010.

[5] S. Förster, K. Meinel, R. Hammer, M. Trautmann, and W. Widdra. Quasicrystalline structure formation in a classical crystalline thin-film system. *Nature*, 502(7470):215–218, 2013.

[6] S. Schenk, S. Förster, K. Meinel, R. Hammer, B. Leibundgut, M. Paleschke, J. Pantzer, C. Dresler, F. O. Schumann, and W. Widdra. Observation of a dodecagonal oxide quasicrystal and its complex approximant in the $SrTiO_3$-Pt(111) system. *Journal of Physics: Condensed Matter*, 29(13):134002, 2017.

[7] H. Tanaka and M. Taniguchi. Single crystalline epitaxial platinum film on Al_2O_3 (0001) prepared by oxygen-doped sputtering deposition. *Japanese Journal of Applied Physics*, 56(5):058001, 2017.

[8] A Nefedov, A Abromeit, Ch Morawe, and A Stierle. High-resolution x-ray scattering study of platinum thin films on sapphire. *Journal of Physics: Condensed Matter*, 10(4):717–730, 1998.

[9] R.F.C. Farrow, G.R. Harp, R.F. Marks, T.A. Rabedeau, M.F. Toney, D. Weller, and S.S.P. Parkin. Epitaxial growth of Pt on basal-plane sapphire: A seed film for artificially layered magnetic metal structures. *Journal of Crystal Growth*, 133(1-2):47–58, 1993.

[10] T. Tachibana, Y. Yokota, K. Kobashi, and M. Yoshimoto. Heteroepitaxial growth of (1 1 1)-oriented diamond films on platinum (1 1 1)/sapphire (0001) substrates. *Journal of Crystal Growth*, page 6, 1999.

[11] T. Suzuki, S. Hishita, K. Oyoshi, and R. Souda. Structure of α-$Al_2O_3(0001)$ surface and Ti deposited on α-$Al_2O_3(0001)$ substrate: CAICISS and RHEED study. *Surface Science*, 437(3):289–298, 1999.

[12] A. Jain, S. P. Ong, G. Hautier, W. Chen, W. D. Richards, S. Dacek, S. Cholia, D. Gunter, D. Skinner, G. Ceder, and K. Persson. Commentary: The Materials Project: A materials genome approach to accelerating materials innovation. *Applied Physics Letters Materials*, 1(1):011002, 2013.

[13] E. R. Dobrovinskaya, L. A. Lytvynov, and V. Pishchik. Radiation Effects in Sapphire. In V. Pishchik, L. A. Lytvynov, and E. R. Dobrovinskaya, editors, *Sapphire: Material, Manufacturing, Applications*, Micro- and Opto-Electronic Materials, Structures, and Systems, pages 177–188. Springer US, Boston, MA, 2009.

[14] C. Train and V. Mathet. Morphology and magnetic properties of $Pt/Co/Pt/Al_2O_3(0001)$ structures: Influence of the growth temperature. *Surface Science*, 412–413:495–501, 1998.

[15] R. Vargas, T. Goto, W. Zhang, and T. Hirai. Epitaxial growth of iridium and platinum films on sapphire by metalorganic chemical vapor deposition. *Applied Physics Letters*, 65(9):1094–1096, 1994.

[16] B. M. Lairson, M. R. Visokay, R. Sinclair, S. Hagstrom, and B. M. Clemens. Epitaxial Pt(001), Pt(110), and Pt(111) films on MgO(001), MgO(110), MgO(111), and $Al_2O_3(0001)$. *Applied Physics Letters*, 61(12):1390–1392, 1992.

[17] M.L. Hildner, T.J. Minvielle, and R.J. Wilson. Epitaxial growth of ultrathin Pt films on basal-plane sapphire: The emergence of a continuous atomically flat film. *Surface Science*, 396(1-3):16–23, 1998.

[18] G. Panomsuwan, O. Takai, and N. Saito. Epitaxial growth of (111)-oriented $BaTiO_3/SrTiO_3$ perovskite superlattices on $Pt(111)/Ti/Al_2O_3(0001)$ substrates. *Applied Physics Letters*, 103(11):112902, 2013.

[19] H Zhou, P Wochner, A Schöps, and T Wagner. Investigation of platinum films grown on sapphire (0001) by molecular beam epitaxy. *Journal of Crystal Growth*, 234(2-3):561–568, 2002.

[20] L. E. Davis, N. C. MacDonald, P. W. Palmberg, G. E. Riach, and R. E. Weber. Handbook of Auger Electron Spectroscopy, 1976.

[21] S. Schmidt, D. O. Klenov, S. P. Keane, J. Lu, T. E. Mates, and S. Stemmer. Atomic structure of (111) $SrTiO_3$/Pt interfaces. *Applied Physics Letters*, 88(13):131914, 2006.

[22] G. Panomsuwan, O. Takai, and N. Saito. Controlled crystalline orientation of $SrTiO_3$ thin films grown on Pt(111)/Ti/alpha-Al_2O_3(0001) substrates: Effect of growth temperature and Ti layer thickness. *Applied Surface Science*, 309:95–105, 2014.

[23] T. C. Tisone and J. Drobek. Diffusion in Thin Film Ti–Au, Ti–Pd, and Ti–Pt Couples. *Journal of Vacuum Science and Technology*, 9(1):271–275, 1972.

[24] B. C. Beard and P. N. Ross. Platinum-titanium alloy formation from high-temperature reduction of a titania-impregnated platinum catalyst: Implications for strong metal-support interaction. *The Journal of Physical Chemistry*, 90(26):6811–6817, 1986.

[25] M. Biesinger. X-ray Photoelectron Spectroscopy (XPS) Reference Pages. http://www.xpsfitting.com/, 2020.

[26] J. F. Moulder, W.F. Stickle, P. E. Sobol, and K. D. Bomben. *Handbook of X Ray Photoelectrfon Spectroscopy: A Reference Book of Standard Spectra for Identification and Interpretation of Xps Data*. Physical Electronics, 1992.

[27] S. Hsieh, D. Beck, T. Matsumoto, and B. E. Koel. Thermal stability of ultrathin titanium films on a Pt(111) substrate. *Thin Solid Films*, 466(1-2):123–127, 2004.

[28] S Ringler, E Janin, M Boutonnet-Kizling, and M Gothelid. Pt_3Ti alloy formation on the Pt111/ surface. *Applied Surface Science*, page 8, 2000.

[29] S. Weng, L. Qiao, and P. . Thermal stability of Pt-Ti bilayer films annealing in vacuum and ambient atmosphere. *Applied Surface Science*, 444:721–728, 2018.

[30] W. Chen, L. Severin, M. Göthelid, M. Hammar, S. Cameron, and J. Paul. Electronic and geometric structure of clean Pt_3Ti(111). *Physical Review B*, 50(8):5620–5627, 1994.

[31] T. Yang, T. T. Song, M. Callsen, J. Zhou, J. W. Chai, Y. P. Feng, S. J. Wang, and M. Yang. Atomically Thin 2D Transition Metal Oxides: Structural Reconstruction, Interaction with Substrates, and Potential Applications. *Advanced Materials Interfaces*, 6(1):1801160, 2019.

[32] G. Panomsuwan, O. Takai, and N. Saito. Orientation control of textured $SrTiO_3$ thin films on platinized α-Al_2O_3(0001) by an ion beam sputter deposition method. *Journal of Physics D Applied Physics*, 45:4003, 2012.

[33] W. Y. Park, M. H. Park, J. H. Lee, J. H. Yoon, J. H. Han, J-H Choi, and C. S. Hwang. Strain evolution of each type of grains in poly-crystalline (Ba,Sr)TiO_3 thin films grown by sputtering. *Scientific Reports*, 2(1):939, 2012.

[34] S. P. Keane, S. Schmidt, J. Lu, A. E. Romanov, and S. Stemmer. Phase transitions in textured $SrTiO_3$ thin films on epitaxial Pt electrodes. *Journal of Applied Physics*, 99(3):033521, 2006.

[35] X. Wang, X. Lu, H. Bo, Y. Liu, Y. Shen, X. Wu, W. Cai, Y. Kan, C. Zhang, Y. Liu, F. Huang, and J. Zhu. The structural and electrical properties of oriented $SrTiO_3$ films prepared by metal organic deposition method. *Solid State Communications*, 150(35):1637–1640, 2010.

[36] M H Tang, Z P Wang, J C Li, Z Q Zeng, X L Xu, G Y Wang, L B Zhang, Y G Xiao, S B Yang, B Jiang, and J He. Bipolar and unipolar resistive switching behaviors of sol–gel-derived $SrTiO_3$ thin films with different compliance currents. *Semiconductor Science and Technology*, 26(7):075019, 2011.

[37] M. Hiratani, K. Imagawa, and K. Takagi. Orientation and Crystal Structure of $SrTiO_3$ Thin Films Prepared by Pulsed Laser Ddeosition. *Japanese Journal of Applied Physics*, 34(Part 1, No. 1):254–260, 1995.

[38] T. Tani, Z. Xu, and D. A. Payne. Preferred Orientations for Sol-Gel Derived Plzt Thin Layers. *MRS Proceedings*, 310:269, 1993.

Chapter 4

Complex 2D oxide phases in reduced $SrTiO_3$ grown on $Pt(111)/Al_2O_3(0001)$

Contents

4.1 Cleaning and annealing procedure 106
4.2 Giant square-like approximant 109
4.3 Large hexagonal approximant 112
4.4 σ-phase approximant 115
4.5 Theoretical investigation of the 2D OQC approximants 117
4.6 Complex hexagonal phases 125
Bibliography 133
Bibliography 140

Dodecagonal oxide quasicrystals (OQCs) and related approximants are 2D structures derived from ternary ultra-thin oxide films supported on metals (UTOx) grown epitaxially on a well oriented (111)-metal as mentioned previously in Chap.1. As a remainder for the reader, the first OQCs were observed at the 2D interface of $BaTiO_3$ and $SrTiO_3$ deposited on a Pt(111) single crystal. Since the discovery of OQCs, four OQC approximant structures have been reported in the literature.
These phases are: the σ-phase approximant, found in the $BaTiO_3$/Pt(111) [1] and in the $BaTiO_3$/Ru(0001) [2] systems; a monoclinic approximant, derived from the $SrTiO_3$/Pt(111) system [3]; a hexagonal approximant, derived from the $BaTiO_3$/Pt(111) [4] system, and a variant of the σ-phase approximant, found in the $BaTiO_3$/Pd(111) system [5] (see Chap.1, Sec.1.2.3). Here, we report the formation of new complex 2D phases after reduction of $SrTiO_3$/(Ti/)Pt(111)/Al_2O_3(0001) synthesized using the thin film stacking approach presented in Chap.3. This method has been successfully tested as a possible way to explore different combinations of UTOx supported on (111)-metals, and search for new types of OQCs. In total we identified by means of LEED and STM three OQC approximants and other complex hexagonal structures. The different phases are formed depending the preparation conditions.

This chapter is organized in six sections as follows: A description of the cleaning and annealing procedures is given in the first part. Second and third sections are dedicated to the giant square-like approximant and the large hexagonal approximant. These OQC approximant phases have not been reported before in the literature. Section four is dedicated to the σ-phase approximant, reported here for the first time in the $SrTiO_3$/Pt(111) system. Section number five, presents the DFT calculations performed on the giant square-like and the large hexagonal OQC approximants (done by T.T. Dorini and E. Gaudry). A comparison between theoretical results and experimental observations is discussed here. Finally, the sixth section evidences the complex hexagonal phases observed after increasing the number of annealing procedures. A honeycomb (HC) structure, formed by the TiO_x network was identified, along with a labyrinth-like structure formed by the Sr atoms located at the hollow sites of the HC structure.

4.1 Cleaning and annealing procedure

Annealing the oxide film at temperatures above 630°C (900 K) could induce a rearrangement of the material leading to the possible formation of a 2D OQC or a variety of approximant structures [6]. OQC derived from $BaTiO_3$ on Pt(111) has been studied in great detail by Förster *et.al* [7]. In particular, it was demonstrated that reduction-oxidation annealing cycles lead to a reversible process of OQC formation and decay [8] (see Chap. 1 for more details).

Here, we applied oxidation-reduction cycles to the $SrTiO_3$ thin film deposited on

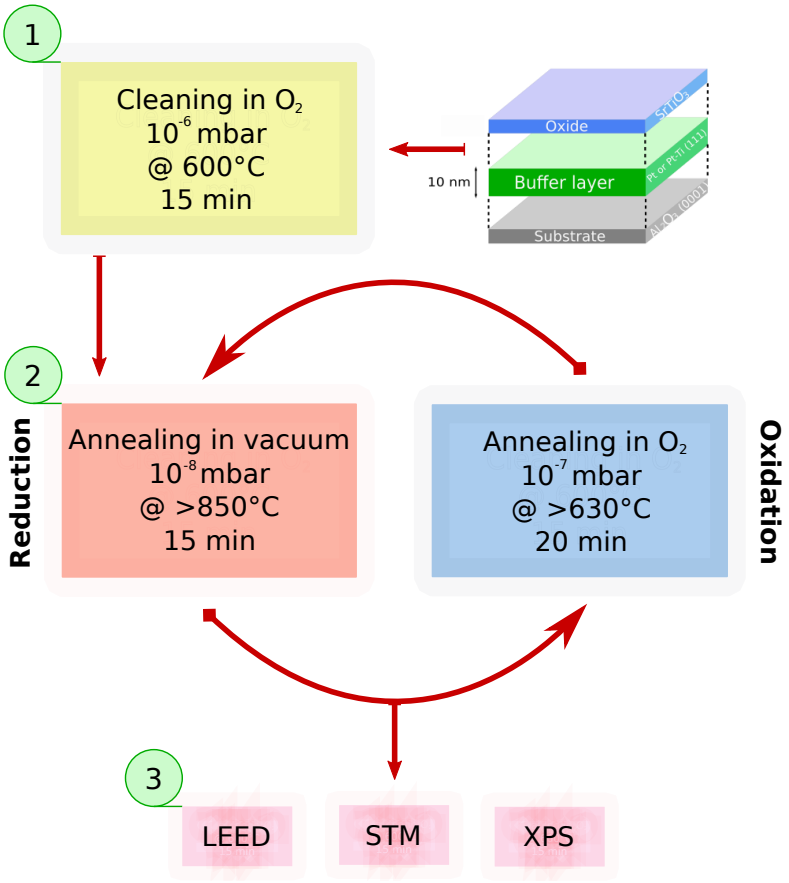

Figure 4.1 – Schematic of the experimental procedure. The sample was transferred after fabrication through air to a second UHV system (ASURE). First, sample surface was cleaned in an oxygen atmosphere. Second, the sample was annealed under vacuum at high temperature. The state of the surface after annealing was monitored by LEED and eventually by STM and XPS. Then, an annealing under oxygen at lower temperature was performed. Again, LEED patterns were taken. This procedure was repeated several times observing the changes in the surface structure.

Pt(111) (or Ti/Pt(111)) grown on α-Al_2O_3(0001) as represented in Fig.4.1 (in collaboration with Julian Ledieu, responsible of the ASURE platform). The $SrTiO_3$ films are stable under ambient conditions, which allowed sample transfer through air from the TUBE to the ASURE platform (see Chap.2 for more details) where high temperature annealing and subsequent *in situ* surface characterizations such as LEED, STM and XPS were performed.

After re-entering the sample in UHV, an annealing in 1×10^{-6} mbar of O_2 at 630°C was performed to remove surface contamination induced by the transfer as illustrated in Fig.4.1 step 1. All temperatures reported here in this chapter were mea-

sured with a bichromatic pyrometer (T_{Pyro}).

The cleanliness of the sample after step 1 was checked by XPS and LEED. The XPS spectra (not shown here) did not show any C 1s core level peak. In addition, LEED patterns such as the one presented in Fig. 4.2, exhibit spots related to a (111)-oriented $SrTiO_3$ surface.

The surface lattice parameter of $SrTiO_3$ is twice as large as that of the Pt(111). Then, by annealing the surface at higher temperatures (> 850°C or 1123 K) in UHV (10^{-8} mbar), step 2 in Fig.4.1, new structures with an apparent dodecagonal symmetry were formed as observed by LEED and STM at room temperature (step 3 in Fig.4.1).

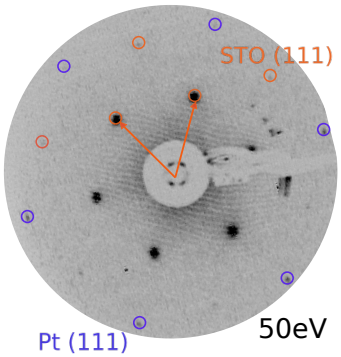

Figure 4.2 – LEED pattern of the $SrTiO_3$ surface (8Å deposited on Pt(111)/Al_2O_3(0001)) after cleaning in oxygen. The blue circles mark the Pt(111) six-fold diffraction pattern and orange circles mark the first order diffraction pattern of $SrTiO_3$(111).

The results reported here were observed in the following three samples, named from now on as:

A (0.8 nm) $SrTiO_3$/(10 nm) Pt(111)/Al_2O_3(0001)

B (2 nm) $SrTiO_3$/(1 nm)Ti/(10 nm) Pt(111)/Al_2O_3(0001)

C (5 nm) $SrTiO_3$/(1 nm) Ti/(10 nm) Pt(111)/Al_2O_3(0001)

Samples with thinner $SrTiO_3$ films (0.4 nm) were tested as well with no significant results. It was found for several samples that after few annealing cycles the Sr signal in XPS was very small, the LEED patterns overall the surface were weak, and the surface was extremely difficult to scan by STM.

This could be explained by a critical thickness. As we will see in the next paragraphs, re-arrangements and depletion of certain species occurs upon high temperatures annealing. Therefore, a reservoir (coming from an initial surface with 3D $SrTiO_3$(111) islands) could be necessary for the formation of complex 2D structures.

4.2 Giant square-like approximant

Once the sample surface was degassed, a subsequent annealing at 850°C (1123 K) in vacuum (10^{-8}mbar) was performed as indicated in the step 2 in Fig.4.1 (this, for the three samples ***A***, ***B*** and ***C***). After annealing, a new structure with an apparent dodecagonal symmetry was formed as observed by LEED and STM. This is illustrated in the LEED pattern at 20 eV with 12 intense diffraction spots as can be seen in Figure 4.3 (b). At higher beam energies (see Fig.4.3 (c)), higher order diffraction spots are observed leading to a LEED pattern very similar to the one reported previously for the OQC [3]. The 6-fold diffraction spots from the Pt buffer layer are marked by the blue circles.

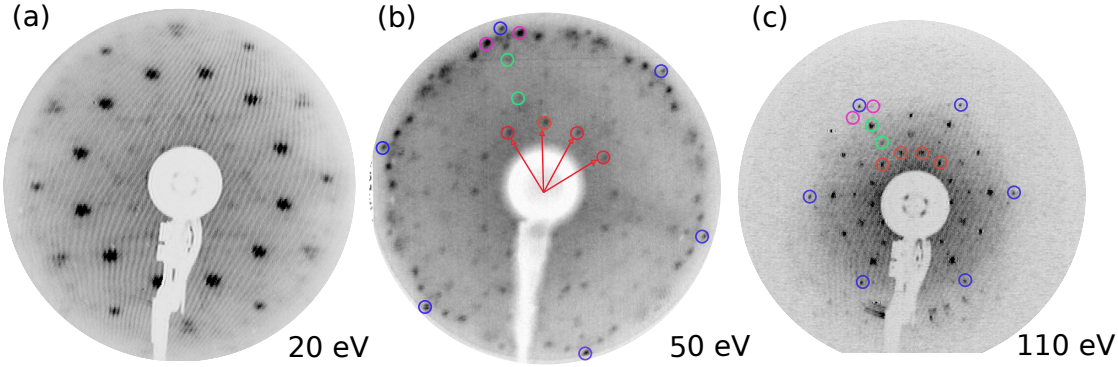

Figure 4.3 – LEED pattern of the approximant formed on Pt(111) at (a) 20 eV, (b) at 50 eV, and at (c) 110 eV. The blue circles in (b) and (c) mark the Pt(111) first order diffraction pattern. First, second and third order diffraction spots of the approximant are marked in red, green and magenta circles respectively. These LEED patterns were obtained from sample ***A***.

The real space structure and the local atomic arrangements were determined from atomically resolved STM images taken at room temperature (figure 4.4 (a)). Although the LEED pattern shows an apparent dodecagonal pattern typical of an OQC, the fast Fourier transform (FFT) of the real space image reveals a periodical almost square lattice, indicating that an approximant was formed instead of an OQC [9, 10]. The FFT was used to determine the lattice parameters. Figure 4.4 (b) gives a more detailed view of the identified approximant unit cell, with the in-plane measured lattice parameters of: 42.2± 0.6 Å× 43.2 ± 0.6 Å, and angle between edges of 89.7 ± 0.4°. The bright protrusions seen in the STM images are at the nodes of the same Niizeki–Gähler tiling elements (NGT) used to describe dodecagonal structures [11]. These tiling elements are arranged such that the unit cell contains 72 tiles, namely 48 triangles, 18 squares and 6 rhombus with a tiling element ratio of 2.66:1:0.33. This is twice the number of tiles needed to describe the previously re-

ported monoclinic approximant [3], but the ratio remains the same. Besides, it is just slightly different from the ideal NGT structure of the dodecagonal QC phase given by 2.73:1:0.37. The unit cell contains 47 vertex atoms, corresponding to an area density of 2.20 nm^{-2}, smaller than the values reported for the OQC phase (2.46 nm^{-2}). From the STM image, an average distance of 6.4 ± 0.3 Å between the bright protrusions is deduced. The edge length of the tiling elements deduced from the ideal unit cell is 42.2 Å/(3 + 2 $\sqrt{3}$) = 6.53 Å, for the vertical axis, and 43.2 Å/(3 + 2 $\sqrt{3}$) = 6.68 Å, for the horizontal axis. One axis of the approximant unit cell is parallel to the [12$\bar{3}$] direction of the hexagonal Pt buffer layer. From the idealized unit cell model, it is possible to obtain a FT of the structure, as shown in the left side of Fig.4.4 (c) where the near 12-fold first order, second order and third order diffraction spots are present as part of a square lattice indicated in green. The calculated FT pattern perfectly matches the FFT of the experimental STM image (right side Fig. 4.4 (c)). The tiling decoration is shown in Fig. 4.4 (d).

The unit cell of the approximant can be expressed as a superstructure with respect to the Pt(111) lattice, resulting in a commensurate matrix given by $\begin{pmatrix} 16 & 0 \\ 9 & 18 \end{pmatrix}$ when the dimensions of the unit cell are slightly modified to 44.87 Å× 43.75 Å, with an angle between edges of 89.7° and the Pt(111) unit cell is fixed to 2.79 Å. Six rotational domains of the approximant, with three unique subpatterns, exist from the square-like structure on the hexagonal lattice of the Pt(111) buffer layer. As a result, some of the diffraction spots in the LEED pattern are split into three reflexes as can be seen at low primary beam energies (Fig. 4.3(b)). The square lattice is not clearly visible in the diffraction pattern (Fig. 4.3), probably due to the fact that many of the diffraction spots may have a weak intensity and the LEED patterns are dominated by the most intense spots.

This approximant phase was found in the samples ***A*** and ***B*** mentioned in the previous section. For the sample ***A*** the dodecagonal pattern was observed after the first UHV annealing. For the sample ***B*** it was obtained only after the fifth annealing cycle.

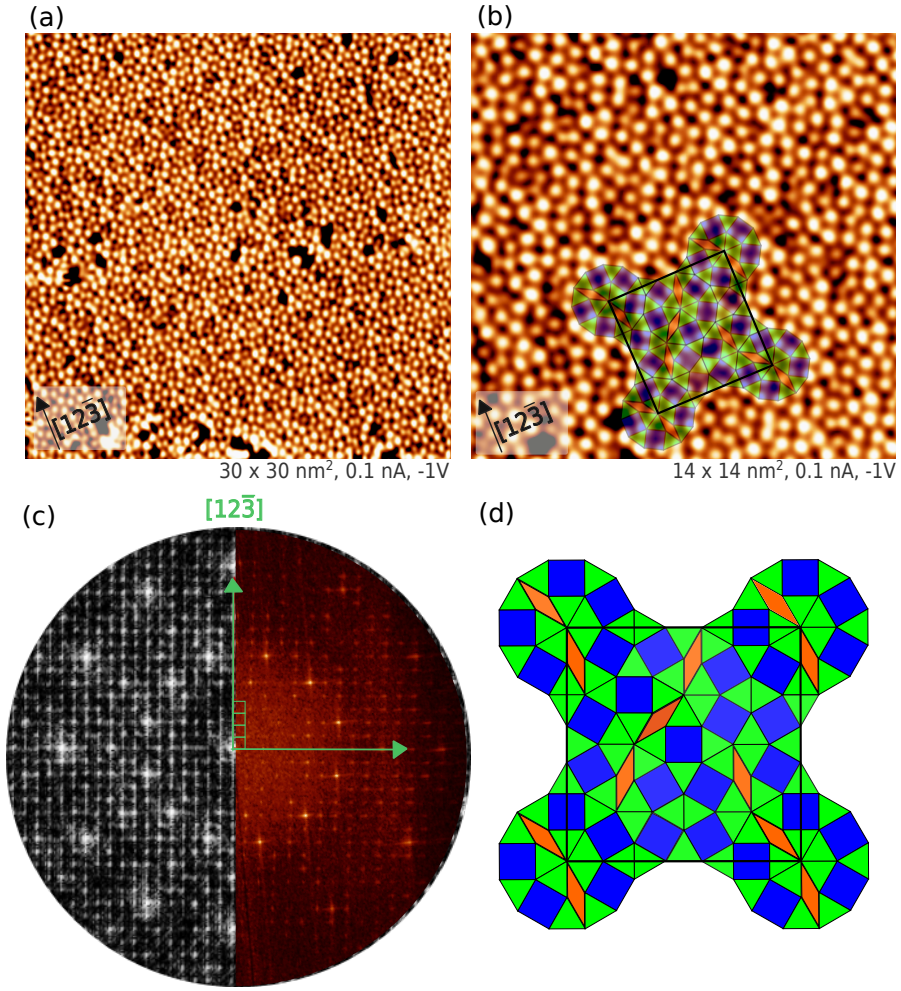

Figure 4.4 – (a) Atomically resolved STM image of the $SrTiO_3$ derived giant square approximant formed on Pt(111). (b) Idealized unit cell of the giant square approximant decorated by the dodecagonal tiling elements: squares, triangles and rhombuses superimposed on the real STM image. (c) *Left:* calculated FT of the idealized tiling. *Right:* FFT of the STM image in (a). The square unit cell is marked in green. (d) Tiling decoration of the square unit cell.

4.3 Large hexagonal approximant

With increasing numbers of oxidation-reduction cycles under the same experimental conditions as described earlier, another new UTOx phase was observed with a large hexagonal unit cell. Figure 4.5 (a) and (b) show high resolution STM images of this structure, as well as the tiling decoration. The FT calculated from this tiling decoration as well as the FFT calculated from the experimental STM image are shown in Fig. 4.5 (c). It is also possible to observe more intense higher-order spots in the calculated FT which form a pseudododecagonal ring which is included in the hexagonal lattice. It reflects the presence of local dodecagonal motifs. The dimensions of the unit cell are 27.8 ± 0.6 Å$\times$ 28.1 ± 0.6 Å. This hexagonal unit cell can be decorated with the same NGT elements. It contains 29 tiles, namely 20 triangles, 6 squares and 3 rhombus as shown in Fig.4.5(c). A common edge length of 6.7 ± 0.2 Å is deduced from the average distance between the bright protrusions. Dodecagonal rings consisting of 6 squares and 12 triangles decorate the node of the unit cell. A protrusion is usually missing at each node of the hexagonal unit cell (ie. at the center of the dodecagonal rings) in the images shown in Fig. 4.5(a) and (b). In other patches of the surface, this site is occupied and appears as a bright dot, suggesting the presence of slightly protruding atoms. The unit cell contains either 19 or 18 vertex, corresponding to an area density between 2.65 and 2.80 nm^{-2}, significantly larger than that of the ideal OQC or its square approximant. The tiling elements ratios of the hexagonal phase is 3.33:1:0.5, which differ considerably from the ideal OQC or the square approximant. The structural evolution of the UTO film, from square-like to hexagonal approximant , could be related to a change in the stoichiometry with the number of annealing cycles.

The LEED pattern of the hexagonal phase is shown in Fig. 4.6. Four non-equivalent domains can be identified, which are rotated with respect to the $[1\bar{1}0]_{Pt}$ direction by 15°, 27°, 34° and 45°. We tentatively ascribed these domains to the following four commensurate structures with matrices given by $\begin{pmatrix} 6 & -5 \\ 5 & 11 \end{pmatrix}$ and $\begin{pmatrix} 5 & -6 \\ 6 & 11 \end{pmatrix}$ for the domains presented in green in Fig. 4.6, when the lattice parameter of the hexagonal phase is 26.61 Å and the Pt(111) unit cell is fixed to 2.79 Å and $\begin{pmatrix} 8 & -3 \\ 3 & 11 \end{pmatrix}$ and $\begin{pmatrix} 3 & -8 \\ 8 & 11 \end{pmatrix}$ for the domains marked in pink in Fig. 4.6 when the lattice parameter of the hexagonal phase is 27.48 Å and the Pt(111) unit cell is fixed to 2.79 Å.

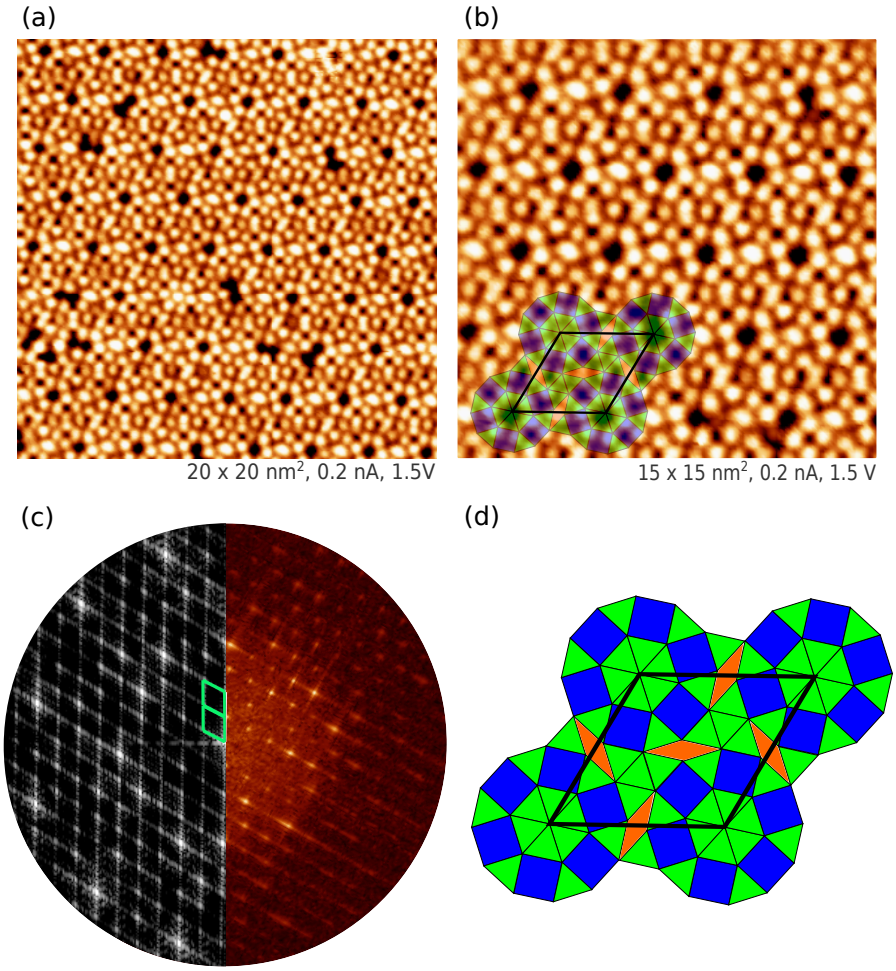

Figure 4.5 – (a) Atomically resolved STM image of the $SrTiO_3$ large hexagonal phase formed on Pt(111). (b) Idealized unit cell of the large hexagonal phase decorated by the dodecagonal tiling elements: squares, triangles and rhombus superposed on the real STM image. (c) *Left*: FT of the pattern from the tiling using the idealized tiling unit cell. *Right*: FFT of the STM image in (a). The hexagonal unit cell is marked in green

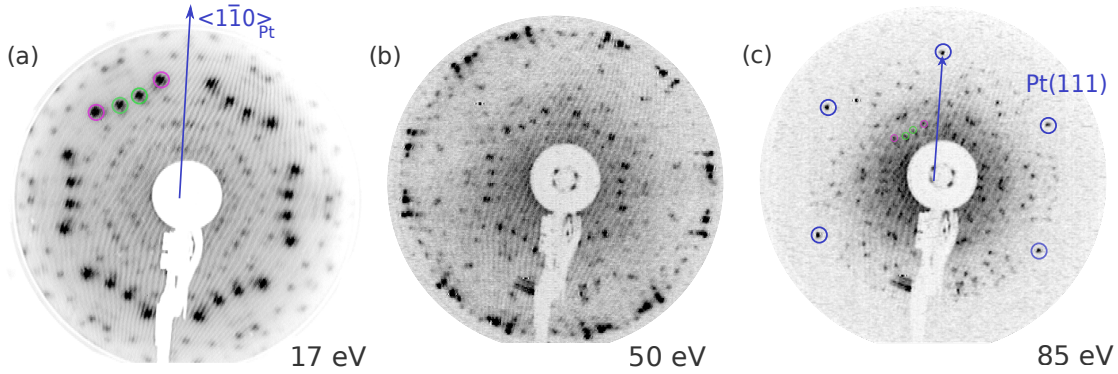

Figure 4.6 – LEED pattern of the large hexagonal phase of $SrTiO_3$/Pt(111). (a) At 17 eV, four non-equivalent domains are identified. Green circles correspond to the diffraction spots of the domains turned by 27° and 34° with respect the $[1\bar{1}0]_{Pt}$ direction. Pink circles mark the diffraction spots corresponding to the domains at 15° and 45° with respect the $[1\bar{1}0]_{Pt}$ direction. (b) At 50 eV higher diffraction order spots are visible and (c) at 85 eV, Pt buffer layer first order diffraction spots are evident. These are highlighted in blue

This approximant phase was first observed in the sample ***B*** (see Sec.4.1) after the first annealing in UHV. It was found as well in the sample ***A*** but only after sixth UHV annealing. Fig.4.7(a) shows the atomically resolved STM image of the hexagonal approximant observed in sample ***B***, where a region with all hollows in Fig.4.5(a) are filled. The hexagonal unit cell decorated with the dodecagonal tiling elements is superimposed on the STM image. Fig.4.7(b) evidences a step with a measured high of 4.5 Å as indicated by the profile in Fig.4.7(c). Although there are not enough images of the terraces to do a statistically measurement of the step high, the obtained profile indicate a high of the step corresponding well to two planes of the of the annealed Ti/Pt(111) (in agreement with the measured interatomic distance d_{111}, reported in table3.1 in Chap.3).

It is noteworthy that the giant square-like and the hexagonal approximant were both found for samples with Pt(111) and Ti/P(111) buffer layers. It suggest that, as discussed in Chap.3, the addition of 1 nm of Ti does not affect the ultrathin films of $SrTiO_3$ deposited on Pt(111) as it interdiffuses into the Pt forming a solid solution. The Ti layer helps to promote the (111)-orientation of thicker layers (> 5 nm) of $SrTiO_3$ on Pt(111).

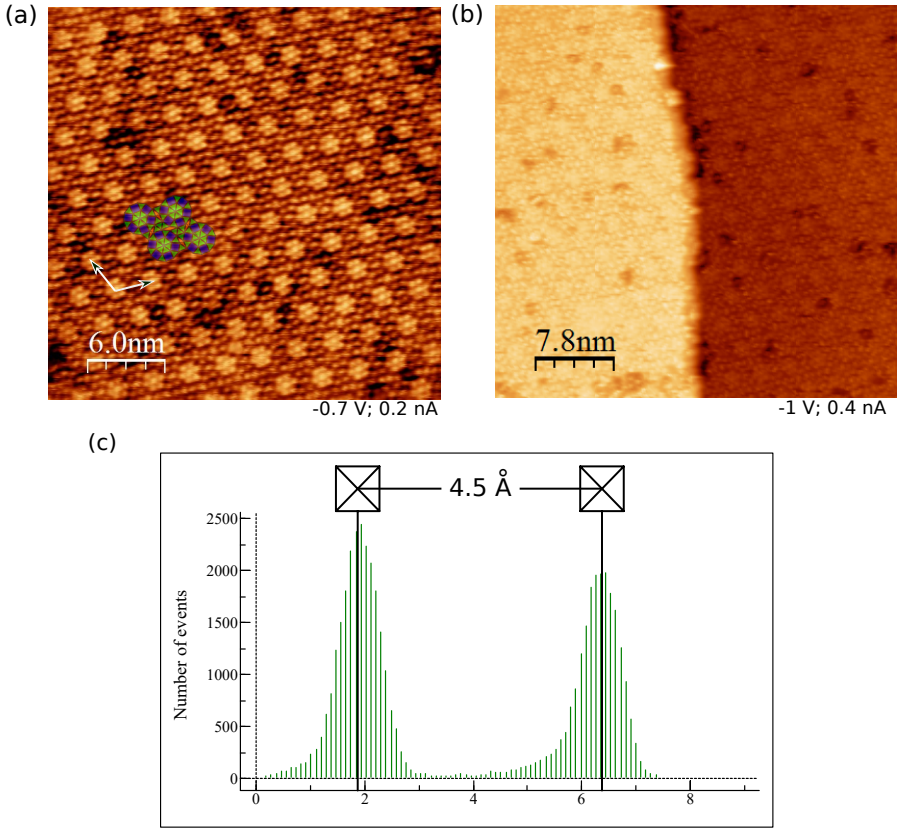

Figure 4.7 – (a) Atomically resolved STM image of the $SrTiO_3$ large hexagonal phase formed on Ti/Pt(111) decorated with the dodecagonal tiling elements.The unit cell vectors are indicated by the white arrows (b) A step. (c) A high histogram of the step high: 4.5 Å.

4.4 σ-phase approximant

For sample ***C*** (see Sec 4.1), the σ-phase approximant (also known as 3^2.4.3.4 Archimedean tiling or snub-square tiling) [1] was found after two cycles when annealing in vacuum (10^{-8}mbar) at 900°C for 15 min. Here we report for the first time the observation of this approximant phase in the $SrTiO_3$/Pt(111) system. Fig.4.8(a) shows the LEED pattern at 20 eV where 12 intense diffraction spots are visible. At higher beam energies, higher order diffraction spots appeared leading to LEED patterns close to the reported OQC structures, as was the case for the giant square-like approximant. These patterns are evidenced in Fig. 4.8(b) and (c). The 6-fold diffraction spots from the Pt buffer layer are marked by the blue circles.

Fig.4.9(a) shows the atomic resolution STM image with a periodic arrangement confirmed by the FFT (right side in Fig. 4.9(c)) which reveals an almost square lattice

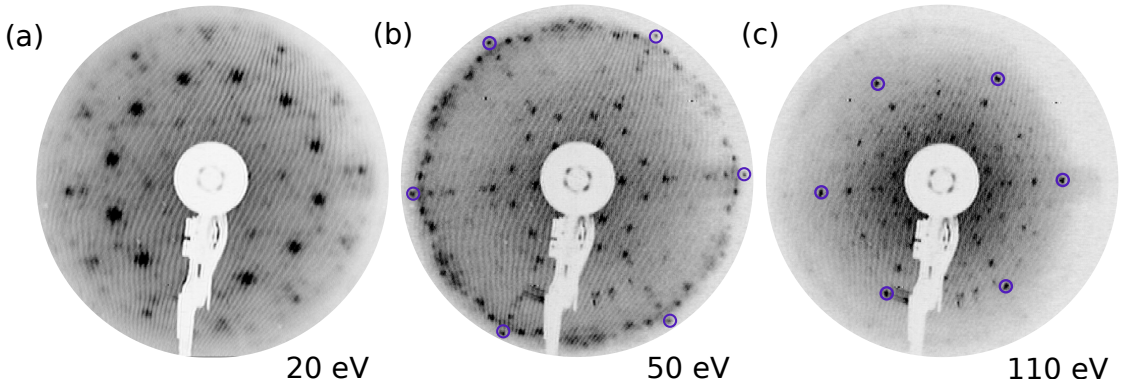

Figure 4.8 – LEED pattern observed after two annealing cycles on sampple ***C*** at 20 eV, (b) at 50 eV and (c) at 110 eV. The blue circles mark the Pt(111) first order diffraction pattern.

with a larger reciprocal lattice parameter when compared with the previously described giant square-like approximant. From the STM image, the distance between the surface atoms was determined as 6.4±0.3 Å . This value is slightly smaller than the average distance of 6.7 Å between protrusions reported for the σ-phase approximant observed in $BaTiO_3$/Pt(111)[1]. The FFT was used to determine the in plane lattice parameters: 12.5 ± 0.2 Å $\times$ 12.5 ± 0.1 Å also smaller than the reported lattice parameters 12.9×13.1 Å of the $BaTiO_3$/Pt(111) σ-phase approximant [1]. Fig.4.9(b) gives a more detailed view of the identified unit cell, with the superposed tiling decoration which includes only two squares and four triangles. The FFT is presented on the right side of Fig.4.9 which matches very well with the FT, on the left, coming from the ideal tiling decoration of the σ-phase structure presented in Fig.4.9(d).

STM image in Fig.4.9(a) presents contrast variations between adjacent unit cells creating a sort of corrugation. A closer view to the FFT of Fig.4.9(a), allow us to see the diffraction pattern of a moiré structure as indicated by the blue circles in Fig.4.10(a). The subsequent STM image was obtained from filtering the diffraction spots of the moiré structure. We determined from the FFT a periodicity of 2.89±0.05 nm, in agreement with the directly measured value (from the STM filtered image in Fig.4.10(a)) of 2.83 nm as evidenced in the profile in Fig.4.10(b), taken along the blue line in (a). This contrast variations were observed as well in the σ-phase approximant derived from $BaTiO_3$/Pt(111), where a 2.8 nm periodic moiré structure was identified from the large length scale STM images [1].

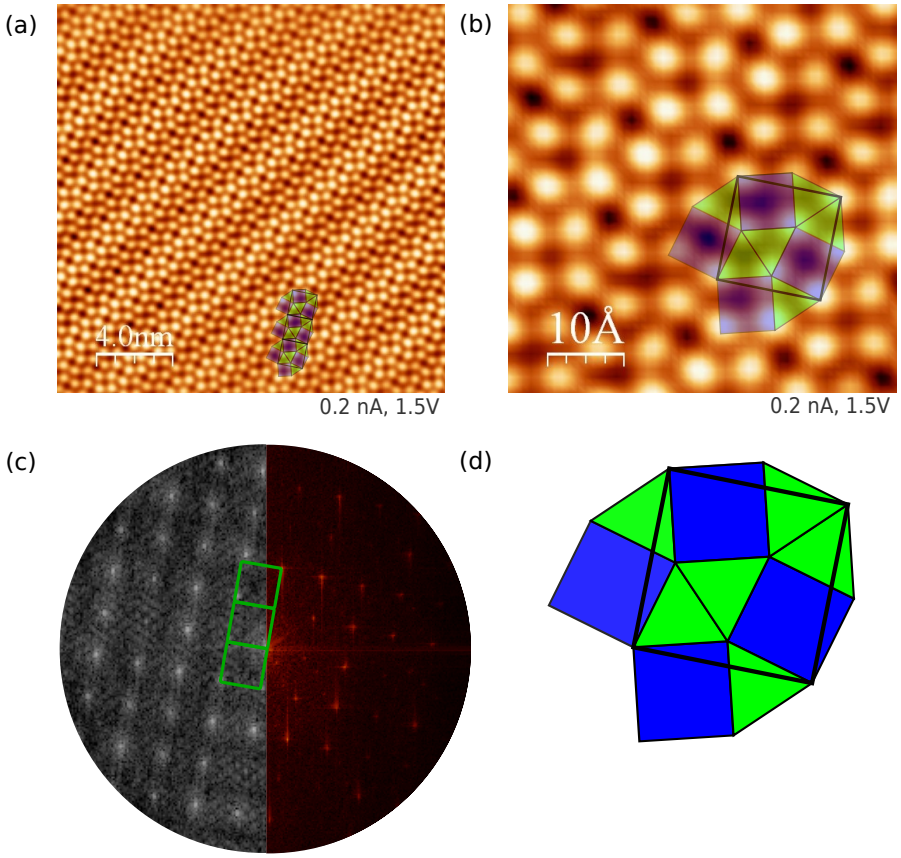

Figure 4.9 – (a) Atomically resolved STM image of the σ-Approximant formed on $SrTiO_3$/Ti/Pt(111). (b) Idealized unit cell of the σ-Approximant phase decorated by the dodecagonal tiling elements: squares, triangles and rhombus superposed on the real STM image. (c) *left*: FT of the pattern from the tiling using the idealized tiling unit cell. *right*: FFT of the STM image in (a). The square unit cell is marked in green (d) Tiling decoration of the σ-Approximant

4.5 Theoretical investigation of the 2D OQC approximants

Density Functional Theory (DFT) calculations were performed using the Vienna *ab initio* simulation package (VASP) [12, 13, 14] combined with the Atomic Simulation Environment (ASE) [15]. Spin-polarised calculations were performed with plane-wave basis set and projector-augmented wave (PAW) method [16, 14], using the optPBE functional [17, 18]. The following electrons were treated explicitly: $4s^2 5p^6 6s^2$ (Sr), $2s^2 2p^4$ (O), $3s^2 3p^6 4s^2 3d^4$ (Ti), $5d^9 6s^1$ (Pt). The strong on-site Coulomb interaction of localized electrons was treated through the GGA+U approach, [19]

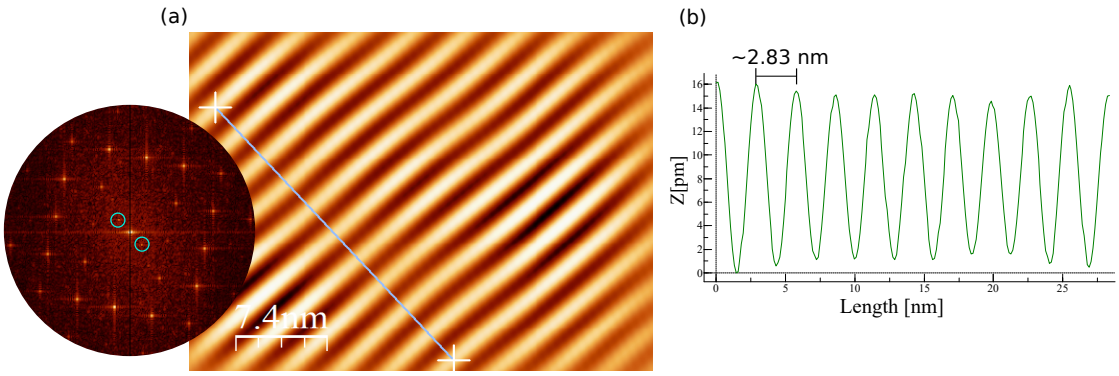

Figure 4.10 – (a) STM filtered image of the moiré periodicity present in the STM image in Fig.4.9. (b) Profile taken along the blue line in (a). The average separation between two pics is about 2.83 nm

using U(Ti) = 1.0 eV[20, 21]. This value has been chosen because it provides a good agreement with theoretical quantities calculated using the hybrid HSE03 exchange correlation potential, as demonstrated recently in the case of an oxide layer with the honeycomb (HC) structure supported on a metal substrate [20, 22]. The one-electron Kohn-Sham orbitals were expanded in a plane-wave basis set with a kinetic energy cutoff of 500 eV. Total energies were minimised until the energy differences were less than 10^{-5} eV between two electronic cycles. The reciprocal space integration was sampled at the Γ-point for total energy calculations. A thinner k-point grid (2×2×1) was used for the DOS (Density of States) calculations for the hexagonal structure (surface cell 28.20 Å × 28.20 Å). This set-up gives cohesive energies and lattice parameters of bulk systems in good agreement with the experimental data [23].

UTOx films supported on Pt(111) have been built using 4-layer thick asymmetric slabs for the giant square-like and the large hexa the σ-phase approximants. They consisted of three Pt(111) layers and one oxide-layer respectively. The outmost bottom layer of the Pt substrate was kept fixed, while all other layers were allowed to fully relax in all directions, using the Conjugate Gradient Algorithm, until all forces were less than 0.1 eV/Å. Adjacent slabs (along the surface normal direction) were separated by a 15 Å thick vacuum layer and a dipole correction was applied to cancel the artificial electric field that develops due to imposed periodic boundary conditions in surface normal direction. The average charges on each atom were calculated using the Bader approach,[24] using the code distributed by the Henkelman group [25, 26, 27, 28]. The STM images were calculated using the Tersoff-Hamman approximation [29, 30]. Charge deformations were calculated by the difference $\rho_{UTO/Pt} - \rho_{Pt} - \rho_{UTO}$, where $\rho_{UTO/Pt}$, ρ_{Pt} and ρ_{UTO} are the charge densities of the UTOx/Pt(111) slab, Pt(111) slab and UTOx free standing layer, respectively.

Structures and STM images were plotted using the VESTA and p4vasp softwares, respectively [31]. The formation enthalpies are given by

$$\Delta H_f = E(Pt_wSr_xTi_yO_z) - wE_{coh}(Pt) - xE_{coh}(Sr) - yE_{coh}(Ti) - \frac{z}{2}\mu_{O_2} \quad (4.1)$$

where E and E_{coh} are total and cohesive energies, respectively and μ_{O_2} is the chemical potential of dioxygen. Adhesion energies are calculated using

$$E_{adh} = E(UTO/Pt) - E(UTO) - E(Pt) \quad (4.2)$$

where E(UTO/Pt), E(UTO) and E(Pt) are the total energies of the supported UTOx, the ideal freestanding UTOx and the Pt(111) substrate, respectively.

The structural and electronic properties of the giant square-like, the hexagonal and the σ-phase 2D $SrTiO_3$/Pt(111) UTOx approximants are investigated using three model structures presented in Fig. 4.11, Fig.4.12 and Fig.**??**, based on the complex tilings identified experimentally. They are made of structural motifs – equilateral triangles, squares and 30^o rhombuses – sharing a common side length. The atomic structure of each type of tiles has been implemented using the models proposed by Cockayne *et al.* [32]. Thus, the chemical compositions of the triangles, squares and rhombuses are $SrTiO_3$, $SrTi_4O_4$ and $SrTi_2O_2$, respectively. The Sr atoms are located at the vertices of the tiling. Each Ti atom is bound to three oxygen atoms (local 3-fold symmetry), and each oxygen atom is located between two Ti atoms. The square and rhombus motifs share common sides with the triangular tiles, while the square and rhombus motifs are connected through the vertices.

The giant square-like and the hexagonal approximant present similar formation enthalpies: -1.03 eV/Å^2 and -1.08 eV/Å^2 respectively. They also present similar adhesion energies: -0.28 eV/Å^2 and -0.30 eV/Å^2 for the giant square-like and the hexagonal approximants respectively. They are much stronger than the one calculated by Dorini *et al.* for the σ-phase (considering the Ti atoms at the vertices of the tiling) (-0.075 eV/Å^2) [23], likely because the atomic surface density is larger for the three former phases than for the latter. They are weaker than the one calculated for the HC structure (-0.403 eV/Å^2) [23] suggesting that the presence of common symmetries between the substrate and the adlayer lead to a stronger interaction.

When supported on Pt(111), UTOx display significant structural relaxations in the z direction, i.e. the surface normal direction. Such corrugation can alleviate the elastic strain due to the size-mismatch between the unsupported and supported films [23, 20]. It is quantified by the vertical separation between the average z-position of the anions (z^-) and cations (z^+). The rumpling $R = z^+ - z^-$ is negative for the three complex systems (Tab. 4.1). Indeed, the mean vertical distance between the topmost Pt atoms and the Ti atoms is much smaller (2.3 Å) than the one between topmost Pt atoms and the oxygen or strontium atoms (3.1 Å and 3.2 Å, respectively),

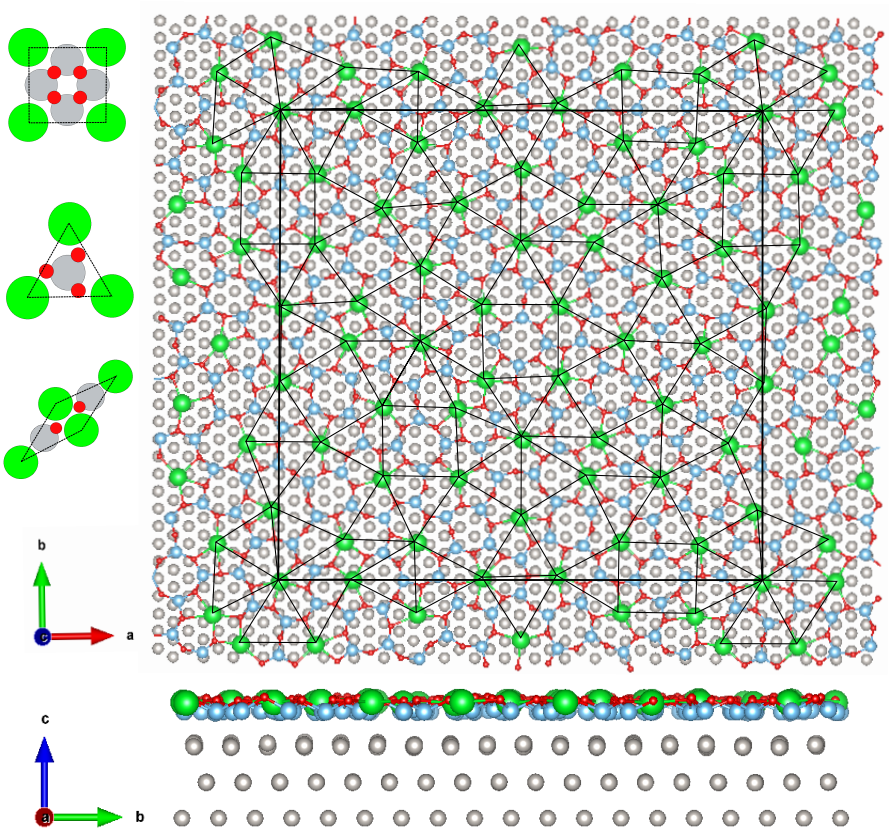

Figure 4.11 – Top and side views of the relaxed approximant structure, along with the three types of tiles used to build it. Sr, Ti, O and Pt atoms are shown in green, blue, red and silver respectively.

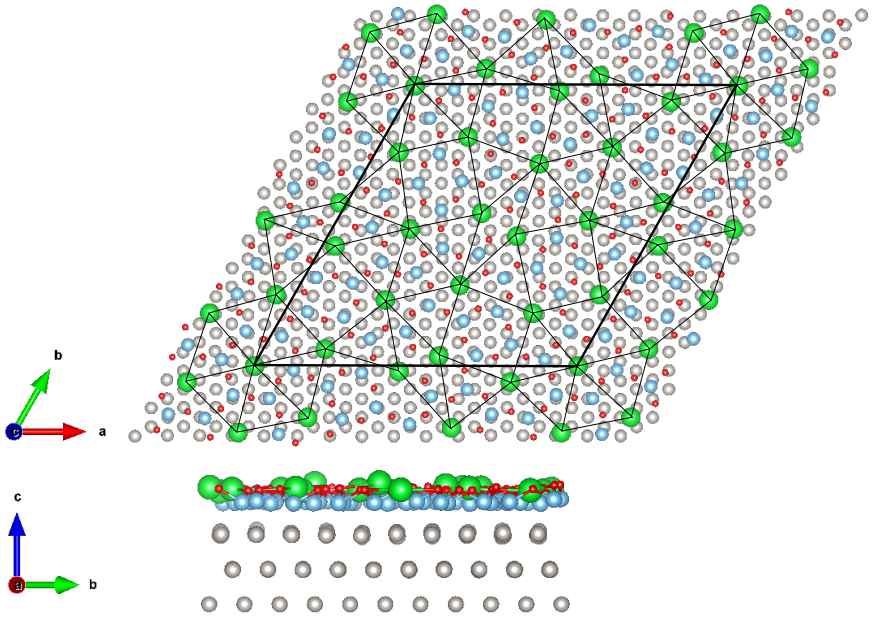

Figure 4.12 – Top and side view of the relaxed hexagonal approximant. Sr, Ti, O and Pt atoms are shown in green, blue, red and silver respectively.

in agreement with the values obtained by Cockayne *et al.* for $BaTiO_3$[32]. The rumpling is found to be: $R^{GSquare} = -0.41$ Å and $R^{Hexa} = -0.47$ Å for the giant square and the hexagonal approximants respectively.

These structural results can be rationalized by a Bader charge analysis. Charge transfer is found to occur at the Pt-UTOx interface, from most electropositive elements (Sr, Ti) to most electronegative elements (Pt and O). Thus, electrostatic interactions likely contributes to the location of Ti cations close to the negatively charged Pt substrate, while repelling the negative O atoms [32]. This is further confirmed by the charge density deformation, which indicates non negligible charge differences at the Pt-UTOx interface. More generally, electronic effects are known to impact the rumpling and the adhesion energies. Using the σ-phase approximant [23], a correlation has been evidenced between the Bader charge carried by the transition metal atoms (Q_{TM}) and both R and E_{adh}. Overall, a larger Q_{TM} leads to a stronger adhesion of the film and a larger R [23]. The same trends are observed in this work.

For each approximant phase (Figs.4.11 and 4.12), STM images were simulated for both positive and negative biases as shown in Fig.4.13 and Fig.4.14. The bright contrast is attributed to the protruding Sr atoms, while the Ti and O atoms are not visible, in agreement with the average z-positions of Sr, Ti and O described previously. Overall, the good agreement between the simulated and experimental STM images (Figs. 4.4-4.5) suggest that the UTOx structural models considered in this

	Giant Sq Approx	Hexa Approx
	Freestanding UTOx	
Q_{Ti} (e)	1.46	1.40
Q_{Sr} (e)	1.51	1.51
Q_O (e)	–1.29	–1.27
	Supported UTOx	
R(Å)	–0.41	–0.47
Q_{Ti} (e)	2.04	2.07
Q_{Sr} (e)	1.48	1.41
Q_{Pt} (e)	–0.11	–0.11
Q_O (e)	–1.22	–1.17
E_{adh} (eV/Å^2)	–0.28	–0.30
ΔH_f (eV/at)	–1.03	–1.08

Table 4.1 – Bader charges on ions, rumpling and the adhesion energies for the giant square-like and the hexagonal approximants.

work are realistic models for the new complex UTOx synthesized here.

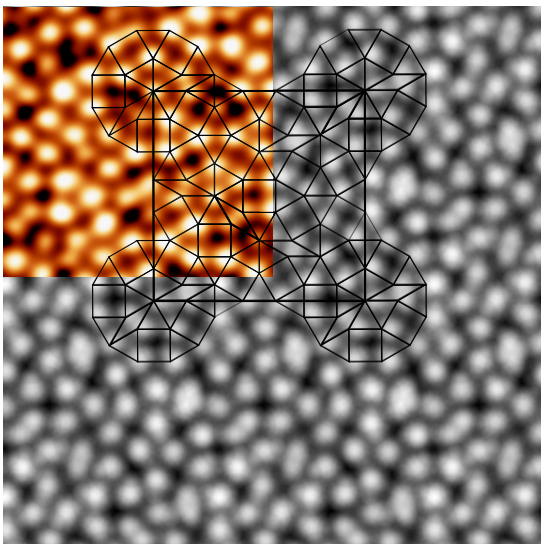

Figure 4.13 – Simulated STM image of the square approximant (V_{bias} = –1 V, isosurface with charge density equal to 0.1 e nm^{-3}). A fraction of the experimental STM image (Fig.4.4) is shown in the upper left corner.

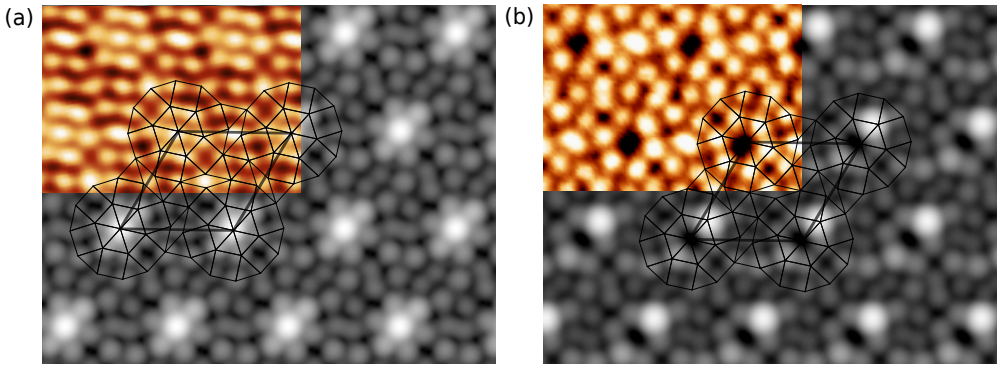

Figure 4.14 – Simulated STM images of the complex hexagonal phase, with (a) and without (b) the central protrusion at the cell nodes (a) $V_{bias} = -1$ V, isosurface with charge density equal to 0.2 e nm^{-3}, (b) $V_{bias} = +1.5$ V, isosurface with charge density equal to 0.1 e nm^{-3}. A fraction of the experimental STM image is shown in the upper left corner.

Density of states calculations have been performed using the two complex UTOx structures (Fig. 4.15). In both cases, the contribution of Sr atoms to the DOS is weak below the Fermi level, while the main contribution to the DOS at the Fermi level originates from Ti atoms. A strong hybridization between Pt-, O- and Ti-states is also visible, between -6 eV and -2 eV for the approximant UTOx, and between -7 eV and -3 eV for the complex hexagonal UTOx. Surprisingly, a sharp pseudogap close to the Fermi level, is noticeable in the DOS of the hexagonal phase, while it seems to be absent in the square UTOx, at least using the Γ-point only calculation performed here. This different electronic feature suggests different chemical and physical properties for the two UTOx.

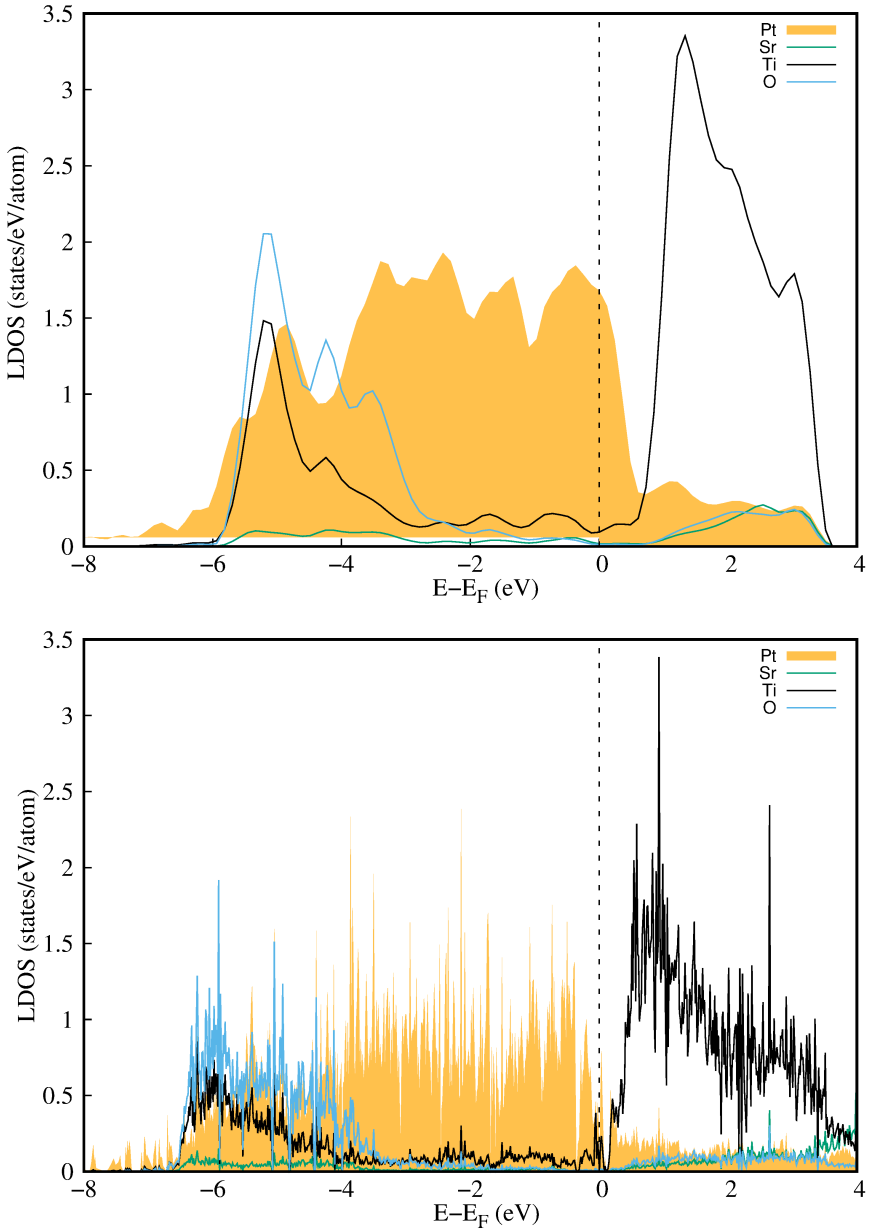

Figure 4.15 – Density of states of the square approximant (left) and of the complex hexagonal phase (right).

4.6 Complex hexagonal phases

Literature reports that when UTOx films of no more than one or two atomic layers are grown on metallic supports, depending on the preparation conditions, may display structures, stoichiometries and properties that are not seen in the bulk crystals [33, 22](see Chap.1).

Here, we report the observation of different morphologies when increasing the number of annealing cycles. A spontaneous 2D ordering of the oxide species occurred, giving rise to a (2 × 2) TiO_x HC ultrathin film [34], where Sr atoms occupy the hollow sites of the HC structure. Depending on the number of Sr adatoms covering the surface, different structures are formed as evidenced by STM.

Labyrinth and honeycomb structures

The phases reported in this section were found in the sample ***A*** (see Sec.4.1) after seven annealing cycles (the giant square-like and the hexagonal approximants were observed previously on this sample). LEED patterns recorded after annealing under UHV and at different positions on the sample are presented in Fig. 4.16. These patterns reveal the inhomogeneity of the structural arrangements. At 20 eV first diffraction order spots allow to have a first idea of the structure. At higher energies, Pt diffraction spots (blue circles) are visible along with higher order diffraction spots revealing the complexity of the surface structures formed. Position 1 shows a diffraction pattern with a dodecagonal symmetry at 20 eV. This dodecagonal pattern is less intense for position 2 and 4. Position 2 shows an hexagonal pattern with spots grouped in three. Position 3 in Fig. 4.16 exhibits a LEED pattern very close to the one observed for the hexagonal approximant. At position 4 and at 20 eV, the LEED pattern looks similar to the one observed at position 2. However, LEED patterns differed at higher energies (50 eV, 110 eV) reveal another complex strucre.

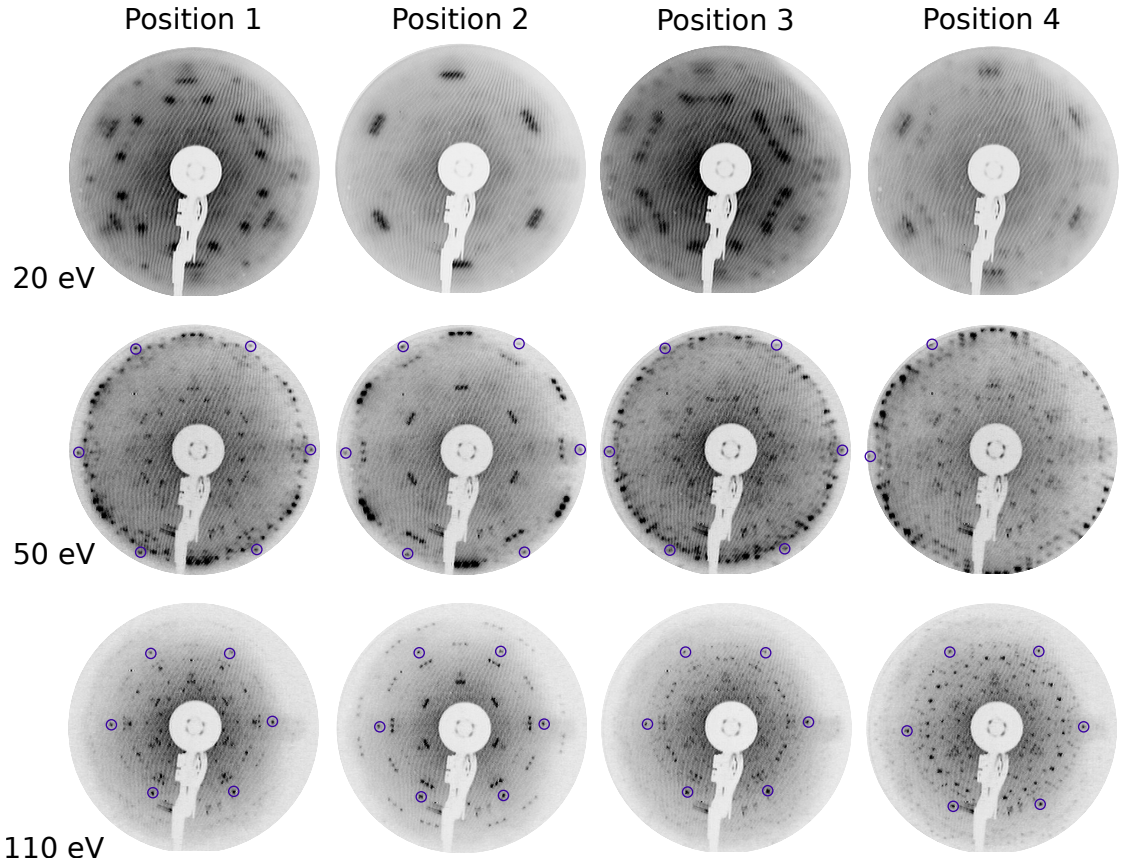

Figure 4.16 – LEED patterns obtained after seven annealing cycles on the sample ***A*** at different positions for a given electron energy. Blue circles highlight the Pt(111) diffraction pattern.

Atomic resolved STM images taken at certain position show a disordered labyrinth-like structure as presented in Fig. 4.17. Wu *et. al* observed similar morphologies on samples where different concentration of Ba atoms were deposited on a TiOx ultra-thin film grown on Au(111) [33]. When increasing the Ba concentration a disordered labyrinth-like phase was observed. This labyrinth morphology has been found as well in 2D magnetic structures such as Ni nanowires [35] and in ferromagnetic garnet thin films where magnetic domains take labyrinth-like patterns [36].

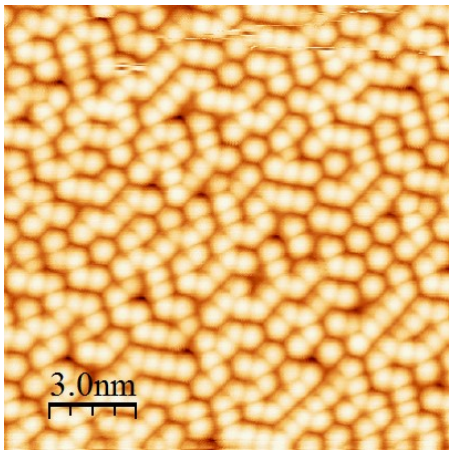

Figure 4.17 – High resolution STM image of the labyrinth phase

On different zones of the surface, more than one structure was found. Fig. 4.18 displays the atomic resolved STM images of four scanned zones and their corresponding FFT, confirming the coexistence of various phases as LEED patterns in Fig. 4.16 suggested. Fig. 4.18 (a) shows the atomic resolved STM image of the labyrinth structure, where the corresponding FFT exposes at least three different hexagonal patterns indicated by the white, pink and green vectors. In another area of the surface, the square-like approximant structure was found as shown in the STM image in Fig. 4.18 (b). The corresponding FFT shows clearly the square periodic lattice where the most intense diffraction spots form a dodecagonal pattern. Exploring a different zone, the hexagonal approximant was observed as well. Fig. 4.18 (c) shows the STM image of the hexagonal approximant structure next to the corresponding FFT which evidences the hexagonal periodic lattice. Fig. 4.18 (d) shows the border between the hexagonal approximant and the labyrinth phase. The corresponding FFT help us to identify the hexagonal lattice (in white) and the vectors observed in the FFT of Fig.4.18 (a). The green spots mark the hexagonal lattice coming from the honeycomb like structure, which will be discussed in the following.

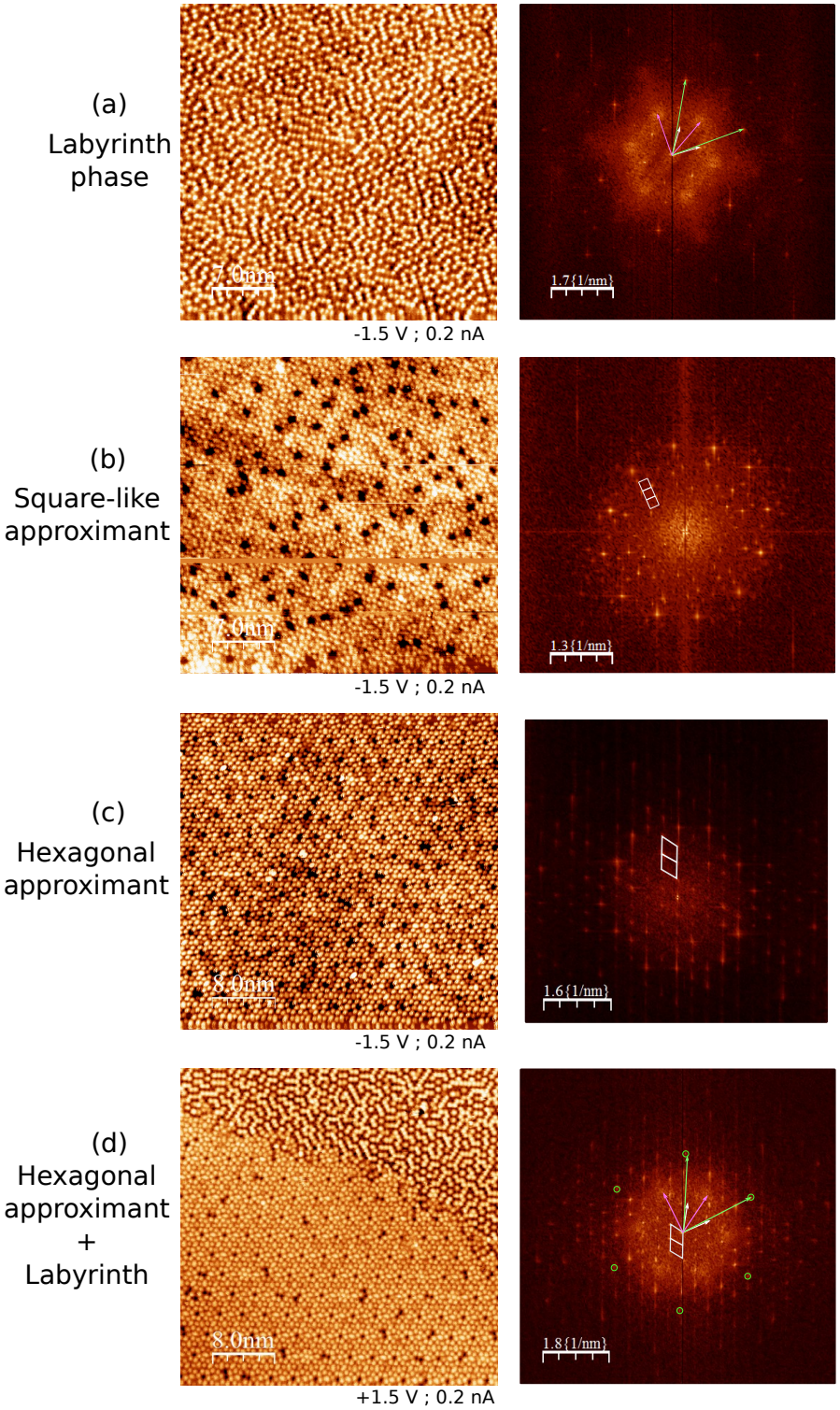

Figure 4.18 – STM images at different zones of the surface after seven redox cycles of the (a) Labyrinth phase, (b) Square-like approx, (c) Hexagonal approx and (c) interface between two phases. The observed phases coexist together.

After eleven annealing cycles, the surface morphology seems to present still some changes. The high resolution STM image in Fig. 4.19 (a) shows bright protrusions located on the top of a HC-like lattice. Based on the studies performed by Wu *et. al.* [34, 33] where a Ti_2O_3(2×2) HC network was grown on Au(111) substrates, and then low concentrations of Ba atoms were evaporated onto the film, we assign the bright protrusions to Sr adatoms which are localized at the hollows of the tentative TiO_x HC lattice.

Fig. 4.19 (b) shows the FFT of (a), where two hexagonal patterns can be identified. The green vectors indicate the reciprocal lattice vectors a* of the honeycomb structure and the green circles mark the first order diffraction spots. White vectors indicate a second structure with a reciprocal lattice vector half of the length of a*. The in plane measured lattice parameters are 5.51±0.08 Å for the HC and 10.72±0.56 Å for the second structure. Fig. 4.19 (c) is a filtered image, where only the HC lattice is visible. The unit cell is marked in green. Fig. 4.19 (d) shows the profile taken along the blue line in Fig. 4.19 (c) giving a lattice parameter of 5.57 ±0.01 Å confirming the previous measure (profiles along different directions rotated by 60° with respect the blue line in (c) were considered as well). This values are in agreement with the reported lattice parameter of the TiO_x HC network (5.9± 0.3Å [34]) supporting our first statement where we assigned the HC structure to a TiO_x lattice with Sr adatoms. Here, this Sr atoms are located (mostly) on one of each two hollows sites of the HC lattice (forming an hexagonal structure with the double of the HC lattice parameter).

Besides, in Fig. 4.18(a) three hexagonal lattices were identified as mentioned previously.
The length of the green, white and pink vectors is 5.50±0.10Å , 10.14±0.22Å and 14.94±0.35Å respectively. This is twice and triple of the length of the HC lattice parameter. Therefore, the labyrinth structure is just the result of the combination of Sr adamtoms located on the top of the HC network with two different occupation rates.

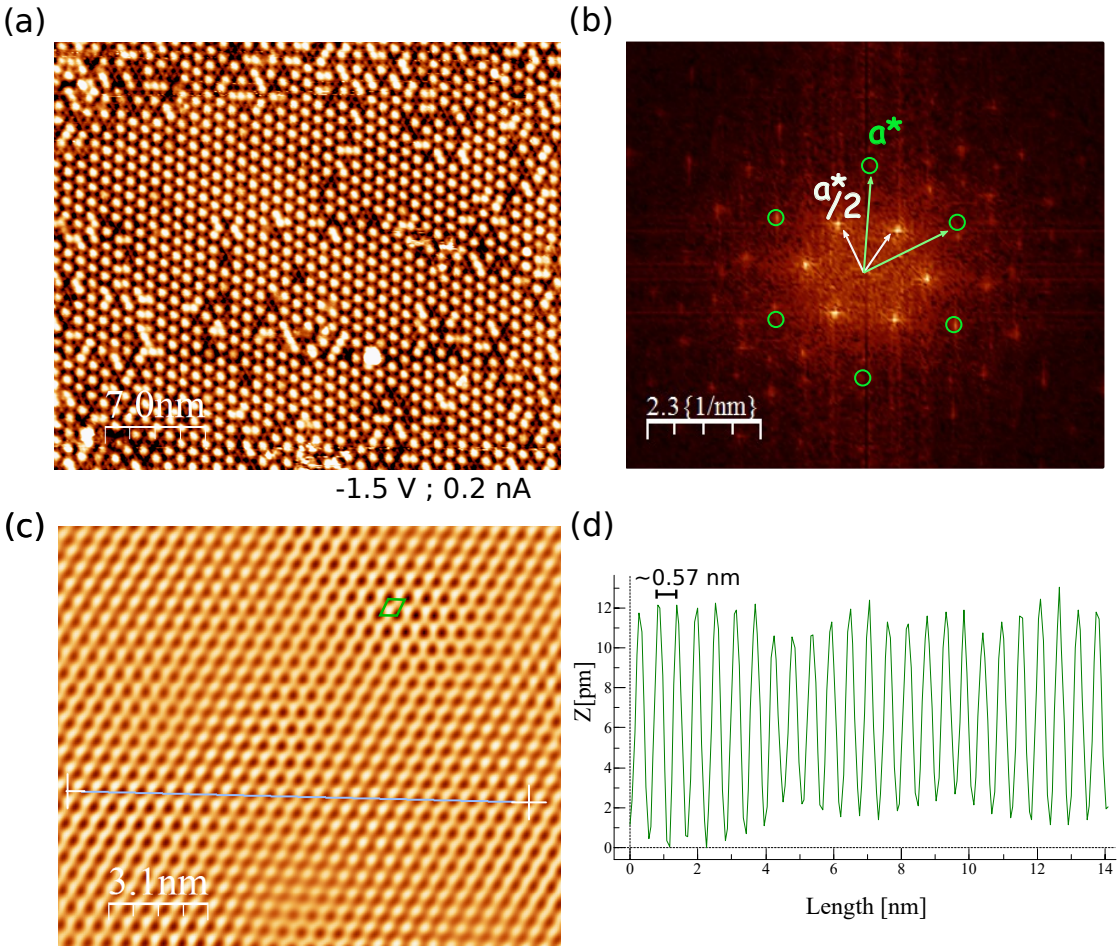

Figure 4.19 – (a) High resolution STM image of the TiO_x honeycomb structure partially covered by Sr atoms (bright protrusions). (b) FFT of (a). Diffraction spots from the honeycomb are marked in green. White vectors indicate the hexagonal pattern coming from the Sr atoms localized on the honeycomb lattice at half of the reciprocal vector of the honeycomb a*. (c) The Honeycomb structure obtained from filtering the green spots marked in (b). The unit cell is indicated in green. (d) Profile taken along the blue line in (c).

This chapter deals with the fabrication of ultra-thin complex phases obtained from $SrTiO_3$ grown on $Pt(111)/Al_2O_3(0001)$. Although the initial target to grow OQCs has not been reached yet, two novel 2D oxide approximants and a new phase has been observed making these results precursor in the field of the OQCs. Besides, the σ-phase approximant was observed for the first time in this system. These structures were obtained after high temperature annealing under high vacuum of the thin film stacking presented in Chap.3. They have been investigated by STM, LEED and DFT. High resolution STM images show bright protrusions located at the node of three different tilings constructed with the same basic square, triangle and 30° rhombus tiles possessing a common edge length of about 6.7 Å. The tile ratio is different for the three phases. The number of tiles needed to describe the square-like approximant is twice as large as for the previously reported monoclinic approximant in the $SrTiO_3/Pt(111)$ system. Using the experimentally derived tilings for these three new phases, structure models have been elaborated by adopting the tile decoration proposed by Cockayne *et al.* [32], in which the Sr atoms are located at the node of the tiling and in which each Ti atom is bound to three oxygen atoms and each oxygen atom is located between two Ti atoms. Thus, the chemical compositions of the triangles, squares and rhombuses are $SrTiO_3$, $SrTi_4O_4$ and $SrTi_2O_2$, respectively, and the global compositions of the square and hexagonal phases are $Sr_{0.36}TiO_{1.54}$ and $Sr_{0.38}TiO_{1.56}$ respectively. The three phases have similar atom densities, formation enthalpies and adhesion energies. Both undergo significant structural relaxation when supported on Pt(111) leading to some buckling of the oxide layer. Charge transfer occurs from most electropositive elements (Sr, Ti) to most electronegative elements (Pt and O). According to the structural optimization, Ti cations lie more closely to the negatively charged Pt substrate compared to O and Sr atoms. Simulated STM images are found in excellent agreement with the experimental ones, thus giving support to the structural models proposed for the two new 2D oxide phases. Accordingly, mainly the Sr atoms are imaged by STM as they are protruding above the mean surface plane of the UTOx thin films, although the main contribution to the DOS originates from Ti atoms. Finally, the DOS calculations for the giant square-like and the hexagonal approximants suggest that the two new UTOx may have different physical and chemical properties.

Other UTOx complex phases were observed as well after increasing the number of annealing cycles. A HC and a labyrinth-like structures were identified by LEED and STM. They appeared normally coexisting at different zones of the surface, along with the approximant phases probably due to an inhomogeneous annealing of the sample surface. The different morphologies observed for these complex phases are assigned Sr adamtoms located on the top of the HC network with two different occupation rates.

As a perspective, it would be necessary to optimize the control of the pressure

and temperature during annealing in order to obtain a unique phase. From the theoretical point of view, the existence of a detailed structure model for OQC approximants, as the one proposed here, is the first step towards a better understanding of quasicrystallinity in UTOx.

Bibliography

[1] S. Förster, M. Trautmann, S. Roy, W. A. Adeagbo, E. M. Zollner, R. Hammer, F. O. Schumann, K. Meinel, S. K. Nayak, K. Mohseni, W. Hergert, H. L. Meyerheim, and W. Widdra. Observation and Structure Determination of an Oxide Quasicrystal Approximant. *Physical Review Letters*, 117(9):095501, 2016.

[2] E. M. Zollner, F. Schuster, K. Meinel, P. Stötzner, S. Schenk, B. Allner, S. Förster, and W. Widdra. Two-Dimensional Wetting Layer Structures of Reduced Ternary Oxides on Ru(0001) and Pt(111). *Physica Status Solidi (B)*, 257(7):1900655, 2020.

[3] S. Schenk, S. Förster, K. Meinel, R. Hammer, B. Leibundgut, M. Paleschke, J. Pantzer, C. Dresler, F. O. Schumann, and W. Widdra. Observation of a dodecagonal oxide quasicrystal and its complex approximant in the $SrTiO_3$-Pt(111) system. *Journal of Physics: Condensed Matter*, 29(13):134002, 2017.

[4] M. Maniraj, L. V. Tran, O. Krahn, S. Schenk, W. Widdra, and S. Förster. Hexagonal approximant of the dodecagonal oxide quasicrystal on Pt(111). *Physical Review Materials*, 5(8):084006, 2021.

[5] F. E. Wührl, O. Krahn, S. Schenk, S. Förster, and W. Widdra. Antiphase Domain Boundary Formation in 2D Ba–Ti–O on Pd(111): An Alternative to Phase Separation. *Physica Status Solidi (B)*, (2100389), 2021.

[6] S. Förster, S. Schenk, E. M. Zollner, O. Krahn, C-T. Chiang, F. O. Schumann, A. Bayat, K-M Schindler, M. Trautmann, R. Hammer, K. Meinel, W. A. Adeagbo, W. Hergert, J. I. Flege, J. Falta, M. Ellguth, C. Tusche, M. DeBoissieu, M. Muntwiler, T. Greber, and W. Widdra. Quasicrystals and their Approximants in 2D Ternary Oxides. *Physica Status Solidi (B)*, 257(7):1900624, 2020.

[7] S. Förster, K. Meinel, R. Hammer, M. Trautmann, and W. Widdra. Quasicrystalline structure formation in a classical crystalline thin-film system. *Nature*, 502(7470):215–218, 2013.

[8] S. Förster, J. Flege, E. M. Zollner, F. O. Schumann, R. Hammer, Al. Bayat, K-M Schindler, J. Falta, and W. Widdra. Growth and decay of a two-dimensional oxide quasicrystal: High-temperature in situ microscopy. *Annalen der Physik*, 529(1-2):1600250, 2017.

[9] C. Ruano M., L. Pasquier, S. Andrieu, K. Dumesnil, J. Ledieu, O. Copie, V. Fournée, and M. Sicot. New quasicrystal approximants in the $SrTiO_3$/Pt(111)/Al_20_3(0001) system. *Proceeding of the ECMetAC Days, online conference*, 2020.

[10] S. Schenk, O. Krahn, S. Förster, and W. Widdra. Dodecagonal oxide quasicrystal approximant with 72 tiling elements. *Proceeding of the ECMetAC Days, online conference*, 2020.

[11] F. Gähler. Crystallography of dodecagonal quasicrystals. *Theoretische Physik, ETH-Honggerberg,*, page 13, 1988.

[12] G. Kresse and J. Hafner. Ab initio molecular dynamics for liquid metals. *Physical Review B*, 47(1):558, 1993.

[13] G. Kresse and J. Hafner. Ab initio molecular-dynamics simulation of the liquid-metal–amorphous-semiconductor transition in germanium. *Physical Review B*, 49(20):14251, 1994.

[14] G. Kresse and D. Joubert. From ultrasoft pseudopotentials to the projector augmented-wave method. *Physical Review B*, 59(3):1758–1775, 1999.

[15] A. H. Larsen. The atomic simulation environment—a Python library for working with atoms. *J. of Phys.: Condens. Matter*, 29:273002, 2017.

[16] P. E. Blöchl. Projector augmented-wave method. *Physical Review B*, 50(24):17953–17979, 1994.

[17] J. Klimes, D. R. Bowler, and A. Michaelides. Chemical accuracy for the van der Waals density functional. *J. Phys.: Condens. Mat.*, 22:022201, 2010.

[18] J. Klimes, D. R. Bowler, and A. Michaelides. Van der Waals density functionals applied to solids. *Physical Review B*, 83:195131, 2011.

[19] S. L. Dudarev, G. A. Botton, S. Y. Savrasov, C. J. Humphreys, and A. P. Sutton. Electron energy loss spectra and the structural stability of nickel oxide: An LSDA+U study. *Physical Review B*, 57:1505, 1998.

[20] J. Goniakowski and C. Noguera. Intrinsic properties of pure and mixed monolayer oxides in the honeycomb structure: M_2O_3 and MM'O_3 (M, M' = Ti, V, Cr, Fe). *Journal of Physical Chemistry C*, 123:7898–7910, 2019.

[21] O. Köksal, S. Baidya, and R. Pentcheva. Confinement-driven electronic and topological phases in corundum-derived 3d-oxide honeycomb lattices. *Physical Review B*, 97:035126, 2018.

[22] J. Goniakowski and C. Noguera. Properties of metal-supported oxide honeycomb monolayers: M_2O_3 and MM 'O_3 on me(111) (M, M' = Ti, V, Cr, Fe; Me = Ag, Au, Pt). *Journal of Physical Chemistry C*, 124:8186–8197, 2020.

[23] T. Trevizam-Dorini, F. Brix, C. Chatelier, A. Kokalj, and E. Gaudry. Two-dimensional oxide quasicrystal approximants with tunable electronic and magnetic properties. *Nanoscale*, 13:10771, 2021.

[24] This software is provided by the Henkelman group (University of Texas) and it can be found at http://theory.cm.utexas.edu/bader.

[25] W Tang, E Sanville, and G Henkelman. A grid-based Bader analysis algorithm without lattice bias. *Journal of Physics: Condensed Matter*, 21(8):084204, 2009.

[26] E. Sanville, S. D. Kenny, R. Smith, and G. Henkelman. Improved grid-based algorithm for Bader charge allocation. *Journal of Computational Chemistry*, 28:899–908, 2007.

[27] R. F. W. Bader. Atoms in Molecules: A Quantum Theory. *Chemical Reviews*, 91:893, 1991.

[28] G. Henkelman, A. Arnaldsson, and H. Jónsson. A fast and robust algorithm for Bader decomposition of charge density. *Computational Materials Science*, 36(3):354–360, 2006.

[29] J. Tersoff and D.R. Hamann. Theory and application for the scanning tunneling microscope. *Physical Review Letters*, 50:1998–2001, 1983.

[30] J. Tersoff and D.R. Hamann. Theory of the scanning tunneling microscope. *Physical Review B*, 31:805, 1985.

[31] K. Momma and F. Izumi. VESTA 3 for three-dimensional visualization of crystal, volumetric and morphology data. *Journal of Applied Crystallography*, 44:1272–1276, 2011.

[32] E Cockayne, M. Mihalkovič, and C. L. Henley. Structure of periodic crystals and quasicrystals in ultrathin films of Ba-Ti-O. *Physical Review B*, 93(2):020101, 2016.

[33] C. Wu, M. R. Castell, J. Goniakowski, and C. Noguera. Stoichiometry engineering of ternary oxide ultrathin films: Ba_x Ti_2O_3 on Au(111). *Physical Review B*, 91(15):155424, 2015.

[34] C. Wu, M. S. J. Marshall, and M. R. Castell. *Surface Structures of Ultrathin TiOx Films on Au(111).* 2011.

[35] J. Escrig, D. Altbir, M. Jaafar, D. Navas, A. Asenjo, and M. Vázquez. Remanence of Ni nanowire arrays: Influence of size and labyrinth magnetic structure. *Physical Review B*, 75(18):184429, 2007.

[36] J. R. Iglesias, S. Gonçalves, O. A. Nagel, and Miguel Kiwi. Modeling two-dimensional magnetic domain patterns. *Physical Review B*, 65(6):064447, 2002.

Conclusions and perspectives

In this thesis, I reported an all thin film approach to investigate perovskite oxides sported on metals (ABO_3/M(111)) in a more versatile and less expensive way than by using single crystal metal substrates. The multilayer stacking consisted in a $SrTiO_3$ thin film deposited by PLD on a Pt(111) buffer epitaxialy grown on Al_2O_3(0001) substrate by MBE. The epitaxial relationships at both the Pt/Al_2O_3 and $SrTiO_3$/Pt interfaces have been characterized by a combination of RHEED, XRD and HRTEM as presented in Chapter 3. It was shown that an additional nm of Ti deposited on top of the Pt layer reduced the interplanar distance and the lattice parameter of the buffer layer reducing the lattice mismatch with the $SrTiO_3$ from 0.4% to 0.1%. HRTEM studies revealed that Ti interdiffuses the Pt layer forming a Pt-Ti solid solution. A local, partial dewetting of the Pt layer was observed by Nano-SAM, when annealing at temperatures above 600°C (T_{Pyro}). Nevertheless, smooth and homogeneous ultra-thin films of about 4 Å of $SrTiO_3$ were deposited on the Pt buffer layer. Thicker oxide films of 8, 20 and 50 Å showed RHEED patterns characteristic of a rough surface, suggesting that $SrTiO_3$ islands are formed at the surface. In fact, the UTOx phases reported in Chapter 4 were obtained from these 3D oxide surfaces supported on a Pt(-Ti)(111) buffer layer grown on Al_2O_3(0001).

Chapter 4 presents the ultra-thin films of oxides (UTOx) phases found at the wetting layer obtained by high temperature annealing of the thin film stacking. Two novel OQC approximants have been discovered: a square-like approximant with a giant unit cell and a large hexagonal approximant. The σ-phase OQC approximant (already found in the $BaTiO_3$/Pt(111) system) was observed for the first time in $SrTiO_3$ supported on Pt(111). Their structures have been investigated by STM, LEED and DFT. High resolution STM images of the three phases show bright protrusions located at the node of three different tilings constructed with the same basic square, triangle and 30° rhombus tiles possessing a common edge length of about 6.7 Å. The tile ratio is different for the three phases. The number of tiles needed to describe the square approximant is twice as large as for the previously reported monoclinic approximant in the $SrTiO_3$/Pt(111) system. Using the experimentally derived tilings for these three new phases, structure models have been elaborated by adopting the tile decoration proposed by Cockayne *et al.* [1], in which the Sr atoms are located

at the node of the tiling and in which each Ti atom is bound to three oxygen atoms and each oxygen atom is located between two Ti atoms. Thus, the chemical compositions of the triangles, squares and rhombuses are $SrTiO_3$, $SrTi_4O_4$ and $SrTi_2O_2$, respectively, and the global compositions of the square and hexagonal OQC approximants are $Sr_{0.36}TiO_{1.54}$ and $Sr_{0.38}TiO_{1.56}$ respectively. The square and hexagonal approximants have similar formation enthalpies and adhesion energies. Both phases undergo significant structural relaxation when supported on Pt(111) leading to some buckling of the oxide layer. Charge transfer occurs from most electropositive elements (Sr, Ti) to most electronegative elements (Pt and O). According to the structural optimization, Ti cations lie more closely to the negatively charged Pt substrate compared to O and Sr atoms. Simulated STM images are found in excellent agreement with the experimental ones, thus giving support to the structural models proposed for the two new 2D oxide phases. Accordingly, mainly the Sr atoms are imaged by STM as they are protruding above the mean surface plane of the UTOx thin films, although the main contribution to the DOS originates from Ti atoms. Finally, the DOS calculations suggest that the two new OQC approximants may have different physical and chemical properties. Additional complex hexagonal phases were observed as well when increasing the number of annealing procedures. A HC lattice and a labyrinth-like structure were observed by STM sometimes coexisting with the square and the hexagonal approximants leading to complex LEED patterns. Depending on the Sr coverage (assigned to the STM bright protrusions) on the top of the TiO_x network different morphologies were formed.

Perspectives

This work represents the first results of the OXYQUASI project. The all-thin-film approach proposed here may be expanded in the future to different families of ABO_3/M(111) systems in order to explore the vast landscape offered by the numerous potential perovskites and metal supports for the discovery of new UTOx 2D materials. For instance, the Pt buffer layer could be replaced by transition metals which grow epitaxially on the α-Al_2O_3(0001) substrate, such as Pd(111) [2] Ir(111) [3] or Ru(0001) [4]. A study concerning the growth of these metals by MBE on Al_2O_3(0001) and the subsequent deposition of ultra-thin films of $SrTiO_3$ by PLD would be needed.

Dorini *et al.* explored computationally more than 60 ABO_3/M(111) systems by permuting the alkali metal A (= Ba, Sr, ans Ca), the transition metal *B* (= Ti, V, Cr, Mn, Fe, Co, Ni) and the metal support M (= Pt, Pd, Au) for the σ phase [5]. The authors found that $BaFeO_3$, $BaCoO_3$ and $BaNiO_3$ are good candidates for structurally stable UTOx when supported on Pt or Au. Besides, these materials could have interesting magnetic properties. Based in this work an ultra-thin film of $BaFeO_3$ could be deposited by PLD on a Pt(111) buffer layer grown on Al_2O_3(0001).

The experimental control of temperature and pressure needs to be improved

during the annealing cycles since several phases were found coexisting at the surface making characterization of a particular UTOx phase difficult. The use of sample plates with no windows contribute to achieve an homogeneous surface annealing. A better pumping system could help to anneal the sample at temperatures above 850°C while maintaining a pressure below 10^{-9}mbar, favouring the obtention of OQCs and OQC approximants.

As the UTOx phases are under stoichiometric in Sr, a Sr source could be installed in order to compensate the Sr deficiency and start over the annealing cycles from a stoichiometric $SrTiO_3$ film.

The electronic structure can be studied by photoelectron emission techniques, in particular angle-resolved photoelectron spectroscopy (ARPES). The possible formation of a 2D electron gas (2DEG) at the surface of an $SrTiO_3$ approximant could be investigated as well. Literature reported that $SrTiO_3$ is the preferred template to create a 2D electron gas [6]. 2D conducting states were observed initially at the interface between $SrTiO_3$ and $LaAlO_3$ [7]. Then, it was discovered at the surface of a bare $SrTiO_3$ single crystal [8]. Therefore, investigation of the 2DEG band structure at the surface of the aproximants discovered in this thesis could be interesting.

So far, the approximants obtained in this thesis have been determined to be one-single layer thick reaching the ultimate 2D limit. We could envisage to regrow on top of such phases thin oxide films as an attempt to obtain thicker approximant or OQCs. if possible, we could therefore study the variation of electronic properties as a function of the thickness of the oxide film.

In addition, a short-term study could be the investigation of the local electronic properties of our samples using low-temperature scanning tunneling microscopy/ spectroscopy (LT-STM/STS). LT-STS gives access to the local density of states with a very low spatial resolution as a function of energy. Such measurements could provide the electronic structure of the approximants with atomic resolution. As an example, a direct comparison between the electronic properties of the different phases could be thus obtain.

These dodecagonal structures could be used as well in nanopatterning. The ordered surface defects observed in the hexagonal OQC approximant (attributed to a vacancy of Sr atoms) may act as nucleation centres for metals deposited on the approximant surface which could lead to the formation of an ordered array of metal nanodots [9].

Other properties of these complex phases, such as catalytic properties could be explored experimentally and theoretically. The most favourable adsorption sites of the approximant phases could be determined by means of *ab initio* calculations, for instance. ABO_3 ternary oxides are materials which contain a transition metal which are well known to be good catalyst. K. Kovnir *et al.* introduced the concept of active-site isolation [10]. Using this approach well defined, stable and site-isolated

catalyst were identified in an intermetallic compound. Using this concept applied for metals in an oxide, could be a beginning to find high selective and stable sites in an OQC approximant.

Bibliography

[1] E Cockayne, M. Mihalkovič, and C. L. Henley. Structure of periodic crystals and quasicrystals in ultrathin films of Ba-Ti-O. *Physical Review B*, 93(2):020101, 2016.

[2] A. Aleman, C. Li, H. Zaid, H. Kindlund, J. Fankhauser, S. V. Prikhodko, M. S. Goorsky, and S. Kodambaka. Ultrahigh vacuum dc magnetron sputter-deposition of epitaxial Pd(111)/Al_2O_3(0001) thin films. *Journal of Vacuum Science & Technology. A*, 36(3):030602, 2018.

[3] Shinji, K., Atsuhito, S, Yuta, S., and Hideyuki, K. Epitaxial growth and electrochemical transfer of graphene on Ir(111)/α-Al_2O_3 (0001) substrates. *Applied Physics Letters*, page 109, 2016.

[4] P. Sutter, P. Albrecht, and E. Sutter. Graphene growth on epitaxial Ru thin films on sapphire. *Applied Physics Letters*, 97:213101–213101, 2010.

[5] T. Dorini Trevizam, F. Brix, C. Chatelier, A. Kokalj, and E. Gaudry. Two-dimensional oxide quasicrystal approximants with tunable electronic and magnetic properties. *Nanoscale*, 13(24):10771–10779, 2021.

[6] S. Gonzalez, C. Mathieu, O. Copie, V. Feyer, C. M. Schneider, and N. Barrett. Room temperature 2D electron gas at the (001)-$SrTiO_3$ surface. *Applied Physics Letters*, 111(18):181601, 2017.

[7] A. Ohtomo and H. Y. Hwang. A high-mobility electron gas at the $LaAlO_3/SrTiO_3$ heterointerface. *Nature*, 427(6973):423–426, 2004.

[8] A. F. Santander-Syro, O. Copie, T. Kondo, F. Fortuna, S. Pailhès, R. Weht, X. G. Qiu, F. Bertran, A. Nicolaou, A. Taleb-Ibrahimi, P. Le Fèvre, G. Herranz, M. Bibes, N. Reyren, Y. Apertet, P. Lecoeur, A. Barthélémy, and M. J. Rozenberg. Two-dimensional electron gas with universal subbands at the surface of $SrTiO_3$. *Nature*, 469(7329):189–193, 2011.

[9] V. Repain, G. Baudot, H. Ellmer, and S. Rousset. Two-dimensional long-range–ordered growth of uniform cobalt nanostructures on a Au(111) vicinal template. *Europhysics Letters (EPL)*, 58(5):730–736, 2002.

[10] K. Kovnir, M. Armbrüster, D. Teschner, T.V. Venkov, F.C. Jentoft, A. Knop-Gericke, Yu. Grin, and R. Schlögl. A new approach to well-defined, stable and site-isolated catalysts. *Science and Technology of Advanced Materials*, 8(5):420–427, 2007.

Résumé La formation d'oxyde quasicristallins dodécagonaux 2D (OQC), ainsi que celle de phases approximantes associées ont été récemment rapportées dans des films minces dérivés des pérovskites $BaTiO_3$ ou $SrTiO_3$, déposés sur des monocristaux de Pt orientés (111). Ces structures 2D ajoutent de nouvelles fonctionnalités aux films ultra-minces d'oxydes ternaires supportés sur des métaux à l'approche de la limite 2D. Ici, nous utilisons une approche d'empilement de couches minces dans laquelle le monocristal est remplacé par une couche tampon de Pt(111), déposée par MBE sur un substrat d'Al_2O_3(0001). Un film ultra-mince de $SrTiO_3$ a ensuite été déposé par PLD. L'empilement de films est entièrement caractérisé par des techniques de diffraction (LEED, RHEED, XRD), de microscopie (STM, Nano-SAM, TEM) et de spectroscopie (XPS, AES). Nous rapportons la découverte de trois nouveaux approximants obtenus par réduction de ce système par recuit à haute température dans des conditions de vide poussé. Ces phases peuvent être décrites par trois pavages différents construits avec des éléments du pavage NGT. Un modèle atomique determiné par DFT, en accord avec les observations expérimentales, est proposé pour chaque approximant. Cette approche en couche mince peut être utile pour explorer la formation de phases d'oxyde 2D complexes dans d'autres combinaisons métal-oxyde.
Mots-clés : Oxydes 2D, approximants d'oxydes quasicristallins, empilement de couches minces, croissance épitaxiale, LEED, STM.

Abstract The formation of 2D dodecagonal quasicrystalline oxides (OQC), as related approximant phases were recently reported in thin films derived from $BaTiO_3$ or $SrTiO_3$ perovskites deposited on (111)-oriented Pt single crystal. These 2D structures add novel functionalities to the ultra-thin films of ternary oxides supported on metals when approaching the 2D limit. Here, we use a thin film stacking approach in which the single crystal is replaced by a Pt (111) buffer layer, deposited by MBE on an Al_2O_3(0001) substrate. An ultra-thin film of $SrTiO_3$ was subsequently deposited by PLD. The film stacking is fully characterized by diffraction (LEED, RHEED, XRD), microscopy (STM, TEM, Nano-SAM) and spectroscopy (XPS, AES) techniques. We report the discovery of three OQC approximants obtained by reducing this system by annealing at high temperature under vacuum conditions. These phases can be described by three different tilings constructed with NGT elements. An atomic model determined by DFT, in agreement with the experimental observations, is proposed for each approximant. This thin-film approach can be useful for exploring the formation of complex 2D oxide phases in other metal-oxide combinations.

Key words: 2D oxides, Oxide quasicrystal approximants, Thin film stacking, epitaxial growth, LEED, STM.